

NORTHWESTERN UNIVERSITY

Engineering Photonic Switches for Quantum Information Processing

A DISSERTATION

SUBMITTED TO THE GRADUATE SCHOOL
IN PARTIAL FULFILLMENT OF THE REQUIREMENTS

for the degree

DOCTOR OF PHILOSOPHY

Field of Electrical and Computer Engineering

By

Neal N. Oza

EVANSTON, ILLINOIS

December 2014

UMI Number: 3669298

All rights reserved

INFORMATION TO ALL USERS

The quality of this reproduction is dependent upon the quality of the copy submitted.

In the unlikely event that the author did not send a complete manuscript and there are missing pages, these will be noted. Also, if material had to be removed, a note will indicate the deletion.



UMI 3669298

Published by ProQuest LLC (2014). Copyright in the Dissertation held by the Author.

Microform Edition © ProQuest LLC.

All rights reserved. This work is protected against unauthorized copying under Title 17, United States Code



ProQuest LLC.
789 East Eisenhower Parkway
P.O. Box 1346
Ann Arbor, MI 48106 - 1346

© Copyright by Neal N. Oza 2014

All Rights Reserved

Abstract

Engineering Photonic Switches for Quantum Information Processing

Neal N. Oza

In this dissertation, we describe, characterize, and demonstrate the operation of a dual-in, dual-out, all-optical, fiber-based quantum switch. This “cross-bar” switch is particularly useful for applications in quantum information processing because of its low-loss, high-speed, low-noise, and quantum-state-retention properties.

Building upon on our lab’s prior development of an ultrafast demultiplexer^[1–3], the new cross-bar switch can be used as a tunable multiplexer *and* demultiplexer. In addition to this more functional geometry, we present results demonstrating faster performance with a switching window of $\simeq 45$ ps, corresponding to >20 -GHz switching rates. We show a switching fidelity of $>98\%$, i. e., switched polarization-encoded photonic qubits are virtually identical to unswitched photonic qubits. We also demonstrate the ability to select one channel from a two-channel quantum data stream with the state of the measured (recovered) quantum channel having $>96\%$ relative fidelity with the state of that channel transmitted alone. We separate the two channels of the quantum data stream by 155 ps, corresponding to a 6.5-GHz data stream.

Finally, we describe, develop, and demonstrate an application that utilizes the switch's higher-speed, lower-loss, and spatio-temporal-encoding features to perform quantum state tomographies on entangled states in higher-dimensional Hilbert spaces. Since many previous demonstrations show bipartite entanglement of two-level systems, we define "higher" as $d > 2$ where d represents the dimensionality of a photon. We show that we can generate and measure time-bin-entangled, two-photon, qutrit ($d = 3$) and ququat ($d = 4$) states with $>85\%$ and $>64\%$ fidelity to an ideal maximally entangled state, respectively. Such higher-dimensional states have applications in dense coding^[4], loophole-free tests of nonlocality^[5], simplifying quantum logic gates^[6], and increasing tolerance to noise and loss for quantum information processing^[7].

Acknowledgments

Since this document will last in perpetuity, I feel it is imperative to recognize *everyone* who has helped me reach this milestone in some way—no matter how small. I know that I am where I am today, not because of my singular efforts, but rather due to the support I have received from the family, friends, mentors, peers, co-workers, and strangers on the journey, thus far. For all their contributions, I am (and eternally will be) thankful.

The logical place to begin is with my twin. Thanks Nick for picking me up when I'm feeling down and pulling me down when I'm feeling up. You're the best friend, constructive competitor, and teammate since day one (or is it month -9?).

Thanks Momzu and Pops for raising us the way you did. Through your laudable personalities filled with kindness, generosity, hard-work, perseverance, humility, intelligence, sacrifice, creativity, positivity, aspiration, interpersonal interaction, and mental/physical strength, we have learned by example how to lead a happy life.

Thank you to my grandparents for giving me such loving parents. Thank you to my cousins, aunts, uncles, nieces, nephews, and other extended relatives for supporting me and blissfully distracting me everytime we meet. An additional thanks to Raj Kakosa for putting NU on my radar, and me on theirs.

Thank you AV, O, and (more recently) Harrison, for making every trip to California another reason to return home.

Thank you to some of my closest friends—Tido, Shyam, Alok, Shamik, Neil, Jason, Sarika, Kavita, Samangi, Nirav, and Ashley—for being such good examples of great people for me to learn from. Also, thanks for making every encounter feel like no time has been lost despite the months between conversations.

Thank you Polly for your unwavering and contagious positivity, effervescence, and desire to improve the world.

Thank you Ryan for the ever-welcome distractions regarding soccer, airbending, or cool science, among many others.

Thank you Mira and Gail for the inevitably late-night hangout sessions, freezing camping, youtube viewing, general bizarreness, and waffles.

Thank you to the Family Friends from way back. Capture the flag, light tag, garage parties, and camping. Need I say more?

Thank you to my friends from elementary, middle, and high school—Gimp, Sandman, Scott, Jeff, Larry, among others—for befriending a pair of undersized guys and treating us like equals regardless of what we did: hockey (roller and floor), hacky-sack, handball, basketball, and football (blacktop and fantasy).

Thank you to the many other classmates, sports teammates, dance teammates, Orange Julius girls, fellow club members, and numerous other friends for the social edification that has helped me become more well-rounded.

Thank you to my SPG friends for providing me with a creative, zany, and hilarious outlet as a contrast to the more logical and structured pursuits of engineering.

Thank you to the Surf For Life volunteers, S4L team, and La Choza Chula team. You epitomize altruism. Now, I understand how the fires of tragedy galvanize the human spirits of camaraderie and generosity. RIP Ajay Ojha (1976-2014).

Thank you to my collegiate and post-collegiate roommates for helping realize what it is like to live with others (and what it is like to live with me).

Thank you to my coaches who taught me to play well in teams: Coach Raul, Coach Ignacio Herrera, Coach Mike Loeber, Coach Gary, Coach Dave Blum, Coach Henke Mao, Coach Randy Drake, Coach Karin Conrad, and Coach John Telfer.

Thank you to the many elementary-, middle-, and high-school teachers I've had for teaching me how to learn, and, equally important, how to teach. For starters, my elementary school teachers for providing the foundation: Mrs. Plambeck, Mrs. Fisher, Mrs. Clonts, Mrs. Wasson née Purvis, Mrs. Brady, Mrs. McRae, Mr. Lack, Mrs. White, Mrs. Jaynes, and Mrs. Emerson. Additionally, my English teachers without whom I wouldn't dream to write a document of this length: Mrs. Lee, Mrs. Hansen, Mr. Lipiani, Mr. Johnson, Mrs. Maser, and Mr. Spain. Also, my arts and crafts teachers for giving me a sense of aesthetic for the figures in this document: Ms. Alexander, Ms. Kwong, Ms. McVeigh, and Mr. Wynn. My social science and spanish teachers for broadening my cultural horizons: Ms. Wallace, Mr. Kelly, Mrs. Arguello, Mr. Borgnino, Mr. Cadenasso, Sra. Henderson, Sra. Wiltsee, and Sra. Morgan. And of course, my math, science, and programming teachers for (hopefully) obvious reasons given this thesis' topic: Mr. Thoma, Mrs. Callahan, Mrs. Swan, Mrs. Rogers, Mrs. Woodruff, Mr. Lund (Jack rocks!), Mr. Beaulieu, Mrs. Gibson, Mr. Gautschi, Mr. Webb (both of them), Mr. Rudner, and Mr. Oza.

Thank you to my many college professors, including Dr. Hua Lee, Dr. Ian Rhodes, Dr. Tim Cheng, Dr. Forrest Brewer, Dr. Steven Denbaars, Dr. Steven Butner, Dr. Selim Shahriar, Dr. S.T. Ho, and Dr. Horace Yuen. A special thank you to Dr. Alan Sahakian for being such a great instructor, TA mentor, and department chairman.

Thank you to Gui Bazan for helping me realize what it means to be down.

Special thanks to Dr. Evelyn Hu, and Dr. Mihai Putinar for helping me get back up.

Thank you to my teaching assistants for being supplemental conduits of information between the professors and us.

Thank you to my students from my days as an undergrad TA, a tutor at SBTS, and a graduate TA for verifying that I actually enjoy teaching. An additional thanks to Albert Sousa and my SBTS families.

Thank you to my peers from MGLC, GLC, and EECS GAB for helping me realize that unity between disparate groups can effect change for the betterment of all.

Thank you to Bruce Lindvall for our long lunches and fun chats about all manner of topics from science outreach to local sports.

Thank you to the entire team at TGS. Special thanks to Dean Dwight McBride, Penny Warren, and Kate Veraldi for your support in my numerous activities academic and non.

Thank you to the many academic staffs who help grease the cogs of bureaucracy. This includes principals, chairs, counselors, IT staffs, lab managers, administrative assistants, and program assistants. At NU, a special thanks to Lana Kiperman, Cindy West, and Carol Surma for your help and guidance on various tasks such as scheduling and purchasing.

Thank you to the many vendors, sales staffs, and engineering teams at numerous companies we have purchased from. A special thanks to the team at Nucrypt (Greg, Dan, Chun, and Shawn) for your countless hours of tech support.

Thank you to the National Science Foundation and Army Research Office for the funding that enabled me to do this research. Thank you to the local NSF IGERT team and Physics department staff for managing the program.

Thank you to my professional mentors: especially Dr. Craig Hawker and Dr. Kenichi Takizawa for seeing potential where others did not. Additional thanks to Dr. Raymond

Thibault, Dr. Joe Cordaro, Bruce Shawler, Todd Gregory, Dr. Nick Dinapoli, and Dr. Aaron Miller for patiently teaching me about fields afar from computer engineering. Further thanks to the many post-docs I have had the pleasure of working with, especially, Oo-Kaw Lim, Amar Bhagwat, Kevin McCusker, and Yu-Ping Huang.

Thank you to the many labmates I have had in both the Hawker and Kumar labs for making them fun, productive places to learn and work. More specifically, thank you to Matt for providing insights and feedback years after you graduated. Thank you Monika for being an excellent physics complement to my engineering background forming, as Joe called us, an “entanglement crack team”. Thank you Tom for your workforce, financial, and brewmaster wisdom. Thank you Tim for your hilarious wit, encouraging me to better utilize my mornings, peanut butter jelly time, and shufflin’ everyday. Thank you Paritosh for your jovial greetings every morning. Thank you Mike for casual (improvised) conversation and for the puzzles. Thank you Sammy (yay multiples!) for being the best protégé ever. Without your patience, skill, and knowledge, our best results would be especially elusive. Last, but not least, thank you to my “arch-nemesis”, Abijith, for whom I could use this space to elaborate lavishly about your greatness, but won’t since it may offend all the humility you possess. Instead, I’ll suffice it to say I only wish we could go back in time to record our countless conversations about topics which run the gamut. It would make for an eclectic, educational, silly book.

Thank you to my committee members, Dr. Hooman Mohseni and Dr. Nate Stern for your time and support, and for ensuring this work is thorough.

A penultimate thank you to two men who I humbly believe have very capably mentored me in the lab. First is Dr. Joe Altepeter, who trained me in ways pertaining to good lab

etiquette and good life ethics. Second is Dr. Greg Kanter, who filled Prof. Kumar's shoes quite adeptly during the end of my graduate student career.

Finally, I'd like to thank my advisor for believing in me, encouraging me, and supporting me in a manner I respond well to: like a respected role model and father figure. Thank you Prof. Prem Kumar. I hope to mentor scores of people as well as you have for all of us.

List of Abbreviations

A	anti-diagonal
ADM	add-drop multiplexer
BS	beam splitter
BPF	band-pass filter
CIRC	circulator
CNOT	controlled NOT gate
CW	continuous wave
CWDM	coarse wavelength division multiplexer
D	diagonal
demux	demultiplexer
DWDM	dense wavelength division multiplexer
DFF	D-type flip-flop
DGF	double grating filter
DRO	dielectric resonator oscillator
EDFA	erbium-doped-fiber amplifier
EM	electromagnetic
EOM	electro-optic modulator
ESA	electrical spectrum analyzer
EPR	Einstein, Podolsky, and Rosen
FPC	fiber polarization controller
FPGA	field-programmable gate array
FWHM	full-width half-maximum
FWM	four-wave mixing
GVD	group velocity dispersion
H	horizontal







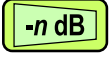


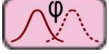








HWP	half waveplate
L	left-circular
LOQC	linear optical quantum computing
LPF	low-pass filter
MEMS	micro-electro-mechanical systems
MUX	multiplexer
MZI	Mach-Zehnder interferometer
NOLM	nonlinear-optical loop mirror
OADM	optical add-drop multiplexer
OSA	optical spectrum analyzer
PBS	polarizing beam splitter
PDD	polarization-dependent delay
PDFA	praseodymium-doped-fiber amplifier
PM	polarization maintaining
R	right-circular
SMF	single-mode fiber
SPM	self-phase modulation
SPD	single-photon detector
TDM	time-division multiplexed
telecom	telecommunications
TOD	tunable optical delay
QIP	quantum information processing
qubit	quantum bit, quantum binary digit
qudit	quantum d -ary digit
qutrit	quantum trinary digit
ququat	quantum quaternary digit
QWP	quarter waveplate
V	vertical
WDM	wavelength division multiplexer
XPM	cross-phase modulation

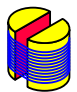
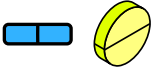
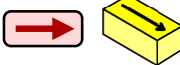


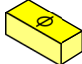

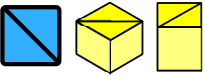






List of Symbols

$\hat{}$	Denotes a matrix (or, rarely, a unit vector)
$\hat{\rho}$	Density matrix used to represent a quantum state
$ \psi\rangle$	Pure quantum state
$ H\rangle$	Horizontally polarized light ($ H\rangle \equiv 0\rangle$)
$ V\rangle$	Vertically polarized light ($ V\rangle \equiv 1\rangle$)
$ D\rangle$	Diagonally polarized light ($ D\rangle \equiv \frac{ H\rangle+ V\rangle}{\sqrt{2}}$)
$ A\rangle$	Anti-diagonally polarized light ($ A\rangle \equiv \frac{ H\rangle- V\rangle}{\sqrt{2}}$)
$ R\rangle$	Right-circularly polarized light ($ R\rangle \equiv \frac{ H\rangle+i V\rangle}{\sqrt{2}}$)
$ L\rangle$	Left-circularly polarized light ($ L\rangle \equiv \frac{ H\rangle-i V\rangle}{\sqrt{2}}$)
$\hat{\sigma}_i$	Pauli matrices ($i \in [0, 3]$)
\mathbb{I}	Identity matrix (Also, a totally mixed state)
$ \phi^\pm\rangle$	Two of the four Bell states ($\frac{1}{\sqrt{2}} (HH\rangle \pm VV\rangle)$)
$ \psi^\pm\rangle$	Two of the four Bell states ($\frac{1}{\sqrt{2}} (HV\rangle \pm VH\rangle)$)
F	Fidelity
T	Tangle
C	Concurrence
S_L	Linear entropy
S	Von Neumann entropy
$ \gamma\rangle$	An arbitrary maximally entangled state
$\text{Tr}(\hat{\rho})$	Trace of a density matrix

Legend for Figures

(Due to 2-D and 3-D versions, some items will have several figures.)

	50- Ω feedthrough terminator
	50- Ω terminator
	Amplitude Modulator
	Beam block
	Circulator (Circ)
	Electrical amplifier
	Electrical attenuator (n dB)
	Electrical cable
	Electrical low-pass filter
	Electrical phase shifter
	Erbium-doped-fiber amplifier (EDFA)
	Faraday mirror
	Fiber/waveguide beamsplitter
	Fiber for C-band (1550-nm) light
	Fiber for O-band (1310-nm) light
	Fiber polarization controller (FPC)
	Fiber spool
	Free-space to fiber collimator/coupler (or vice versa)

	Fiber stretcher (FS)
	Half waveplate (HWP)
	Isolator
	Mirror
	Optical band-pass filter (or coarse WDM)
	Phase Modulator
	Photodetector (can be PIN or Single-photon)
	Polarizing beamsplitter (PBS)
	Power splitter
	Praseodymium-doped-fiber amplifier (PDFA)
	Quarter waveplate (QWP)
	Semiconductor optical amplifier (SOA)
	Tunable optical delay line (TOD)
	Wavelength division multiplexer (WDM) or add-drop multiplexer (ADM)

To Nick,

*For always playing the game hard,
talking the talk, then walking the walk
—or, at least, challenging me to,
smiling throughout our every win,
learning from our every loss,
and being the perfect teammate:
skilled; trusting; honest; intelligent; fun.*



Table of Contents

Abstract	3
Acknowledgments	5
List of Abbreviations	11
List of Symbols	13
Legend for Figures	14
List of Figures	21
Chapter 1. Overview	25
Chapter 2 synopsis: Single-mode fibers and nonlinear optics	28
Chapter 3 synopsis: Introduction to quantum information processing	29
Chapter 4 synopsis: Survey of alternative technologies and demonstrations	29
Chapter 5 synopsis: Generation of pump pulses and photonic entanglement	29
Chapter 6 synopsis: Cross-bar switching operation and performance	30
Chapter 7 synopsis: Generation and measurement of higher-dimensional states	30
Chapter 8 synopsis: Conclusion and future work	30
Chapter 2. Single-Mode Fibers and Nonlinear Optics	31
2.1. Maxwell's equations	31
2.2. Fundamentals of single-mode optical fiber	34

	18
2.3. Nonlinear optics	37
2.4. Quantization of the electric field	44
Chapter 3. Introduction to Quantum Information Processing	50
3.1. Representations of single-qubit states	50
3.2. Representations of multiple-qubit states	55
3.3. Representations of higher dimensional states	57
3.4. Measures of quality of entanglement	63
Chapter 4. Survey of Alternative Technologies and Demonstrations	67
4.1. Survey of optical switching technologies	67
4.2. Survey of entanglement in higher-dimensional Hilbert spaces	72
Chapter 5. Generation of Pump Pulses and Photonic Entanglement	75
5.1. Generation of XPM pump pulses	76
5.2. Generation of FWM pump pulses	83
5.3. Photon-pair source	99
5.4. Time-bin entanglement source	105
5.5. Polarization entanglement source	106
Chapter 6. Cross-bar Switching Operation and Performance	109
6.1. All-optical changeover quantum switch	110
6.2. All-optical cross-bar quantum switch	116
6.3. Cross-bar switch characterization	118
6.4. Polarization-entanglement retention characterization	126
6.5. High-speed demultiplexing of a quantum data stream	128

	19
Chapter 7. Generation and Measurement of Higher-Dimensional States	133
7.1. Project overview	134
7.2. Detailed experiment	137
7.3. Higher-dimensional state reconstruction	146
7.4. Experimental results	150
Chapter 8. Conclusion and Future Work	162
8.1. Future work	164
References	171
Appendix A. Dark-Count Subtraction Calculations	186
A.1. Dark-count-subtracted coincidences	187
A.2. Calculated and dark-count-subtracted accidentals	189
Appendix B. Tomographic Simulations	191
B.1. Example tomography simulation code	193
B.2. Code used to obtain error bars for tomography measurements	197
Appendix C. Real-time Entangled Photon Polarimetry	198
C.1. Introduction	198
C.2. Two-qubit polarimetry	199
C.3. Building the polarimeter	202
C.4. Hardware	207
C.5. Software	215
C.6. Characterization and calibration	221
C.7. Experimental details	223

	20
C.8. Entangled photon polarimeter performance	227
C.9. Troubleshooting	230
C.10. Derivation of polcon driving equations	231
Appendix D. Interfacing with various lab equipment	236
D.1. Determining the serial port for a connected device	236
D.2. Setting up minicom	238
D.3. Interfacing with and Plotting from Lab Instruments	241
Appendix E. Dirac Bracket Notation, Linear Algebra, and Hilbert Spaces	257

List of Figures

2.1	Core and cladding of SMF-28	35
3.1	Limits for states that violate higher-dimensional Bell inequalities	64
5.1	First-generation XPM pump pulse preparation	77
5.2	Second-generation XPM pump pulse preparation	78
5.3	Autocorrelation of new XPM pulses	81
5.4	Third-generation XPM pump pulse preparation	83
5.5	Original FWM pulse-chopping system	85
5.6	Example of 2:1 MUX as an AND gate	86
5.7	First-generation FWM pulse-picking system	88
5.8	Second-generation FWM pulse-picking system	90
5.9	Third-generation FWM pulse-picking system	91
5.10	Fourth-generation FWM pulse-picking system	93
5.11	Fifth-generation FWM pulse-picking electronics	95
5.12	Autocorrelation of filtered O-band pulses	98
5.13	Correlated Photon Pair Source	99
5.14	Photon-pair production rate characterized using both detectors	101
5.15	Example of measured coincidence and accidental counts	102

5.16	Coincidence-to-accidental ratio vs pump power	103
5.17	Coincidence-to-accidental ratio vs coincidence counts	104
5.18	Polarization-entangled photon pair source	107
6.1	Changeover quantum switch	111
6.2	Explanation of the switching window	113
6.3	Cross-bar quantum switch	117
6.4	Test setup for cross-bar switch characterization	118
6.5	Classical contrast characterization of cross-bar switch	120
6.6	Classical switching window characterization of cross-bar switch	121
6.7	Passively minimized 10-GHz switching using fifth-generation FWM electronics	122
6.8	Passively maximized 10-GHz switching using fifth-generation FWM electronics	122
6.9	Single-photon switching window characterization	124
6.10	Coincidence-count switching window characterization	125
6.11	Entanglement retention through cross-bar switch (Input A)	127
6.12	Entanglement retention through cross-bar switch (Input B)	127
6.13	Experimental TDM-MI schematic	128
6.14	Demultiplexing one-channel from two-channel quantum data stream	130
7.1	Overview of proposed higher-dimensional Hilbert space experiment	134
7.2	Overview of higher-dimensional Hilbert space experiment	137
7.3	Clock and synchronization electronics	138
7.4	XPM pump pulse preparation	139

7.5	FWM pump pulse preparation	140
7.6	Photon-pair source for time-bin entanglement	142
7.7	UMZI to map time-bin superpositions onto the polarization bases	142
7.8	UMZI polarization stability	144
7.9	Cross-bar switch for selecting a time-bin	145
7.10	Polarization analyzers to measure polarization state	146
7.11	Measured density matrix for a time-bin-entangled qubit state	151
7.12	Qubit and qutrit tomography simulations	153
7.13	Measured density matrix for a qutrit state at low power	155
7.14	Measured density matrix for a qutrit state at an intermediate power	156
7.15	Measured density matrix for a qutrit state at high power	157
7.16	Qubit and qutrit fidelity vs coincidence counts per measurement	158
7.17	Measured density matrix for a ququat state	160
B.1	Flowchart for tomographic simulations	192
C.1	Tomographic simulations of polcon performance	201
C.2	High-level block diagram of the polcon	203
C.3	Polcon connections	204
C.4	Model of circuitry for each stage of the polcon	209
C.5	Electrical schematic of the amplifier circuitry	209
C.6	Heat sink assembly	210
C.7	Electrical schematic of the power supply	211

	24
C.8 High-level diagram showing the cable connections	213
C.9 Pinout numbering for male and female DB-25 connectors	214
C.10 Experimental schematic of polcon test setup	224
C.11 Frames from polcon video using Altepeter visualization	228
C.12 Frames from polcon video showing transition of a quantum state	229
C.13 Cross-section of the index ellipsoid	233
E.1 Soccer field as a Hilbert space	258

CHAPTER 1

Overview

Buoyed by lofty goals of outperforming classical counterparts for particular applications—e.g., rapidly factoring numbers^[8], performing quick unsorted searches^[9], and ensuring cryptographic security^[10,11]—*quantum information processing* (QIP) has rapidly developed over the past three decades. These developments have required researchers from various disciplines, including engineering, mathematics, physics, computer science, and materials science, to collaborate on various implementations. Their efforts have yielded QIP demonstrations in technologies such as nuclear magnetic resonance spins^[12,13], Bose-Einstein condensates^[14,15], atom- & ion-traps^[16–19], quantum dots^[20,21], superconducting circuits^[22,23], diamond-based NV centers^[24], rare-earth-ion-doped crystals^[25], and photons^[26–28].

Although there is some debate^[29–31], common consensus believes that, for any practical, scalable, real-world applications, the field requires further developments to realize the lofty promises in any of the aforementioned mediums. Fortunately, the telecommunications (telecom) industry has *very* successfully used photons as practical information carriers. Transmission of photons between various parties is rapid, robust, and reliable. Additionally, manipulating a photon is well understood for its various degrees of freedom. As such, our lab opts to use photons—often from the telecom band—as our information carrier for QIP.

A critical resource for many QIP systems is the ability to generate entanglement. We can loosely analogize this phenomenon using a pair of coins. We say these coins are “entangled” if flipping the coins produce random, yet correlated results. In others words, if we flip one

coin, we will randomly obtain a heads or tails. When we flip the other coin, we find that its result will always be identical to the first. If prepared appropriately, this completely random, yet perfectly correlated behavior between the coins happens instantly regardless of the physical separation between the two coins. Based on our day-to-day interactions, this should be very surprising since we are unaware of any other phenomenon that behaves across vast distances instantly.

In fact, in March 1947, Albert Einstein wrote a letter to Max Born describing entanglement as “spukhafte Fernwirkung”, translated as “spooky action at a distance”. He and his colleagues, Boris Podolsky and Nathan Rosen, famously decried entanglement as evidence that quantum theory was incomplete^[32]. Fortunately, following the initial efforts of John S. Bell, we know now that the principle of locality, upon which Einstein and others based their argument against entanglement, is not a required condition of nature^[33]. Many scientists have since verified the existence of entanglement; google “Bell’s inequality violations” for evidence. Others have employed entanglement for QIP demonstrations such as Shor’s algorithm^[12,34], and quantum teleportation^[35,36]. For other QIP applications, such as the BB84 quantum key distribution protocol^[10], we do not require entanglement, but instead just a correlated-particle source.

As such, our group has previously demonstrated several photon-pair, and photon-based entanglement sources^[37–41]. Other groups—most specifically the Takesue group—have also demonstrated entangled-pair and photon-pair sources for the telecom band^[42–44]. As alluded to earlier, telecom-band QIP is a beneficiary of the many decades of prior investment and development that yielded mature technologies—such as the internet—and cheaper components. Additionally, when we overcome the experimental challenges for photonic QIP, part of

the present network of fibers can immediately be used for point-to-point information transfer since much of the fiber around the globe is currently "dark", i. e., unused.

Unfortunately, this network cannot be used as-is. Current photon routers and repeaters, which detect the incoming light and re-emit a new pulse to the appropriate destination, destroy the quantum state of any QIP photon. Hence, new switches and routers need to be developed. Prior members in our group laid down groundwork towards realizing photonic QIP in the O-band (1260-1360 nm). In this thesis, we will investigate projects that parlay their efforts to further promote the use of photonics for QIP applications. The first project focuses on the further development of switching technology for quantum information applications. The new work shown in this thesis primarily involve improvements to the switch's functionality, via the addition of a second input, and demonstrations of higher rate switching performance.

The second project uses the switch in a unique application that measures two-photon entanglement in higher-dimensional Hilbert spaces. Such entanglement is useful for other QIP applications such as dense coding^[4], more robust quantum information transfer^[7], simpler quantum logic gates^[6], and loophole-free tests of nonlocality^[5]. Additionally, since it is a largely unexplored space, there is potential for applications yet unknown to researchers. Since many prior realizations of entanglement have been two-particle, two-bases demonstrations, for the purposes of this thesis, we define *high-dimensional* or *higher-dimensional* as any system that is larger than two bases per photon. We will investigate this definition further in Chp. 3.

In order to test and use higher-dimensional states, we must first generate them. In many cases, such as the demonstration shown in this thesis, generation of higher-dimensional entanglement is not too difficult. Unfortunately, the ability to manipulate such states and

then measure them is more challenging. Even authors Imre and Gyongyosi recognize this in their book, “Advanced Quantum Communications: An Engineering Approach”, when they say, “We can also immediately note that a qutrit can contain more information than a two-level qubit, however, the manipulation of these quantum systems is still very difficult”. The aforementioned “qutrit” is an example of one such higher-dimensional state. Although still challenging, one of the goals of our implementation for higher-dimensional states is to better enable their manipulation and measurement. Fortunately, the switch we developed for the first project is such an enabler.

For both of these projects, we must first generate the desired signals that we wish to switch and/or measure. As such, part of this dissertation also describes the systems employed to create narrow (<100 ps) pulses that arrive at high rates (up to 10 GHz) for use in generating and routing single photons with similar characteristics.

In the following sections, we provide an outline for the remainder of this dissertation with the intent of summarizing the topics found in each chapter.

Chapter 2 synopsis: Single-mode fibers and nonlinear optics

We begin the dissertation by laying the theoretical, mathematical, and conceptual groundwork for the forthcoming discussion. We start by explaining introductory ideas for electromagnetic wave propagation in a medium, more specifically, single-mode fibers. Developing on this, we delve into an introduction of nonlinear optics phenomena observed in optical fibers. This will specifically focus around cross-phase modulation and four-wave mixing since these two phenomena play important roles in our experiments. We then look at these phenomena again, except under the lens of quantum mechanics.

Chapter 3 synopsis: Introduction to quantum information processing

In the third chapter, we present the appropriate discussion to understand quantum states. We start by presenting the definitions and notations for a single qubit (quantum binary digit). We then look at multiple qubits and the implications for phenomena such as entanglement. The next section moves from qubits to qudits, states that have more than two bases, i. e., states that are not binary. We finish the chapter by briefly defining various metrics which can quantify the quality of a quantum state.

Chapter 4 synopsis: Survey of alternative technologies and demonstrations

Chapter 4 investigates the efforts of other groups to realize comparable goals as the experiments presented in this dissertation. We break this up into two sections: the first is a look at alternative switching technologies for single-photons; the second is a look at demonstrations for alternative higher-dimensional state creation and measurement.

Chapter 5 synopsis: Generation of pump pulses and photonic entanglement

In this chapter, we turn our attention to the systems we use to generate the various signals required to test our switch. These entail the generation of optical pulses that will later be used to activate our switch. Additionally, we describe the systems used to produce our entangled photon pairs. Since both of these systems must be synchronized, we devote a decent portion of this chapter to look at the electronics that we use to carve or pulse-pick the respective optical pulses. Since this was a significant effort, we describe the various generations of designs. Each iteration is accompanied by a brief discussion of the problems observed with that design motivating the modifications for the next iteration of the design. We conclude the chapter with a discussion of how to use the generated test pulses to create

entangled photons in fiber. The entangled pair discussion is divided between generating time-bin entanglement and polarization entanglement.

Chapter 6 synopsis: Cross-bar switching operation and performance

This chapter is dedicated to discussing the switches developed in our lab. We begin by briefly detailing the operation of simpler one-input, two-output switch^[1-3]. Once we understand how that switch works, we segue the discussion to the operation of the two-input, two-output (cross-bar) switch. We then characterize the cross-bar switch classically. Next, we look at the single-photon characterizations of the switch. We finish with a demonstration of the cross-bar switch's ability to select one channel from a two-temporal-channel quantum data stream.

Chapter 7 synopsis: Generation and measurement of higher-dimensional states

Chapter 7 describes our efforts to generate, manipulate, and measure higher-dimensional, time-bin-entangled states. We begin this chapter with an operational overview of the various components needed to create and measure such quantum states. We follow this with an in-depth look at the various subsystems and their respective purposes for the experiment. We finish the chapter with experimental results demonstrated for qubit states, qutrit states, and ququat states.

Chapter 8 synopsis: Conclusion and future work

We briefly conclude the dissertation with a recap of the work performed and the results obtained. We then extend the discussion to see what the future holds for the technologies described herein. The look into the future is broken down into near-term tasks, medium-term options, and long-term possibilities.

CHAPTER 2

Single-Mode Fibers and Nonlinear Optics

This chapter establishes the appropriate groundwork to discuss all of the fiber-optics-related concepts, phenomena, and experiments in latter chapters. We begin with a brief introduction to Maxwell's equations, which describe the propagation of electromagnetic (EM) waves. We then extend this framework to discuss, more specifically, the propagation of EM waves in optical fibers, the medium of interest for this dissertation. In that discussion, we address the specific parameters needed for the experiments described later in the thesis. In the following section, we further extend our understanding of EM propagation in optical fiber to describe the nonlinear optical effects, such as cross-phase modulation and four-wave mixing, that we utilize for our experiments. The mathematical treatment provided in this document follows the derivations available from Agrawal^[45]. We then conclude with a look at the quantum-mechanical treatment of the nonlinear processes.

We remark here that much of the material covered in this chapter can be found in numerous and various types of texts and resources. Hence, this chapter and the next also serve to unify notation for the remainder of this dissertation.

2.1. Maxwell's equations

Any discussion of optics would be remiss if Maxwell's equations were not the beginning of the discussion. Maxwell's equations, shown in Eq. (2.1), unify the field of EM theory. They mathematically describe the behavior of electric charges (electric currents) as sources

of electric (magnetic) fields. They also describe the interaction between time-varying electric and magnetic fields.

$$\nabla \cdot \mathbf{D} = \rho_f \quad (2.1a)$$

$$\nabla \cdot \mathbf{B} = 0 \quad (2.1b)$$

$$\nabla \times \mathbf{E} = -\frac{\partial \mathbf{B}}{\partial t} \quad (2.1c)$$

$$\nabla \times \mathbf{H} = \mathbf{J}_f + \frac{\partial \mathbf{D}}{\partial t} \quad (2.1d)$$

$$\mathbf{D} = \epsilon \mathbf{E} = \epsilon_0 \mathbf{E} + \mathbf{P} \quad (2.1e)$$

$$\mathbf{B} = \mu_0 (\mathbf{H} + \mathbf{M}) \quad (2.1f)$$

Here \mathbf{E} is the electric field (V/m), \mathbf{H} is the magnetic field (A/m), \mathbf{D} is the electric flux density (C/m²), \mathbf{B} is the magnetic flux density (V·s/m²), ρ_f is the free charge density (C/m³), \mathbf{J}_f is the free current density (A/m²), \mathbf{P} is the electric polarization (C/m²), and \mathbf{M} is the magnetization (A/m). $\epsilon_0 = 8.8542 \times 10^{-12}$ F/m is the vacuum permittivity, and $\mu_0 = 4\pi \times 10^{-7}$ H/m is the vacuum permeability (H/m).

We note that we are using Maxwell's "macroscopic" equations, thus we ignore the individual bound charges and bound currents from a dielectric medium's atoms' and molecules' electric dipole moment and magnetic moment. Instead, we bundle their cumulative effect into the terms for electric polarization and magnetization. We also note here that bold-face terms denote vectors that are functions of space and time. This notation will apply for the remainder of this thesis. Finally, at optical frequencies or for the optical mediums used in this research, where there are no free electrons, we can safely make the approximations $\mu = \mu_0$, $\rho_f = 0$, $\mathbf{J}_f = 0$, and $\mathbf{M} = 0$.

By taking the curl of Eq. (2.1c) and substituting in Eq. (2.1d), we get

$$\nabla \times \nabla \times \mathbf{E} = -\frac{\partial}{\partial t}(\nabla \times \mathbf{B}) = -\mu\epsilon \frac{\partial^2 \mathbf{E}}{\partial t^2} \quad (2.2)$$

Using the vector identity $\nabla \times \nabla \times \mathbf{V} = \nabla(\nabla \cdot \mathbf{V}) - \nabla^2 \mathbf{V}$ on Eq. (2.2), we obtain the wave equation in a linear medium

$$\nabla^2 \mathbf{E} - \frac{\epsilon_r}{c^2} \cdot \frac{\partial^2 \mathbf{E}}{\partial t^2} = 0 \quad (2.3)$$

where $c = \sqrt{1/\mu_0\epsilon_0}$ is the speed of light in a vacuum, a universal constant, and ϵ_r is the relative permittivity of the medium. The general solution to the wave equation takes the form of $f(\omega t - \mathbf{k} \cdot \mathbf{r})$. We note here that the angular frequency is defined as $\omega = 2\pi c/\lambda$ (radians/s), and the wavenumber of the wavevector \mathbf{k} is defined as $k = |\mathbf{k}| = 2\pi/\lambda$ (radians/m). For completeness, we show the trivial relations $c = \nu\lambda = \omega/k$ where ν is the ordinary frequency of our EM wave.

We introduce here the concept of the refractive index n , which defines the speed of light (or electromagnetic field) travelling in a medium, v , according to the relation $n = c/v = \sqrt{(\epsilon/\epsilon_0)(\mu/\mu_0)}$. Here, ϵ is the electric permittivity of the medium. In order to more clearly define ϵ , we write the definition of electric polarization of a linear medium as

$$\mathbf{P} = \epsilon_0\chi\mathbf{E} \quad (2.4)$$

where χ is the electric susceptibility (unitless) of the medium. Based on this equation, it is trivial to deduce that $\epsilon = \epsilon_0\epsilon_r = \epsilon_0(1 + \chi)$ and $\mathbf{D} = \epsilon\mathbf{E}$ using the electric constitutive relation, Eq. (2.1e). Thus far, we have assumed a nondispersive medium, but if the EM wave is in a dispersive medium, then χ behaves as a function of the frequency of the EM wave. This is justified because a medium cannot polarize immediately. This response time

defines a frequency dependence. As a result of this frequency dependence of the electric susceptibility, we see that the refractive index is also frequency dependent. Thus we remark that from this point forth, when we use n , it actually means $n(\omega)$. Fortunately, for small deviations from a central ω , the dispersion is relatively constant thereby justifying treating n as a constant.

2.2. Fundamentals of single-mode optical fiber

Now that we have established a basic platform for discussion of EM waves propagating through a medium, we turn our focus to the medium. For the research presented here, our focus will predominantly be on propagation through optical fiber and occasionally through air. The motivation for using optical fiber is that it is one of the lowest loss mediums for photon propagation. Additionally, fiber optics is a well-developed technology built upon decades of investment from the telecom industry thereby making it compact and affordable. Although there are many types of fibers, we limit the discussion to the commonly available single-mode fiber—often called SMF or SMF28—since that is what we use in all of the experiments discussed in this thesis.

Aptly named, SMF only guides one transverse mode (or electromagnetic profile). The guiding happens using the process of total internal reflection. The mode that propagates through the fiber is defined by the material's properties, especially its geometry and molecular composition.

The standard SMF fiber we use (Corning SMF-28e) is an example of a step-index fiber. Step-index fiber is a type of fiber composed of two regions, the core and the cladding. These regions are different in their size and material composition. The core has an index of refraction n_1 , while the cladding has a smaller index of refraction n_2 . We now introduce the

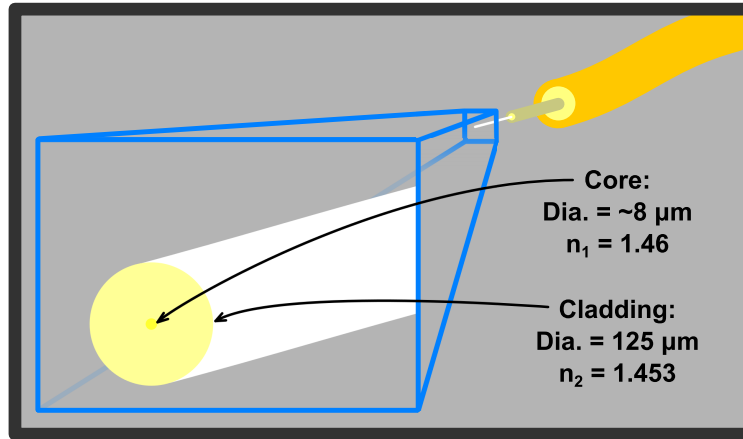


Figure 2.1. The typical diameter of the core of SMF-28 is $\simeq 8 \mu\text{m}$. The diameter of the cladding is $125 \mu\text{m}$. Most of the guided wave exists in the core, and propagates down the fiber due to total internal reflection caused by the difference in the indices of refraction between the core ($n_1 = 1.46$) and cladding ($n_2 = 1.453$). Figure is not to scale.

V number, or normalized frequency, for an optical fiber.

$$V = k_0 a \sqrt{n_1^2 - n_2^2} \quad (2.5)$$

where k_0 is the wavenumber in vacuum, and a is radius of the core.

If $V < 2.405$, the fiber is defined to be single-mode. Typical values for SMF-28e are core radius $a = 4.1 \mu\text{m}$, cladding radius $b = 62.5 \mu\text{m}$, $n_1 = 1.46$, and $n_2 = 1.453$. Using these values, it is easy to see that $k_0 < 4.859 \mu\text{m}^{-1}$, i.e. $\lambda > 1290 \text{ nm}$. This fact is convenient as it allows us to use the same medium for propagation of signals in the O-band (1260-1360 nm) and the C-band (1530-1565 nm). As you will see later, photons from both of these bands are used in our experiments.

Once again, we find that our discussion has been done with dispersion in absentia. Of course, we realize that in real-world systems, dispersion is present. Intuitively, we can imagine an EM wave propagating down a step-index waveguide. By comparing the ratio of

the wavelength to the core radius, we see that if the EM wave has a shorter wavelength, the electric field will have better confinement in the core, i. e., less of the propagating wave will exist in the evanescent wave travelling in the cladding. By varying the wavelength, while still adhering to the single-mode condition specified, we find that the “effective index” experienced by the EM wave varies with wavelength since varying amounts of the EM wave will exist in the core and cladding. It is conventional to define here the mode-propagation constant $\beta(\omega) = n(\omega)\omega/c_0$. Since it is difficult to derive an explicit functional form of β , it is conventionally expressed using its Taylor expansion,

$$\beta(\omega) = \beta_0 + \beta_1 \cdot (\omega - \omega_0) + \frac{\beta_2}{2} \cdot (\omega - \omega_0)^2 + \dots + \frac{\beta_m}{m!} \cdot (\omega - \omega_0)^m + \dots \quad (2.6)$$

where

$$\beta_m = \left(\frac{d^m \beta}{d\omega^m} \right)_{\omega=\omega_0}, (m = 0, 1, 2, \dots) \quad (2.7)$$

and ω_0 is the central frequency of the pulse spectrum. For fiber optics, we often limit the discussion to just β_1 and β_2 , explicitly written below.

$$\beta_1 = \frac{1}{c_0} \left(n + \omega \frac{dn}{d\omega} \right) = \frac{n_g}{c_0} = \frac{1}{v_g} \quad (2.8)$$

$$\beta_2 = \frac{1}{c_0} \left(2 \frac{dn}{d\omega} + \omega \frac{d^2 n}{d\omega^2} \right). \quad (2.9)$$

We use this opportunity to introduce the terms n_g and v_g for the group index and group velocity, respectively. We also remark that β_2 represents the group velocity dispersion. This describes how quickly the pulse broadens over time.

Rather than using the frequency of light in fiber optic systems, the wavelength of the propagating beam is commonly used in literature and among optics engineers. As such, we

define the dispersion parameter D as follows:

$$D = \frac{d\beta_1}{d\lambda} = -\frac{2\pi c_0}{\lambda^2} \beta_2 \quad (2.10)$$

We remark here that for a given input wavelength, if $D < 0$, we are operating in the “normal” dispersion regime, and if $D > 0$, we are operating in the “anomalous” dispersion regime. Based on this, we can then define a wavelength λ_D for which $D = 0$. We refer to this wavelength as the zero-dispersion wavelength of the medium. We note that the optical pulses still experience some dispersion due to higher-order dispersion effects. For pure bulk-fused silica fiber, λ_D is approximately around 1.27 μm . By adjusting the doping and geometry of this fiber, λ_D can be shifted up to 1.31 μm , which is the condition for SMF-28e, the fiber we use in the experiments presented in this thesis.

2.3. Nonlinear optics

We have discussed Maxwell’s equations, which describe how EM fields propagate through mediums. We have also discussed optical fibers since they are our choice of medium. We now focus our attention to what happens to the EM fields in a medium when higher intensities of the field are present. Under such situations, we incite a nonlinear response from the medium. For completeness, we define intensity as $I \triangleq n c \epsilon_0 |E|^2 / 2$, where E is the complex amplitude of the electric field \mathbf{E} .

2.3.1. Introduction of $\chi^{(3)}$

Previously, when we introduced the polarization term \mathbf{P} in Eq. (2.4), we noted it was for a linear medium. At higher intensities of light, the dielectric medium reacts more strongly with the field and behaves nonlinearly. In order to understand this, we start by rewriting

Eq. (2.4) into its power series decomposition,

$$\mathbf{P} = \epsilon_0 \left(\chi^{(1)} \mathbf{E} + \chi^{(2)} : \mathbf{E}\mathbf{E} + \chi^{(3)} : \mathbf{E}\mathbf{E}\mathbf{E} + \chi^{(4)} \mathbf{E}\mathbf{E}\mathbf{E}\mathbf{E} + \dots \right) \quad (2.11)$$

where $\chi^{(m)}$ for $(m = 1, 2, 3, \dots)$ is the m th order electric susceptibility. Note that the first term typically dominates, and contributes to the linear treatment earlier. It also contributes to the ϵ_r coefficient in Eq. (2.3). Hence, we recognize the terms $\chi^{(2)}$ and higher as the components that contribute to higher order nonlinear phenomena. $\chi^{(2)}$ is responsible for phenomena like sum-frequency generation, and second-harmonic generation in other mediums, but in isotropic medium like optical fiber, it and all other even-order susceptibilities are necessarily zero due to symmetry arguments. As such, the dominant nonlinear term for fiber is the $\chi^{(3)}$ term. Equipped with this knowledge, we rewrite Eq. (2.3) as

$$\nabla^2 \mathbf{E} - \frac{1}{c_0^2} \cdot \frac{\partial^2 \mathbf{E}}{\partial t^2} = -\mu_0 \frac{\partial^2 \mathbf{P}_L}{\partial t^2} - \mu_0 \frac{\partial^2 \mathbf{P}_{NL}}{\partial t^2} \quad (2.12)$$

where the linear part is described by $\mathbf{P}_L = \epsilon_0 \chi^{(1)} \mathbf{E}$ and the nonlinear part is described by $\mathbf{P}_{NL} = \epsilon_0 \chi^{(3)} \mathbf{E}\mathbf{E}\mathbf{E}$. Higher order terms can safely be ignored due to the negligibly small values of the susceptibilities in optical fiber.

For this thesis, the two nonlinear phenomena of most importance are cross-phase modulation (XPM), in which one strong field affects the phase of another co-propagating field, and four-wave mixing (FWM), in which two photons scatter in the medium generating two other photons. Unfortunately, we also see other phenomena, more specifically self-phase modulation (SPM) and Raman scattering, which work against our goals. As such, in the proceeding sections, we will investigate all of these phenomena.

2.3.2. Phase modulation in Optical Fiber

SPM is arguably the most common $\chi^{(3)}$ phenomena since any intensities required to achieve other phenomena will also be strong enough to witness SPM. That stated, we are not interested so much in the intense fields that will generate the SPM, but rather their effect on single-photon-level beams that co-propagate with them through the fiber. Since our interest lies in the XPM between the intense beam (pump, p) and the weak beam (signal, s), we will discuss SPM in conjunction with the development of XPM rather than describe SPM separately.

In an effort to clearly describe the nonlinear processes in optical fiber, we limit the properties of electric fields to being linearly polarized, and satisfying the quasi-monochromatic approximation, $\Delta\omega_m \ll \omega_m$, where $m \in p, s$. The latter approximation is fair for pulses that have pulse widths >0.1 ps. Thus we write the electric field as

$$\mathbf{E}(\mathbf{r}, t) = \frac{1}{2}\vec{x}[E_p \exp(-i\omega_p t) + E_s \exp(-i\omega_s t)] + \text{c.c.} \quad (2.13)$$

where \vec{x} is the optical polarization unit vector, ω_p and ω_s are the pump and signal carrier frequencies, and E_p and E_s are the pump and signal's slowly varying electric field envelopes. Based on this, we obtain the following nonlinear polarization.

$$\begin{aligned} \mathbf{P}_{\text{NL}}(\mathbf{r}, t) = & \frac{1}{2}\vec{x} [P_{\text{NL}}(\omega_p) \exp(-i\omega_p t) \\ & + P_{\text{NL}}(\omega_s) \exp(-i\omega_s t) \\ & + P_{\text{NL}}(2\omega_p - \omega_s) \exp(-i(2\omega_p - \omega_s)t) \\ & + P_{\text{NL}}(2\omega_s - \omega_p) \exp(-i(2\omega_s - \omega_p)t)] + \text{c.c.} \end{aligned} \quad (2.14)$$

where the four nonlinear polarization terms are defined by

$$P_{\text{NL}}(\omega_p) = \frac{3\epsilon_0}{4}\chi_{xxxx}^{(3)}(|E_p|^2 + 2|E_s|^2)E_p \quad (2.15a)$$

$$P_{\text{NL}}(\omega_s) = \frac{3\epsilon_0}{4}\chi_{xxxx}^{(3)}(|E_s|^2 + 2|E_p|^2)E_s \quad (2.15b)$$

$$P_{\text{NL}}(2\omega_p - \omega_s) = \frac{3\epsilon_0}{4}\chi_{xxxx}^{(3)}E_p^2E_s^* \quad (2.15c)$$

$$P_{\text{NL}}(2\omega_s - \omega_p) = \frac{3\epsilon_0}{4}\chi_{xxxx}^{(3)}E_s^2E_p^* \quad (2.15d)$$

The last two terms oscillating at $2\omega_p - \omega_s$ and $2\omega_s - \omega_p$ arise from the four-wave mixing process, which we will discuss in the following section. Since these terms require appropriate phase-matching to become appreciable, we will assume that the conditions are such that the pump and signal are phase-mismatched, and hence we will ignore them in the current context. The other two terms can now be shown to provide a nonlinear contribution to the index of refraction. Combining these terms with their linear part, we can write them as $P(\omega_m) = \epsilon_0\epsilon_m E_m$ where $\epsilon_m = \epsilon_m^{\text{L}} + \epsilon_m^{\text{NL}} = (n_m^{\text{L}} + \Delta n_m)^2$. Here, n_m^{L} is the linear part of the refractive index, and Δn_m is the change to the index of refraction caused by the nonlinear effects. Making the assumption that $\Delta n_m \ll n_m^{\text{L}}$, we obtain the nonlinear contributions

$$\Delta n_p \approx \epsilon_p^{\text{NL}}/2n_p^{\text{L}} \approx n_2(|E_p|^2 + 2|E_s|^2) \quad (2.16a)$$

$$\Delta n_s \approx \epsilon_s^{\text{NL}}/2n_s^{\text{L}} \approx n_2(|E_s|^2 + 2|E_p|^2) \quad (2.16b)$$

where $n_2 = 3\epsilon_0\text{Re}\chi_{xxxx}^{(3)}/8$ is the nonlinear-index coefficient. As such, we see that the refractive index of an optical field inside fiber is dependent on not only its own intensity, but also the intensity of other optical fields that are copropagating. Hence, we can define the

intensity-dependent nonlinear phase shift experience by a field propagating in fiber as

$$\phi_p^{\text{NL}}(z) = (\omega_p/c)\Delta n_p z = n_2(\omega_p/c)(|E_p|^2 + 2|E_s|^2)z \quad (2.17a)$$

$$\phi_s^{\text{NL}}(z) = (\omega_s/c)\Delta n_s z = n_2(\omega_s/c)(|E_s|^2 + 2|E_p|^2)z \quad (2.17b)$$

The first term on the right hand side in each of these arises courtesy of SPM, while the second term comes from XPM.

We can now plug the nonlinear polarization into the nonlinear Schrödinger equation. Here, we assume the transverse dependence of the electric field can be factored out, and thus takes the form of

$$E_m(\mathbf{r}, t) = F_m(x, y)A_m(z, t) \exp(i\beta_{0m}z) \quad (2.18)$$

where $F_m(x, y)$ is the transverse distribution of the fiber mode, $A_m(z, t)$ is the slowly varying amplitude, and β_{0m} is the propagation constant corresponding to the carrier frequency ω_m . Dispersive effects are accounted for using the expansion of β as done earlier. Since the transverse spatial mode does not vary very much for different telecom wavelengths propagating down single-mode fiber, we will treat it as a constant for the following calculations. Based on this, we obtain the propagation equations for the pump and signal as

$$\frac{\partial A_p}{\partial z} + \frac{1}{v_{gp}} \frac{\partial A_p}{\partial t} + i \frac{\beta_{2p}}{2} \frac{\partial^2 A_p}{\partial t^2} + \frac{\alpha_p}{2} A_p = i\gamma_p(|A_p|^2 + 2|A_s|^2)A_p \quad (2.19a)$$

$$\frac{\partial A_s}{\partial z} + \frac{1}{v_{gs}} \frac{\partial A_s}{\partial t} + i \frac{\beta_{2s}}{2} \frac{\partial^2 A_s}{\partial t^2} + \frac{\alpha_s}{2} A_s = i\gamma_s(|A_s|^2 + 2|A_p|^2)A_s \quad (2.19b)$$

where $\gamma_m = n_2\omega_m/(cA_{eff})$, α_m is the linear loss coefficient, and A_{eff} is the effective core mode area. Once again, we see the first term on the right hand side corresponds to SPM, and the second term corresponds to XPM.

Now that we have developed this model, let us consider the effects of group velocity mismatch, dispersion, and loss in fiber on the propagation and phase accumulation in the fiber. In order to do so, we begin by defining three useful lengths. The first is the walk-off length, i. e., the length over which the nonlinear interaction between the pump and signal fields will occur. This is defined as $L_w = T_0/|d|$ where T_0 is the pulse width, and $d = v_{gs}^{-1} - v_{gp}^{-1}$. The second length is the dispersion length defined as $L_D = T_0^2/|\beta_2|$. The last length is the effective fiber length over which the fiber is essentially lossless for the propagating field. This is defined as $L_{eff} = [1 - \exp(-\alpha L)]/\alpha$.

These parameters provide us some baseline for which to operate XPM experiments. For instance, if the length of fiber, L , is much longer than L_D , then we can ignore dispersion effects. Alternatively, increasing the fiber length such that $L > 2L_w$ will not provide any additional phase modulation since the pulses will not interact after that length. Similarly, if $L \gg L_{eff}$, the signal will be lost in the fiber due to loss. Hence we can design an XPM switch with these parameters in mind.

2.3.3. Four-wave mixing in Optical Fiber

Now that we have developed a model considering SPM and XPM, we will move our focus to looking at FWM which is useful for photon-pair generation. In our previous consideration of the SPM and XPM, we ignored the contributing terms due to FWM. We were able to do so by making the assumption that there existed a phase-mismatch that suppressed that action. While any four-wave interaction is an example of four-wave mixing, in this section we will address specifically the FWM where the phases match and thus contribute to photon generation at new frequencies.

To begin this analytical discussion, let us then consider four distinct waves oscillating at $\omega_1, \omega_2, \omega_3,$ and ω_4 . Let us assume all of these waves are linearly polarized along the \vec{x} axis, and propagating along the \vec{z} axis. We can therefore write the total electric field as

$$\mathbf{E} = \vec{x} \frac{1}{2} \sum_{j=1}^4 E_j \exp[i(\beta_j z - \omega t)] + \text{c.c.} \quad (2.20)$$

where $\beta_j = n_j \omega_j / c$. If we supply this equation into the relation $\mathbf{P}_{\text{NL}} = \epsilon_0 \chi^{(3)} : \mathbf{E} \mathbf{E} \mathbf{E}$, then we can write \mathbf{P}_{NL} in the same form.

$$\mathbf{P}_{\text{NL}} = \vec{x} \frac{1}{2} \sum_{j=1}^4 P_j \exp[i(\beta_j z - \omega t)] + \text{c.c.} \quad (2.21)$$

We note here that each P_j consists of a large number of terms arising from the products of the three electric fields. We will also make the assumptions of a quasi-CW case—to ignore pulse propagation effects—and a lossless transmission medium. By factoring the electric field's transverse component out, as done in Eq. 2.18, and assuming that the transverse spatial profile in fiber is guided, we obtain the equations governing the field's amplitude propagation through the fiber, shown here:

$$\frac{dA_1}{dz} = i\gamma_1 \left[\left(|A_1|^2 + 2 \sum_{j \neq 1} |A_j|^2 \right) A_1 + 2A_2^* A_3 A_4 \exp(i\Delta k z) \right] \quad (2.22a)$$

$$\frac{dA_2}{dz} = i\gamma_2 \left[\left(|A_2|^2 + 2 \sum_{j \neq 2} |A_j|^2 \right) A_2 + 2A_1^* A_3 A_4 \exp(i\Delta k z) \right] \quad (2.22b)$$

$$\frac{dA_3}{dz} = i\gamma_3 \left[\left(|A_3|^2 + 2 \sum_{j \neq 3} |A_j|^2 \right) A_3 + 2A_1 A_2 A_4^* \exp(i\Delta k z) \right] \quad (2.22c)$$

$$\frac{dA_4}{dz} = i\gamma_4 \left[\left(|A_4|^2 + 2 \sum_{j \neq 4} |A_j|^2 \right) A_4 + 2A_1 A_2 A_3^* \exp(i\Delta k z) \right] \quad (2.22d)$$

where we have introduced the wave-vector mismatch parameter $\Delta k = \beta_3 + \beta_4 - \beta_1 - \beta_2$. In this definition, $\beta_j = \tilde{n}_j \omega_j / c$, and \tilde{n}_j is the effective mode index at the frequency ω_j . Analyzing these equations, we see that the first term on the right hand side is once again the SPM term. The summation term describes the XPM between that wave and each other wave separately. Finally, the last term on the right hand side corresponds to the FWM process.

In order to have an efficient FWM process, we want to minimize the wave-vector mismatch, Δk . We also note that FWM is a parametric process, i. e., no energy is transferred between the medium and the light. This latter point implies that we must conserve energy and momentum and thus, $\omega_1 \pm \omega_2 = \omega_3 + \omega_4$. Since phase matching highly detuned frequencies is difficult, it is quite often seen that this aforementioned energy relation is $\omega_1 + \omega_2 = \omega_3 + \omega_4$.

It is often easier to limit the number of frequencies involved in this interaction and employ some form of degeneracy. This can occur if the source uses two pump photons such that $\omega_1 = \omega_2$, or if two detuned pump photons generate degenerate signal and idler photons such that $\omega_3 = \omega_4$. From this point forth we will simply call the former case FWM, and the latter case degenerate FWM. The photon-pairs (and entangled photons) generated in the sources described in Chp. 5 occur due to a spontaneous FWM process. The “spontaneous” qualifier indicates that we do not seed the signal and idler frequencies, ω_3 and ω_4 . Based on the treatment above, this scenario should yield no signal and idler photons since $A_3 = A_4 = 0$, but as we will show in the following section, vacuum fluctuations lead to spontaneous emissions in the signal and idler bands.

2.4. Quantization of the electric field

In the previous section, we introduced the nonlinear optical phenomena of FWM and XPM. These are important to the experiments discussed in this thesis. We applied the

classical treatment to derive these relations. Since we are interested in *quantum* information processing, in this section, we derive the aforementioned nonlinear phenomena using the quantum mechanical treatment. We start our quantum mechanical analysis of FWM by first quantizing the electric field, and then using that formalism to describe XPM and FWM. The Hamiltonian of a simple harmonic oscillator is

$$\hat{H} = \frac{1}{2m}\hat{p}^2 + \frac{m}{2}\omega^2\hat{q}^2, \quad (2.23)$$

where \hat{p} and \hat{q} represent the particle's momentum and location, respectively. We remark that the symbols that “wear hats” are operators. This conventional notation for operators will be used for the remainder of this dissertation.

Using those terms for position and momentum, we can respectively define the annihilation and creation operators as

$$\hat{a} = \sqrt{\frac{m\omega}{2\hbar}}\hat{q} + \frac{1}{\sqrt{2m\hbar\omega}}\hat{p}, \quad (2.24)$$

and

$$\hat{a}^\dagger = \sqrt{\frac{m\omega}{2\hbar}}\hat{q} - \frac{1}{\sqrt{2m\hbar\omega}}\hat{p}. \quad (2.25)$$

Supplying Eqs. (2.24) and (2.25) into Eq. (2.23), we obtain the following equation.

$$\hat{H} = \frac{1}{2}\hbar\omega (\hat{a}\hat{a}^\dagger + \hat{a}^\dagger\hat{a}) \quad (2.26)$$

Using the commutation relation, $[\hat{a}, \hat{a}^\dagger] = 1$, this equation simplifies to

$$\hat{H} = \hbar\omega \left(\hat{a}^\dagger\hat{a} + \frac{1}{2} \right) = \hbar\omega \left(\hat{N} + \frac{1}{2} \right) \quad (2.27)$$

where $\hat{N} = \hat{a}^\dagger \hat{a}$ is the number operator. Based on this derivation, it is easy to see that the Hamiltonian acting on the vacuum state, $|0\rangle$, yields

$$\hat{E}|0\rangle = \hat{H}|0\rangle = \hbar\omega\hat{N}|0\rangle + \frac{\hbar\omega}{2}|0\rangle = \frac{\hbar\omega}{2}|0\rangle. \quad (2.28)$$

This result tells us that, even in the absence of all particles, there is a non-zero energy. For our subsequent discussion, this implies that, although there may seem to be no present energy at the signal and idler wavelengths classically, the vacuum field is always present. This background due to vacuum provides the impetus for the spontaneous generation of FWM photons.

2.4.1. Quantum mechanical treatment of spontaneous FWM and XPM

The sources discussed in this thesis make the assumption of a strong undepleted pump. As such, the pump in the forthcoming discussion will not be treated quantum mechanically. For simplicity, we will also assume the fiber used is short enough to ignore any dispersion effects and loss. The following discussion is based on the work of Lin et al.^[46], and makes the assumption that the signal and idler are co-polarized with the pump.

The commutation relation of the optical fields is

$$\left[\hat{A}(z, \omega_m), \hat{A}^\dagger(z, \omega_n) \right] = 2\pi\delta(\omega_m - \omega_n) \quad (2.29)$$

where the 2π is an artifact of the Fourier transform. We introduce a parameter \hat{m} to describe the noise operator arising from the presence of the phonon reservoir and its coupling with the optical field due to the Raman process. This parameter is introduced to preserve the commutation relation while allowing for spontaneous Raman scattering. Conservation of the

previous commutation relation requires the following equality.

$$[\hat{m}(z, \Omega_u), \hat{m}^\dagger(z', \Omega_v)] = 2\pi g_{\parallel}(\Omega_u)\delta(z - z')\delta(\Omega_u - \Omega_v) \quad (2.30)$$

where Ω_j is the detuning from the classical pump field, and g_{\parallel} is the measured co-polarized Raman gain.

Similar to what we showed before during the classical treatment, we will not try to solve directly for the equations describing the pump propagation through the fiber. Unlike what we did in Eq. (2.18), we will not factor out the transverse spatial profile or phase information from the slowly varying field envelope. Thus, we have $A_p(z) = A_{p0} \exp(ik_p z + \gamma P_0 z)$ where we define the pump power $P_0 = |A_{p0}|^2$. Based on this, we can describe the signal and idler evolution using

$$\frac{\partial \hat{A}_s}{\partial z} = i [k_s + \gamma \xi(\Omega_{sp}) P_0] \hat{A}_s + i \gamma \eta(\Omega_{sp}) A_{p0}^2 \hat{A}_i^\dagger + i A_{p0} \hat{m}(z, \Omega_{sp}) \quad (2.31a)$$

$$\frac{\partial \hat{A}_i}{\partial z} = i [k_i + \gamma \xi(\Omega_{ip}) P_0] \hat{A}_i + i \gamma \eta(\Omega_{ip}) A_{p0}^2 \hat{A}_s^\dagger + i A_{p0} \hat{m}(z, \Omega_{ip}) \quad (2.31b)$$

where $\Omega_{jp} = \omega_j - \omega_p, j \in (s, i)$. Here, we also introduced the terms $\xi(\Omega_{jp})$, and $\eta(\Omega_{jp})$. The former describes the nonlinear phase shift due to XPM and Raman scattering. The latter describes the FWM efficiency. These two terms are more precisely defined as

$$\xi(\Omega_{jp}) = 2 - f_R + f_R g_{\parallel}(\Omega_{jp}), \quad (2.32)$$

and

$$\eta(\Omega_{jp}) = \xi(\Omega_{jp}) - 1, \quad (2.33)$$

where f_R is the fractional contribution of the Raman response to the nonlinear index of refraction. For both of these terms, the constant dominates. If we set $f_R = 0$, then we will be ignoring the Raman contribution as we did in the analysis earlier.

Using the equations above, we obtain the following general solutions for the electric field amplitude after propagation through fiber of length L .

$$\hat{A}(L, \omega_s) = \left[\alpha(L, \omega_s) \hat{A}(0, \omega_s) + \beta(L, \omega_s) \hat{A}^\dagger(0, \omega_i) + \hat{N}(L, \omega_s) \right] \exp[i(k_p + \gamma P_0)z] \quad (2.34a)$$

$$\hat{A}(L, \omega_i) = \left[\alpha(L, \omega_i) \hat{A}(0, \omega_i) + \beta(L, \omega_i) \hat{A}^\dagger(0, \omega_s) + \hat{N}(L, \omega_i) \right] \exp[i(k_p + \gamma P_0)z] \quad (2.34b)$$

The first two terms in each of these come from FWM, while the last term is a result of Raman scattering. The coefficients in these equations are defined as follows:

$$\alpha(L, \omega_u) = [\cosh(gL) + (i\kappa/2g) \sinh(gL)] \exp[i(k_u - k_{u'})L/2] \quad (2.35)$$

$$\beta(L, \omega_u) = (i\gamma\eta/g) A_p^2 \sinh(gL) \exp[i(k_u - k_{u'})L/2] \quad (2.36)$$

$$\hat{N}(L, \omega_u) = i \int_0^L \hat{m}(z, \Omega_{up}) [A_p \alpha(L - z, \omega_u) - A_p^* \beta(L - z, \omega_u)] dz \quad (2.37)$$

where $u \in (s, i)$, $u' = i$ if $u = s$, and $u' = s$ if $u = i$. We define the phase mismatch using $\kappa = k_s + k_i - 2k_p + 2\gamma P_0(\xi - 1)$, and the parametric gain coefficient g by $g^2 = (\gamma\eta P_0)^2 - (\kappa/2)^2$.

The aforementioned equations are very general, and account for stimulated and spontaneous processes. For the desired entanglement, we want to limit the stimulated processes. This is achieved by maintaining $\gamma PL \ll 1$. We also make the assumption that the signal and idler are centered near the phase-matching location such that $\text{Re}(\kappa) \approx 0$. Finally, we will assume that the signal and idler are filtered using square, band-pass filters with bandwidth $\Delta\nu$ (in Hz).

We now define the signal/idler photon flux as $I_u = \langle \hat{A}_u^\dagger(L, t) \hat{A}_u(L, t) \rangle$. The angle brackets denote averaging with respect to the vacuum input state. We also make the assumption that the phonon reservoir is described by a thermal population, $n(\Omega_{uv}) = [\exp(\hbar|\Omega_{uv}|/k_B T) - 1]^{-1}$, for the frequency $\Omega_{uv} = \omega_u - \omega_v$, and at temperature T . We remark that k_B is the Boltzmann constant. We define $\mathcal{N}(\Omega_{uv}) = n(\Omega_{uv}) + u(-\Omega_{uv})$ where $u(x)$ is the unit step function.

Using this, we can write the photon flux as

$$I_u = \Delta\nu (|\gamma P_0 L \eta(\Omega_{up})|^2 + P_0 L |g_{\parallel}| \mathcal{N}(\Omega_{up})) \quad (2.38)$$

Based on this, we see that the photon flux due to FWM photon pairs is proportional to $P_0^2 L^2$, while the contribution from Raman scattering is linearly proportional. We see later that the quadratic nature of the photon pairs also impacts the switching performance. Based on this, we have two parameters that we can use to reduce the effect of Raman contributing to the photon flux. The first way is to adjust the detuning. The other is to cool the fiber significantly. The latter effect is the reason all the photon-pair or entangled photon sources described in this thesis are cooled to the liquid nitrogen temperature of 77 K.

Now that we understand some of the background information for fiber optics that is necessary to understand the forthcoming discussion, we will look at how to describe quantum states.

CHAPTER 3

Introduction to Quantum Information Processing

In this chapter, we provide the groundwork for discussing quantum information processing. We will take a look at the basics of quantum states. We begin with a brief look at pure and mixed qubit states; the latter will require an understanding of density matrices. We will then look at multiple-qubit states, therein introducing the concepts of entangled and separable states. This will encompass polarization-entangled states. We then turn our attention to higher-dimensional states which we can use to describe time-bin-entangled states. We will conclude with a discussion of various metrics one can use to measure the entanglement quality and purity of a state.

3.1. Representations of single-qubit states

In traditional computing, i.e., for classical information, the fundamental piece of information is a binary digit, a.k.a. *bit*. The “binary” descriptor indicates that our data is represented by either a 0 or 1. For quantum information processing, the fundamental unit is called a quantum binary digit, or *qubit* for short. Unlike the classical case, the qubit can exist in a superposition of both 0 and 1 simultaneously. Since this state has two bases (0 and 1), we say that it exists in a two-dimensional Hilbert space. Utilizing Dirac’s bracket notation (see appendix E), we can describe any pure single qubit state (or ensemble of *identical* pure qubit states) as

$$|\psi\rangle = \alpha |0\rangle + \beta |1\rangle, \tag{3.1}$$

where α and β are complex coefficients ($\alpha, \beta \in \mathbb{C}$) which obey the normalization relation $|\alpha|^2 + |\beta|^2 = 1$. Alternatively, by ignoring the global phase, we can write this state vector as

$$|\psi\rangle = A|0\rangle + Be^{i\phi}|1\rangle. \quad (3.2)$$

Here, A , B , and ϕ are real coefficients, i. e., $A, B, \phi \in \mathbb{R}$. Also, by applying the normalization constraint, we obtain $B = \sqrt{1 - A^2}$. For convenience, we often set $A = \cos(\theta)$ and $B = \sin(\theta)$, thereby implicitly satisfying the normalization condition.

In this thesis, much of the work we discuss deals with polarization-based QIP. As such, we define $|H\rangle \equiv |0\rangle$ and $|V\rangle \equiv |1\rangle$ as the basis states. Using these, we can then define other useful polarization states:

$$\begin{aligned} |D\rangle &\equiv (|H\rangle + |V\rangle)/\sqrt{2} \\ |A\rangle &\equiv (|H\rangle - |V\rangle)/\sqrt{2} \\ |R\rangle &\equiv (|H\rangle + i|V\rangle)/\sqrt{2} \\ |L\rangle &\equiv (|H\rangle - i|V\rangle)/\sqrt{2}. \end{aligned} \quad (3.3)$$

These states represent diagonal, anti-diagonal, right-circular, and left-circular polarization states of light.

3.1.1. Density matrix representation

Density matrices are another representation for describing a state. For the aforementioned pure states, we can write the respective density matrix as

$$\hat{\rho} \equiv |\psi\rangle\langle\psi| \quad (3.4)$$

We remind the reader that the “hat” on the ρ indicates that this is an operator. As before, this definition will also describe an ensemble of identical states.

Unfortunately, not all possible state ensembles that we see or measure are pure states. For instance, photons from a thermal light source will seem to be mixed. Similarly, if we measure an ensemble of pure states such that the pure states are not identical, then we will also obtain a mixed state. For states like these, which have some mixture, we must describe them as a sum of pure states. Hence, a more general definition for a single-qubit density matrix is

$$\hat{\rho} \equiv \sum_j P_j |\psi_j\rangle \langle\psi_j| = \begin{array}{c} \langle 0| \\ \langle 1| \end{array} \begin{pmatrix} A & Ce^{i\phi} \\ Ce^{-i\phi} & B \end{pmatrix}. \quad (3.5)$$

There are several characteristics of a density matrix which always hold true. It is Hermitian ($\hat{\rho} = \hat{\rho}^\dagger$), is positive semi-definite ($A, B, C \in \mathbb{R}; A, B, C \geq 0$), and has a trace of one ($\text{Tr}(\hat{\rho}) = A + B = 1$). Consequently, as a byproduct of the trace condition, the coefficients P_j are probability weights, i. e., $\sum_j P_j = 1$. Also, the bras and kets denote that this density matrix represents the state measured in the $|0\rangle, |1\rangle$ basis.

Of course, we can rotate the state onto other bases. As such, we note that *any* physical density matrix can be diagonalized as

$$\hat{\rho} = \begin{array}{c} \langle\psi| \\ \langle\psi^\perp| \end{array} \begin{pmatrix} E_1 & 0 \\ 0 & E_2 \end{pmatrix} = E_1 |\psi\rangle \langle\psi| + E_2 |\psi^\perp\rangle \langle\psi^\perp|. \quad (3.6)$$

In this case, E_1 and E_2 represent the eigenvalues of the density matrix and $|\psi\rangle$ and $|\psi^\perp\rangle$ are the corresponding eigenvectors. By definition, eigenvectors are orthogonal, which we

explicitly denote using the \perp symbol. As an aside, any two states, $|\psi_m\rangle$ and $|\psi_n\rangle$, are orthogonal if $|\langle\psi_m|\psi_n\rangle| = 0$.

One convenient benefit of using the density matrix to describe our state is that we can quickly determine if the state is pure or mixed. We perform this test by supplying our state $\hat{\rho}$ into the following relation $\text{Tr}(\hat{\rho}^2) \leq 1$. If and only if we satisfy the equality condition, then $\hat{\rho}$ is a pure state, otherwise, it is mixed. Another benefit of the density matrix is that we can compare how similar or dissimilar two states are with respect to one another. We investigate how to do this in §3.4.

3.1.2. Stokes parameters

Now that we understand a little bit about density matrices, we turn our attention to a unique decomposition of them. Any single-qubit density matrix can be decomposed and described using three parameters, $\{S_1, S_2, S_3\}$ such that

$$\hat{\rho} = \frac{1}{2} \sum_{j=0}^3 S_j \hat{\sigma}_j. \quad (3.7)$$

Here, $\hat{\sigma}$ are the identity and Pauli matrices. Explicitly written, they are defined as

$$\begin{aligned}
 \hat{\sigma}_0 &\equiv \begin{pmatrix} 1 & 0 \\ 0 & 1 \end{pmatrix}, \\
 \hat{\sigma}_1 &\equiv \begin{pmatrix} 0 & 1 \\ 1 & 0 \end{pmatrix}, \\
 \hat{\sigma}_2 &\equiv \begin{pmatrix} 0 & -i \\ i & 0 \end{pmatrix}, \\
 \hat{\sigma}_3 &\equiv \begin{pmatrix} 1 & 0 \\ 0 & -1 \end{pmatrix}.
 \end{aligned} \tag{3.8}$$

We obtain the S -parameters, referred to as the Stokes parameters, using

$$S_j \equiv \text{Tr}\{\hat{\sigma}_j \hat{\rho}\}. \tag{3.9}$$

Often, we use the S -parameters to define the polarization of an EM-field. They can be used to describe any polarization from an unpolarized light, to partially polarized elliptical light, to fully polarized light. Mapping the S_1 – S_3 terms to the Cartesian coordinates x, y, z , one can directly plot the polarization on a unit sphere.

Again, a quick test can determine whether this state is pure or mixed. If $\sum_{j=1}^3 S_j^2 = 1$, the state is pure. If $\sum_{j=1}^3 S_j^2 < 1$, the state is partially mixed. For a completely mixed state, $\sum_{j=1}^3 S_j^2 = 0$. Finally, $S_0 = 1$ due to normalization. Also, note that $S_j \in \mathbb{R}$.

Minds much smarter than mine have realized that the Stokes parameters have a physical meaning. They can be physically measured by determining probabilities of projective

measurements as follows:

$$\begin{aligned}
S_0 &= P_{|0\rangle} + P_{|1\rangle} \\
S_1 &= P_{\frac{1}{\sqrt{2}}(|0\rangle+|1\rangle)} - P_{\frac{1}{\sqrt{2}}(|0\rangle-|1\rangle)} \\
S_2 &= P_{\frac{1}{\sqrt{2}}(|0\rangle+i|1\rangle)} - P_{\frac{1}{\sqrt{2}}(|0\rangle-i|1\rangle)} \\
S_3 &= P_{|0\rangle} - P_{|1\rangle}.
\end{aligned} \tag{3.10}$$

Here, $P_{|\psi\rangle}$ is the probability of measuring the state $|\psi\rangle$. This probability can be determined using $P_{|\psi\rangle} = \langle\psi|\hat{\rho}|\psi\rangle = \text{Tr}\{|\psi\rangle\langle\psi|\hat{\rho}\}$. In other words, this is the probability of projecting a given state $\hat{\rho}$ onto the pure state $|\psi\rangle$. Note that $P_{|\psi\rangle} + P_{|\psi^\perp\rangle} = 1$. This equality can sometimes simplify other equations.

3.2. Representations of multiple-qubit states

Now that we know how to describe and compose a single-qubit state, we can investigate how to describe states that have more than one qubit. Any m -qubit pure state can be written as

$$|\psi\rangle_m = |\psi_1\rangle \otimes |\psi_2\rangle \otimes \cdots \otimes |\psi_m\rangle, \tag{3.11}$$

where $|\psi_j\rangle$ for $j \in \{1, \dots, m\}$ are all single-qubit states of the form shown in Eq. (3.1). Also, \otimes indicates a tensor product, which mathematically describes how we combine Hilbert spaces. We can write this state more explicitly as

$$|\psi\rangle_m = \sum_{q_1, q_2, \dots, q_m \in \{0, 1\}} \alpha_{q_1 q_2 \dots q_m} |q_1\rangle \otimes |q_2\rangle \otimes \cdots \otimes |q_m\rangle, \tag{3.12}$$

where $\alpha_q \in \mathbb{C}$ and $\sum_q |\alpha_q|^2 = 1$. In order to help the reader understand this more clearly, we briefly provide two examples below. The first is the most general representation of any

two-qubit pure state:

$$|\psi\rangle_2 = \alpha_{00} |00\rangle + \alpha_{01} |01\rangle + \alpha_{10} |10\rangle + \alpha_{11} |11\rangle. \quad (3.13)$$

We introduce here the shorthand notation that $|00\rangle = |0\rangle_1 \otimes |0\rangle_2$ where the subscripts label the photon. Going one step further, we show the most general form a three-qubit pure state:

$$\begin{aligned} |\psi\rangle_3 = & \alpha_{000} |000\rangle + \alpha_{001} |001\rangle + \alpha_{010} |010\rangle + \alpha_{011} |011\rangle \\ & + \alpha_{100} |100\rangle + \alpha_{101} |101\rangle + \alpha_{110} |110\rangle + \alpha_{111} |111\rangle. \end{aligned} \quad (3.14)$$

As an aside, we introduce here some of the most common two-qubit pure states, the maximally entangled Bell states^[33].

$$\begin{aligned} |\phi^\pm\rangle &= \frac{1}{\sqrt{2}}(|00\rangle \pm |11\rangle) \\ |\psi^\pm\rangle &= \frac{1}{\sqrt{2}}(|01\rangle \pm |10\rangle) \end{aligned} \quad (3.15)$$

These states are useful since they form an orthonormal state basis, and are fundamental to testing Bell's theorem.

Just as we did for the single-qubit state, we can represent an m -qubit state using density matrices instead. This enables us to discuss mixed m -qubit states. Hence, we define the $(2^m \times 2^m)$ -dimensional density matrix as

$$\hat{\rho} = \sum_j P_j |\psi_j\rangle \langle \psi_j|, \quad (3.16)$$

which is an incoherent sum of pure states. Although the equations look identical, the difference between Eq. 3.5 and Eq. 3.16 is that $|\psi_j\rangle$ is a single-qubit state in the former equation, and a m -qubit state in the latter equation.

Now that we have established the density matrix formulation for an m -qubit state, we turn our attention to a particular example of mixed states, the Werner states^[47]. These states represent maximally entangled states that have an added mixed component. The mixed part is similar to introducing uniform noise to an ideal state. Mathematically, we express this as

$$\hat{\rho}_W = p|\gamma\rangle\langle\gamma| + (1-p)\frac{1}{m}\mathbb{I}, \quad (3.17)$$

where $|\gamma\rangle$ is an arbitrary maximally entangled state, \mathbb{I} is the identity matrix, and $0 \leq p \leq 1$. The identity matrix represents a totally mixed state. Since this state represents the addition of noise to an ideal state, it is useful to use when simulating entangled state generation.

3.3. Representations of higher dimensional states

In this section, we explore how to represent states that are not binary, i.e., two dimensional. If we have a state that exists in a d -dimensional Hilbert space, then, recalling our naming convention for qubits, we call this quantum d -ary digit a *qudit*. A pure state of this form can be written as

$$|\psi\rangle_d = \alpha_0 |0\rangle + \alpha_1 |1\rangle + \cdots + \alpha_{d-2} |d-2\rangle + \alpha_{d-1} |d-1\rangle, \quad (3.18)$$

where $\alpha_j \in \mathbb{C}$ and $\sum_{j=0}^{d-1} |\alpha_j|^2 = 1$. The subscript on the left-hand-side ket denotes that this a qudit state.

If we pick $d = 3$, then we have a trinary state. We call this quantum trinary digit a *qutrit*. Explicitly written with the global phase removed, we can write any qutrit state as

$$|\psi\rangle_3 = A_0 |0\rangle + A_1 e^{i\phi_1} |1\rangle + A_2 e^{i\phi_2} |2\rangle, \quad (3.19)$$

where $A_j, \phi_j \in \mathbb{R}$, and $\sum_{j=0}^2 A_j^2 = 1$. Similarly, a quantum quaternary ($d = 4$) state—called a *ququat* state—can be explicitly written as

$$|\psi\rangle_4 = A_0 |0\rangle + A_1 e^{i\phi_1} |1\rangle + A_2 e^{i\phi_2} |2\rangle + A_3 e^{i\phi_3} |3\rangle \quad (3.20)$$

with $A_j, \phi_j \in \mathbb{R}$, and $\sum_{j=0}^3 A_j^2 = 1$.

Thus far, the higher-dimensional states described are all unipartite. If we expand to multi-partite systems, then we write that state as

$$|\psi\rangle_{m,d} = |\psi_1\rangle_d \otimes |\psi_2\rangle_d \otimes \cdots \otimes |\psi_m\rangle_d. \quad (3.21)$$

Here, each state $|\psi_j\rangle_d$ is a qudit state as denoted by the subscript d . We remark here that, in the preceding equation, all parts of the state have the same dimension d . This is not necessary, i. e., a state described as a tensor product of a d -dimensional state and d' -dimensional state, with $d \neq d'$, is equally valid. We limit the scope to equi-dimensional particles since those describe the states developed in this dissertation.

Additionally, since the states of interest for this dissertation are bipartite, we assume $m = 2$. Thus, we can represent any two-qudit pure state as

$$\begin{aligned} |\psi\rangle_{2,3} &= |\psi_1\rangle_3 \otimes |\psi_2\rangle_3 \\ &= \alpha_0 \beta_0 |00\rangle + \alpha_0 \beta_1 |01\rangle + \alpha_0 \beta_2 |02\rangle \\ &\quad + \alpha_1 \beta_0 |10\rangle + \alpha_1 \beta_1 |11\rangle + \alpha_1 \beta_2 |12\rangle \\ &\quad + \alpha_2 \beta_0 |20\rangle + \alpha_2 \beta_1 |21\rangle + \alpha_2 \beta_2 |22\rangle \end{aligned} \quad (3.22)$$

The coefficients α_j and β_j are from $|\psi_1\rangle_3$ and $|\psi_2\rangle_3$, respectively, in accordance with Eq. (3.18).

For completeness, we can similarly write any two-ququat pure state as

$$\begin{aligned}
 |\psi\rangle_{2,3} &= |\psi_1\rangle_3 \otimes |\psi_2\rangle_3 \\
 &= \alpha_0\beta_0 |00\rangle + \alpha_0\beta_1 |01\rangle + \alpha_0\beta_2 |02\rangle + \alpha_0\beta_3 |03\rangle \\
 &\quad + \alpha_1\beta_0 |10\rangle + \alpha_1\beta_1 |11\rangle + \alpha_1\beta_2 |12\rangle + \alpha_1\beta_3 |13\rangle \\
 &\quad + \alpha_2\beta_0 |20\rangle + \alpha_2\beta_1 |21\rangle + \alpha_2\beta_2 |22\rangle + \alpha_2\beta_3 |23\rangle
 \end{aligned} \tag{3.23}$$

The density matrix form for qudits is identical to that shown in Eq. (3.5) with one small change; each state $|\psi\rangle$ is now a qudit rather than a qubit. As such, the bipartite density matrix for equi-dimensional qudits exists is a $(d^2 \times d^2)$ -dimensional matrix.

As we move to higher dimensions, more maximally entangled qudit states are possible. An example two-photon, maximally entangled qudit state can be written as

$$|\psi\rangle = \alpha_0 |00\rangle + \alpha_1 |11\rangle + \cdots + \alpha_d |dd\rangle \tag{3.24}$$

In Chp. 7, we will show results from our efforts to generate and measure maximally entangled, two-photon qutrit and ququat states of this form. In the next section, we see how to determine the Stokes parameters for such higher-dimensional states so that we can use a tomography to reconstruct them.

3.3.1. Qudit Stokes parameters

Earlier, in §3.1.2, we showed how to determine the Stokes parameters for a single-qubit state. Akin to that we can develop a formalism for higher-dimensional states. The work

in this section is based on a paper from Thew, et al.^[48] and mimics the notation from Joe Altepeter's thesis^[49].

We can write the density matrix for a one-qudit state as

$$\hat{\rho}_d = \frac{1}{d} \sum_{j=0}^{d^2-1} S_j \hat{\sigma}_j. \quad (3.25)$$

This equation can take a different form, akin to the form seen earlier for a one-qubit example.

In order to do so, we expand this equation as

$$\hat{\rho}_d = S_0 \hat{\sigma}_0 + \sum_{k=1}^{d-1} \sum_{j=0}^{k-1} (S_{j,k}^X \hat{\sigma}_{j,k}^X + S_{j,k}^Y \hat{\sigma}_{j,k}^Y) + \sum_{l=1}^{d-1} S_l^Z \hat{\sigma}_l^Z \quad (3.26)$$

Here, we define the Stokes matrices and parameters as

$$\begin{aligned} \hat{\sigma}_0 &= \mathbb{I}, S_0 = 1, \\ \hat{\sigma}_{j,k}^X &= |j\rangle\langle k| + |k\rangle\langle j|, \\ S_{j,k}^X &= P_{\frac{1}{\sqrt{2}}|j\rangle+|k\rangle} - P_{\frac{1}{\sqrt{2}}|j\rangle-|k\rangle}, \\ \hat{\sigma}_{j,k}^Y &= -i(|j\rangle\langle k| - |k\rangle\langle j|), \\ S_{j,k}^X &= P_{\frac{1}{\sqrt{2}}|j\rangle+i|k\rangle} - P_{\frac{1}{\sqrt{2}}|j\rangle-i|k\rangle}, \\ \hat{\sigma}_l^Z &= \sqrt{\frac{2}{l(l+1)}} \left[\left(\sum_{j=0}^{l-1} |j\rangle\langle j| \right) - l|l\rangle\langle l| \right], \\ S_l^Z &= \sqrt{\frac{2}{l(l+1)}} \left[\left(\sum_{j=0}^{l-1} P_{|j\rangle} \right) - lP_{|l\rangle} \right]. \end{aligned} \quad (3.27)$$

Note that for all states shown here, the vectors' and matrices' indices range from 0 to $d-1$, i. e., we label the rows and/or columns from 0 to $d-1$. Additionally, we note that, at most, we require a superposition of two orthogonal states in order to determine all the Stokes

parameters. Thus, to determine any state, we need only the ability to measure pairwise superpositions of all orthogonal bases. This will later become important when determining how to reconstruct qutrit and ququat states using quantum state tomographies.

We now explicitly write the Stokes matrices and parameters for a qutrit state as follows:

$$\begin{aligned}
 \hat{\sigma}_0 &= \begin{pmatrix} 1 & 0 & 0 \\ 0 & 1 & 0 \\ 0 & 0 & 1 \end{pmatrix} & \hat{\sigma}_1^Z &= \begin{pmatrix} 1 & 0 & 0 \\ 0 & -1 & 0 \\ 0 & 0 & 0 \end{pmatrix} & \hat{\sigma}_2^Z &= \begin{pmatrix} 1 & 0 & 0 \\ 0 & 1 & 0 \\ 0 & 0 & -2 \end{pmatrix} \\
 \hat{\sigma}_{0,1}^X &= \begin{pmatrix} 0 & 1 & 0 \\ 1 & 0 & 0 \\ 0 & 0 & 0 \end{pmatrix} & \hat{\sigma}_{0,2}^X &= \begin{pmatrix} 0 & 0 & 1 \\ 0 & 0 & 0 \\ 1 & 0 & 0 \end{pmatrix} & \hat{\sigma}_{1,2}^X &= \begin{pmatrix} 0 & 0 & 0 \\ 0 & 0 & 1 \\ 0 & 1 & 0 \end{pmatrix} \\
 \hat{\sigma}_{0,1}^Y &= \begin{pmatrix} 0 & -i & 0 \\ i & 0 & 0 \\ 0 & 0 & 0 \end{pmatrix} & \hat{\sigma}_{0,2}^Y &= \begin{pmatrix} 0 & 0 & -i \\ 0 & 0 & 0 \\ i & 0 & 0 \end{pmatrix} & \hat{\sigma}_{1,2}^Y &= \begin{pmatrix} 0 & 0 & 0 \\ 0 & 0 & -i \\ 0 & i & 0 \end{pmatrix}
 \end{aligned}$$

and

$$\begin{aligned}
S_0 &= 1, \\
S_1^Z &= P_{|0\rangle} - P_{|1\rangle}, \\
S_2^Z &= \frac{1}{\sqrt{3}} (P_{|0\rangle} + P_{|1\rangle} - 2P_{|2\rangle}), \\
S_{0,1}^X &= P_{\frac{1}{\sqrt{2}}(|0\rangle+|1\rangle)} - P_{\frac{1}{\sqrt{2}}(|0\rangle-|1\rangle)}, \\
S_{0,2}^X &= P_{\frac{1}{\sqrt{2}}(|0\rangle+|2\rangle)} - P_{\frac{1}{\sqrt{2}}(|0\rangle-|2\rangle)}, \\
S_{1,2}^X &= P_{\frac{1}{\sqrt{2}}(|1\rangle+|2\rangle)} - P_{\frac{1}{\sqrt{2}}(|1\rangle-|2\rangle)}, \\
S_{0,1}^Y &= P_{\frac{1}{\sqrt{2}}(|0\rangle+i|1\rangle)} - P_{\frac{1}{\sqrt{2}}(|0\rangle-i|1\rangle)}, \\
S_{0,2}^Y &= P_{\frac{1}{\sqrt{2}}(|0\rangle+i|2\rangle)} - P_{\frac{1}{\sqrt{2}}(|0\rangle-i|2\rangle)}, \\
S_{1,2}^Y &= P_{\frac{1}{\sqrt{2}}(|1\rangle+i|2\rangle)} - P_{\frac{1}{\sqrt{2}}(|1\rangle-i|2\rangle)}.
\end{aligned}$$

Prior discussion has been limited to one qudit. We can extend this for an m -qudit state as follows:

$$\hat{\rho}_{md} = \frac{1}{d^m} \sum_{j_0, \dots, j_m=0}^{d^2-1} S_{j_0, \dots, j_m} \hat{\sigma}_{j_0} \otimes \dots \otimes \hat{\sigma}_{j_m}. \quad (3.28)$$

We will not consider an explanation beyond this mention since we only discuss the Stokes parameters for qudits to highlight that we require pairwise superpositions of all bases to tomographically reconstruct the states.

Now that we have discussed the ability to describe higher-dimensional states using density matrices, we can quantify how close a given state is to a maximally entangled quantum state. We will take a look at various metrics to do so in the next section.

3.4. Measures of quality of entanglement

In this section, we briefly define and describe three useful measures that compare the similarity of two different states. If we define one of these states as a maximally entangled state, then we can use these metrics to determine the quality of entanglement. Additionally, as a measure for the “quantumness” of our state, if it can violate Bell’s inequality^[33], then we say our state is a quantum state. Using some of the metrics shown in this section, we can determine whether the measured state will violate Bell’s inequality^[50]. The first such measure is fidelity. The next is linear entropy. The final metrics, which we will not use in this thesis, but include for the reader’s knowledge, are the related measures, concurrence and tangle.

3.4.1. Fidelity

The fidelity measures the overlap between two states, i. e., how similar two states are with respect to one another^[51]. Mathematically speaking, this is defined as

$$F(\hat{\rho}_1, \hat{\rho}_2) = \left[\text{Tr} \left(\sqrt{\sqrt{\hat{\rho}_1} \hat{\rho}_2 \sqrt{\hat{\rho}_1}} \right) \right]^2, \quad (3.29)$$

where $\hat{\rho}_1$ and $\hat{\rho}_2$ are the density matrices for two states $|\psi_1\rangle$ and $|\psi_2\rangle$. We remark that if $|\psi_1\rangle$ and $|\psi_2\rangle$ are pure states, then this formula simplifies to $F(\hat{\rho}_1, \hat{\rho}_2) = \text{Tr}(\hat{\rho}_1 \hat{\rho}_2) = |\langle \psi_1 | \psi_2 \rangle|^2$. This calculation yields a value between 0 and 1, but it is more common to express the value as a percentage.

For the remainder of this thesis, if we do not mention both states, i. e., we use only $F(\hat{\rho}_1)$ instead of $F(\hat{\rho}_1, \hat{\rho}_2)$, then we are reporting the fidelity of the given density matrix $\hat{\rho}_1$ to the density matrix $|\gamma\rangle\langle\gamma|$, where $|\gamma\rangle$ is a maximally entangled state. For two-qubit applications,

the maximally entangled state takes the form of $|\gamma_2\rangle = (|00\rangle + e^{i\phi} |11\rangle)/\sqrt{2}$. For three qubit applications, it has the form $|\gamma_3\rangle = (|00\rangle + e^{i\phi_1} |11\rangle + e^{i\phi_2} |22\rangle)/\sqrt{3}$.

Additionally, for switching applications, we define the switching fidelity $F_S \equiv F(\hat{\rho}, \hat{\rho}')$ where the absence or presence of the prime superscript indicates passive- or active-mode operation of the switch, respectively. See Chp. 6 for more details about switching.

For a quick test to determine whether a state with a given fidelity is in fact quantum, we show in Fig. 3.1(a) the range of higher-dimensional states (up to $d = 8$) that do or do not violate the appropriate Bell inequality^[50]. States with a measured fidelity corresponding to the shaded region cannot violate Bell inequalities and therefore we cannot know for certain they are quantum states.

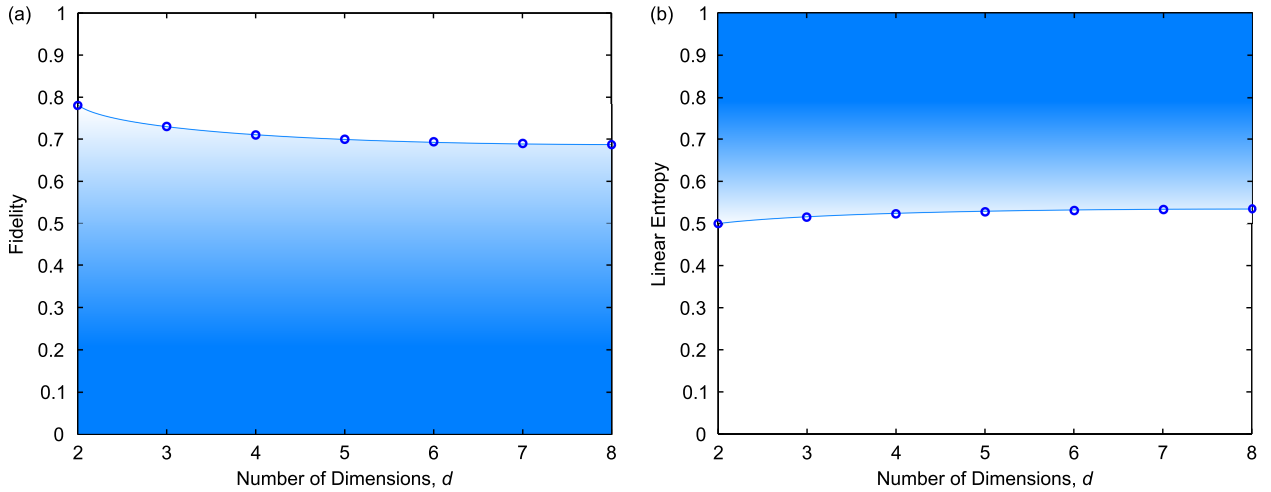


Figure 3.1. (a) Fidelity and (b) linear entropy as a function of the number of dimensions, d , for a qudit. The blue shaded area represents states that will not violate the appropriate higher-dimensional Bell inequality.

3.4.2. Linear Entropy

The Von Neumann entropy of a quantum state describes the amount of mixture of a state^[52].

This is defined as

$$S(\hat{\rho}) \equiv -\text{Tr}(\hat{\rho} \ln \hat{\rho}) = -\sum_i \hat{\rho}_i \ln \hat{\rho}_i. \quad (3.30)$$

A more analytically convenient description of state's mixture is provided by the linear entropy, which for a two-qubit system is defined as

$$S_L(\hat{\rho}) = \frac{4}{3} (1 - \text{Tr}(\hat{\rho}^2)) = \frac{4}{3} \left(1 - \sum_{a=1}^4 p_a^2 \right). \quad (3.31)$$

Here, p_a are the eigenvalues of $\hat{\rho}$. Thus, the linear entropy ranges from 0 for pure states to 1 for totally mixed states. For a two-qudit system, we define the linear entropy as

$$S_L(\hat{\rho}) = \frac{d}{d-1} (1 - \text{Tr}(\hat{\rho}^2)) = \frac{d}{d-1} \left(1 - \sum_{a=1}^d p_a^2 \right). \quad (3.32)$$

Using the aforementioned for two-qudit linear entropy equation, we can again determine the “quantumness” of the measured state by comparing the measured linear entropy to the plot shown in Fig. 3.1(b). Again, the shaded region represents states that do not violate the appropriate Bell inequality, and therefore cannot be known as quantum states. In other words, classical states can yield those results as well.

3.4.3. Concurrence and Tangle

Concurrence and tangle is another metric which can be used to characterize the quality of entanglement^[53]. More specifically, it measures the non-classical properties of a quantum state. Since, in this thesis we often consider two-qubit states, we show here the definition of concurrence and tangle for this case.

We start by considering the non-Hermitian matrix, $\hat{R} = \hat{\rho}\hat{\Sigma}\hat{\rho}^T\hat{\Sigma}$. Here, $\hat{\rho}$ is the density matrix for a quantum state $|\psi\rangle$, superscript T designates transpose, and $\hat{\Sigma}$ is the ‘spin flip matrix’ defined as

$$\hat{\Sigma} \equiv \begin{pmatrix} 0 & 0 & 0 & -1 \\ 0 & 0 & 1 & 0 \\ 0 & 1 & 0 & 0 \\ -1 & 0 & 0 & 0 \end{pmatrix}. \quad (3.33)$$

By solving \hat{R} for its eigenvalues, and arranging them in decreasing order such that $r_1 \leq r_2 \leq r_3 \leq r_4$, we define the concurrence as

$$C = \text{Max}(0, \sqrt{r_1} - \sqrt{r_2} - \sqrt{r_3} - \sqrt{r_4}). \quad (3.34)$$

Given this definition of concurrence, the tangle is simply defined as

$$T \equiv C^2. \quad (3.35)$$

Here we note that for separable, product states, the tangle is 0, whilst for any maximally entangled state such as the Bell states, the tangle equals 1.

CHAPTER 4

Survey of Alternative Technologies and Demonstrations

In this chapter, we present a survey of existing technologies that have been used for routing photonic information. We also motivate the framework for the design of our all-optical, fiber-based switch. In addition, we review alternate demonstrations of higher-dimensional quantum entanglement. As such, we divide the chapter into two sections. Section 4.1 will investigate other experimental switching technologies. The second section, §4.2, will take a look at generating and measuring high-dimensional entanglement. For comparison with the work done in this thesis, we show only bipartite demonstrations where each part exists in a Hilbert space of dimension greater than two.

4.1. Survey of optical switching technologies

Switching is a fundamental requirement for any networked information transfer. Unfortunately, we cannot use the currently available photonic switches, such as those used for transmitting information across the internet, since they use a detect-and-reemit paradigm. Quantum mechanically speaking, the detection process measures our state, thereby obscuring access to much of the potential information that was encoded on the photon.

Fortunately, for QIP, there are currently many implementations that use a variety of switching mechanisms, all of which do not require detection. For each switch, the designers must make trade-offs to obey a certain set of constraints depending on the switch's intended use. As such, in this section, we will investigate the design parameters that are of interest

for the most general switch. While doing so, we introduce some other switching designs as a means to highlight their advantages or disadvantages.

Decoherence and linear loss: In most QIP implementations, decoherence and loss of the qubit are often the performance limiting metrics. For optical QIP, while decoherence is not usually a concern, linear loss is detrimental to the extent that it limits the feasibility of any practical implementation. This enforces exacting criteria on the design of devices that are intended for QIP and long-distance quantum communications (LDQC). For example, ideal linear optical quantum computing requires $>82\%$ transmission through the entire system for fault-tolerant algorithms to succeed^[54,55]. Hence, every component (including switching) needs to be as lossless as possible. Until improvements are made by material scientists, this rules out switches with lossy propagation mediums. Examples of such designs are those based on cascaded $\chi^{(2)}$ processes^[56,57] implemented in materials such as lithium niobate^[58,59]. These technologies suffer from scattering losses in the material as well as coupling losses. Currently, one of the lowest loss mediums is standard optical fiber made from silica. A switch based on this is preferred since it is immediately compatible with the fibers used for long-distance transmission. Other fibers such as hollow core fibers^[60] and photonic crystal fibers^[61,62] exhibit higher scattering and coupling losses.

In-band noise: We also need to make sure that our signal does not accrue additional noise while traveling through the switch. Any noise that obscures our signal requires techniques such as redundancy to accurately receive the message. Silicon-based implementations are impeded by the presence of noise photons due to the free-carriers present^[63-67]. Additional background noise may arise in the form of spontaneous emission in resonant systems^[17,68,69]. These designs rely on the state of an atom, which coherently absorbs the information-carrying photon, to route the photon. Unfortunately the fact that absorption is possible necessarily

means that spontaneous emission is possible. This latter effect leads to in-band photons which act as noise in the quantum channel—precisely the opposite of our desired goal. Hence, we want a design that operates far off of resonance on the anti-Stokes side for the signal photons. In so doing, any noise photons generated due to spontaneous emission or Raman production can be easily filtered out.

High-speed: In order for LDQC to be feasible, existing classical data rates—which are near TB/s—need to be matched. While in principle, each quantum state can store an infinite "amount" of information, encoding and decoding such states is impractical. Therefore, in a realistic scenario, due to the presence of loss and using quantum error correction codes (QECC) for combating loss, high-speed switching is crucial in any implementation. High-speed switching enables faster transmission of information for quantum communications applications. Resonant atom-photon type switches are limited to MHz rates^[17,68,69]. This slow speed offsets other benefits of such switches like having near single-photon level switching energies. The desire to switch at high rates excludes any technologies that rely on moving parts such as MEMS^[70–73], acousto-optical^[74], or opto-mechanical^[75] switches. This indicates that we want a switching technology that is either electro-optical or all-optical.

All optical and coherent: Between switches that do not have physical moving parts, an all-optical switch is preferable to an electro-optical one. The reason for this is that an electro-optical modulator (EOM) type switch^[76–78] dissipates all of the RF energy used to activate the switch in the form of heat. In other words, the microwaves and optical waves are irreversibly coupled. Reversible coupling (or identically, unitary gates) for optical interactions are highly preferred since they reduce the power threshold, and comparatively, little optical energy is actually dissipated. As scalable technologies come to the fore, dissipation needs to be addressed as it will otherwise become a bottleneck for any all-optical circuit.

Moreover, a coherent all-optical switching mechanism can reuse the optical pulses that activate the switch, since the activation process is dissipation free. This is advantageous because of its implications for fan-in and fan-out of the switch.

State preserving: A very important criteria for QIP is that the switching technology must retain the transmitted quantum state. Ideally, the switch retains the quantum state for every possible degree of freedom of a photon including frequency, pulse shape, polarization, and phase. In other words, for optical QIP switching, propagating a photonic state through a switch should not affect its spectral, temporal, spatial or other properties of the photons in any manner. Such an adjustment could corrupt the desired state. Additionally, the switch should not entangle the signal photons to the environment or the activation source. The latter would be an implementation of a CNOT gate, thereby coupling the signal to another particle and changing its state. $\chi^{(2)}$ based switches are prone to pulse distortion. Thus, they are not desired for applications where the spatio-temporal profile is important. For polarization-based QIP, switches that are polarization sensitive, such as EOM-based switches^[76-78], are nonideal since both polarizations are not switched identically. For much of the work presented in this thesis, polarization is important, so our design will need to address the issue of polarization sensitivity.

Scalable: As we hope to grow the QIP infrastructure, we also desire our switch to be scalable. In this sense, technologies that require significant overhead and additional support equipment, such as atomic switches^[17,68,69], are nonideal. Currently, integrated photonics based switches^[63-67] have made significant progress. In fact, an on-chip photon-pair source has been manipulated and measured using reconfigurable photonic circuits^[79].

Network integrable: Another feature of an ideal switch for QIP is for it to be network integrable. Since there are many dark fibers currently laid across the globe, it would be best

if the switching technology could integrate with that framework. This would remove the need to create new channels between nodes in a quantum internet^[80]. Such a switch should be able to route photons that exist in telecom bands and be fiber-pigtailed for low-loss coupling into and out of the device. This is amenable with silicon photonic^[63–67], EOMs^[76–78], and fiber-based switches^[61,81], but rules out technologies such as cascaded $\chi^{(2)}$ and atomic switches.

Low activation energy: In order to be energy efficient, an ideal switch should require very little energy to toggle the switch from one position to another. For an all-optical switch, that entails operating the switch with a low-photon number pump. We note that coherent states have a photon-number uncertainty $\sqrt{\bar{n}}$, where \bar{n} is the mean photon number. Therefore, for low-photon number switching energies, it is highly desirable for the switching mechanism to be insensitive to pump energies past a minimum threshold. This ensure that the switch remains a deterministic gate. We remark that while a truly single-photon pump is interesting, it may not be desired for switching applications because such a design entangles the pump and signal photons therein changing the quantum state of the system.

Large dynamic range: An auxiliary feature of a the ideal switch is for it to have a large dynamic range for potential as transistor-type applications. By this, we mean that the switch performance works equally well for one photons as it does for millions of photons. Such a switch can be useful for routing classical signals equally as well as quantum signals. This could theoretically be used in a feed-forward type experiment where a time-multiplexed classical signal precedes the quantum-information-carrying photon to determine the traveled route. This feature implies that we cannot use resonator-based switches^[82–84], since the presence of a signal photon often changes the resonance condition blocking subsequent signal photons from coupling into the device.

Self-stabilizing: In terms of more economical goals, we prefer a self-stabilizing design—one that does not require active stabilization—made of low-cost components because these factors reduce the overhead and cost for implementing many switches. For this, we desire a design that is intrinsically stable. Such designs include integrated photonics based switches^[63–67] or designs that are built around stable geometries like a Sagnac interferometer^[85–89].

Low cost: The ideal switch should not cost very much to produce. We recognize that if a technology is sufficiently capable and superior to alternate options, the free-market will try to find ways to reduce the cost of that item. As such, more mature technologies, like silicon-based switches^[63–67], EOMs^[76–78] are increasingly affordable. Alternatively, built upon decades of telecom component development, a switch that uses standard optical fiber components can be made at comparatively cheaper costs.

4.2. Survey of entanglement in higher-dimensional Hilbert spaces

In this section, we briefly take a look at various realizations of higher-dimensional entanglement. As mentioned before, for comparison sake, we limit the scope to bipartite demonstrations.

4.2.1. Orbital angular momentum entanglement

Demonstrations that use orbital angular momentum (OAM) for their operational degree of freedom offer the benefit of working in very large Hilbert spaces^[7,90–92]. Unfortunately, they also require free-space transmission and spatial light modulators. Free-space transmission raises concerns about unequal phase variation between the different transverse spatial modes. Compensating for these phase differences requires the use of a spatial light modulator (SLM). An SLM is also used as a holographic mask with which one can generate the

OAM transmission profile. The challenge with using SLMs is that, at best, they operate at MHz rates. This limits the rate of operation for any desired QIP application that uses OAM for higher-dimensional entanglement. As such, these can serve as great exploration tools for higher-dimensional spaces, but are impractical for LDQC applications and quantum information transfer.

4.2.2. Energy-time entanglement

Rather than using a photon's OAM degree of freedom, we can use another d -dimensional degree of freedom. One such method is to use energy-time entanglement. In this type of system, one uses a downconversion source to generate frequency-correlated pairs. Then, by playing some dispersion games with the photons, the user can obscure the arrival timing information. This process entangles the photons in the energy-time degree of freedom. Several groups have used this type entanglement to demonstrate higher-dimensional entanglement^[93–96].

4.2.3. Time-bin entanglement

Another degree of freedom that we can use is the arrival time of the photon at the single-photon detectors. If we discretize the arrival time into short windows, we create time-bins within which our photon can exist. If two photons arrive at the same time, they form the state $|t_a t_a\rangle$ indicating they arrived at time t_a . We can entangle this by generating pairs of photons in various time-bins without generating them in multiple time-bins simultaneously. In other words, if we generate photon-pairs in a single time-bin (out of d total time-bins), but we do not know which one, then we can describe our state as $|t_1 t_1\rangle + |t_2 t_2\rangle + \dots + |t_d t_d\rangle$, an example of a d -dimensional maximally entangled state.

As we will explain in §5.4, generating this type of entanglement is rather easy for photonic QIP. Hence, others have attempted to realize such higher-dimensional entanglement. Unfortunately, they lack high-speed switches to measure such states quickly. As such, they are forced to either reduce their source rate^[97], apply frequency conversion on the signal^[98], or incur a photon losses by using splitters^[99]. We show in this thesis our efforts to realize such a system using the high-speed cross-bar switch described in the next chapter.

4.2.4. Hyperentanglement

Hyperentanglement is a type of entanglement where in we obtain higher dimensionality by entangling different degrees of freedom. Such systems have been demonstrated (mostly by the Kwiat group) using combinations of polarization, spatial, time-bin, OAM, and/or time-energy degrees of freedom^[4,100–104]. While such systems do provide access to additional degrees of freedom, they also require additional complexity and care to ensure appropriate manipulation and measurement of the quantum state is performed without affecting the other degrees of freedom of the hyperentangled state. In particular, long-distance fiber transport of such entangled states will likely require photonic crystal fiber. As discussed earlier, this introduces the additional challenges of scattering and coupling losses for us to overcome.

Now that we have surveyed the landscape of other switching efforts and higher-dimensional demonstrations, we turn our attention to the design of our switch.

CHAPTER 5

Generation of Pump Pulses and Photonic Entanglement

In order for us to create reliable quantum information processors, we must have a source that creates photon pairs. Sometimes we want that source to be a simple correlated photon-pair source. Correlated photon-pair sources are useful for those applications that use heralding, where the detected presence of one photon informs the user of the presence of a partner photon. But for other desired quantum protocols, correlated photons are not suitable enough. In such cases, we may require entangled photons. Ideal entangled-photon sources should satisfy several key functions and characteristics. They should generate an entangled-photon pair efficiently—ideally on-demand. The quantum state of the generated entangled photons should be tunable between completely separable and maximally entangled. Regardless of the choice of one’s preferred metric (fidelity, tangle, linear entropy, or another), the quantum state generated should have great accuracy and precision with the desired state. Another key characteristic is that the entangled photon source should operate at speeds fast enough to create pairs at the desired communications rate. Oftentimes, in practice, generation speeds are not the problem, but rather detection rates. In other words, for photonic QIP, it is easy to generate photon pairs at fast rates, but detecting these photons at such high rates is significantly more difficult. Since such ideal sources do not currently exist, we shall use the remainder of this chapter to describe the efforts from our lab to develop photon-pair and entangled-pair sources which satisfy as many of these goals as possible.

As we discussed in Chp. 2, there are two important nonlinear optical phenomena we utilize in our experiments. The first is XPM, which we use to achieve switching, and the second is FWM, which we use to generate our photon pairs and/or entangled photons. In this chapter, we describe the various experimental setups we used to create the pump pulses for XPM (§5.1) and FWM (§5.2). We start this chapter with a description of the various XPM pump pulse preparation systems we used. Since we generate the FWM pulses by either chopping a CW laser or pulse picking using an amplitude modulator, most of the effort for that system involves designing the electronics that drive the modulator. Hence, the following section describes the multiple generations of electrical systems used. Finally, we will describe the optical setups used to generate photon-pairs (§5.3), time-bin entanglement (§5.4), and polarization entanglement (§5.5). Further details of the polarization entanglement source can be found in other references from our group^[3,37].

5.1. Generation of XPM pump pulses

In this section, we describe a source that prepares the optical pulse that we use as our control signal for our switch (discussed later in Chp. 6). The critical property we desire for this XPM pump pulse is that it has two frequency components that are orthogonally polarized. We want these components to propagate together and have equal intensities. The purpose of these criteria is to ensure that our switch is polarization-insensitive.

5.1.1. First-generation XPM pump pulse preparation

The first pump pulse preparation was inherited from previous projects in our lab, including prior switching demonstrations. The general schematic is shown in Fig. 5.1(a). We seed this source with a broadband, femtosecond fiber laser (IMRA Femtolite BX-60) centered at

1550 nm. We route this to a free-space grating filter, shown in Fig. 5.1(b), to spatially divide the frequency components. After reflecting the signal off a mirror and a second traversal through the grating filter, we pick off the separated frequency components at 1545 nm and 1555 nm. Later, these selected frequencies were changed to 1551 nm and 1559 nm since we could obtain more optical power from the IMRA at those frequencies.

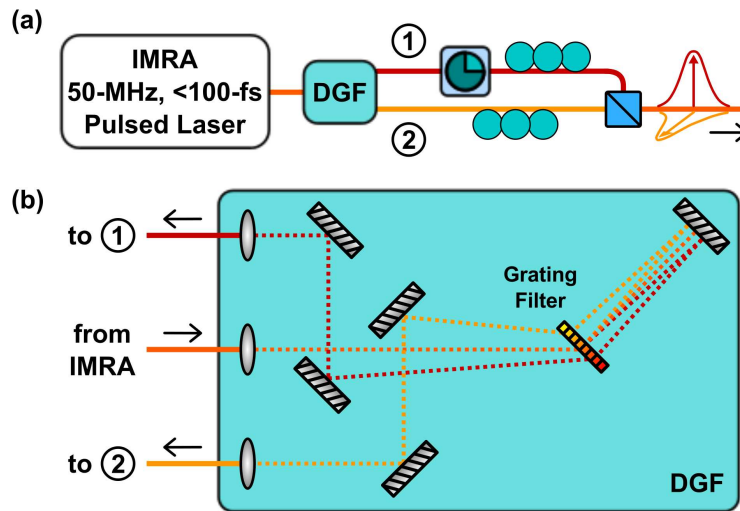


Figure 5.1. (a) This schematic shows the first-generation optical system that prepares the XPM pump pulses for use in switching. We use a broadband, narrow-pulse-width, fiber laser (IMRA) as the seed. From this we pick-off two wavelengths using a free-space double-pass grating filter (DGF). Recombining these wavelengths at a PBS yields dual-wavelength, orthogonally-polarized pump pulses. A tunable optical delay for one of the colors ensures that the orthogonally-polarized pulses are cotemporal. (b) We show the schematic of the system employed to pick off the two distinct frequencies from the broadband input pulse. Initially, the two selected frequencies were 1545 nm and 1555 nm. Later, we used 1551 nm and 1559 nm since they were better balanced in power.

Once we have selected these two frequencies, we route them to opposite inputs of a fiber-coupled polarizing beamsplitter (PBS). Using the respective FPC in each path, we maximize the power out from the same port of the PBS. This naturally imposes the orthogonality condition on the two frequencies. A tunable delay line in the 1551-nm path enables us to

temporally overlap the frequencies. Hence, we have the desired XPM pump pulse—a dual-frequency, orthogonally-polarized, cotemporal pulse with a width of approximately 10 ps.

5.1.2. Second-generation XPM pump pulse preparation

Upon the arrival of higher-rate (1.25 GHz) detectors in our lab, we needed to design a system that is capable of generating pulses at this higher rate. Unfortunately, that meant that we could no longer use the IMRA as our XPM pump pulse source. As such, we need to devise a new method to generate the C-band optical pump pulses.

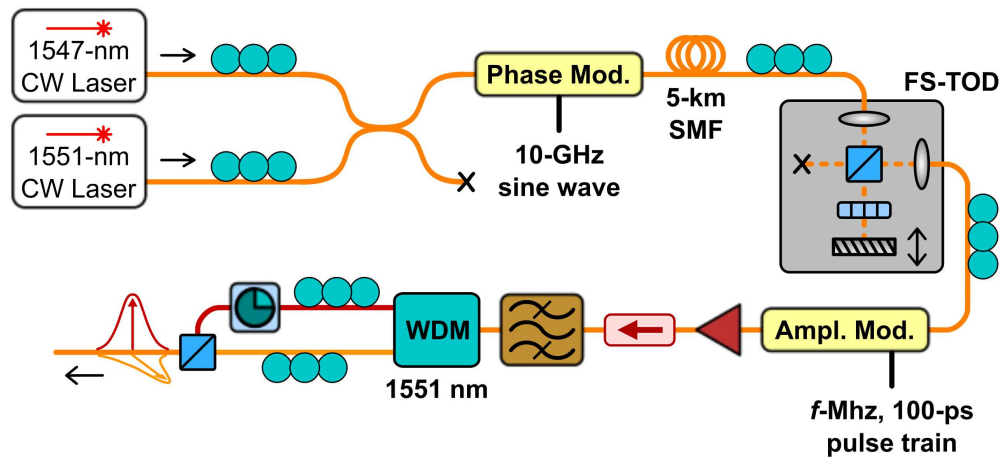


Figure 5.2. This schematic shows the second-generation optical system that prepares the XPM pump pulses. Akin to the first system, this system generates two orthogonally-polarized, cotemporal optical pulses. These pulses are centered at 1547 nm and 1551 nm. The phase modulator chirps the CW seed laser. The subsequent 5-km fiber spool compresses the chirped pulses to yield a 10-GHz pulse train with $\simeq 20$ -ps pulse widths. The free-space tunable optical delay (FS-TOD) enables us to control the arrival time of this pulse train into the amplitude modulator. This modulator pulse picks from the 10-GHz train to yield a downcounted train with a tunable repetition rate of f MHz. In this thesis, we use both $f=50$ MHz and $f=250$ MHz. After amplification and filtering, we use a 1551-nm WDM to split the two frequencies apart, and then recombine them at a PBS to ensure orthogonal polarizations.

The first design solution, shown in Fig. 5.2, uses two CW distributed-feedback (DFB) lasers as the source lasers. The first laser is centered around 1547 nm, while the second laser is centered around 1551 nm. We chose these frequencies because of their availability in the lab. Other CW lasers can be used, but this requires changing the following filtering. The two CW seed lasers are combined at a 50:50 beamsplitter and sent through a phase modulator that is driven with a 10-GHz sine wave. This modulation causes sidebands to appear in the frequency space.

As a brief aside, we show the mathematical derivation of these sidebands here. Imagine we have a pure sine wave at frequency ω_c . We can describe this signal using the equation

$$Ae^{i\omega_c t}. \quad (5.1)$$

If we modulate the phase of this signal using a sine wave at ω_m and with small amplitude β , then we can describe the field at the output using

$$Ae^{i\omega_c t + i\beta \sin(\omega_m t)} = Ae^{i\omega_c t} (1 + i\beta \sin(\omega_m t)). \quad (5.2)$$

Here, we show the first two terms of the Taylor expansion on the right hand side. Using Euler's formulas, we can rewrite the right hand side as

$$Ae^{i\omega_c t} \left(1 + \frac{\beta}{2} (e^{i\omega_m t} - e^{-i\omega_m t}) \right) = A \left(e^{i\omega_c t} + \frac{\beta}{2} (e^{i\Omega^+ t} - e^{i\Omega^- t}) \right). \quad (5.3)$$

Thus, we see that we have generated two new terms located at $\Omega^\pm = \omega_c \pm \omega_m$. These represent the creation of sideband frequencies that are detuned from the central frequency by the modulated frequency. Of course, earlier, we arbitrarily took only the first two terms of the Taylor expansion. Instead, if we include all the terms from the Taylor expansion, then

we obtain

$$\begin{aligned}
 Ae^{i\omega_c t + i\beta \sin(\omega_m t)} &= Ae^{i\omega_c t} \left(J_0(\beta) + \sum_{k=1}^{\infty} J_k(\beta) (e^{ik\omega_m t} + (-1)^k e^{-ik\omega_m t}) \right) \\
 &= A \cdot J_0(\beta) e^{i\omega_c t} + \sum_{k=1}^{\infty} A \cdot J_k(\beta) \left(e^{i\Omega_k^+ t} + (-1)^k e^{-i\Omega_k^- t} \right)
 \end{aligned} \tag{5.4}$$

We use the Jacobi-Anger expansion, a useful identity involving the Bessel functions $J_k(\beta)$, to obtain the previous result. This time we see an infinite number of sidebands corresponding to $\Omega_k^\pm = \omega_c \pm k\omega_m$ with varying amplitudes. These sidebands appear at integer multiples of the modulation frequency. Since our modulation frequency is 10 GHz, we expect to see sidebands detuned by that amount from each of the central frequencies of the DFB lasers.

When looking at this signal in the time domain, it will resemble a 10-GHz pulse train. By sending this pulse train into the 5-km spool of fiber, the chirped pulses' widths compress due to dispersion yielding us with pulse widths $\simeq 20$ ps. We show the autocorrelation of this pulse in Fig. 5.3. We chose the length of fiber to be 5-km because we had the spool in lab. We also had another 2-km spool, but tests using just the 2-km spool or the (2+5)-km spools yielded wider pulse widths. If required, better dispersion engineering, either by using a dispersion-shifted fiber or performing a precise calculation for the length of SMF, can be used to improve the pulse width.

Now that we have a 10-GHz pulse train with narrow pulses, we route the pulses to a free-space tunable optical delay (FS-TOD). Since both frequencies are co-polarized, we use a PBS to discriminate between incoming and outgoing beams. That is to say, the incoming beam is adjusted to be H-polarized using the preceding FPC, thereby transmitting through the PBS. After passing through the QWP (set to 22.5°), reflecting off a translatable mirror, and passing through the QWP a second time, this H-polarized light should become V-polarized.

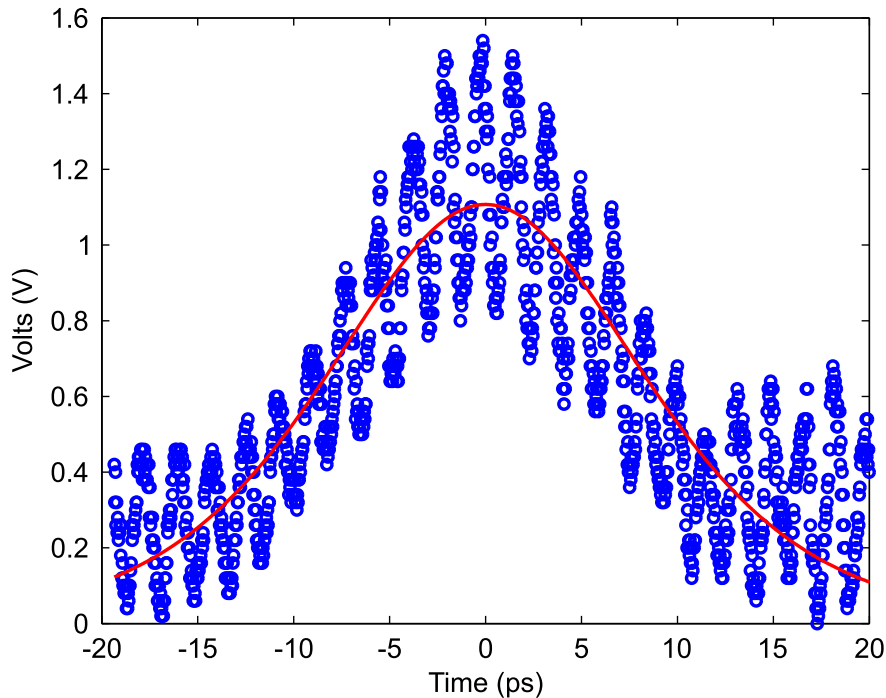


Figure 5.3. When both colors are present, we see the optical interference yielding into the beat note on the pulse envelope. If we fit to the pulse using a squared hyperbolic secant (red line), we can calculate the width of this pulse to be 19.3 ps.

Thus, it reflects off the PBS toward the output collimator. By placing the mirror on a linear translation stage, we can adjust the path length, thereby creating a tunable optical delay.

This tunability allows us to align the arrival time of the optical pulses with the electrical pulses in the amplitude modulator. The amplitude modulator pulse-picks, and thereby downcounts, the 10-GHz pulse train to match our detection gating repetition rate (or an integral divisor of said quantity). We will discuss the system used to generate the electronic signals later in §5.2.6, but for now, suffice it to say, we downcount to 50-MHz and 250-MHz for various tests shown in this thesis.

After amplifying the downcounted pulse train and using a wide bandwidth filter, we use a narrowband WDM centered at 1551 nm to spatially separate the two pump frequencies.

As done in the first generation, we individually route each frequency through an FPC and onto a PBS. We adjust the FPCs to maximize the power at the output of the PBS. Again, there is a tunable optical delay in one of the paths that we use to temporally align the two pulses at the output of the PBS. This yields the desired XPM pump pulse.

5.1.3. Third-generation XPM pump pulse preparation

Although the second generation design can be used, it often drifted in power. These power fluctuations resulted from random thermal fluctuations of the 5-km fiber spool which affected the pulse-picking performance of the amplitude modulator. The fluctuations were particularly problematic since the subsequent 2-W EDFA's safety checks would automatically turn itself off if the input power fell below a minimum threshold (0.08 mW). Hence, we made a few changes to the second generation's design.

The first change is to wrap the fiber spool with bubble wrap and styrofoam to provide thermal isolation. The goal is to minimize the effect of ambient environmental temperature fluctuations that cause the fiber length to change.

The second change is to remove the FS-TOD. This apparatus, although not too lossy, does introduce additional loss, particularly from free-space-to-fiber coupling. More importantly, we can reproduce its functionality by simply adjusting the relative frequencies of the input CW wavelengths. Adjusting their frequencies modifies their group velocity difference, albeit only slightly. Nonetheless, since we use km-length scales of fiber, that small change can yield enough temporal tunability to align the XPM pulse train with the electronic pulse train at the amplitude modulator. Conveniently, our DFB modules provide us with limited tunability, thus, we can safely eliminate the free-space delay optics from our system.

Finally, the third change to improve the output power from this system involved replacing the 50:50 beamsplitter at the input with an optical add-drop multiplexer (OADM). The OADM adds in a specific narrow frequency band into the desired spatial path. In this case, we matched the OADM frequency with the later WDM's frequency at 1551-nm. If necessary, this affords us the flexibility to still change the 1547-nm laser to a different frequency in the future. The schematic of this final design is shown in Fig. 5.4.

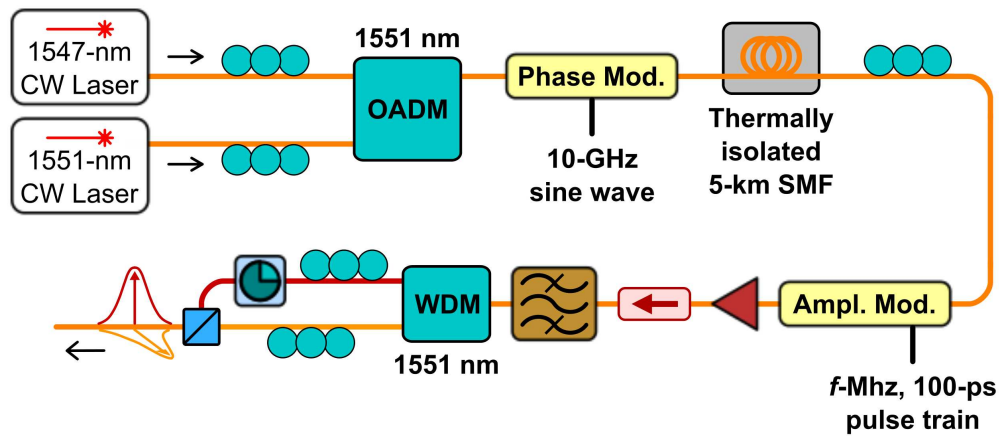


Figure 5.4. This schematic shows the third-generation optical system that prepares the XPM pump pulses. This system makes few modifications to the second-generation system (shown in Fig. 5.2). These include the replacement of the 50:50 beamsplitter with an optical add-drop multiplexer (OADM), addition of thermal isolation around the fiber spool, and removal of the FS-TOD.

5.2. Generation of FWM pump pulses

For all the sources described in this chapter, we have a system where an input laser is sent through an EOM to either *chop* the signal when the input is the tunable continuous-wave (CW) laser (Santec TSL-210V), or to *pulse pick* the signal when the laser is a pulsed laser (U2T Photonics TMLL-1310). The U2T laser generates femtosecond pulses at a 10-GHz rate. These pulses are temporally broadened after sending the broadband laser through a

WDM. We require the WDM to select a narrow bandwidth pulse around the desired FWM pump frequency at 1305 nm. This filtering broadens their width from 2 ps^[39] to widths on the order of 20 ps.

For the remainder of this section, “CW source” refers to the usage of the chopped Santec setup, and “pulsed” or “U2T source” refers to the usage of the pulse-picked U2T setup. Detailed descriptions of both configurations are provided in the sections which follow. Described in §5.2.1, the CW source was used to demonstrate early versions of the switching technology and entanglement generation. In an effort to demonstrate faster switching, we moved to the higher-rate, narrower pulse-width U2T source. We describe modifications and improvements to the setup and its operation in §5.2.2, §5.2.3, §5.2.4, and §5.2.5. Finally, learning from the lessons of the previous generations, we designed and built the electrical pulse preparation electronics system described in §5.2.6. Aspirations to use a higher-rate detection system, remove effects from neighboring pulses, and generate narrowly-separated pulse packets at tunable intervals motivated us to build the latest system.

All of the source preparations discussed in this section follow a simple paradigm. We start by generating a square wave with the shortest rise and fall times as possible. Next, we perform an AND operation on the square-wave with a temporally displaced version of itself to generate a narrow pulse. In later designs, we add a third step of cleaning up the pulse’s rise/fall times and trailing overshoot fluctuations by using a D-flip-flop to discretize the output.

5.2.1. Original FWM pump pulse preparation

In Fig. 5.5, we show the original schematic of the chopping circuitry used to generate test pulses demonstrated in Matthew Hall’s PhD Thesis, and for his entanglement source^[3,37].

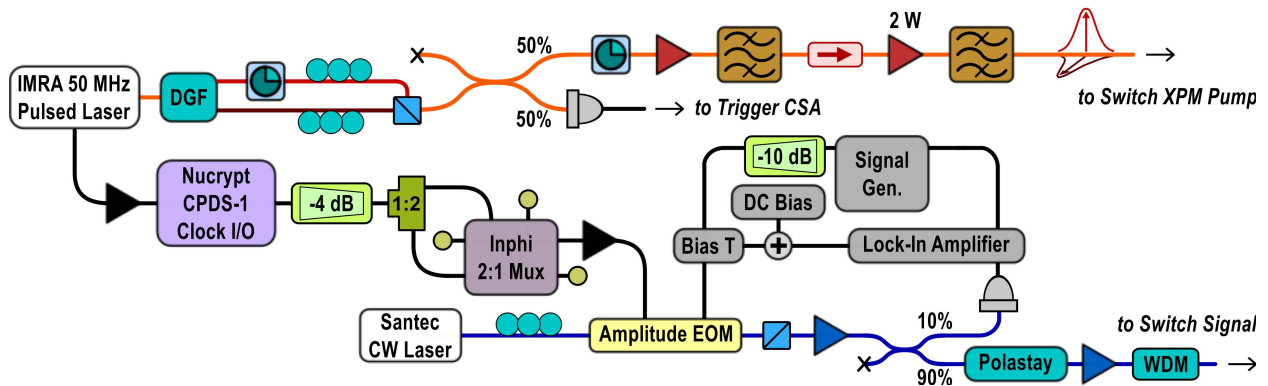


Figure 5.5. Schematic showing the original chopping scheme. The C-band XPM pump preparation, along the orange (top) path, shows the creation of the dual-wavelength, orthogonally-polarized XPM pump and its subsequent amplification for use in the switch. Along the blue (bottom) path, we show the CW laser being chopped into 50-MHz, 100-ps pulses and then amplified for demonstration of switching. Following the black (middle) path, is the electronics which determines the chopping frequency, and pulse-shape. Also, shown is feedback loop implemented for long-term stability.

In this scheme, for convenience, everything was triggered from a 50-MHz C-band pulsed laser, thus establishing the fundamental clock for the system. The electrical output of the laser/clock was used to trigger the gated Geiger-mode detectors (Nucrypt CPDS-1). These detectors were at the time not used for any detection but rather for the regular 50-MHz square wave they generate at their CLK OUT port. This output was split such that one path was sent to the first data port (In_1) of a 13-GHz multiplexer (Inphi 20709SE) hereafter referred to as MUX. The other path from output clock was sent to the select port ($SEL=S_p-S_n$) of the MUX. The second data port (In_2) of the MUX was connected to ground. In this configuration, whenever the SEL was high, the MUX would output the value of In_1 , and whenever SEL was low, the MUX would output the value of In_2 , i.e. zero. Thus, this MUX behaves functionally as a traditional AND gate. Since both provided inputs are square waves, varying the relative path between the In_1 path and SEL path, a tunable width pulse

was obtained at the output of the MUX. The output of this MUX was then sent to an EOM driver/amplifier (Picosecond Pulse Labs 5865). This amplifier is naturally connected to the EOM which then performs the chopping operation on the source. For this design, while we were able to obtain 100-ps chopped CW pulses, our pulse would contain ~ 300 -ps tail which would reduce our switching contrast.

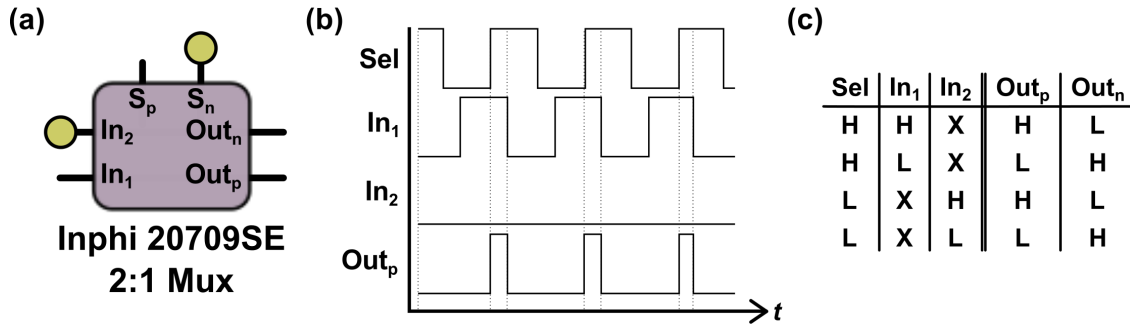


Figure 5.6. (a) Pin-layout of Inphi 20709SE with voltage connections. Note that the subscripts ‘p’ and ‘n’ designate complementary ports. Since S_n is connected to ground, $SEL = S_p - S_n = S_p$. (b) We show here four contemporary plots to pictorially describe the operation of the Inphi 20709SE. Note that when the SEL and In_1 traces are both high, the Out_p is also high. Otherwise, since In_2 is set to GND, if SEL or In_1 is low, then Out_2 is low. (c) Truth table for the operation of Inphi 20709SE.

After the EOM and the first EDFA, we have a 90:10 coupler. While the 90% port is sent to be used in the experiment and is amplified, the 10% port is used for a feedback mechanism. This feedback is necessary to compensate for any long-term drifts in polarization and bias voltage. The polarization drift is accounted for by placing a linear polarizer (ThorLabs IFP1310PM-FC) after the EOM. This polarizer is inserted in a fashion to be on-axis with the EOM’s active axis. By doing so, off-axis polarization components are removed from the transmitted signal. While this would normally yield a fluctuating output power, using the PDFA in Automatic Level Control (ALC) mode ensures a constant output power. Thus, the first PDFA along with the polarizer account for any polarization drift.

The voltage and source drift leading to poorer extinction through the EOM is compensated using feedback electronics that Matthew Hall designed and implemented. A 100.5-kHz sine wave is generated using a sine-wave function generator (Elenco GF-8026). This sine wave is combined with a DC bias voltage from a power supply (Elenco XP-581) using a bias-tee (Mini-Circuits ZFBT-6GW-FT). Monitoring the 10% port mentioned earlier on a photodiode, and sending the electrical signal to a lock-in amplifier (Stanford Research Systems SR530) which is synchronized with the 100.5-kHz sine wave, the extinction is monitored and additional voltage is applied as necessary to maintain highest extinction.

5.2.2. First-generation FWM pulse-picking source

While switching with CW light is convenient, we are limited to the ~ 100 -ps pulse widths obtained from the chopping window. Due to imperfect chopping, these pulses also tend to have a low-amplitude tail that extends for ~ 300 -ps after the main pulse which will reduce the switching contrast and switching performance. If we wish to demonstrate even faster switching, we need to move to narrower pulses. In order to accomplish this, we change our 1310-nm laser from the CW Santec to a pulsed U2T laser which outputs pulses at 10-GHz repetition rate and 100-fs pulse widths. These pulses are spectrally filtered to the desired 1305-nm wavelength and thus temporally broadened to approximately 20 ps.

Unfortunately, since the pulse-picking window operates at 50 MHz, we need a method to lock the 10-GHz pulse train to the 50-MHz clock. This lock should prevent the 10-GHz signal from "walking around" with respect to the 50-MHz chopping window. For this reason, we employ the pulse-picking system shown in Fig. 5.7. Rather than using the electrical clock from the IMRA laser as the source, we instead opted to photodetect a portion of the optical output obtained using a 95/5 beamsplitter. This clock signal was then amplified, and sent

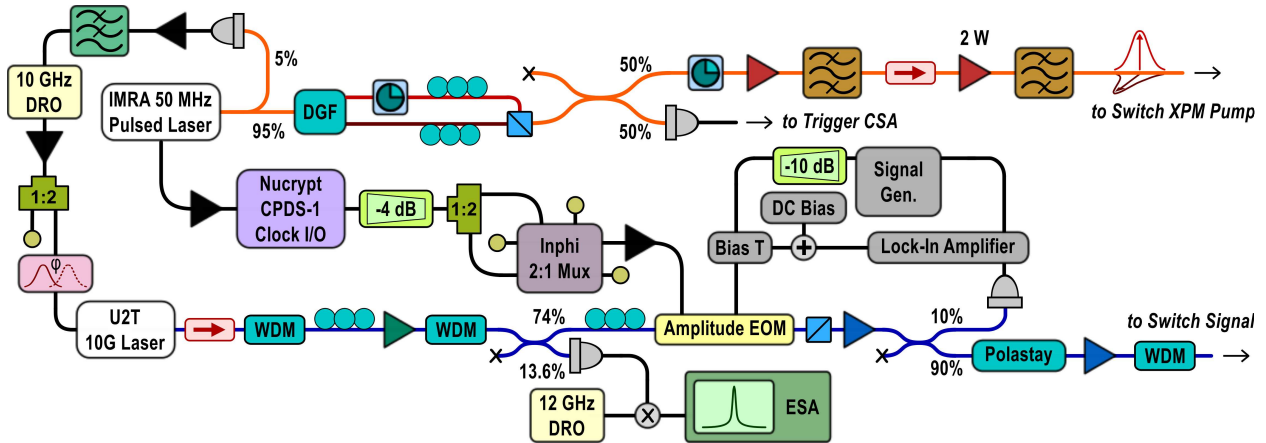


Figure 5.7. First-generation pulse-picking laser source. While the pump pulse generation and the chopping circuitry remain the same as the original chopping scheme, we replace the CW Santec laser with the 10-GHz pulsed U2T laser. In order to ensure that the 10G pulses are stable with respect to the 50-MHz chopping clock, additional electronics are employed to hybrid mode-lock the U2T laser.

through an electrical low-pass filter yielding a 50-MHz sine-wave. This pure tone was then sent as a reference to a 10-GHz dielectric resonator oscillator (DRO) which was locked to the 50-MHz signal. The output from this was amplified by about 30 dB, then slightly attenuated using a 6 dB splitter, and finally passed through a phase-shifter before being sent as the reference for hybrid mode-locking of the U2T.

Since the U2T outputs temporally-narrow, spectrally-broad pulses, further pulse conditioning is required. Hence, we introduced an isolator to prevent back-reflections into the laser, followed by a WDM at the desired operating wavelength of 1305 nm. Since this filtering reduces the power, we pass the signal through an FPC and the semiconductor optical amplifier (SOA). The FPC is necessary to maximize transmission and gain through the polarization-dependent SOA. Finally, we pass the signal through another WDM filter before sending it along to the same EOM setup, now used as a pulse-picker instead of a chopper.

We note the addition here of a beamsplitter and photodetector after the second WDM. This photodetected signal is mixed with a 12-GHz oscillator and monitored on an electrical spectrum analyzer (ESA). This is done to keep a watchful eye on the hybrid mode-lock established between the 10-GHz DRO and the passive mode-lock condition of the U2T laser. It is necessary to have this because we observe drift over the course of several hours between these two which would require tuning the passive mode-lock of the U2T to re-obtain the lock. The 12-GHz oscillator is only used to produce a beat signal so that we can monitor the signal on our ESA since our ESA is limited to seeing up to 3-GHz signals.

5.2.3. Second-generation FWM pulse-picking source

While the first generation pulse-picker was able to do the trick, it had a couple problems. The first such problem was that it used the CLK OUT from the Nucrypt detectors tying up these detectors without using them for the desired intent. It was also found that the square-wave from the Nucrypt detectors was not ideal inasmuch as it provided a reasonable source of jitter and therefore temporal walk-off. We theorized that this led in part to signal walk-off between our 50-MHz and 10-GHz signals and required the retuning of the U2T's passive mode-lock rather regularly.

As shown in Fig. 5.8, in an effort to clean up the square-wave and use the Nucrypt CPDS-1 for detection rather than as a triggered square-wave generator, our second generation laser source preparation entailed replacing the Nucrypt CPDS-1 with an FPGA board (Digilent Spartan-3E). The FPGA board would accept a trigger from an optically detected pulse and generate a 50-MHz square-wave, 47% duty cycle at the output. Following the same 2:1 MUX, we would generate short pulses. Unfortunately, while we were at times able to generate pulses shorter than 100-ps, stability of this system was a lingering issue.

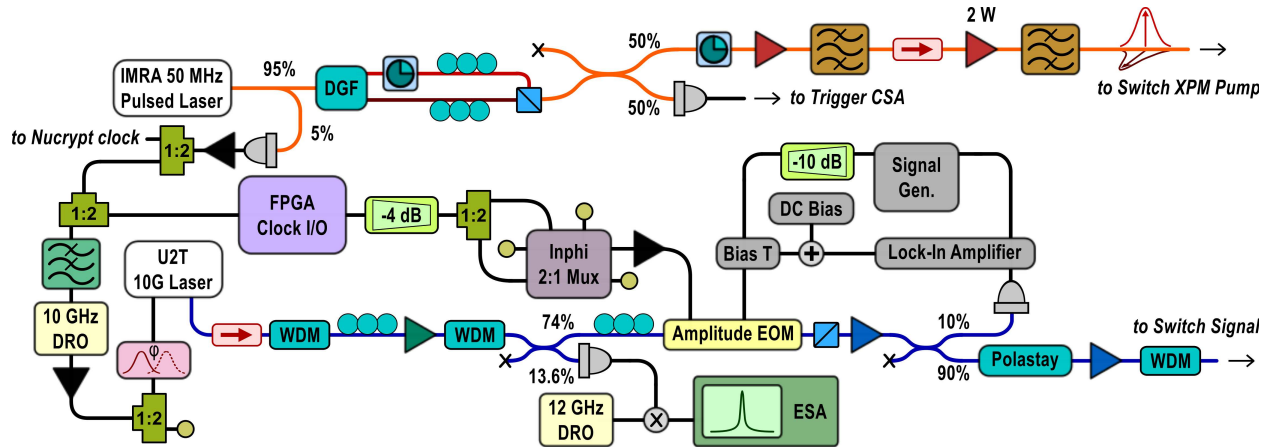


Figure 5.8. Second-generation pulse-picking laser source. While functionally very similar to the previous generation, this design replaces the use of the Nucrypt CPDS-1 CLK I/O for an FPGA with code used to generate a 50-MHz square wave based on an input 50-MHz trigger. It also modifies the source of the 50-MHz trigger from the electrical output of the IMRA to the photodetected output previously only used to hybrid mode-lock the U2T.

When further investigated, it was determined that there were two errors. First source of this issue was the electrical output of the IMRA. For some reason, as yet unknown, this output was not providing a regular 50-MHz pulse train which would be useful for synchronizing with the IMRA’s optical pulse train. It has been noticed that varying torque and tension on the electrical output also corrupts the optical signal. As such, it was decided to not use this port, and instead, simply use the photodetected pick-off already being used to lock the U2T. This change is also noted in Fig. 5.8.

A second issue with this setup is that the DRO which was used to lock the U2T to the IMRA began malfunctioning. After repair, a neater signal was witnessed, but this time with a persistent 100-ps jitter. A jitter of that magnitude obscures any ability to view a 100-ps-wide pulse. While we were able to later track the source of timing jitter to the slow and inconsistent clocking of the FPGA, at this time, we were uncertain what was the cause,

and instead set out to eliminate the jitter. As such, another source preparation mechanism was necessitated.

5.2.4. Third-generation FWM pulse-picking source

Our first attempt to remedy the large jitter entailed using a D-type flip-flop (DFF) to clean up the signal. When we first implemented this solution, the hope was to be able to clearly delineate between low and high values over the 100-ps pulse and be able to use the high-speed operation of the DFF to create sharp rising and falling edges. Also, it was hoped that the 100-ps jitter would disappear since we are now clocked at 10-GHz, i. e. only once every 100 ps would we select the value of the MUX's output to be either low or high. Hence, the DFF was used to discretize the MUX output to eliminate the 100-ps jitter while also providing regular low or high levels to eliminate spurious ripples caused by electrical overshoot.

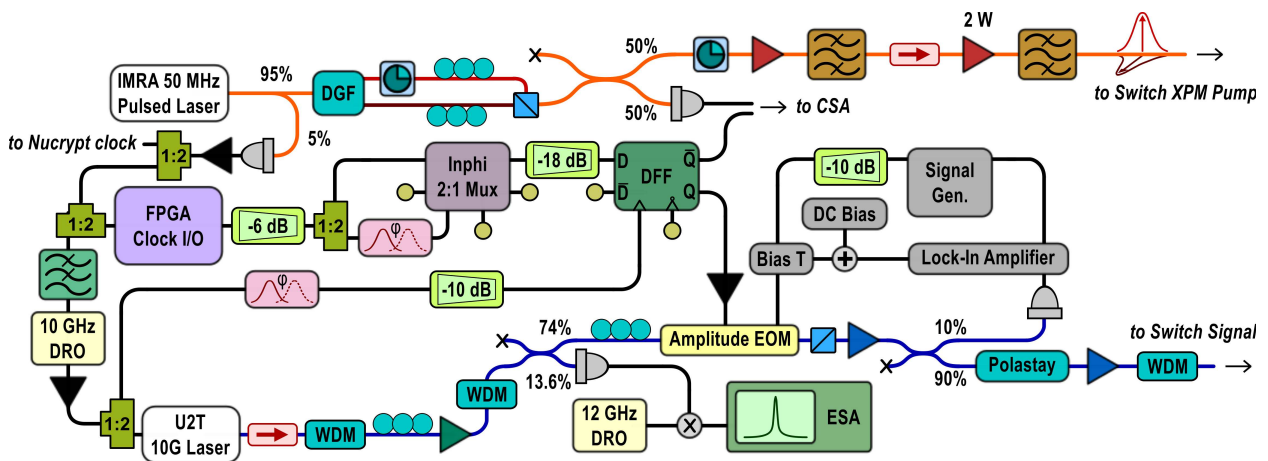


Figure 5.9. Third-generation pulse-picking laser source. We now added a D-type flip-flop (DFF) to aid us in discretizing the pulse output to eliminate the 100-ps jitter, and also provide us with regular low and high voltage levels to reduce electrical overshoot generated by the MUX.

We show in Fig. 5.9 the changes to the setup. In this new setup, we also note the relocation and addition of the phase shifters. We have added one phase-shifter to only

one input of MUX. This enables us to select a relative difference between the two paths of MUX—and thus the output pulse width from the MUX—in a continuous fashion. This merely allows for more precise tuning and was very useful in conjunction with the DFF used to discretize this output.

While the data obtained using this source preparation was good and we were able to obtain 100-ps pulse with <10 -ps jitter and minimal ripples after the main peak, it had one lingering problem. Due to the aforementioned 100-ps jitter, the discretization operation of the DFF would often lead to identical pulses to the main pulse, but shifted ± 100 -ps. Although these neighboring pulses were present less often than the main pulse, they were still present, and would lead to worse results than originally hoped. It was at this time that we finally traced the source of the original jitter to the FPGA and required a new solution for the generation of the square-wave.

5.2.5. Fourth-generation FWM pulse-picking source

In order to resolve the jittering problem, the system was tested with a DFF instead of the FPGA. The DFF was used because it was clocked at 10-GHz rate which already inspired confidence insofar as enabling faster signals with low jitter. The general principle in using a DFF for generating a square-wave is to discretize an input pulse of arbitrary pulse-width into its low and high values thereby generating a square wave. This method only works satisfactorily if the input pulse has a “clean” pulse shape. Here, “clean” is used to mean that the pulse has regular rising and falling edges which are largely devoid of abnormal spikes. These spikes can yield additional square pulses which can complicate the ANDing process that follows.

By sufficiently attenuating the input of the DFF, one can clean up the noise on a signal and obtain a decent input pulse. Although the width of the pulses generated using this mechanism are significantly smaller than the previous methods of generating pulses, the pulse width does not matter if it is larger than the desired 100-ps pulse since we will again reduce the pulse width to the desired 100-ps value using the ANDing procedure.

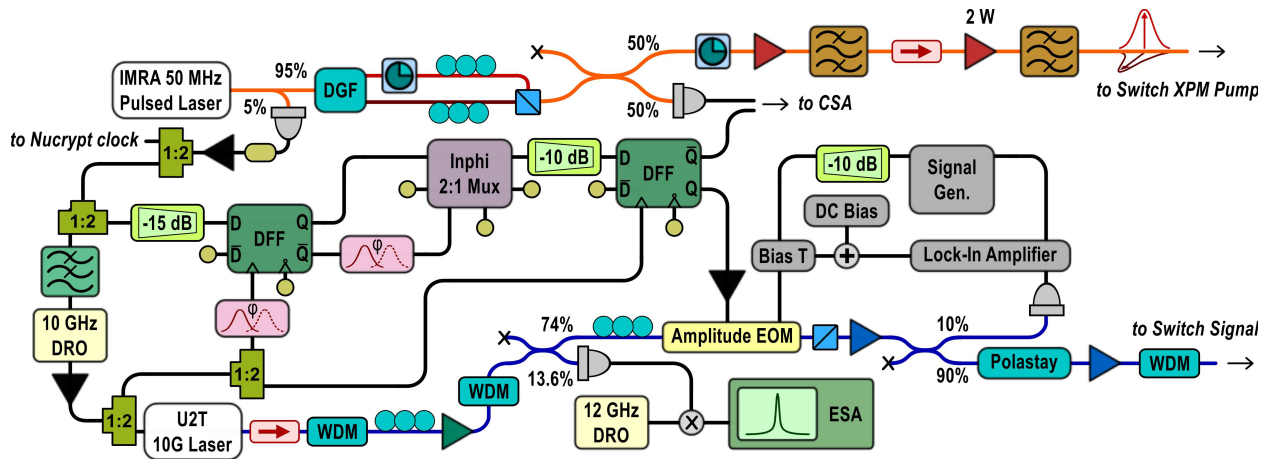


Figure 5.10. Fourth-generation pulse-picking laser source. We now introduce a second DFF, this time serving the purpose of creating the square wave used for the ANDing procedure performed by the 2:1 MUX.

We show in Fig. 5.10 the new setup for obtaining the pulse-picking pulse. Here, we have replaced the FPGA with a DFF which is also clocked using the 10-GHz output from the DRO. This DFF discretizes the pulse obtained from the pick-off port of the IMRA and generates a square-wave. Note that we have also changed the pick-off from a 95/5 beamsplitter to the reflect port of a PBS with a HWP in front. This allows for more transmission, and less loss for the XPM pump pulse condition, while also having the added advantage of enabling us to tune the width of the square-wave generated by tuning the reflected power of the PBS.

Given that this method of generation for the pulse-picking laser source was stable, easily tunable, and satisfactory, we used this for some of the tests shown later in Chp. 6. The other tests use the newest setup discussed in the next section.

5.2.6. Fifth-generation FWM pulse-picking source

One of the challenges we observed in previous generations of the FWM pulse preparation was that we always seemed to have some overshoot and broadening of the electrical pulse. This resulted in the amplitude modulator pulse-picking neighboring pulses. Since all of the electronics chips that we used were rated for 13-GHz operation, we theorized that maybe using higher frequency electronics will reduce some of these effects. As such, we embarked on designing a new electronics setup from the ground up.

As luck would have it, we also procured new higher-rate single-photon detectors (Nucrypt CPDS-2000) around this time. Since we wanted our new electronics to harmoniously work with those detectors and the previous version of the detectors (Nucrypt CPDS-4), our system design needed to have an adjustable clock rate.

An additional design goal was to afford the ability to select a varying number of pump pulses when we pulse-pick from the 10-GHz source. We desire this functionality because it enables us to vary the number of time-bins that we generate as explained later in §5.4.

With these two main goals in mind, we designed and built the system shown in Fig. 5.11. Since we want an adjustable clock source, we can no longer use the IMRA as our reference clock generator. Instead, we opted to use a clock generator (Stanford Research Systems CG635) tuned to 100 MHz and 50% duty cycle. We select this frequency since it matches the phase-locking frequency of the 10-GHz and 20-GHz DROs (Microwave Dynamics PLO-2020-10.00 and PLO-3070-20.00, respectively). The clock generator has two inverse outputs.

We use split one output and use that to drive each of the aforementioned DROs. We use the 10-GHz DRO to hybrid mode-lock the U2T laser just as we did before. We also use the 12-GHz DRO mixed with a photodetected 10-GHz optical signal to monitor this phase-lock quality on the ESA, as before. The 20-GHz DRO and subsequent phase shifter tune the arrival time into the clock input of a latched comparator (Inphi 25707CP), which we denote LC.

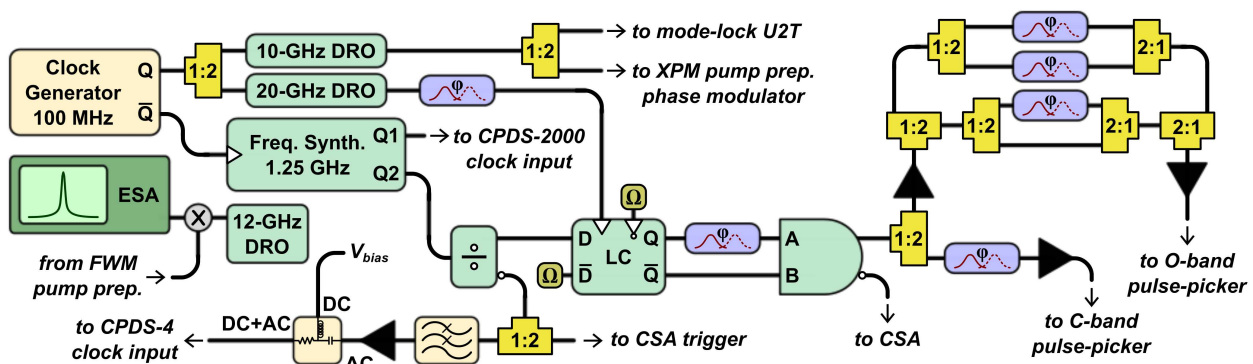


Figure 5.11. Fifth-generation FWM pulse-picking source. Starting from square one, but using what we learned in the first four generations, we developed the entire electronics system shown here. This design uses higher-speed electronics (>20 GHz). The latched comparator (LC) replaces the functionality of the DFF. We now use an AND gate, instead of a 2:1 MUX, to yield the ANDing operation. By adjusting the integer divisor of the frequency divider (\div), we can change our pulse-picking frequency to any quotient, $1.25/n$ GHz, where $n \in [2, 32]$. We often choose $n = 25$ or $n = 5$ to yield a 50-MHz or 250-MHz pulse train, respectively. There are two important outputs to this design. The first output pulse picks from a 10-GHz pulse train at the aforementioned rate for use as a C-band XPM pump pulse. The second output pulse picks up to four consecutive pulses from a 10-GHz pulse train at the repetition rate mentioned above. We route this output to an O-band amplitude modulator to create the FWM pump pulses.

The other output of the clock generator phase-locks a tunable frequency generator (Valon Technologies 5008). Since the CPDS-2000 detector is clocked at 1.25 GHz, we set one output of the frequency generator to match that. Ideally, we would set the other output to 50 MHz

to match the CPDS-4 detector gating rate, but the Valon 5008 has a minimum frequency output of 138 MHz. Thus, we opt to set the other independent output to 1.25 GHz also.

At this output, we place a frequency divider (Hittite HMC394LP4). This divider, denoted by the \div symbol, can divide an input frequency by any integer between 2 and 32. Hence, we set it to divide-by-25 to obtain a 50-MHz repetition rate signal. Alternatively, we can set it to divide-by-5 for a 250-MHz repetition rate. We use the latter setting to demonstrate higher rate switching. One output (shown as the negated port denoted by the \circ at the output) of the divider is split and sent to two locations: (1) the trigger to the communications signal analyzer, CSA (HP CSA803 with SD-40 and SD-24 sampling heads), our active time-domain monitor; (2) the clock input of the Nucrypt CPDS-4 detector array. On the output fed to the detectors, we use a bias tee to add a DC offset voltage to protect the detector electronics.

The positive output of the frequency divider is an input to the LC. The LC is used to create a sharp rise and fall time using the same principle as the DFF described earlier. Unlike the DFF operation, which was clocked at a rate of 10-GHz, we designed this system to use a 20-GHz clock. This increases the sampling of the signal, and thereby should improve the rise and fall times.

As an aside, the LC, like many other high-speed electronics, is meant to be used with common-mode logic designs. This means that it has positive and negative inputs (and output). If we use each pair by inputting a signal and its inverse to the respective inputs, then we are operating in double-ended mode. This has benefits of reducing noise on the signal and improving signal fidelity at higher rates. Despite these advantages, we opt to use these devices in single-ended operation mode since it gives us the flexibility to use the other outputs as monitors or signals elsewhere. As a consequence of this, we need to terminate

unused inputs to these devices with $50\text{-}\Omega$ terminators to ensure proper internal impedance matching and also protect the device from accidental electric shocks.

Just as we did before with the DFF, we route both outputs to two of the inputs of an AND gate (Hittite Microwave HMC852LC3C). In one path, we insert a phase shifter to allow us to control the relative overlap between the two signals. The AND gate replaces the 2:1 MUX from previous iterations of the electronics setup. We remark here that the AND gate actually has four inputs, although only two are shown in Fig. 5.11. The other two inputs are the respective inverse inputs for the shown inputs A and B, and are $50\text{-}\Omega$ terminated as mentioned above.

We route one output of the AND gate to the CSA to actively monitor the shape of the pulses we are generating. The other output is split twice to create four identical pulses. Using phase shifters in three of their paths, we can tunably delay them with respect to the phase-shifter-less pulse. By recombining them using 2:1 electronic combiners (Marki Microwave PBR-0012), we generate up to four pulses with 100-ps delays between them in one cable. If we want fewer than four pulses, we can simply disconnect the undesirable channels and terminate them with $50\text{-}\Omega$ terminators. By changing the number of pulses, we modify the number of time-bins our time-bin entanglement source creates, as described later in §5.4. Because of the method of generation of these pulses, our current operational limit is four pulses, but an additional “layer” of splitter and combiners can yield up to 8 time-bins. Hence, growing this system, while doable, can be an expensive solution. Thus, we suggest future designers to possibly reconsider their method of generating a sequence of pulses. Nonetheless, this output can then drive the amplitude modulator to generate the desired FWM pump pulses.

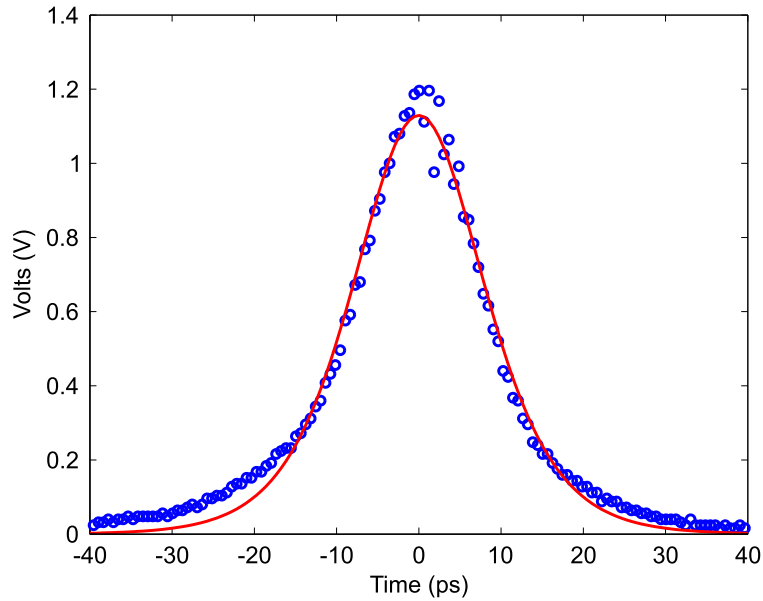


Figure 5.12. Autocorrelation of the filtered O-band pulse. When fit using a squared hyperbolic secant (red line), and accounting for the autocorrelation factor of 30 ps/ms, we obtain a corresponding width of 18.7 ps for our filtered U2T pulses.

5.2.7. Characterization of O-band pulses

Setting the fifth-generation FWM pump pulse setup to select only one pulse, we can drive the amplitude modulator to generate a 50-MHz pulse train. In Fig. 5.12, we show the autocorrelated trace. Fitting this to a squared hyperbolic secant function, we obtain a pulse width of $\simeq 19$ ps. This width defines the narrowest duration for each time-bin. Since this width is due to broadening from filtering, we assume that if we increase the number of consecutive pulses selected, they all have roughly this width. Now that we have electronic pulses that chop or pulse-pick our laser source appropriately, we will investigate how to use the resulting optical pulses to generate photon pairs.

5.3. Photon-pair source

In this section, we will discuss a simple, basic design for photon-pair generation. In the preceding section, we described the electronic systems used to drive the amplitude modulator. The optical input to the amplitude modulator is a 10-GHz optical pulse train with center wavelength of 1305 nm. After pulse picking, we have a f -MHz pulse train with $\simeq 20$ -ps widths and the same wavelength. As mentioned in the previous section, f can be tuned, but often we set it to either 50 MHz or 250 MHz. Once we have this optical pulsed source, we can route it to the elements that generate the photon pairs.

In Fig. 5.13, we see the laser source is fed through a circulator and into a 500-m spool of standard SMF-28 optical fiber. Due to the $\chi^{(3)}$ nonlinearity of the fiber, FWM generation of signal and idler photons occurs. We submerge this fiber in a liquid nitrogen bath. By cooling our fiber to 77 K, we suppress much of the spontaneous Raman photon generation that could add background noise to single-photon measurements.

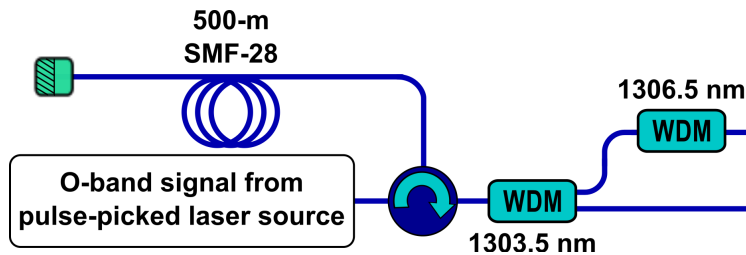


Figure 5.13. This correlated photon pair source is a 500-m spool of SMF-28 optical fiber cooled to 77 K with a sequence of WDMs to filter out the pump wavelength and enable access to the signal and idler photons. Usage of the Faraday mirror and double-pass geometry via the circulator ensures long-term polarization stability.

After propagating through a single pass of the fiber spool, the pump pulse is incident on a Faraday mirror. Using the Faraday mirror yields two primary benefits. First, it doubles the path travelled by the pump, thereby increasing the time during which the FWM process can

occur. Second, it makes the source more phase stable by undoing any birefringence-induced phase mismatch accumulated from travelling to the mirror on the return trip through the fiber. This second benefit occurs because the photons' rate of travel through the fiber is significantly faster than the time-scale for any birefringence fluctuations to happen. By routing this returned light through the circulator again, and then through a series of WDMs, we can filter the signal and idler wavelengths from the pump wavelength. These photon pairs can subsequently be routed to whatever following experimental apparatus/setup the user desires.

5.3.1. Photon-pair-source performance

Using a stream of photon pairs, which arrive at a rate of 50 MHz, we characterized the photon pair source described above. We performed these characterizations using the slower CPDS-4 detectors and the faster CPDS-2000 detectors. In order to be able to clock both detector arrays, we use the pulse generation electronics described earlier in this chapter (See §5.2.6). By tuning the pump pulse power, we can affect the photon-pair-production rate. Figure 5.14 shows the pair production rate as a function of the average measured pump power. We have measured that, for varying powers, we can create photons with pair-production rates on the order of 10^{-3} – 10^{-2} photons per pulse.

We obtain this figure by measuring coincidence counts and then back-calculating to determine the number of photons produced at the source. This measurement requires two detectors, one at each end of the signal (idler) paths. A coincidence count occurs when these two detectors fire simultaneously, highlighted in green in Fig. 5.15. Throughout the remainder of this thesis, we will simply refer to coincidence counts as coincidences. The

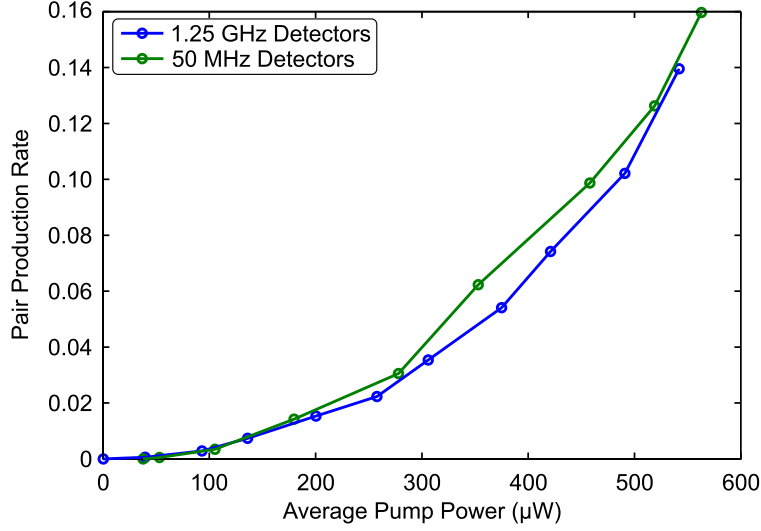


Figure 5.14. Photon-pair production rate. We show here the photon-pair production rate as a function of FWM pump pulse power for our source operating at 50-MHz, and measured using both single-photon detector arrays available to us. To avoid multi-pair production, we operate in the regime with a PPR between 5×10^{-3} to 1×10^{-2} , corresponding to a pump power of 100–150 μW .

actual calculation for the pair-production rate (PPR) used is

$$PPR = \frac{C}{g \cdot \eta_d^2 \cdot \eta_f^2}. \quad (5.5)$$

Here, C is the measure coincidences, g is the number of detection windows (gates) used to collect them, η_d is the detection efficiency, and η_f is the transmission loss through fiber. For this calculation, we estimate $\eta_d \simeq 0.1$ and $\eta_f \simeq 0.33$ as approximates for our experimental conditions. We remark that the aforementioned PPR has units of number of photon pairs per gate. Since the gate clock matched the pulse rate, this translates to photon pairs per pump pulse.

We also characterize our sources by looking at the coincidence-to-accidental ratio (CAR). This metric is useful because it essentially measures the signal to noise ratio of the source at various pump powers.

G	0	1	2	3	4	5	6	7	8	9	10	11	12	13	14	15	16	17	18	19	20
S_1		*			*		*					*	*					*			*
S_2		*					*		*				*			*		*			*
C_{12}	0	1	0	0	0	0	1	0	0	0	0	0	0	0	0	0	0	1	0	0	1
A_{12}	0	0	0	0	0	0	1	0	1	0	0	0	0	1	0	0	0	0	0	0	0

Figure 5.15. Example of measured coincidence and accidental counts. Here, we show an example of how to obtain count coincidence and accidental counts. The little red stars denote when detectors 1 or 2 have fired. S_1 and S_2 represent the single counts when the detectors fire. C_{12} and A_{12} represent the coincidence and accidental counts. These events are highlighted in green and orange ovals, respectively. For this example, we assume that the accidental delay is set to two gates, where the enumerated gates (G) indicate the detection window during which counting happens.

An accidental count, heretofore referred to as an accidental, also exists when the detectors both fire, but not due to two correlated photons. Accidentals can occur due to a single photon in one path randomly firing simultaneously with a detector dark count in the other path, or when both detectors have random dark count events. As a sidenote, a dark count event happens due to random excitations in detectors since our detectors are not perfect devices. We can artificially measure accidentals by comparing the signal photons' data stream with a time-delayed idler-photon data stream, as highlighted in orange in Fig. 5.15. In the example shown, the accidentals' delay for comparing the data streams is two gates. While measuring accidentals is nice for quick sanity checks when performing experiments, more often than not, we use calculated accidentals. We direct the reader to appendix A for details on how we calculate dark-count-subtracted coincidences, calculated accidentals, and dark-count-subtracted accidentals.

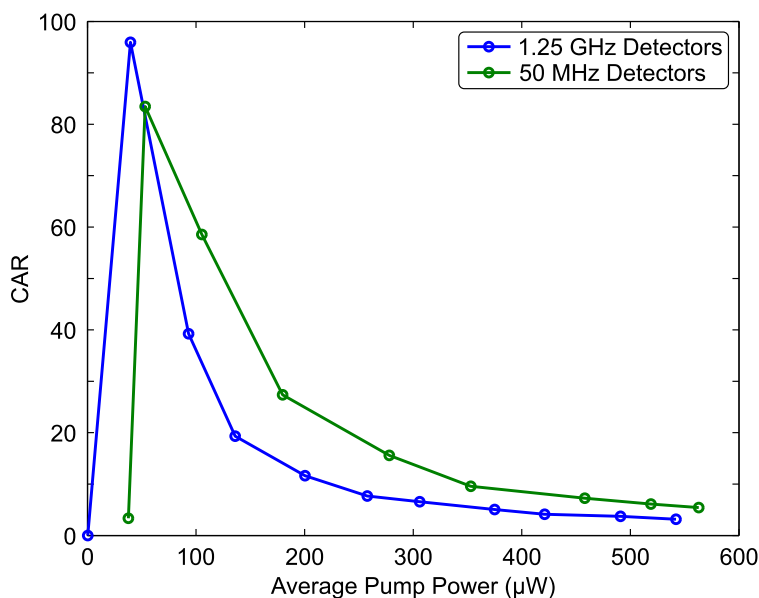


Figure 5.16. Coincidence-to-accidental ratio (CAR). We show the CAR as a function of the average FWM pump power for the 50-MHz repetition rate pump.

We show in Fig. 5.16, the CAR of our system as a function of the average pump power. Ideally, we want to operate at the highest CAR ($\simeq 100$). Unfortunately, if we compare to the pair production rate, this corresponds to very few coincidence counts per gate. This means that we must count for a long time to obtain sufficient count statistics. Given that tomographies can take a while, and higher-dimensional tomographies will take even longer, we opt to strike a compromise wherein we operate our source with a pump power corresponding to a measured CAR of 10.

Another way to consider this situation is to look at the CAR as a function of the measure coincidence counts per million gates. By doing so, we can ask, what CAR will we obtain if we measure n coincidences count during a specified duration. This enables us to find a balance between coincidence count rates and the best signal-to-noise ratio. This metric helps us avoid counting for exorbitant durations to yield decent counting statistics with low error

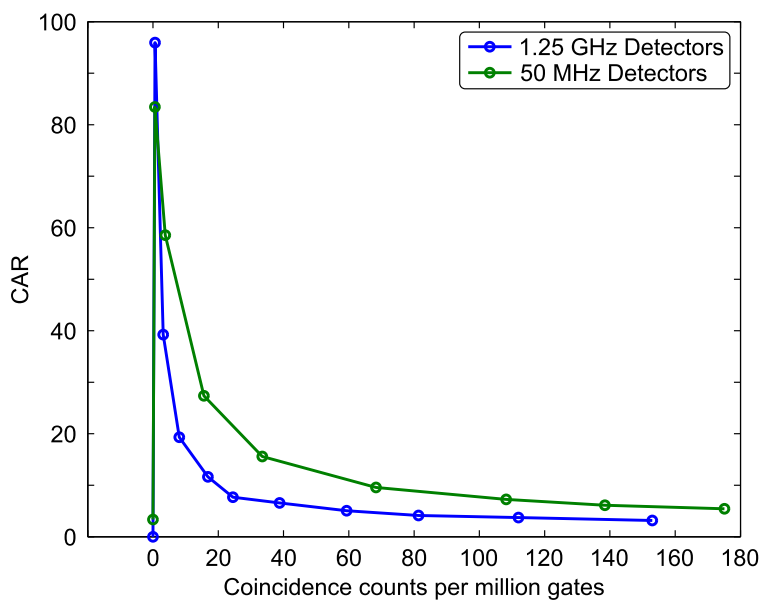


Figure 5.17. Coincidence-to-accidental ratio (CAR). We show the CAR as a function of measure coincidences per million gates for the 50-MHz repetition rate pump. Using this metric, it is clear that sufficiently low coincidence-detection rates yield high CAR, but this requires a long data collection time to obtain decent statistics.

bars. Based on this chart, we operate at approximately 10 coincidence counts per million gates.

We caution here that, if the optical system downstream is very lossy and yields very few measured single-photons or coincidences, we cannot simply turn the pump power up. Based on the information above, it should be evident that, although turning up the pump power increases the number of generated photon pairs, it also increases the likelihood that multiple pairs of photons are generated by a single pump pulse. We call this event a “multi-pair emission”, and the resulting photons “multi-pair photons”. This is nonideal because these photons can obscure information by acting as background noise. These extra photons also increase the number of accidental coincidences that we measure since almost every time slot

will have a photon-pair or more. This is part of the reason we see the decrease in CAR as we increase the pump power.

Additionally, as we discuss in the next section, multi-pairs for time-bin entangled states can yield crosstalk between neighboring time bins. As such, we must ensure that our multi-pair probability is low. The simplest method to do this is reduce the pump power until our photon-pair production rate is smaller than 0.01. We select this value since it implies that the multi-pair production rate is $(0.01)^2 = 0.0001$, i. e., one multi-pair per 10,000 pulses. Experience tells us that this is sufficiently small to mitigate multi-pair emissions while not requiring exorbitant durations for data collection.

5.4. Time-bin entanglement source

Fortunately, generating time-bin entangled photons is quite trivial using the photon-pair source described in the previous section. We start by assuming that the pump power is set to avoid multi-pair generation. Doing so, if we send in a single pump pulse (one time-bin), which we label t_0 , it will generate photon-pairs, which we label $|t_0t_0\rangle$, or more simply $|00\rangle$. The first term in the ket identifies that the signal photon was generated by pulse t_0 , and the second term identifies the same for the idler photon.

Extending this to two subsequent pump pulses (two time-bins) labelled t_0 and t_1 , respectively, we generate state $|00\rangle + |11\rangle$. This happens because the FWM process independently generates signal and idler photons pairwise by each pump pulse. Here, the numbers in the kets identify the subscript of the pump pulse that generates the photon-pair. This state is a maximally entangled state akin to the polarization-based Bell state $|\Phi^+\rangle$ described in the previous chapter. We note that, in reality, we obtain this maximally entangled state after

postselection based on a coincidence detection. The postselection is necessary because the actual state includes contributions from the vacuum state and Raman photons.

We remark here that if we increase the pump power to allow multi-pairs, then we anticipate seeing coincidence counts between different signal and idler time-bins. This generates the state $|00\rangle + |01\rangle + |10\rangle + |11\rangle$, which is a mixed state. Hopefully, this highlights the importance of operating at pump powers that minimize multi-pairs while increasing pair-production rates.

Naturally, we can extend the number of pulses ad infinitum. In this case, we generate d time-bins by producing d subsequent pump pulses. Enumerating each pump pulse, we generate the two-photon state $|00\rangle + |11\rangle + \dots + |dd\rangle$. This state exists in an $(d \times d)$ -dimensional Hilbert space. In fact, it is one of the maximally entangled states within said space. Recalling from §3.3, we see that, by selecting $d = 3$ or $d = 4$ time-bins, we can generate maximally-entangled, two-photon qutrit and ququat states.

5.5. Polarization entanglement source

By modifying the photon-pair source ever so slightly, we can achieve a polarization-based entanglement source. As seen in Fig. 5.18(a), we have added a polarization-dependent delay (PDD) between the circulator and the spool of SMF-28. As shown in Fig. 5.18(b), the PDD is a folded Mach-Zehnder interferometer built around a PBS. Since one loop of the interferometer is longer than the other, that polarization experiences a relative delay with respect to the other polarization.

As shown, any V-polarized light which enters Input 1 cotemporally with H-polarized light will leave delayed. In other words, all light which enters will be divided into its V-polarized and H-polarized components with the former lagging the latter. Similarly, if the light enters

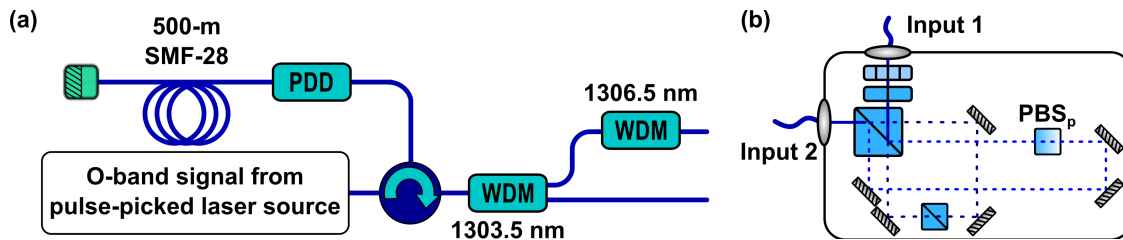


Figure 5.18. (a) Schematic of a polarization-based entanglement source. The inclusion of a polarization-dependent delay (PDD) enables obscuration between photon creation. This obscuration between the generation of H-polarized and V-polarized photon pairs creates the entangled state $|HH\rangle + e^{i\phi}|VV\rangle$, where ϕ is determined by the input state $|\psi\rangle = |H\rangle + e^{i\phi/2}|V\rangle$. (b) Diagram of the polarization-dependent delay. The PDD is a folded Mach-Zehnder interferometer. The two looped paths are discriminated by a PBS. Additional PBSs are included in each loop to maximize extinction. PBS_p is used to denote a PBS turned 90° in order to transmit V-polarized light.

Input 2, then the V-polarized light will be delayed with respect to the H-polarized light. The reversible nature of the PDD in conjunction with the Faraday mirror adds some stability while also automatically compensating for any length differences between the paths travelled between the H-polarized and V-polarized light.

Since FWM retains the polarization state of the pump, the H-polarized pump photons will generate H-polarized signal and idler photon-pairs. Similarly, for the V-polarized pump photons. When reincident on the PDD during the return trip through the photon-pair source, the H-polarized photon-pairs will again be contemporaneous with the V-polarized photon-pairs. Since we operate using pump powers such that the photon-pair creation process is very infrequent, we cannot know whether the photon-pairs generated are of the V-polarized variety or H-polarized variety without observing them. This lack of knowledge creates the entangled state $|HH\rangle + |VV\rangle$ for D-polarized input light before the first PBS. If the input light at the PBS was R-polarized, then we would have the state $|HH\rangle - |VV\rangle$. Alternatively, if the input is only H-polarized or V-polarized, then the output will yield the separable states,

$|HH\rangle$ or $|VV\rangle$ respectively. Thus by tuning the HWP and QWP before the PBS, we can choose between a maximally entangled state and a completely separable state.

Thus, we have demonstrated an easily deployable source which can be tuned to generate the desired photon-pair state. These states can be simple correlated photon pairs, time-bin-entangled photons, or polarization-entangled photons. Now that we have these photons, we will look at how we can route them without changing their quantum state.

CHAPTER 6

Cross-bar Switching Operation and Performance

Most demonstrations of quantum communications and information processing have used direct links between two nodes^[105–107]. While this is satisfactory for nascent proof-of-principle concept demonstrations, it is resource inefficient for larger network topologies which are desired as the field matures^[80]. Therefore, development of a photonic router or switch is a necessity since it obviates the need for additional transceivers and channels between every node in a network. Additionally, photonic switches can multiplex parallel quantum data streams to one channel. One example where this serialization is useful for QIP is for producing a higher-rate single-photon source by multiplexing separate single-photon sources to a single output channel^[108]. Conversely, the photonic switches can be used to demultiplex a high-speed quantum data stream into multiple spatial channels which are routed to slower single-photon detectors^[109] without sacrificing communication rates.

In this chapter, we investigate our efforts to develop such a switch. We start by discussing how a changeover (one-input, two-output) switch operates in §6.1. In §6.2, we explain the modifications to the changeover switch’s design that yield a cross-bar (*two*-input, two-output) switch. We look at the experimental performance of the cross-bar switch in the following section. These results include the loss and speed metrics. Then, in §6.4, we demonstrate that our switch retains polarization-encoded quantum information upon transmission or reflection. In the final section, §6.5, we discuss an experiment that demonstrates our ability to use the switch to select one channel of a temporally-multiplexed two-channel quantum

data stream. Almost all of the results in this section utilize the FWM pump preparation shown in §5.2.5. If that is not the case, it will be noted to provide clarity.

6.1. All-optical changeover quantum switch

In this section, we discuss the configuration and operation of the all-optical quantum changeover switch demonstrated in our lab^[1-3]. Since this work is described in greater detail elsewhere, we only introduce the relevant details here to describe the mechanism by which we obtain switching. We direct the reader to the aforementioned references for characterizations of the changeover switch’s performance. The novel experimental geometry and results are presented in the following sections.

Very simply, the changeover switch is a one-input, two-output switch wherein the switching operation simply chooses between the outputs, as shown in Fig. 6.1(a). The “changeover” nomenclature comes from the simple fact that the switch “changes over” between the two output possibilities depending on whether it is passively off or actively on. The actual switch, schematically shown in Fig. 6.1(b), employs the traditional NOLM geometry demonstrated by Bülow and Veith^[89]. There are two main differences between their demonstration and ours: (1) we use this design for single-photon-level signals (attenuated classical pulses or quantum correlated photons); (2) our signal frequency is significantly detuned from the XPM pump’s frequency. We make the latter modification because the large detuning allows us to satisfactorily filter out most pump photons. This minimizes in-band noise photons despite the required high XPM pump powers.

We summarize the basic design for the switch thus: if we send our O-band (signal) light into port A, then depending on the presence or absence of the C-band (pump) pulse, the O-band light will reflect to port B, or transmit to port C. To more clearly explain the

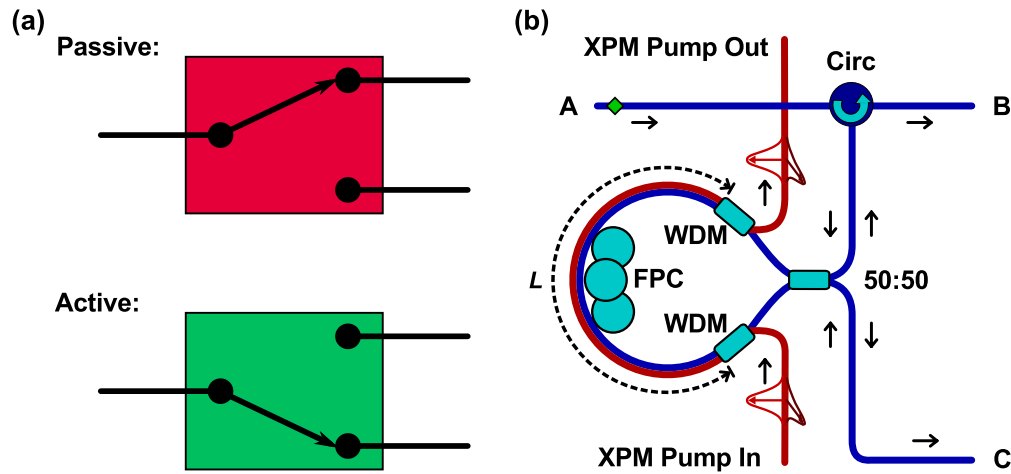


Figure 6.1. (a) Simplified diagrams of the changeover switch's operation in passive and active mode. (b) We show here the geometry of a changeover, nonlinear optical loop mirror switch used for quantum switching. It is comprised of a circulator (Circ), a 50:50 beamsplitter, a pair of WDMs for injecting and removing the XPM pump, an FPC, and a common path of fiber of length L in the Sagnac geometry.

processes that enable this, let us begin by looking at the *passive* operation of the switch, i. e., in absence of a pump pulse.

After injecting O-band light into port A, it passes through the circulator and is incident on the 50:50 beamsplitter. Here, the light is divided into two parts, the clockwise (\odot) propagating component, and the counterclockwise (\ominus) propagating component of the Sagnac interferometer. When the \odot - and \ominus - parts are reincident on the 50:50 beamsplitter, they have a relative phase difference that affects their interference condition. By tuning the FPC in the Sagnac loop, we adjust the relative phase difference, and select between constructive and destructive interference at port B. In essence, this adjustment chooses whether our switch reflects the signal to port B, or transmits the signal to port C. The reflected light passes through the circulator again and out at port B. We remark here that the circulator introduces a small difference in loss ($\simeq 0.5$ dB) between the two outputs of the switch. We

also note that the circulator is necessary in order to detect the photons since, otherwise, we would route the signal back to the source as done by Mortimore in his seminal work^[110].

Let us now consider the *active* operation of the switch. When we introduce the pump light at XPM Pump In, we modify the operation of the switch slightly. During this active switching, the co-propagating (\odot) signal light accumulates additional phase via the nonlinear response of XPM discussed in §2.3.2. We remark here that the \odot -propagating component of the signal light does not acquire any significant phase because its interaction time with the pump pulse is very brief. The phase accumulated by the \odot -path due to XPM is an intensity-dependent process. Hence, the user can tune the pump power to achieve zero, partial, or complete switching.

We remark now that the only parameter that defines the switching-rate limit is the length of fiber (L in Fig. 6.1) commonly travelled by the signal and pump. This is due to the fact that the signal and pump experience different refractive indices in fiber. According to Corning’s datasheet for SMF-28e, the 1310-nm light experiences an index of refraction $n_{1310} = n_s = 1.4676$, while the 1550-nm light sees an index of refraction $n_{1550} = n_p = 1.4682$. The subscripts simply demarcate O-band (signal) light versus C-band (pump) light. Based on these numbers, we calculate the walkoff parameter, defined in Eq. (6.1), to be approximately 2 ps/m.

$$d_w \equiv \frac{1}{v_p} - \frac{1}{v_s} = \frac{1}{c}(n_p - n_s) \quad (6.1)$$

v_p and v_s are the pump’s and signal’s respective group velocities. In other words, a pulse at the signal frequency will travel through a 1-m SMF fiber patchcord 2 ps faster than a pulse at the pump frequency. This implies that the arrival time and length of the common path for these wavelengths are the only factors that affect the switching window, the time

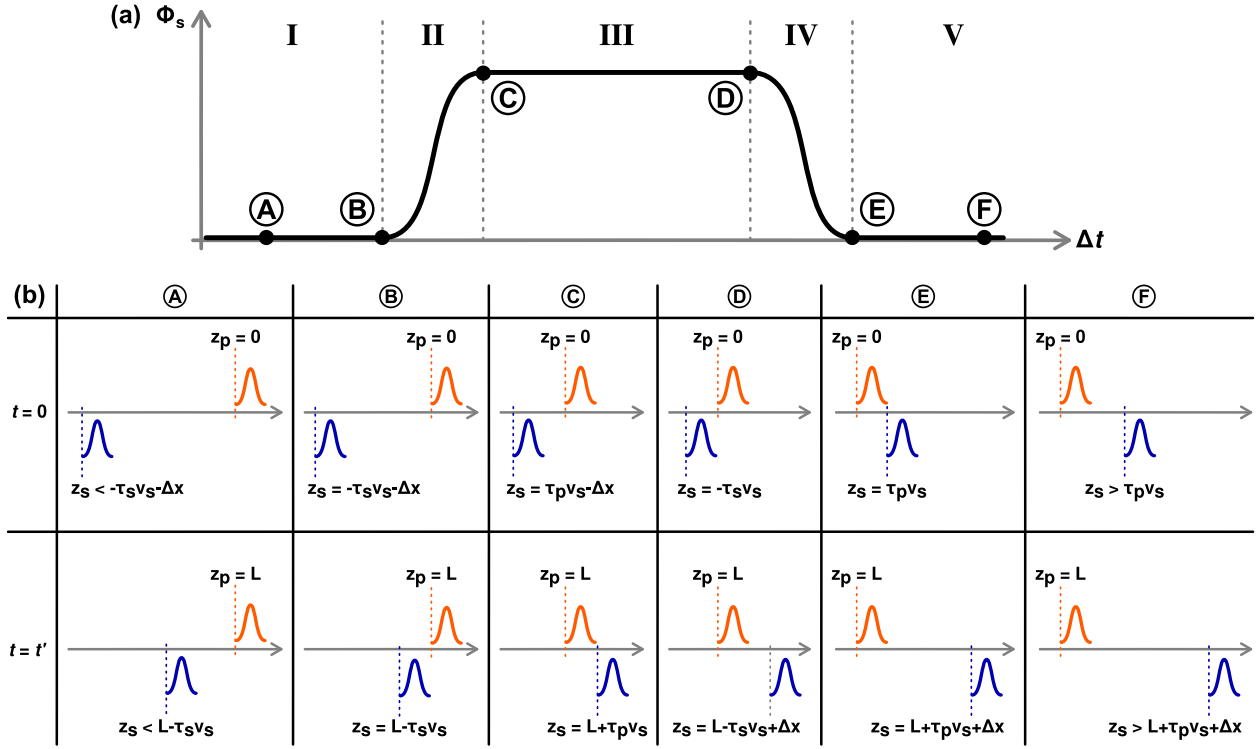


Figure 6.2. Explanation of switching window. (a) Switching window. Phase accumulated by the signal photons as a function of the relative delay, Δt , between the arrival times of the C-band pump and O-band signal. (b) We look at the location of the signal pulse, z_s , relative to the location of the pump pulse, z_p , at the beginning ($t = 0$) and end ($t = t'$) of the Sagnac spool fiber of length, L . This is done in the pump pulse's frame of reference for the six transition locations on the switching window. We label these locations \textcircled{A} – \textcircled{F} . τ_p and τ_s are the temporal widths of the pump and signal pulse, respectively. v_p and v_s are the velocities of the C-band and O-band pulses in fiber, respectively. Δx is the additional distance traveled by the signal pulse in the time t' .

during which switching is possible. This walk-through behavior has the added benefits that the switching operation is also independent of the pump pulse's shape, and a uniform phase is applied to the signal, thereby enabling high-contrast switching.

There are five general regimes, shown in Fig. 6.2(a), that determine the switching window. We label these regimes I, II, III, IV, and V, and will discuss them in more detail below. In Fig. 6.2(b), we show the transition cases, \textcircled{A} – \textcircled{F} , between each regime. For each of these

cases, we show a cartoon of the relative positions of the pump (shown in orange) and signal (shown in blue) pulses at the beginning and end of their common travel path. We remark that all of these are shown with respect to when the pump pulse has first completely entered the Sagnac loop—defined as $t = 0$ —and when the pump pulse has completely left the Sagnac loop—defined as $t = t'$. Defining the time with respect to the pump's propagation through the fiber allows us to focus on the signal's relative distance from the pump at different locations, z , in the fiber. It also defines Δt as the delay in time between the pump's entry to the Sagnac loop and the signal's entry into the Sagnac loop. We also remark that the pump requires t' seconds to travel the length of the fiber, L . Due to the different group velocities in fiber, the signal will travel $L + \Delta x$ in the same amount of time. As such, we can define the following relations,

$$t' = \frac{L}{v_p} = \frac{L + \Delta x}{v_s} \quad (6.2)$$

$$\tau_w = \frac{\Delta x}{v_s} = Ld_w \quad (6.3)$$

In the latter equation, we define the switching window width, τ_w . This is useful to determine the minimum length of fiber required to theoretically obtain complete switching.

Based on these equations and the pictorial example, if $L = 0$, then $\textcircled{\text{B}}$ and $\textcircled{\text{D}}$ (or $\textcircled{\text{C}}$ and $\textcircled{\text{E}}$) are the same point, and thus, a switching window does not exist. In other words, for this hypothetical example, regimes II–IV do not exist since the two pump and signal pulses never travel together. Instead, if we consider the scenario where $\textcircled{\text{C}}$ and $\textcircled{\text{D}}$ are the same point, then we have the L with which we first obtain complete switching. In this case, we find that $\tau_w = \tau_p + \tau_s$, where τ_p and τ_s are the temporal pulse widths of the pump and signal, respectively. This scenario, where regime III does not exist and the relative delay between the arrival times of the pump and signal equals the sum of their pulse widths, is the

critical walk-through case. Thus, we can define the shortest length of fiber, L_{crit} , required for complete switching because the use of any shorter length of fiber does not allow enough time for the pump to modulate the signals phase completely. For completeness, we include below the definition of the critical length,

$$L_{\text{crit}} = \frac{\tau_p + \tau_s}{d_w} \quad (6.4)$$

So based on this discussion, we see that the only parameter which determines the switching window is the common length of fiber in the Sagnac loop. The switching window can then be measured by simply doing a scan of the relative delays between the pump and signal.

So now to describe the behavior of the pulses for each regime. The first regime is where the pump pulse arrives too early with respect to the signal pulse. In this regime, despite the group velocity difference, the signal never temporally overlaps with the pump and hence does not acquire any phase.

In regime II, the pump arrives early and the signal arrives soon thereafter such that only during the latter part of their common path do they overlap. In this case, the signal accumulates some phase, but not the entire amount since it does not experience the complete pump pulse's power. This corresponds to the rising edge of the switching window.

Regime III is the ideal switching regime where the pump pulse still arrives before the signal pulse, and the difference in their arrival times is such that the signal can travel completely through the pump and accumulate the entire phase desired. Note that for sufficiently short pump and signal pulses and long common fiber path, the switching could happen early or late in the fiber. Intuitively, it is in this manner that the length of fiber is the only parameter which determines the switching window.

In regime IV, the signal pulse arrives at such a time that it only experiences XPM with part of the pump pulse during the early portion of the fiber. This corresponds to the falling edge of the switching window.

Finally, the fifth regime is when the O-band light arrives too early and travels too quickly, therefore it again experiences no phase from the slow and tardy pump pulse. Based on these five regimes, we have now defined the switching window, and we have also demonstrated why the common fiber path defines said switching window.

6.2. All-optical cross-bar quantum switch

While the changeover switch is suited for demultiplexing quantum data streams and performing routing operations between one input and two outputs, any operation that requires two inputs and two outputs—for example, path switching of independent data streams, creating discrete temporal delays, or acting as a variable beamsplitter—must use the cross-bar switching geometry described in this section. We show the simplistic behavior of the switch in Fig. 6.3(a). When in passive mode, the switch reflects incident signals at each input to the output on the same side, hence looking like two “bars”. When in active mode, the incident signals “cross” paths to reach the opposite output. From this, we discover the derivation of the name “cross-bar”.

In order to achieve the cross-bar functionality, this design builds on the changeover switch, described in §6.1, by adding a circulator at port B, schematically shown in Fig. 6.3(b). Looking more closely, we see that the new circulator enables its port of the Sagnac interferometer to be an input *and* an output port, serving the same purpose as the other circulator. This simple adjustment enables our switch to route photons incident at both inputs simultaneously. That is to say, we can simultaneously reflect (or transmit) incident photons to both

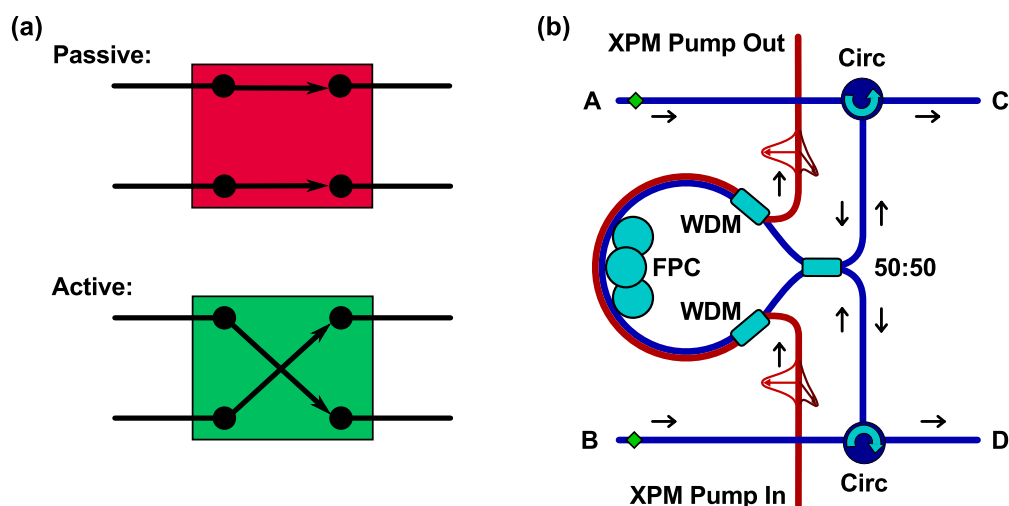


Figure 6.3. (a) Simplified diagram demonstrating the switch’s operation in passive and active modes. (b) We show here the geometry of our cross-bar quantum switch. This switch is identical to the changeover switch except for an additional circulator.

output ports, as shown in Fig. 6.3(a). For this geometry, we determine the switching window exactly the same way as we did for the changeover geometry. This is true regardless of which port the light is input, since incident light on either port has a co-propagating (\odot) component in the Sagnac loop that experiences XPM with the pump pulse.

With the addition of this circulator, the cross-bar switch can be used as a functionally “reversible” quantum gate. The unitarity of the gate is maintained by the dual-in, dual-out geometry. The quantum nature of this gate is seen through the switch’s ability to entangle temporal modes or spatial modes. We will explain this in further detail in §6.5. As such, this switch is not only useful for the obvious routing, serialization, and deserialization applications, but also for other potential applications in QIP. We discuss one such example in Chp. 7.

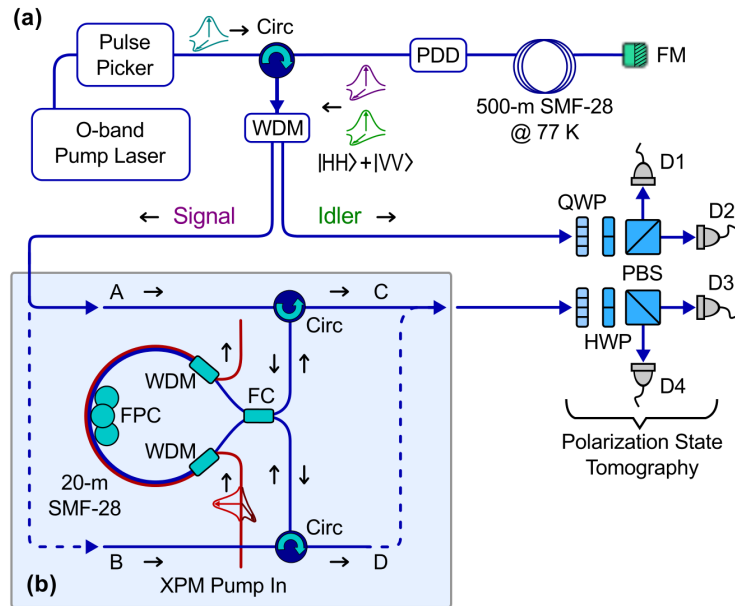


Figure 6.4. (a) Entanglement source^[37] and switch test setup. We show here the setup that we use to characterize the cross-bar switch’s performance. We route the signal photon from the entanglement source (described in §5.5) through the switch, whereas we route the idler photon is routed directly to the polarization analyzers. (b) Cross-bar switch. The dashed lines designate the ability to test different permutations of input ports (A,B) and output ports (C,D).

6.3. Cross-bar switch characterization

Now that we understand how the switch operates, we can turn our attention to how well it performs. We show the general setup for single-photon tests in Fig. 6.4. Note that this is the most complete example of the test setup. We remove elements from this setup to test particular parameters.

6.3.1. Classical switching characterization

Here, we look at the results for the switch operation using a classical source. In this scenario, we take the laser pulse picking source, filter it to 1305 nm, and send it directly to the switch’s

input. This is in lieu of sending the pulses to the FWM fiber. Looking at Fig. 6.4, this test corresponds to bypassing the entanglement generation setup, and routing the light from the pulse picker directly to the inputs A or B of the cross-bar switch.

First, we provide the trivial insertion loss specification for the switch. For this test, we send light to each input of the switch and measure the passive transmission at each output. Comparing the total power at the output (sum of both outputs) with respect to the input, we can estimate the insertion loss of the switch. Based on the insertion losses of each in-situ component, we expect the inherent loss of the switch to be $\simeq 1.8$ dB. The actual measured loss for one input is $\simeq 2.3$ dB. The other input has slightly more loss at $\simeq 2.7$ dB. We attribute the additional 0.5-dB (0.9-dB) loss to fiber-fiber coupling of various components in the Sagnac loop. The measured difference between the two inputs comes from the fact that one circulator is spliced to the 50:50 beamsplitter, whereas the other circulator is not spliced.

In other words, we expect that we can reduce the overall loss of the switch by splicing all of the components together. Additionally, other research is done in our group to demonstrate a different geometry switch that uses the same XPM switching mechanism to reduce the total insertion loss to < 0.3 dB^[111]. The advantage of this design compared to the lower-loss geometry is that the NOLM switch geometry does not require any active stabilization.

Next, we present the contrast obtained using the cross-bar switching configuration. In Fig. 6.5, we show the normalized switching probability as a function of the XPM pump power. That is to say, we input light at ports A and B, and measure the power at ports C and D while adjusting the EDFA's output power setting.

We show this for light input at both inputs of the cross-bar switch to demonstrate that the switch behaves similarly regardless of which input is used. Based on these curves, we see

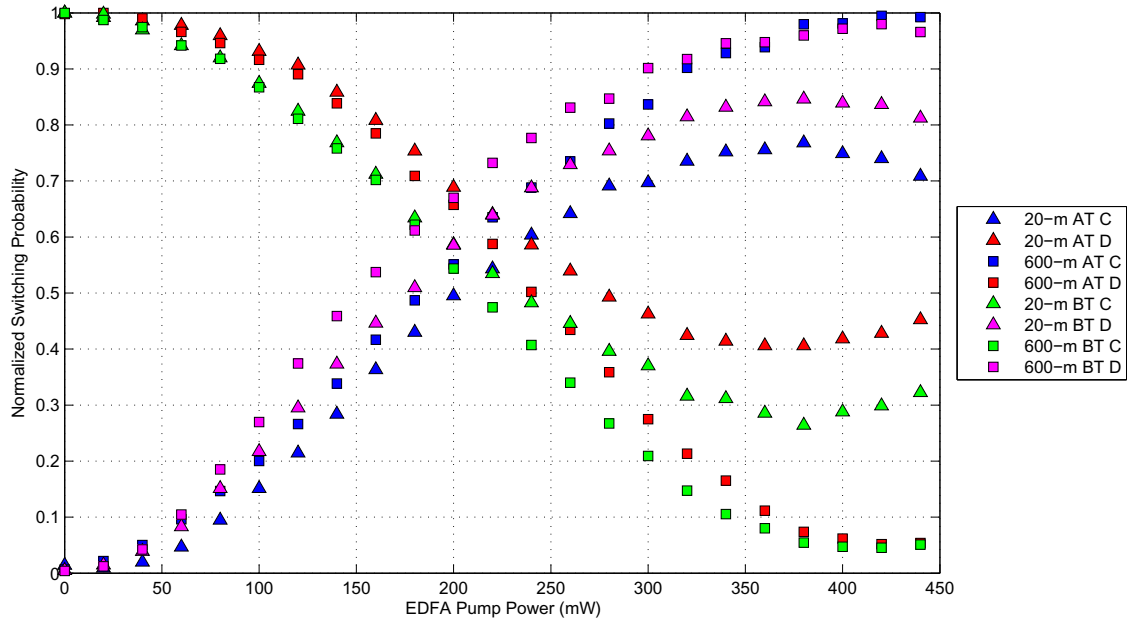


Figure 6.5. Classical characterization of cross-bar switch. We show the normalized switching probability as a function of the input pump power. This is show for the transmission and reflection from both inputs of the switch.

that our switching contrast is about 3:1 for the 20-m switch, and about 20:1 for the 600-m switch. We show later that by improving the pulse-picking electronics, we can improve from the 3:1 to approximately 14:1.

Figure 6.6 shows the normalized switching probability as a function of the delay between the 1550 path and the 1310 path. If we fit these traces to a Gaussian curve using the least-squares fitting technique, we obtain a full-width half-maximum (FWHM) for these pulses of $\simeq 55$ ps. These widths correspond well to the expected switching window widths for a $L=20$ m switch, assuming the ~ 20 -ps width for the U2T signal pulse, and ~ 10 -ps width for the IMRA XPM pump pulse.

We note here that the switching window curves have neighboring pulses (peaks). These are due to imperfect pulse-picking wherein the pulse-picking electronics and EOM also select

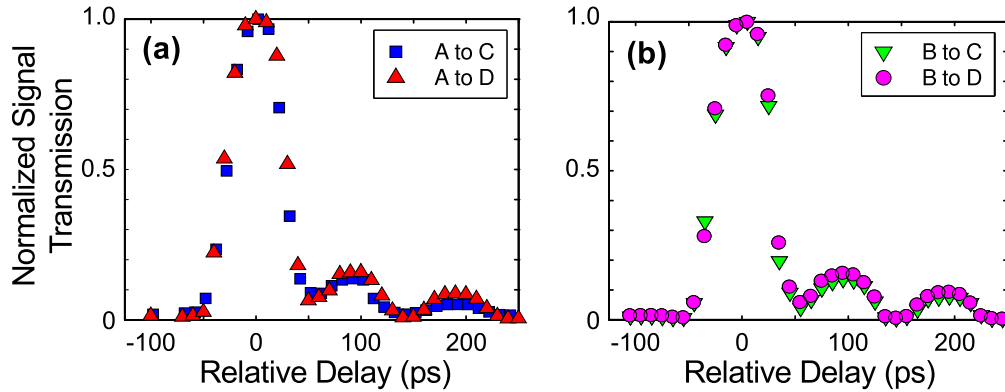


Figure 6.6. In (a) and (b), we show the classical switching windows at output ports C and D when the signal is input to port A and B, respectively. If we fit these curves with a Gaussian curve, we find the FWHM for these pulses are: $\text{FWHM}_{AC}=53.0$ ps; $\text{FWHM}_{AD}=57.7$ ps; $\text{FWHM}_{BC}=55.7$ ps; and $\text{FWHM}_{BD}=56.4$ ps.

a small amplitude of neighboring pulses from the U2T laser's 10-GHz pulse train. We believe that the measured FWHM widths are slightly wider than expected because this tail and the neighboring pulse broaden the calculated fits. As mentioned before, improving this factor motivated us to develop the fifth-generation FWM pulse-picking electronics.

To test the improvement of the switch using the faster electronics, we performed a quick classical test. We input a 10-GHz pulse train into port A, and looked at the output on port C. If we passively minimize and maximize the light at port C, then we obtain the direct detected waveforms shown below in Figs. 6.7 and 6.8, respectively. We used the optical input of a digital communication analyzer (Agilent 86100A with the 86105A measurement module) to perform this direct measurement. The bandwidth is 20 GHz, thereby broadening the U2T pulses to about 50 ps. Based on the two plots below, we calculate that our contrast is about 140/10 or 14:1. This is certainly an improvement over previous results, and we believe that it can be improved further based on the classical results obtained for the changeover switch.

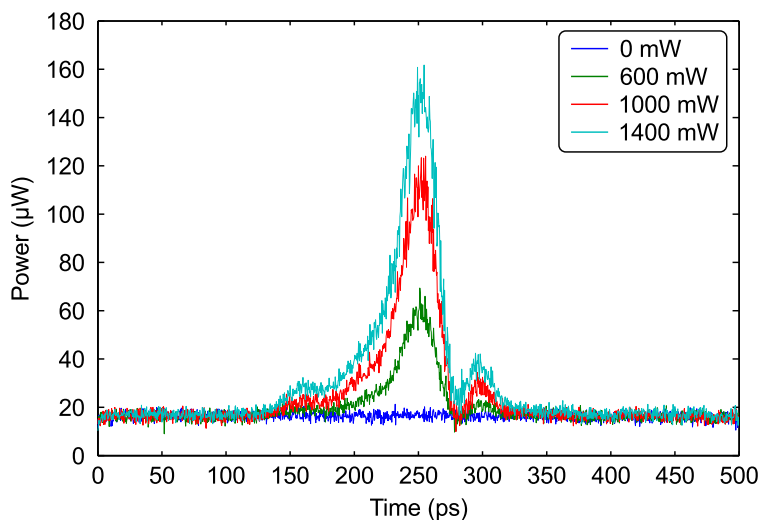


Figure 6.7. Inputting at 10-GHz pulse train at port A, and measuring at port C, we see our pulse begin to appear as we increase the switching pump power. This scenario assumes that our switch is passively minimized, hence the baseline around $20 \mu\text{W}$ is a measurement artifact of the detector.

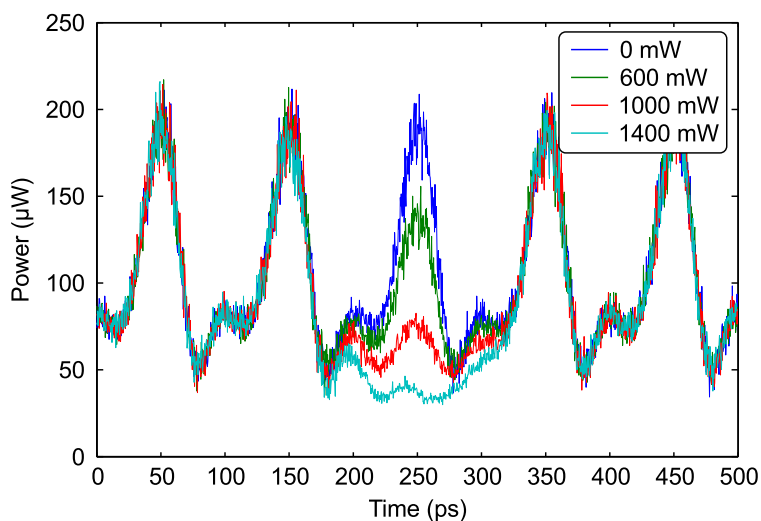


Figure 6.8. Inputting at 10-GHz pulse train at port A, and measuring at port C, we see our pulse begin to disappear as we increase the switching pump power. This scenario assumes that our switch is passively maximized. The minimum is around $30 \mu\text{W}$, which is only slightly higher than the baseline at $20 \mu\text{W}$.

Based on the results obtained and shown in this section, we claim that we are capable of obtaining decent switching with the narrower switching windows and faster laser source. This is encouraging since it enables us to switch even faster signals in the future.

6.3.2. Single-photon switching characterization

Now that we investigated the classical performance of the switch, we turn our attention to the single-photon regime. This is necessary in order to demonstrate quantum states since classical states obscure the quantum interactions, thereby making it difficult to observe quantum phenomena like entanglement. In order to measure single photons, we replace standard P-I-N type detectors with InGaAs single-photon detectors.

We must also generate single-photons. We obtain them using FWM, as described earlier. In other words, we return the setup to that shown in Fig. 6.4. We now insert WDMs and the photon-pair source after the source. At the detector, we merely count the number of single counts at the output of each detector. Using this configuration, we obtain the results shown below in Fig. 6.9. We demonstrate switching from both inputs to the various outputs. We obtain these results using the ideal XPM pump power determined using the classical switching setup described in the previous section.

Once again, we see the narrow switching window widths corresponding well to the convolution of the signal and pump pulse widths. We also see the nearest neighboring peak, but now they are significantly smaller in magnitude than previously. This is due to the quadratic improvement of the photon flux described in §2.4.1. Finally, we remark here that, although not shown, the switching contrast for this data is approximately 10:1 for the 20-m switch.

While we see a drop in contributions from the neighboring pulses, we can theoretically obtain even better performance by looking instead at coincidences between signal and idler

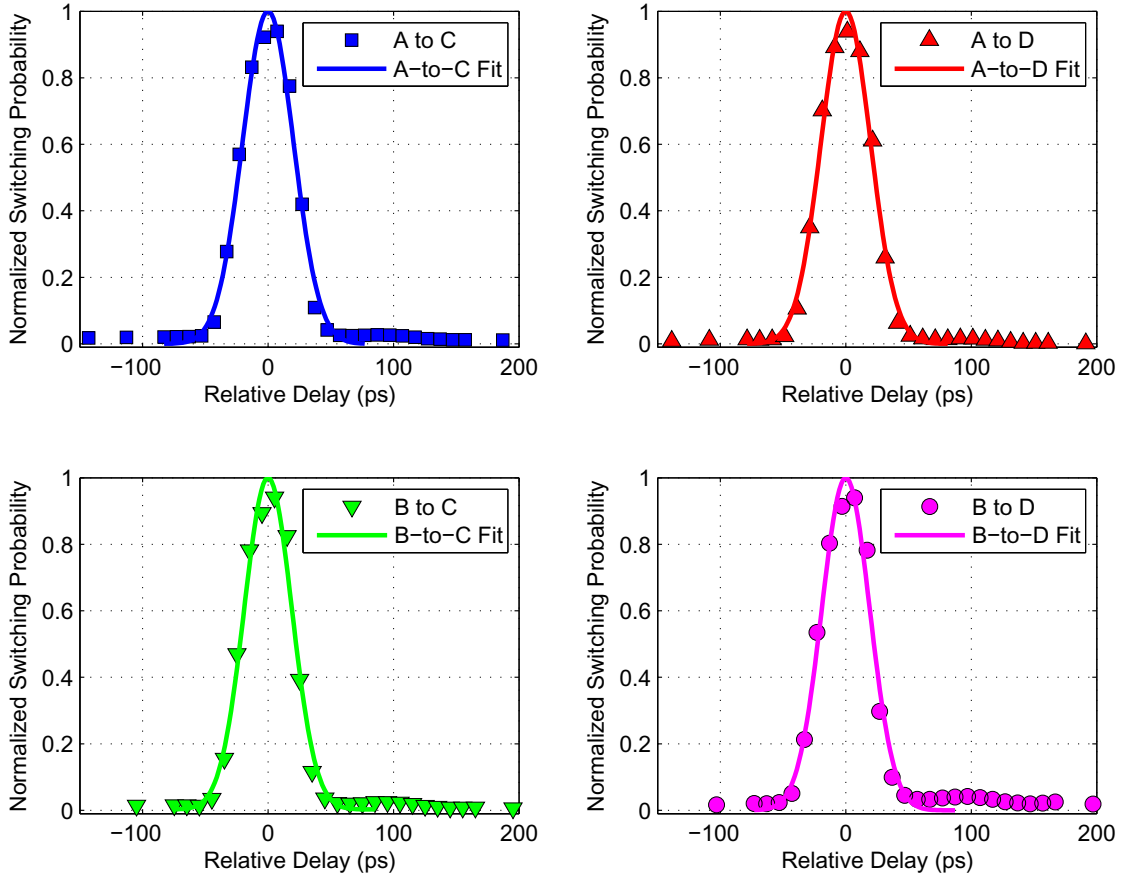


Figure 6.9. Single-photon regime characterization of cross-bar switch. Here we show the normalized switching probability vs relative pump-signal path delay. The traces shown were obtained for active single-photon switching from both inputs to both outputs. The solid lines shown for each trace are Gaussian fits to the largest peak and used to obtain the FWHM for each trace. The FWHM pulse widths for these are $\text{FWHM}_{AC}=47.8$ ps, $\text{FWHM}_{AD}=46.5$ ps, $\text{FWHM}_{BC}=44.6$ ps, and $\text{FWHM}_{BD}=44.9$ ps. The subscripts designate the corresponding input port and output port as labeled.

while only delaying one arm with respect to the others. Since we should have temporal distinguishability from the ~ 70 -ps windows provided by the Nucrypt detectors, we should be capable of using that distinguishability to reduce the neighboring photons contribution even more.

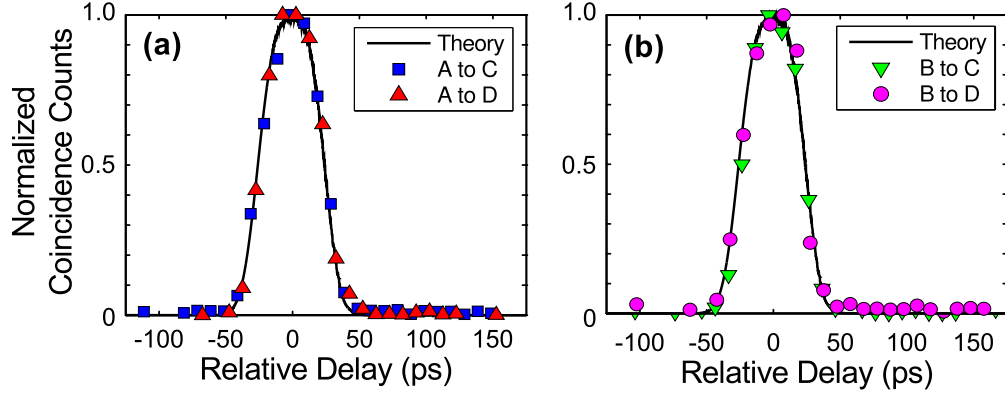


Figure 6.10. In (a) and (b), we show the coincidence-counted switching windows at output ports C and D when the signal is input at port A and B, respectively. In these figures, the black line shows the theoretical switching window for our switch parameters^[112]. By fitting these with a Gaussian, we obtain the following FWHM widths: $\text{FWHM}_{AC}=46.5$ ps; $\text{FWHM}_{AD}=45.4$ ps; $\text{FWHM}_{BC}=41.8$ ps; and $\text{FWHM}_{BD}=44.2$ ps.

In Fig. 6.10, we show the switching windows obtained using coincidence counts rather than single-photon counts. Note that the results shown are true coincidences for two cases—routing photons through port A and port B. The coincidences shown are accidentals subtracted, but no correction is applied to compensate for detector dark counts. In other words, these counts include coincidence events due to detector dark-count events. Again, as a sidenote, the switching contrast for this case is approximately 15:1.

Yet again, for all of these measurements, we obtain a FWHM τ_w of $\simeq 45$ ps. This corresponds well not only with the expected width calculated earlier, but also with the theoretical model of the quantum description of a fiber-loop Sagnac interferometer^[112], as shown by the black curves in Figs. 6.10(a) and (b). We remark that theoretical model does not require any fitting parameters. Based on these measurements, using the 20-m Sagnac loop, we have demonstrated that we can switch pulses at a theoretical rate of >20 -GHz.

Now that we have characterized the cross-bar switch and its operation, we move to demonstrating that it retains the polarization entangled state of the transmitted qubits.

6.4. Polarization-entanglement retention characterization

We demonstrate the entanglement-preserving properties of our switch by measuring the quantum state generated by our entanglement source (cf. Fig. 6.4(a)) after the signal portion of the state is transmitted through the switch under passive and active conditions. Unlike the measurements made in the previous, we do not merely count single-photons and coincidence events. Instead, we perform complete 36-measurement polarization-state tomographies by compiling the aforementioned counts for all pairwise combinations of the six canonical polarization states, $|H\rangle, |V\rangle, |D\rangle, |A\rangle, |R\rangle$ and $|L\rangle$. We reconstruct the entangled state using both linear-least-squares-fit and maximum-likelihood tomographies. In general, these results do not vary significantly. The results shown here correspond to the maximum-likelihood tomographies.

We use the switching fidelity, F_S , to characterize the performance of the switch. Although it is defined in §3.4.1, for convenience and as a reminder for the reader, we define the switching fidelity as $F_S \equiv F(\rho_a, \rho_{a'})$, where the absence or presence of the prime superscript indicates the passive- or active-mode operation of the switch, respectively.

In Fig. 6.11(a), we show the reconstructed density matrix of the quantum state under passive operation of the switch, with signal light entering port A and exiting port C. Figure 6.11(b) shows the reconstructed density matrix of the quantum state under active operation of the switch with signal light transmitted from port A to port D. Based on these reconstructed density matrices, we determine $F_S = 99.6 \pm 0.3\%$. Inputting signal light at port B yields comparable results with a measured F_S of $98.5 \pm 0.5\%$, shown in Fig. 6.12.

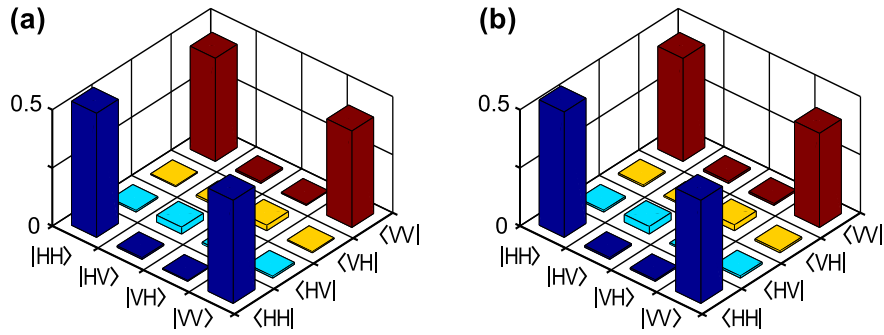


Figure 6.11. We show the density matrices for the (a) passively unswitched (reflected) and (b) actively switched (transmitted) output polarization-entangled states, $|O_R\rangle$ and $|O_T\rangle$, respectively, for a state input to port A. The respective fidelities to a maximally entangled Bell state are $F(\rho_{O_R}) = 91.7 \pm 0.2\%$ and $F(\rho_{O_T}) = 91.4 \pm 0.3\%$. The switching fidelity is $F_S = F(\rho_{O_R}, \rho_{O_T}) = 99.6 \pm 0.3\%$, thereby demonstrating that the switch does not degrade the entanglement properties of the transmitted photons.

From these results, we conclude that our switch introduces very little degradation ($< 1.5\%$) to the entangled quantum state of the photons passing through it.

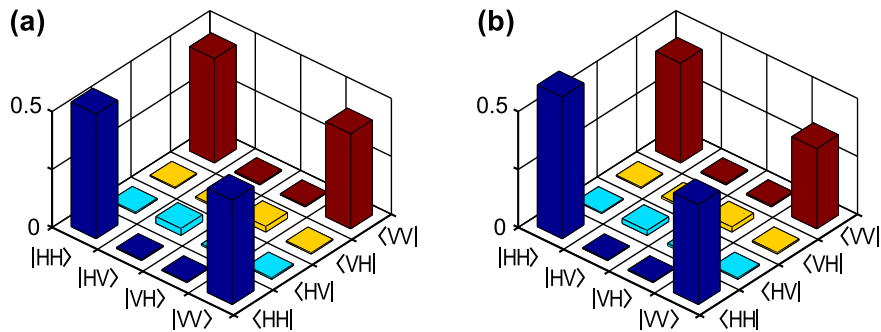


Figure 6.12. We show the density matrices for the (a) passively unswitched (reflected) and (b) actively switched (transmitted) output polarization-entangled states, $|O_R\rangle$ and $|O_T\rangle$, respectively, for a state input to port B. The respective fidelities to a maximally entangled Bell state are $F(\rho_{O_R}) = 92.4 \pm 0.4\%$ and $F(\rho_{O_T}) = 90.8 \pm 0.5\%$. The switching fidelity is $F_S = F(\rho_{O_R}, \rho_{O_T}) = 98.5 \pm 0.3\%$, thereby demonstrating that the switch does not severely degrade the entanglement properties of the transmitted photons.

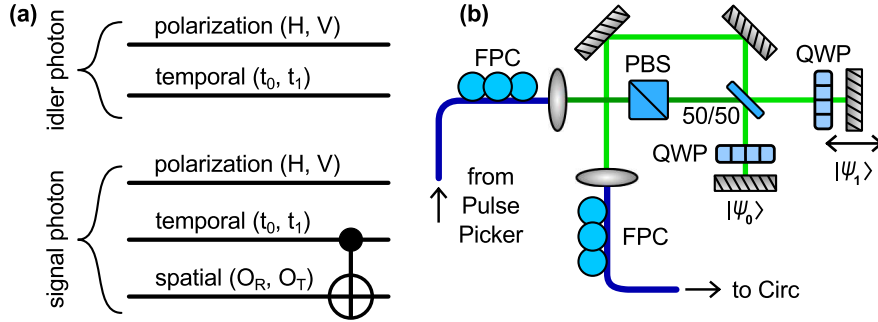


Figure 6.13. (a) Diagram showing five degrees of freedom in a multiplexed entangled-photon data stream which can be demultiplexed by applying a controlled switch operation. (b) Schematic of the time-division multiplexing Michelson interferometer that we insert between the pulse-picker and the circulator shown in Fig. 6.4. The path difference in the two arms gives rise to two independent quantum channels, $|\psi_0\rangle$ and $|\psi_1\rangle$, separated by $\simeq 155$ ps.

6.5. High-speed demultiplexing of a quantum data stream

To demonstrate the speed and utility of our cross-bar switch as a spatio-temporal manipulation device, we perform a test wherein the goal is to demultiplex a single quantum channel from a dual-channel entangled-photon data stream. We begin by encoding two maximally entangled polarization states into adjacent temporal modes, t_0 and t_1 , separated by $\Delta t = t_1 - t_0$. Since we route the signal photon through our switch, this system describes five-qubit hyperentanglement (see Fig. 6.13(a)) embodied on two photons, where there are two signal and idler polarization qubits ($|H\rangle_{s,i}$, $|V\rangle_{s,i}$), two signal and idler temporal qubits ($|t_0\rangle_{s,i}$, $|t_1\rangle_{s,i}$), and a single signal spatial qubit ($|O_R\rangle_s$, $|O_T\rangle_s$)^[1]. The term “hyperentanglement” refers to states that are simultaneously entangled in multiple degrees of freedom; in this case, they are polarization and time.

To experimentally realize such five-qubit hyperentanglement, we insert a time-division multiplexing Michelson interferometer (TDM-MI), as schematized in Fig. 6.13(b), between the pulse-picking electronics and the circulator shown in Fig. 6.4(a). One arm of the TDM-MI

is constructed such that its mirror is mounted on a linear translation stage providing control of the relative delay Δt of that arm with respect to the other (fixed) arm of the interferometer. The QWPs in the TDM-MI and the subsequent FPC (see Fig. 6.13(b)) are adjusted such that the O-band pump drives the entanglement source in Fig. 6.4(a) to produce a hyperentangled signal-idler quantum state^[2]

$$|\Phi\rangle = c_0 |\psi_0\rangle |t_0\rangle_s |t_0\rangle_i |O_R\rangle_s + c_1 |\psi_1\rangle |t_1\rangle_s |t_1\rangle_i |O_R\rangle_s,$$

where

$$|\psi_0\rangle \equiv \frac{1}{\sqrt{2}} (|H\rangle_s |R\rangle_i - i |V\rangle_s |L\rangle_i),$$

$$|\psi_1\rangle \equiv \frac{1}{\sqrt{2}} (|H\rangle_s |H\rangle_i + |V\rangle_s |V\rangle_i),$$

and c_0, c_1 are arbitrary constants. If we measure $|\Phi\rangle$ using polarization-basis tomography while *tracing out* the temporal degrees of freedom and *projecting* into the signal output spatial mode $|O_R\rangle_s$, then we anticipate the outcome to be a highly mixed state. This is the result one would expect when simultaneously measuring multiple, but separately entangled, quantum data streams. If instead, we use a switch to implement a controlled-NOT operation to couple the signal photon's temporal and spatial modes (see Fig. 6.13(a)), then we transform $|\Phi\rangle$ to

$$|\Phi'\rangle = c_0 |\psi_0\rangle |t_0\rangle_s |t_0\rangle_i |O_T\rangle_s + c_1 |\psi_1\rangle |t_1\rangle_s |t_1\rangle_i |O_R\rangle_s.$$

We anticipate this demultiplexed quantum state to exhibit maximal entanglement since the switching operation *already* projected it into the signal spatial mode $|O_R\rangle_s$. This will be true

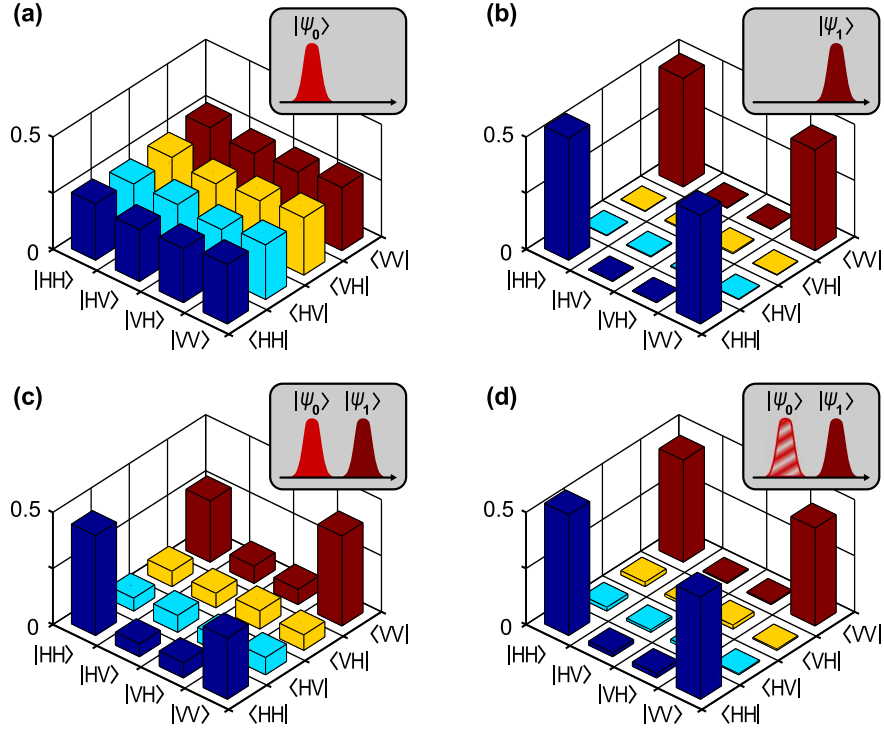


Figure 6.14. (a) Density matrix of the leading state $|\psi_0\rangle$ with $F(\rho_{\psi_0}) = 97.6 \pm 0.6\%$. (b) Density matrix of the trailing state $|\psi_1\rangle$ with $F(\rho_{\psi_1}) = 97.5 \pm 0.7\%$. The states' mutual fidelity is $F(\rho_{\psi_0}, \rho_{\psi_1}) = 1.8 \pm 1.0\%$. (c) Density matrix obtained when both channels are transmitted through the switch and measured together. The measured fidelity is $F(\rho_{\Phi}) = 68.6 \pm 1.0\%$. (d) Density matrix of the state measured when we switch out $|\psi_0\rangle$, obtaining a fidelity of $F(\rho_{\Phi'}) = 93.6 \pm 1.0\%$. This recovered state has a fidelity of $F(\rho_{\Phi'}, \rho_{\psi_1}) = 96.2 \pm 1.2\%$ with the state $|\psi_1\rangle$. Insets show cartoons of which states are measured, ordered by arrival time from left to right. The dashed pulse in the inset in (f) indicates that the state $|\psi_0\rangle$ is switched out and, therefore, not measured.

even after tracing out the temporal degrees of freedom because only the maximally entangled state $|\psi_1\rangle$ would be present.

For the demultiplexing results demonstrated here, $c_1/c_0 \simeq 1.07$ and $\Delta t \simeq 155$ ps. We used a high-speed photodetector (EOTech, Model ET-3500F) to directly measure the delay Δt . Figure 6.14(a) shows the reconstructed density matrix for the leading state $|\psi_0\rangle$ corresponding to the temporal mode t_0 . We obtain this density matrix by blocking the

$|\psi_1\rangle$ -generating arm in the TDM-MI. The measured fidelity of this state to a maximally entangled state is $F(\rho_{\psi_0}) = 97.6 \pm 0.6\%$. By blocking the $|\psi_0\rangle$ -generating arm of the TDM-MI, we obtain the reconstructed density matrix shown in Fig. 6.14(b) for the trailing state $|\psi_1\rangle$ corresponding to the temporal mode t_1 .

Its fidelity to the nearest maximally entangled state is $F(\rho_{\psi_1}) = 97.5 \pm 0.7\%$. The measured overlap between these two states is $F(\rho_{\psi_0}, \rho_{\psi_1}) = 1.8 \pm 1.0\%$, which is close to zero, showing that the quantum states prepared in the two temporal modes t_0 and t_1 are nearly orthogonal to each other. When both of these states are measured simultaneously, we obtain the density matrix shown in Fig. 6.14(c). The measured fidelity of this state to the nearest maximally entangled state is $F(\rho_{\Phi}) = 68.6 \pm 1.0\%$, therein exhibiting the characteristics of a highly mixed state, as expected. Finally, when a control pulse is applied to the switch to demultiplex $|\psi_0\rangle$ from the data stream, we obtain the density matrix for $|\Phi'\rangle$ —shown in Fig. 6.14(d)—with fidelity to a maximally entangled state of $F(\rho_{\Phi'}) = 93.6 \pm 1.0\%$. The fidelity between this state and the reference trailing state $|\psi_1\rangle$ is $F(\rho_{\Phi'}, \rho_{\psi_1}) = 96.2 \pm 1.2\%$, thus showing that we are able to recover the desired state with high fidelity. We suspect that the small measured degradation of the recovered state relative to the original state is due to the aforementioned presence of the background photons caused by nuances of the pulse-picking electronics. Although Raman photons can also lead to significant degradation of performance, they did not reduce the switching fidelities measured in §6.4, hence we believe their contribution to be minimal. Striking a balance between high operation speed and low in-band background photons, we selected $\Delta t = 155$ ps, which corresponds to a 6.5-GHz operating rate, as opposed to the highest possible rate of >20 GHz allowed by the 45-ps switching windows.

We have demonstrated the operation of a cross-bar, entanglement-preserving switch for use in quantum communications and networking. We have shown that our switch is a low-loss (3 dB) device, can operate at high rates (>6.5 GHz), and retains the polarization-encoded quantum state of the input photons. Further improvements can be made to the switch by directly splicing the fibers rather than using connectorized fiber adapters and by using custom-made low-loss fiber components to further reduce the loss (<1.5 dB achievable). Additionally, shortening the common Sagnac-loop fiber path should enable even shorter switching windows, thereby further improving the speed metric of the switch. Better pulse-preparation electronics would enable the switch to operate at even faster rates (>20 GHz), while also improving the switching contrast. Thus, the switch presented here is potentially an enabling device for future applications in quantum communications, and more specifically, quantum networking.

Next, we will discuss and develop a system that utilizes this switch to measure time-bin entangled states. In this fashion, we can explore higher-dimensional Hilbert spaces by potentially creating and measuring exotic states.

CHAPTER 7

Generation and Measurement of Higher-Dimensional States

Higher-dimensional entangled states are of interest to the QIP community because they can potentially enable quantum information transfer with larger bits per photon encoding^[4], and higher robustness to noise or loss^[7]. The latter is courtesy of the fact that higher-dimensional states increase the noise threshold below which quantum key distribution is secure^[113]. Another application of interest for higher-dimensional entangled states is performing loophole-free tests of nonlocality^[5]. Inspired by these applications, and the potential for yet unbeknownst benefits, we present our initial efforts to realize a higher-dimensional quantum information system.

The system described in this chapter generates time-bin entangled photons. These photons are then converted to polarization and measured to tomographically reconstruct the state. We start this chapter by looking at an overview of the experiment and its various subsystems in §7.1. In the following section (§7.2), we discuss the subsystems in more depth while also highlighting the connections between them. Section 7.3 briefly investigates how we combine the smaller two-qubit polarization tomographies to yield the larger qutrit and ququat tomography results. Finally, in §7.4, we conclude the chapter with a review of the results we have achieved thus far. This last section will include the generation and measurement of an entangled qubit state, entangled qutrit states, and an entangled ququat state.

7.1. Project overview

In this section, we present an overview of our project to explore higher-dimensional Hilbert spaces. The primary goal of this project is to generate, manipulate, and measure entangled states with more than two bases. The original proposal goes so far as to strive for a two-photon, 10-time-bin state, therein generating, manipulating, and measuring a 20-qubit maximally entangled state.

As discussed in §5.4, our FWM source is capable of generating such states using the arrival time as our operational degree of freedom. Our high-speed switch, described in §6.2, acts as a high-speed, low-loss, spatio-temporal gate, and is thus a logical, yet unique means to manipulate and measure the temporally-encoded states. With these two pieces of the puzzle securely in hand, we look at the high-level schematic of the experimental setup, shown in Fig. 7.1, to identify the various elements of the system, and their respective functions. There are eight main subsystems which we will briefly explore here.

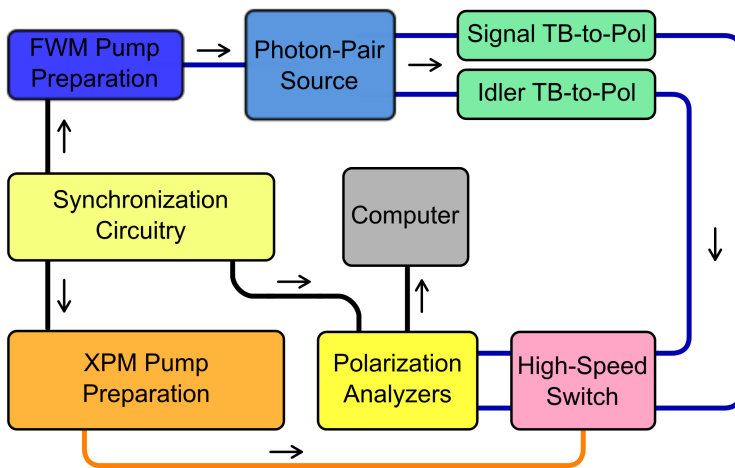


Figure 7.1. We show here a pictorial overview of the subsystems desired to generate, manipulate, and measure a 20-qubit maximally entangled state.

Synchronization Circuitry: This circuitry serves as the heart of the system. It ensures that the various signals traveling through the subsystems stay locked, i. e., do not drift with respect to one another. The primary signals that it synchronizes are the detector gating clock, and repetition rates of the FWM- and XPM-pump pulse trains. The FWM and XPM pumps must be locked in order for the switch to operate reliably. Meanwhile, the detectors must be gated at a matching rate to increase photodetection efficiencies—an unmeasured photon is a lost photon.

FWM Pump Preparation: This subsystem generates the optical O-band pump pulse that we use to drive the photon-pair source. It takes an input from the synchronization circuitry to ensure that the pulses it generates are locked with other signals. The pulse widths of the FWM pump pulses are important because they affect how narrow a time-bin can be.

Photon-Pair Source: This subsystem generates the photon pairs that we use for quantum information processing. Since the process that generates the pairs is FWM, sending in a stream of pump pulses produces a temporally entangled state.

Signal/Idler Time-Bin-to-Polarization (TB-to-Pol): This subsystem is the first part of the measurement apparatus for time-bin entangled photons. We use this subsystem to map the temporal information of our quantum state onto the polarization degree of freedom of the transmitted photons. This enables us to use the well-established polarization state tomography setup to measure the quantum state. We perform the mapping by routing two distinct time-bins onto opposite inputs of a PBS. This essentially superposes two time-bins. A tunable delay before one input of the PBS enables us to select which two time-bins to superpose. Note that this operation superposes all time-bins that are separated by selected delay. That is to say, if the delay is set to one time-bin for a four-time-bin state, then the superposed states will be 1+2, 2+3, and 3+4, where the numbers represent the enumerated

time-bins. In this case, the first time-bin shown will be mapped one polarization (say H), and the second to the orthogonal polarization (V). We note that this subsystem is the time-bin analog of quarter- and half-waveplates in a polarization state tomography.

High-Speed Switch: Once we have a train of superposed time-bins, we must select the orthogonal pair upon which to perform the polarization state tomography. We use the high-speed switch, capable of switching a single time-bin out from pulse train, to achieve this functionality. The switching window determines how narrow the time-bin can be, and as discussed in §6.1, the critical length depends on the pulse widths of the XPM pump and signal photon. The latter depends on the FWM pump pulse's width. If the TB-to-Pol subsystem is analogous to waveplates, then the switch is the time-bin equivalent of a PBS in a polarization state tomography setup. Therefore, this is the second part of the time-bin state tomography apparatus.

XPM Pump Preparation: This subsystem generates the optical C-band pump pulse that provides the desired π phase shift to the signal photons transmitted through the cross-bar switch. Just as with the FWM pump pulses, the pulse widths of the XPM pump pulses are an important parameter to tune the minimum time-bin window.

Polarization Analyzers: The traditional use of a QWP-HWP-PBS-SPD yields us the ability to project the input quantum state onto various bases. Performing a joint measurement on these projections, we can recreate the state of the measured ensemble of photons.

Computer: The last, but not least, subsystem is the computer. We use this to collect and process all the data recorded by the single-photon detector arrays. This subsystem also controls various automated systems such as the automated waveplates used to perform the polarization state tomography.

7.2. Detailed experiment

Now that we have discussed the general function of each subsystem, we take a more in depth look at each. Although some of the subsystems are identical to subsystems shown earlier, we include them here for the reader’s convenience, for pictorial consistency, and for highlighting the interconnects between the subsystems.

Again, we begin with a project overview, shown in Fig. 7.2. Unlike before, this time we label the inputs and outputs for each subsystem. All of the labels in this section remain consistent, thereby indicating that a node is identical across different figures.

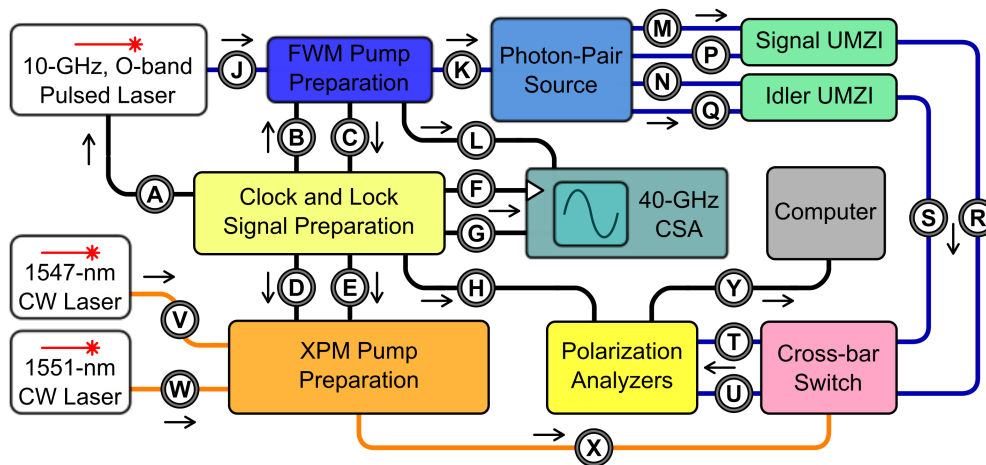


Figure 7.2. We use this overview schematic to highlight the various interconnects between subsystems shown later. We also include the O-band and C-band source lasers explicitly. Finally, we show the CSA, which is one tool we use to actively monitor some of our signals in the time-domain.

There are three base lasers we use for all our optical signals. The O-band laser is the 10-GHz, femtosecond semiconductor laser (U2T Photonics TMLL-1310). For the C-band, we use two DFB lasers centered at 1547 nm and 1551 nm, as described in §5.1.

Additionally, we include the CSA. This useful instrument enables us to monitor several signals in (virtually) real-time to determine if our systems are properly synchronized. If

one of the signals starts to display excessive jitter or amplitude loss, we can recognize it immediately and tune the appropriate dials (typically on phase shifters or tunable optical delays) to remedy the problem.

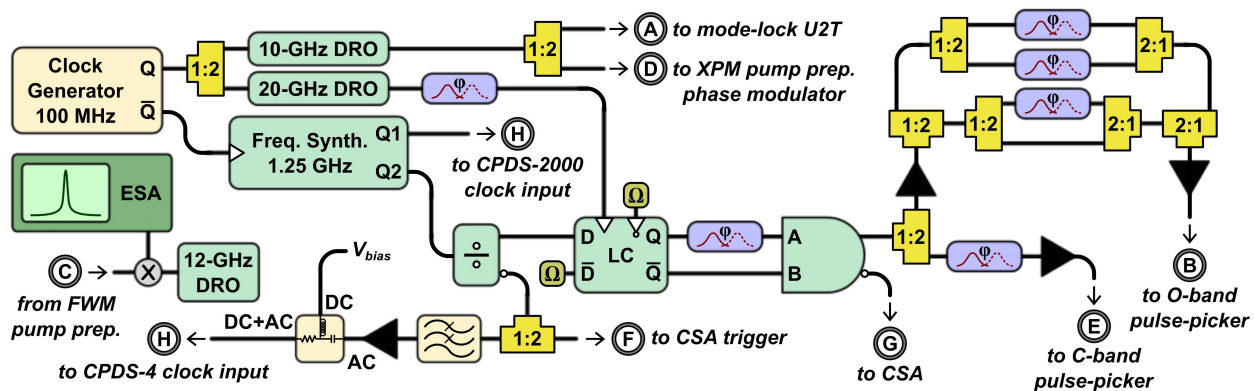


Figure 7.3. We use the clock and lock electronics shown here to ensure that signal generation, manipulation, monitoring, and measurement apparatus are locked and remain so.

As mentioned earlier, we use an electrical apparatus that synchronizes the many subsystems. Although shown in Fig. 5.11, we show it again here in Fig. 7.3 with the additional labels. From this, we see that (A) represents the signal that hybrid mode-locks our 10-GHz O-band laser. An identical signal, (D), drives the phase modulator in the XPM pump preparation source. Also, we drive the amplitude modulator in the same source using the narrow pulses generated by the AND gate. These yield a synchronized, narrow pulse train at the appropriate downcounted rate (50 MHz or 250 MHz) at (E). A similar pulse train, designated by (B), drives the amplitude modulator in the FWM pump preparation setup at the same repetition rate. As described in §5.2.6, the difference with this pulse train is that it can pulse-pick up to four consecutive 10-GHz pulses. In order to ensure that the 10-GHz laser stays hybrid mode-locked, we pick off a signal, (C), from the FWM pump preparation setup, mix it with a 12-GHz DRO, and monitor the beat note on an ESA. We described

this process earlier in §5.2.1. We use the signal at \textcircled{F} to trigger the CSA. The signal at \textcircled{G} accurately reflects the signals we use to drive the amplitude drivers in both the XPM and FWM pump preparation subsystems, hence we monitor it on the CSA in real-time. Finally, using the signal at \textcircled{H} , we clock the detectors. The alert reader will recognize that we show \textcircled{H} twice. This is to simplify notation since we never use both single-photon detector arrays (Nucrypt CPDS-4 and CPDS-2000) simultaneously.

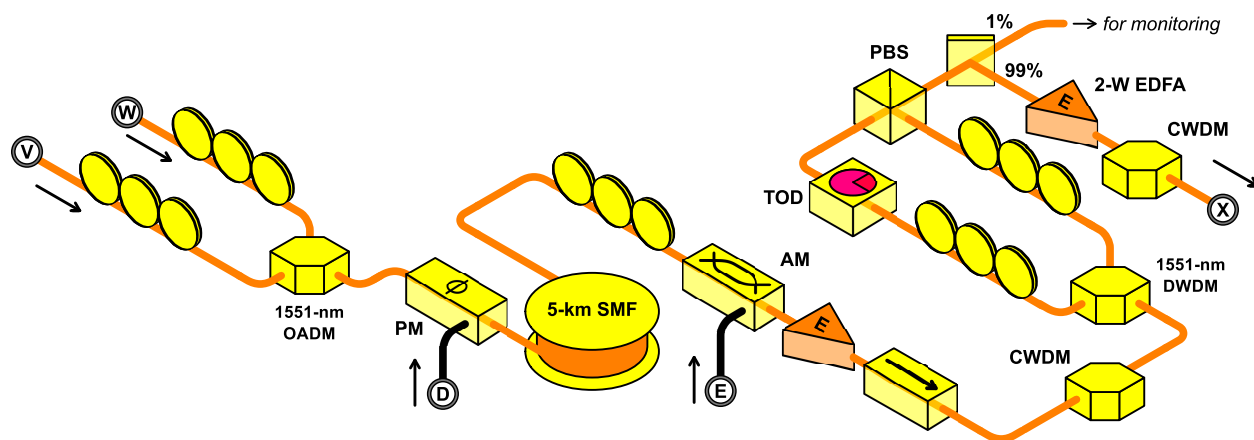


Figure 7.4. This figure is the 3-D version of the figure shown in Fig. 5.4. We highlight the four inputs (\textcircled{D} , \textcircled{E} , \textcircled{V} , and \textcircled{W}) from the clock and lock preparation subsystem, and the two CW DFB lasers. The output, \textcircled{X} , drives the XPM process in the cross-bar switch.

Shown in Fig. 7.4 is the 3-D version of the figure shown in Fig. 5.4. As such, we only highlight three points here. First, the inputs \textcircled{D} and \textcircled{E} come from the clock and lock preparation subsystem to generate the appropriate downcounted pulse train. Second, we insert the two CW DFB lasers to be modulated at \textcircled{V} and \textcircled{W} . Finally, the output at \textcircled{X} controls whether the cross-bar switch is in passive mode or active mode.

Figure 7.5 shows the optical elements used to generate our FWM pump pulse. This is in conjunction with the electrical setup discussed in Fig. 5.11. We note here that the setup is almost identical to the O-band optical path shown in Fig. 5.10. This setup has two inputs

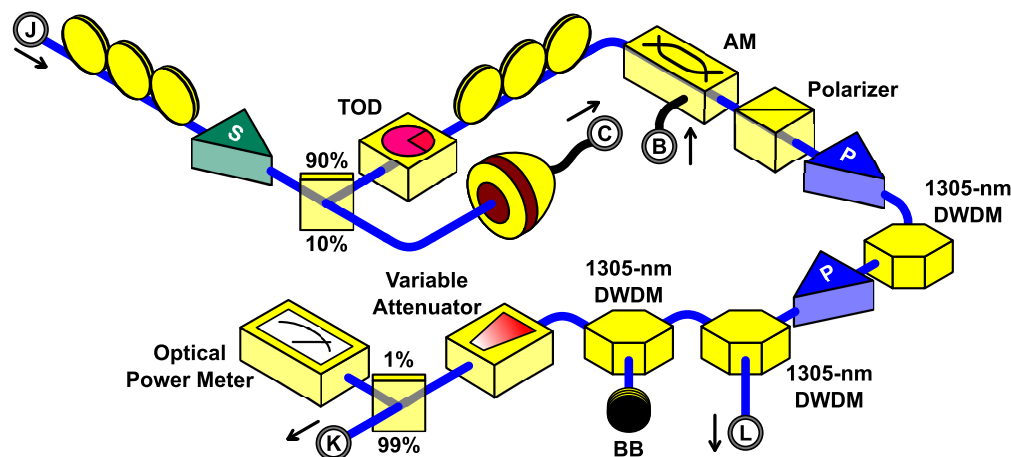


Figure 7.5. We show here the experimental setup, which in concert with the electronics shown in Fig. 5.11, prepares the FWM pump pulses. This setup has two inputs ((J) and (B)), and three outputs ((C), (K), and (L)).

at (J) and (B), and three outputs at (C), (L) and (K). The signal at (J) comes from the 10-GHz O-band laser, where an isolator and DWDM centered at 1305 nm are not shown. We amplify this signal using a semiconductor optical amplifier. The amplified signal is split using a 90:10 beamsplitter. The output of the 10% port is photodetected and sent to the mixer to ensure the 10-GHz laser stays hybrid mode-locked. The 90% port is fed through a tunable optical delay which enables us to tune the arrival time of the 10-GHz optical pulse train with respect to the electrical pulse-picking pulses at (B). We pass the output from the amplitude modulator through a linear polarizer (shown as a PBS) to maximize extinction. This signal is then amplified, filtered, and amplified again to provide us with sufficiently high powers to drive our FWM process. Shown at (L), we use the reject port of the first 1305-nm DWDM to monitor the optical pulse shapes on the CSA. We filter and subsequently attenuate the light at the pass port to the appropriate color and powers. We use a 99:1 beamsplitter to monitor the power of the attenuated pulse at the 1% port. We use this measured power to calibrate the PPR and CAR of our photon-pair source, as shown

in §5.3. At the 99% port (\textcircled{K}), we have a sequence of up to four FWM pump pulses, each separated by 100 ps. The entire group repeats every 20 ns for the 50-MHz setting of the frequency divider.

In order to ensure that we will be able to superpose the various time-bins, we performed a quick test measuring the pair-wise coherence between these pulses. This test entails passing the pulses through a Mach-Zehnder interferometer (MZI) and measuring the interference visibilities by tuning the pulse's relative arrival times at the second beamsplitter. For this test, the MZI was actively stabilized using a reverse propagating pulse and an Arduino-based PID feedback circuit (see Fig. 7.7). If we label our pulses 1 through 4, then the measured interference visibilities between pulse 1 and itself (1-1), was $>95.6\%$. Similarly, the 2-2, 3-3, and 4-4 visibilities were $>96.5\%$, $>95.3\%$, $>96.4\%$, respectively. Note that for all four of these tests, the MZI has no relative delay between both arms. Instead, if we introduce a 100-ps delay in one arm, corresponding to a one pulse delay, then we obtain 1-2, 2-3, and 3-4 visibilities of $>90.5\%$, $>95.5\%$, and $>96\%$, respectively. A two pulse delay yields interference visibilities of $>91.7\%$ and $>93.5\%$ for 1-3 and 2-4 pulse superpositions, respectively. Finally, we use a three pulse delay to measure a 1-4 interference visibility of $>88.4\%$. These results seem to keep with the results found in Monika Patel's thesis for the same U2T 10-GHz laser^[39], wherein we observed approximately 90% interference visibilities for up to eight pulses. Additionally, we measured a 50% visibility around a 17 pulse delay. These provide us with an approximate upper bound on the number of pulses that our system can successfully generate and use.

Figure 7.6 shows the photon-pair source. This image is very similar to that shown in Fig. 5.13. The only difference is that, in this case, we recycle the reject 1305-nm light for use in stabilizing the unbalanced Mach-Zehnder interferometers.

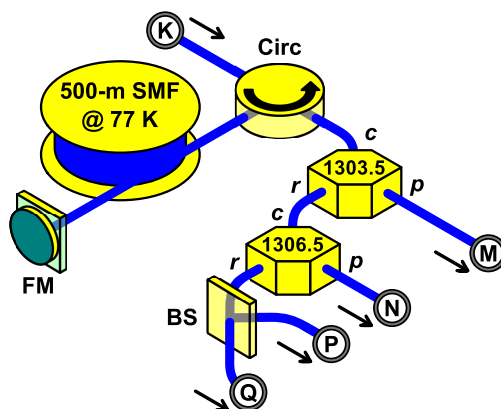


Figure 7.6. We show a photon-pair source akin to that shown in Fig. 5.13. This design has one input at \textcircled{K} and four outputs at \textcircled{M} , \textcircled{N} , \textcircled{P} , and \textcircled{Q} . The first two outputs correspond to the signal and idler single-photons. The only difference between the two designs is that we recycle the 1305-nm light from the reject port after both signal/idler WDMs.

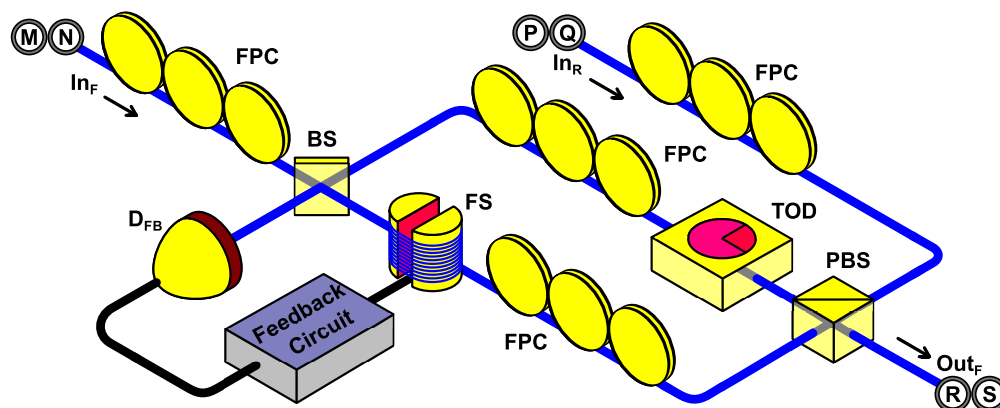


Figure 7.7. We use an unbalanced Mach-Zehnder interferometer, shown here, to map two time-bins onto the orthogonal polarization bases.

We use an unbalanced Mach-Zehnder interferometer (UMZI) to achieve the time-bin-to-polarization conversion. We achieve this by splitting the time-bin encoded pulse-train (\textcircled{M} , \textcircled{N}) at a 50:50 beamsplitter. One path of the UMZI is longer than the other path by a tunable amount. By selecting the delay increments to be integer multiples of one time-bin, we can temporally overlap any two time-bins. A motorized tunable optical delay (TOD) provides us with the temporal tunability. Unfortunately, it can only move 560 ps, therein

limiting the maximum number of time-bins to five. We select four time-bins as our maximum to match the electronic splitter/combiner network shown in the clock/lock setup.

In order to map the time-bins onto polarization, we feed the two opposite paths onto the the orthogonal inputs of a PBS. By tuning the FPCs, we can ensure that the photons from each input are routed to the same output ($\textcircled{\text{R}}$, $\textcircled{\text{S}}$).

We note that one path of the UMZI has a fiber stretcher (FS), which we use to ensure that our UMZI remains phase stable. This homemade fiber stretcher uses a piezoelectric to push two semicircular 3-D printed rods around which we wrap a length of fiber. Depending on the length of fiber, we can change the amount of phase achieved by tuning the voltage applied to the piezoelectric. For our designs, we can achieve a π phase for $\simeq 1305$ -nm light by applying $\simeq 1.5$ V. The signal we use to maintain the phase stability of the UMZI is the 1305-nm FWM pump pulses ($\textcircled{\text{P}}$, $\textcircled{\text{Q}}$). To minimize their contribution to background photons, we inject this light at In_R so that it is reverse propagating through the UMZI. We photodetect this light using D_{FB} , then use an Arduino Uno to read in the voltages. The Arduino then performs a software based PID operation—actually, only integrator—to correct for drifts. This correction signal is then applied to the FS to obtain phase stability. A copy of the Arduino feedback control code can be found in Appendix D.

In order to measure the phase stability, we sent in classical, polarized light to In_F and monitored its polarization at Out_F using a polarimeter. The polarimeter measures the three Stokes parameters used to define the polarization of the beam. By plotting these three over time, as shown in Fig. 7.8, we note that the polarization drifts $< 5\%$ over the duration of 1000 s. We deem this acceptable for now, but recognize that it can potentially be improved.

The cross-bar switch shown in Fig. 7.9 is very similar to that shown earlier in Fig. 6.3(b). Among the differences are the additional FPCs, TODs, and WDMs at the inputs or outputs

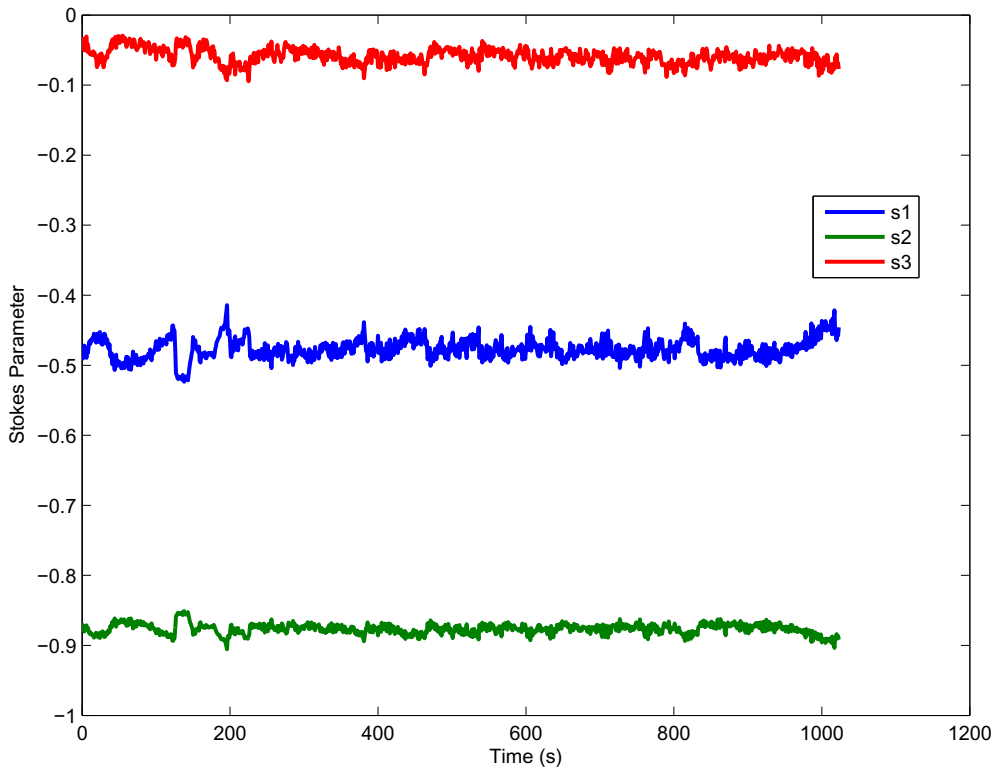


Figure 7.8. We show here the three Stokes parameters (S_1 – S_3) that describe our state’s input polarization to demonstrate the polarization stability of the UMZI. Based on this measurement, our phase locking and compensation optics satisfactorily stabilize the output polarization of the signal and idler photons with variance $<5\%$ over 1000 s.

of the switch. We route the signal and idler pulse train of superposed time-bins at $\textcircled{\text{R}}$ and $\textcircled{\text{S}}$, respectively. We note that the superposed time-bins are encoded onto the polarization bases of a single temporal window. By setting the in-Sagnac FPC to passively reflect light, no photons will reach the outputs at $\textcircled{\text{T}}$ and $\textcircled{\text{U}}$ because the WDMs filter them out. Instead, when a XPM pump pulse is present at $\textcircled{\text{X}}$, the switch will transmit the desired superposition of time-bins to the respective output, and only that pair of time-bins will be measured. In this fashion, the cross-bar switch acts as a temporal shutter for the time-bin superpositions. We remark here that this functionality can also be reproduced using separate changeover switches

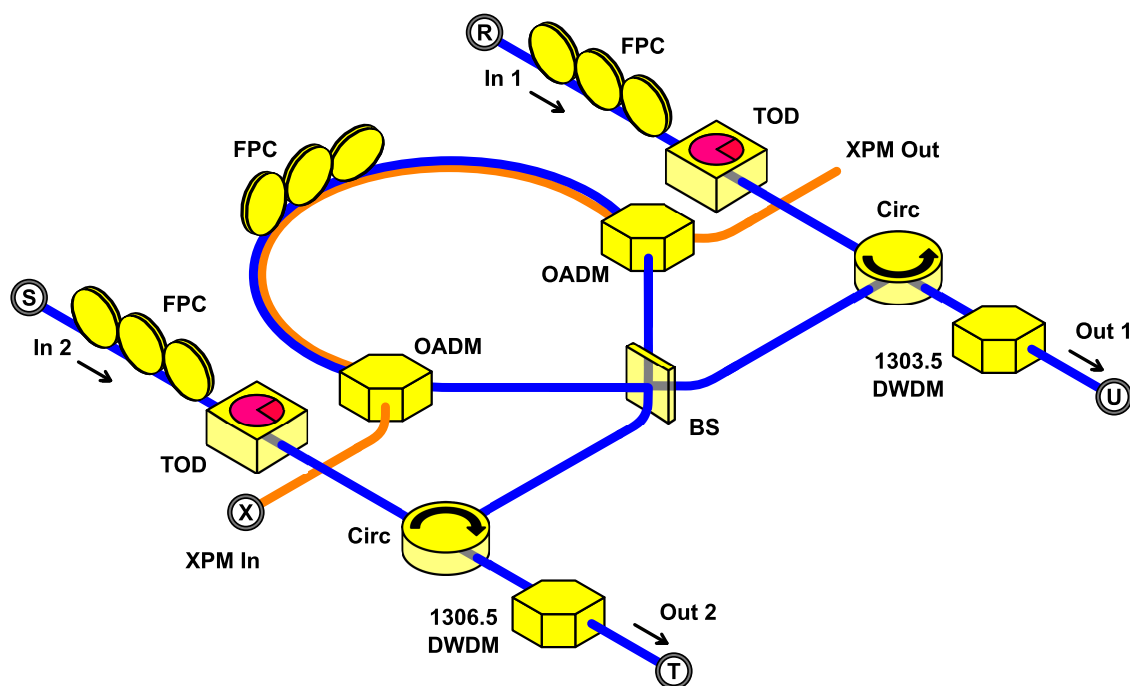


Figure 7.9. This switch shown here is very similar to the switch shown in Fig. 6.3(b). The few differences here are the addition of FPCs and TODs at both inputs, and WDMs at both outputs. The TODs enable us to pick which superposed pair of time-bins we want to switch, and the WDMs omit all of the unswitched superposed pairs of time-bins.

in the signal and idler paths. The benefit of the cross-bar design is that we can perform the selection simultaneously using just one XPM pump pulse and appropriate adjustment of the TODs.

Figure 7.10 show the standard free-space polarization state tomography optics (QWP-HWP-PBS-SPD) for both signal and idler photons. We also show some QWPs and HWPs before these which we can use to birefringence compensation. Alternatively, we can artificially perform this rotation using software. For convenience, we often opt for the latter, especially when processing larger tomographies.

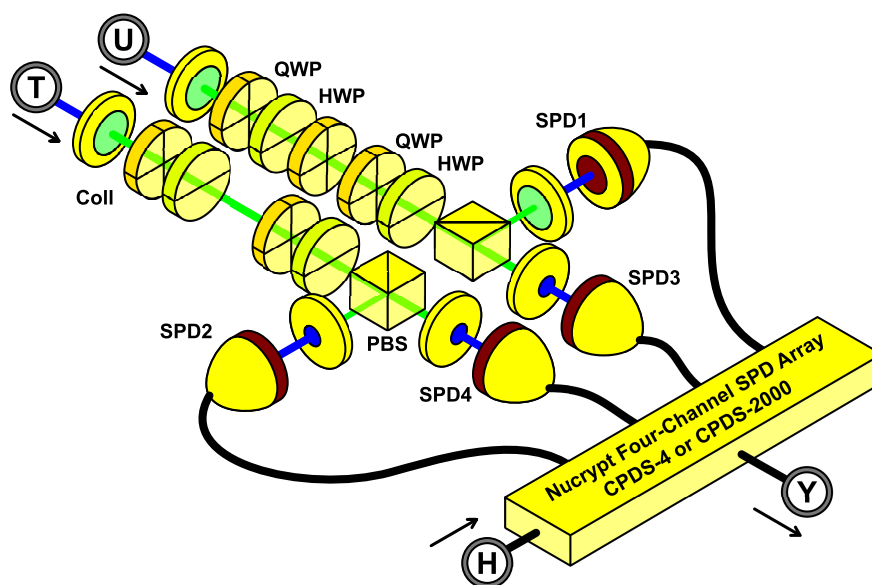


Figure 7.10. We show here a standard free-space polarization state tomography setup preceded by several waveplates which can be used to compensate for fiber birefringence. Often, we do not adjust the birefringence compensating waveplates, and instead perform that polarization state “rotation” in software, after calculating our state.

7.3. Higher-dimensional state reconstruction

Now that we understand the experimental setup, it should be clear that, since we perform polarization-based tomographies, every tomography can at most recreate a two-qubit state. This is because polarization is fundamentally a binary basis, i. e., we cannot use polarization to realize qutrit and ququat states directly. Hence, this may seem insufficient for measuring qutrit or higher-dimensional states. Fortunately, as discussed earlier in §3.3.1, by measuring pairwise superpositions of time-bins—now encoded onto polarizations—we can recreate an entire higher-dimensional state.

A single qutrit state requires us to determine the nine Stokes parameters that depend on the probabilities of measuring 15 basis states. Explicitly written, the 15 time-bin projective

measurements are:

$$\{M_3\} = \begin{pmatrix} |0\rangle \\ |1\rangle \\ |2\rangle \\ \frac{1}{\sqrt{2}}(|0\rangle \pm |1\rangle) \\ \frac{1}{\sqrt{2}}(|0\rangle \pm |2\rangle) \\ \frac{1}{\sqrt{2}}(|1\rangle \pm |2\rangle) \\ \frac{1}{\sqrt{2}}(|0\rangle \pm i|1\rangle) \\ \frac{1}{\sqrt{2}}(|0\rangle \pm i|2\rangle) \\ \frac{1}{\sqrt{2}}(|1\rangle \pm i|2\rangle) \end{pmatrix} \quad (7.1)$$

If we select two time-bins, t_a and t_b , and map them to the H and V polarizations respectively, then we can use the polarization analyzers to perform six of the 15 required projective measurements, shown here:

$$\begin{pmatrix} |t_a\rangle \\ |t_b\rangle \\ \frac{1}{\sqrt{2}}(|t_a\rangle \pm |t_b\rangle) \\ \frac{1}{\sqrt{2}}(|t_a\rangle \pm i|t_b\rangle) \end{pmatrix} \implies \begin{pmatrix} |H\rangle \\ |V\rangle \\ \frac{1}{\sqrt{2}}(|H\rangle \pm |V\rangle) \\ \frac{1}{\sqrt{2}}(|H\rangle \pm i|V\rangle) \end{pmatrix} \quad (7.2)$$

Here, $t_a, t_b \in \{0, 1, 2\}$, and the double arrow represents the mapping between time-bins and polarizations. By selecting various pairs of time-bins, we can obtain all 15 projective measurements, and thus measure a single qutrit. But, since we actually measure a two-photon state—signal and idler—we must perform projective measurements corresponding to $|\psi_a\rangle \otimes |\psi_b\rangle$ where $|\psi_a\rangle, |\psi_b\rangle \in \{M_3\}$. We write this relation explicitly in Eq. 7.3. In order to do this, we require the ability to superpose any two time-bins for the signal and

idler, independently. Recall that the UMZI in each path—signal and idler—enables us to superpose any two time-bins, and the tunable optical delay at each input of the switch allows us to select which arbitrary pair of superpositions we wish to measure, thereby selecting the desired two-qutrit projective measurement.

$$\begin{pmatrix} |0\rangle \\ |1\rangle \\ |2\rangle \\ \frac{1}{\sqrt{2}}(|0\rangle \pm |1\rangle) \\ \frac{1}{\sqrt{2}}(|0\rangle \pm |2\rangle) \\ \frac{1}{\sqrt{2}}(|1\rangle \pm |2\rangle) \\ \frac{1}{\sqrt{2}}(|0\rangle \pm i|1\rangle) \\ \frac{1}{\sqrt{2}}(|0\rangle \pm i|2\rangle) \\ \frac{1}{\sqrt{2}}(|1\rangle \pm i|2\rangle) \end{pmatrix} \otimes \begin{pmatrix} |0\rangle \\ |1\rangle \\ |2\rangle \\ \frac{1}{\sqrt{2}}(|0\rangle \pm |1\rangle) \\ \frac{1}{\sqrt{2}}(|0\rangle \pm |2\rangle) \\ \frac{1}{\sqrt{2}}(|1\rangle \pm |2\rangle) \\ \frac{1}{\sqrt{2}}(|0\rangle \pm i|1\rangle) \\ \frac{1}{\sqrt{2}}(|0\rangle \pm i|2\rangle) \\ \frac{1}{\sqrt{2}}(|1\rangle \pm i|2\rangle) \end{pmatrix} \quad (7.3)$$

The ququat example follows quite similarly, with the only difference being the larger number of required projective measurements, shown below for one ququat.

$$\{M_4\} = \begin{pmatrix} |0\rangle \\ |1\rangle \\ |2\rangle \\ |3\rangle \\ \frac{1}{\sqrt{2}}(|0\rangle \pm |1\rangle) \\ \frac{1}{\sqrt{2}}(|0\rangle \pm |2\rangle) \\ \frac{1}{\sqrt{2}}(|0\rangle \pm |3\rangle) \\ \frac{1}{\sqrt{2}}(|1\rangle \pm |2\rangle) \\ \frac{1}{\sqrt{2}}(|1\rangle \pm |3\rangle) \\ \frac{1}{\sqrt{2}}(|2\rangle \pm |3\rangle) \\ \frac{1}{\sqrt{2}}(|0\rangle \pm i|1\rangle) \\ \frac{1}{\sqrt{2}}(|0\rangle \pm i|2\rangle) \\ \frac{1}{\sqrt{2}}(|0\rangle \pm i|3\rangle) \\ \frac{1}{\sqrt{2}}(|1\rangle \pm i|2\rangle) \\ \frac{1}{\sqrt{2}}(|1\rangle \pm i|3\rangle) \\ \frac{1}{\sqrt{2}}(|2\rangle \pm i|3\rangle) \end{pmatrix} \quad (7.4)$$

The coincidence counts from these projective measurements are then fed into the tomography program—either maximum-likelihood^[114,115] or linear-least-squares-fit algorithms^[116]—to produce the density matrices that describe the incident quantum state.

As a sidenote, in order to ensure that our bases are aligned to the H and V bases of the PBSs in the signal and idler polarization analyzers, we can rotate the birefringence compensating waveplates. This can be experimentally tedious, so we often perform the rotation in software. This is a trivial process for two-qubit states, but for two-qutrit and two-ququat states, we must be more careful since they are composed of an several qubit measurement tomographies. We determine the appropriate rotation by first taking the qubit states for all combinations of signal and idler superposed time-bins and identifying the transformation required to rotate the measured state into the expected ideal state's bases. Equipped with these transformation matrices, we rotate all the measurements supplied to the tomography code by a single transformation matrix and calculate the measured state. We repeat this process for all other transformation matrices. Comparing the resulting states with the ideal maximally entangled state, we can determine which rotation most closely aligns us to the H and V bases of the signal and idler PBS. All states measured in the following section use this method of rotation.

Now that we know how to reconstruct our quantum state, we turn our attention the experimental results wherein we create and measure such states.

7.4. Experimental results

In this section, we present the results of the aforementioned experimental setup. As described in the previous section, all the results shown here use the fifth-generation FWM pump preparation (§5.2.6), third-generation XPM pump preparation (§5.1.3), and the Nuclecrypt CPDS-4 single-photon detector array. Additionally, all tomographies use the linear least-squares fit algorithm rather than the maximum-likelihood tomography^[114,115] to save on time. We have calculated density matrices using a maximum-likelihood tomography for

several of the states shown in this section, and their fidelities agree to within 1% of the linear least-squares fit tomography results. Because we use the linear least-squares fit tomography algorithm, we also verify that the retrieved density matrix is legal by ensuring that its diagonal elements are positive and its trace is one^[116]. Finally, we obtain all the error bars by running a Monte Carlo simulation using Poissonian-randomized measured coincidence counts.

The first task was to measure a basic qubit state. This state is established by sending two FWM pump pulses into the photon-pair source. The ideal measured state should be $|\gamma_2\rangle = |00\rangle + |11\rangle$. Herein, any state $|\gamma\rangle$ represents an “ideal” two-photon, maximally entangled state where the subscript denotes the dimensionality. We show in Fig. 7.11 the measured density matrix of this state. The fidelity of the measured state $|\psi_{m2}\rangle$ to the ideal state is $F(\hat{\rho}_{m2}, \hat{\rho}_{\gamma_2}) = 96.3 \pm 0.7\%$. The measured linear entropy of this state is $S_L(\hat{\rho}_{m2}) = 0.076 \pm 0.019$. By comparing these parameters to the values of fidelity and linear entropy in Fig. 3.1, we can safely say that this measured state can violate Bell’s inequality.

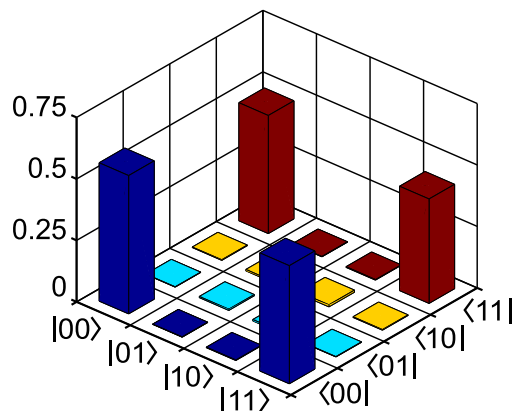


Figure 7.11. We show the density matrix of a two-qubit state. This state has a fidelity to $|00\rangle + |11\rangle$ of $96.3 \pm 0.7\%$. Its linear entropy is $S_L(\hat{\rho}_{m2}) = 0.076 \pm 0.019$. This data corresponds to a detected coincidence count rate of 200 per measurement.

This result corresponds to detecting approximately 200 coincidence counts per measurement. We initially selected this count rate because it corresponded to a source $CAR > 15$. Also, when we say “measurement”, we refer to each projective measurement used in a polarization state tomography. Hence, for a complete four-detector tomography, we use 36 projective measurements corresponding to independently setting the signal and idler to $\{H, V, D, A, R, L\}$, respectively. Each projective measurement is 300 million gates at 50 MHz, the same for all qutrit tomographies shown hereafter.

To give the reader a sense of time, each complete tomography takes $\simeq 1$ minute to prepare the waveplates and collect dark-count data, $\simeq 9$ minutes to rotate the waveplates, and $\simeq 2$ minutes to collect 3600 million gates of data (36 measurements \times 100 million gates per measurement). Thus, a complete qubit tomography that uses 300 million gates per measurement takes $\simeq 16$ minutes to complete. For a complete qutrit tomography, we require $9 \times 36 = 324$ measurements, or in time $9 \times 16 = 144$ minutes ($\simeq 2.4$ hours). Finally, a complete ququat tomography needs $36 \times 36 = 1296$ measurements. This requires $\simeq 576$ minutes, i. e., $\simeq 9.6$ hours. Hence, for the ququat measurement shown later, we opted to use 100 million gates per measurement, thereby reducing the data collection time to $\simeq 7.2$ hours.

With a qubit successfully generated and measured, the next logical step is to attempt measuring a qutrit state. Since the qutrit state measurements are composed of projections that can generate qubit states, we asked ourselves “What is the expected qutrit state given a qubit state with a known measured fidelity?” In order to give us an idea of the expected limits for such a qutrit state, we performed some tomographic simulations. These simulations use the methodology discussed in Appendix B. We use Werner states to simulate imperfect measured states. We rewrite here the Werner state, mentioned in §3.2, for the reader’s

convenience.

$$\hat{\rho}_W = p|\gamma\rangle\langle\gamma| + (1-p)\frac{1}{d^2}\mathbb{I}, \quad (7.5)$$

where p is the percent of the state that is entangled, d is the dimensionality of the qudit, and $|\gamma\rangle$ is an arbitrary maximally entangled qudit state. By adjusting p , we can simulate the expected fidelities of qubit and qutrit states with varying contributions due to mixed states, i. e., noise. We plot the effect of the added mixture on the measured qubit and qutrit states in Fig. 7.12.

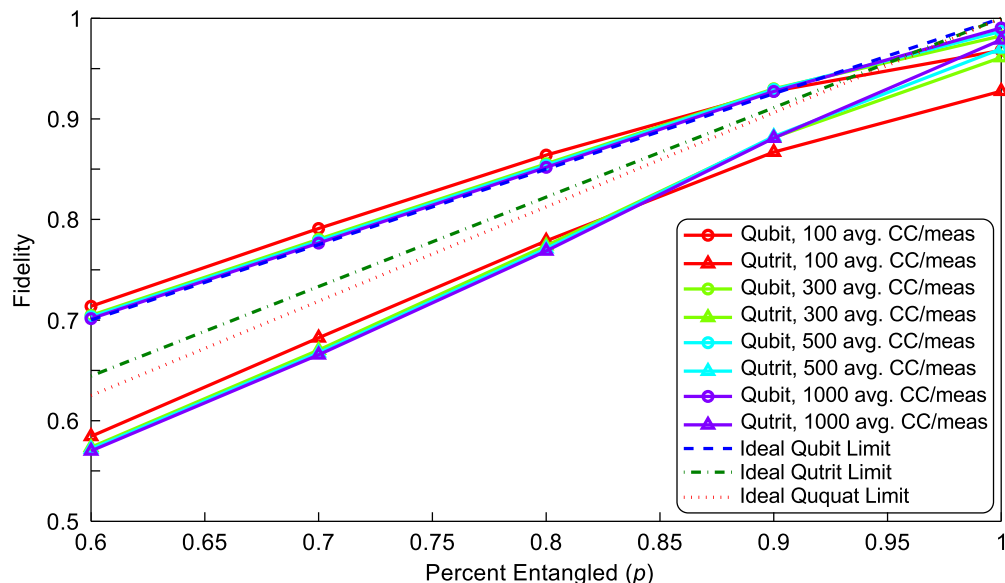


Figure 7.12. We show here the simulated fidelities of Werner states with varying degrees of mixture added. The simulations randomize the coincidence counts according to a Poissonian distribution. We plot qubit (\circ) and qutrit (Δ) fidelities to the respective maximally entangled state versus the percentage of the state that is entangled, p . Additionally, we vary the number of average coincidence counts (100, 300, 500, and 1000 CC/meas) to see the effect of poor count statistics on the expected results. We also show the limits corresponding to an unrandomized, ideal Werner state for the qubit (blue dashed line), qutrit (green dot-dashed line), and ququat (red dotted line). All simulations shown here use the linear-least-squares-fit algorithm.

In order to simulate real measurements, we randomize the coincidence counts per measurement. The randomization obeys a Poissonian distribution around a given average coincidence count rate. In addition to varying the amount of mixture, we change the average number of coincidence counts per measurement (CC/meas) to be 100, 300, 500, and 1000. We note that as we collect fewer coincidence counts for a tomography, we cannot achieve perfect fidelity—even in the absence of any added noise. This reinforces our intuition that we need sufficient counts to measure high-quality states.

As a reference, we also show the theoretical limits on fidelity for qubits, qutrits, and ququats. These ideal limits do not assume any randomization on the coincidence counts. When compared to randomized data, we note that as we add more mixture (move left on the plot), the simulated qubits yield higher fidelities than the theoretical limit. This is due to the variance from randomizing the coincidence counts.

Figure 7.12 also provides us with an approximate sense of the expected qutrit values given a qubit value. We make two assumptions in order to do so: (1) random noise is the only source of degradation of the fidelity, and (2) that noise—due to effects such as decoherence, Raman photons, or loss—affects qubits and qutrits identically. Based on this, we note that for a 90% entangled Werner state ($p = 0.9$), we expect a qubit fidelity of $\simeq 93\%$, which is near the fidelity of our measured qubit state. For the same amount of mixture, we expect a qutrit state to have a fidelity of 88% with a maximally entangled qutrit state.

Expecting a qutrit state fidelity around 88%, we attempted to measure the state $|\gamma_3\rangle = |00\rangle + |11\rangle + |22\rangle$. The resulting state, shown in Fig. 7.13, has a fidelity with this ideal state of $F(\hat{\rho}_{m3}, \hat{\rho}_{\gamma_3}) = 84.7 \pm 1.0\%$. This state's measured linear entropy is $S_L(\hat{\rho}_{m3}) = 0.302 \pm 0.017$. Once again, if compared to Fig. 3.1, we can use this state to violate the appropriate 3-D

Bell inequality. In order to obtain this state, we set the power to collect approximately 350 coincidence counts per measurement.

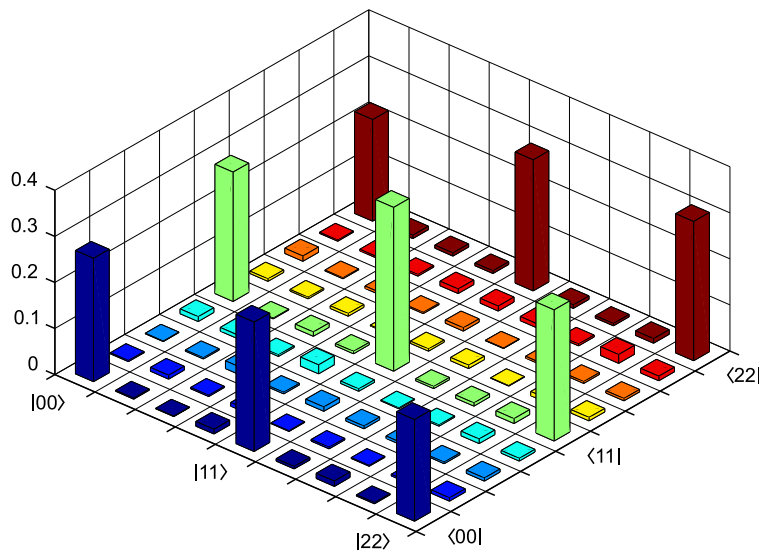


Figure 7.13. We show the density matrix for a qutrit state at a low FWM pump power. The fidelity of this state to $|00\rangle + |11\rangle + |22\rangle = 84.7 \pm 1.2\%$. The measured linear entropy is $S_L(\hat{\rho}_{m3}) = 0.302 \pm 0.017$. This corresponds to approximately 350 coincidence counts per measurement.

Out of curiosity, we took qutrit measurements at varying FWM pump power levels to see the effect on the degradation of fidelity. We discovered that we can increase the power almost 2.5 times and not see much degradation in the states quality. This indicates that although we initially selected a lower power, where the CAR was greater than 15, to mitigate the effect of multi-pair events, we can instead operate at a higher power to increase our coincidence collection rate without significant degradation in performance due to multi-pairs. We show this state in Fig. 7.14, wherein we see a fidelity of $F(\hat{\rho}_{m3}, \hat{\rho}_{\gamma3}) = 85.7 \pm 0.8\%$. This state's linear entropy is $S_L(\hat{\rho}_{m3}) = 0.281 \pm 0.014$. Yet again, this state can violate the Bell inequality. This state used about 1800 coincidence counts per measurement.

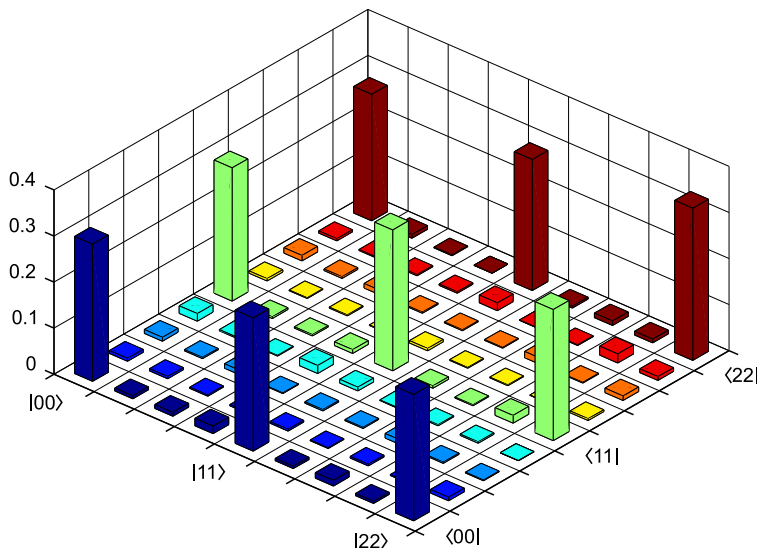


Figure 7.14. We show the density matrix for a qutrit state at an intermediate FWM pump power. The fidelity of this state to $|00\rangle + |11\rangle + |22\rangle = 85.7 \pm 0.8\%$. The state's linear entropy is $S_L(\hat{\rho}_{m3}) = 0.281 \pm 0.014$. This corresponds to approximately 1800 coincidence counts per measurement.

Earlier in §5.4, we posited that if we increase the FWM pump power, our pure entangled state will become more mixed and separable due to the presence of multi-pair events. Evidently, we did not increase the power enough to witness multi-pair events. Since we did not observe such behavior, we increased the FWM pump power further. The resulting measured density matrix, shown in Fig. 7.15 and corresponding to $\simeq 5100$ coincidence counts per measurement, yields a fidelity with the ideal qutrit state of $F(\hat{\rho}_{m3}, \hat{\rho}_{\gamma 3}) = 41.2 \pm 0.5\%$. This state's measured linear entropy is $S_L(\hat{\rho}_{m3}) = 0.825 \pm 0.003$. Clearly, when compared to Fig. 3.1, this state falls into the shaded area, therefore it is unable to violate Bell's inequality. This, once again, verifies our intuition that multi-pair events lead to crosstalk, and highlights the detrimental impact of such events on our ability to use such states for QIP.

Of course, since operating at higher pump powers increases multi-pairs (bad) while also increasing our coincidence collection rate (good), we must strike a balance. One of the

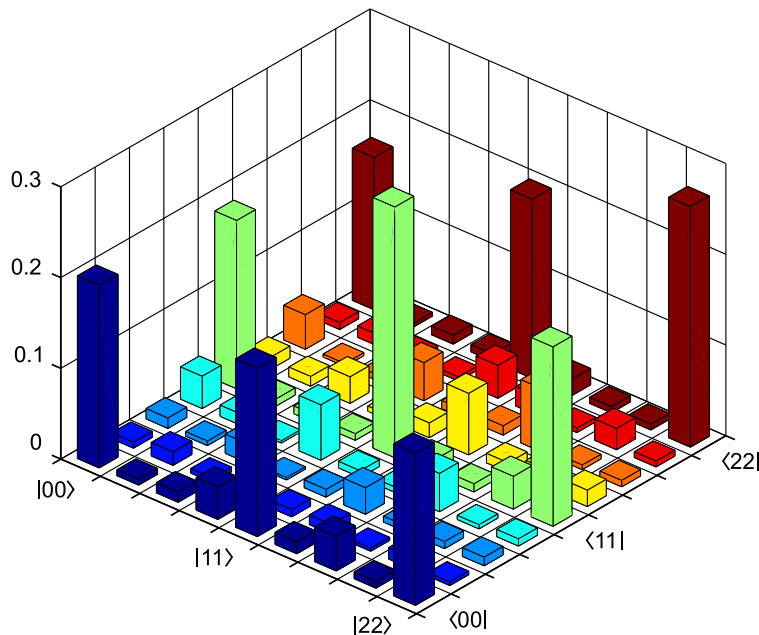


Figure 7.15. We show the density matrix of a qutrit state at a high FWM pump power. The fidelity of this state to $|00\rangle + |11\rangle + |22\rangle = 41.2 \pm 0.5\%$. This state's measured linear entropy is $S_L(\hat{\rho}_{m3}) = 0.825 \pm 0.003$. This corresponds to $\simeq 5100$ coincidence counts per measurement.

benefits of operating at higher coincidence count rates per measurement is that we can reduce the run time required to obtain decent statistics. This then relaxes the duration over which our system must remain stable. As such, we want to operate at as high a coincidence count rate per measurement while maintaining a reasonable fidelity to the desired maximally entangled state. Since the system stability is even more important when taking longer measurements for a ququat state, we opted to find the appropriate balance point using qutrit states before attempting a ququat state. We plotted the measured qutrit states' fidelities as a function of coincidence counts per measurement (cf. Fig. 7.16). Based on these results, the aforementioned rate of 1800 coincidence counts per measurement seems suitable.

We remark that the average qubit fidelities shown in this figure correspond to the maximally entangled qubit states obtained during each qutrit measurement. In other words,

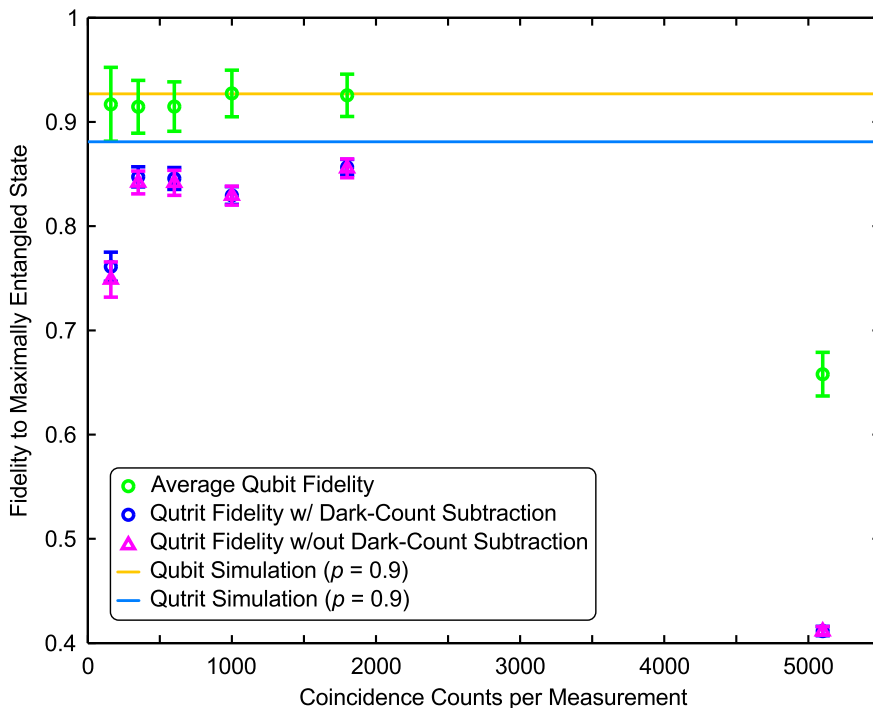


Figure 7.16. We investigate the effect of coincidence count collection on the measured qubit (green \circ) and qutrit (blue \circ) fidelities (compared to the maximally entangled qubit and qutrit states, $|\gamma_2\rangle$ and $|\gamma_3\rangle$). Both of these represent dark-count-subtracted coincidence counts. We also show non-dark-count subtracted results (pink \triangle) to note that the tomographies improve by a small amount when using dark-count subtracted counts, especially at lower count rates. Based on these results, we choose to operate at a collection rate of $\simeq 1800$ coincidence per measurement. For reference, we also show the simulated qubit and qutrit fidelities for a 90% entangled Werner state (cf. Fig. 7.12 for $p=0.9$). Based on these references we see that for a state with $\simeq 93\%$ qubit fidelity, we expect a qutrit state with fidelity of $\simeq 88\%$. Thus our $\simeq 85\%$ states are close albeit with room for improvement.

there are three maximally entangled qubit tomographies obtained when the measured signal and idler time-bin superpositions match which we use to calculate the average qubit fidelity.

Figure 7.16 also includes lines that correspond to the simulated qubit and qutrit reference points for a Werner state with $p = 0.9$ (cf. Fig. 7.12). We plot these to show that for the measured average qubit fidelities around 93%, we expect a qutrit fidelity to be around 88%.

The plot clearly shows that although we are close—measured fidelities are $\simeq 85\%$ —there is room for improvement. We attribute this slight degradation between the expected and measured values to system instabilities and drift over the 2.5 hour duration of the experiment.

Another set of data was also included in Fig. 7.16. As mentioned earlier in this chapter, all the results shown in this chapter correspond to dark-count-subtracted data. We decided to compare the results of such data with non-dark-count-subtracted data. In doing so, and shown in Fig. 7.16, we find that performing dark-count subtraction does not improve the results significantly. This is good for two reasons. First, it means that we are operating at sufficiently high coincidence count rates that detector dark-count events are a minimal contribution to the coincidences. Additionally, we have biased our single-photon detectors well to minimize contribution of the dark counts. Second, and more importantly, to reduce the time for a complete tomography, we can omit the step wherein we measure the dark counts without a significant penalty in fidelity. This removes approximately one minute from the 16 minutes required to perform a complete 36-measurement tomography—a fractional improvement—but as we aim to scale this system to large dimensions, any reduction in time will help. We remark that none of the results shown in this chapter omit the dark-count collection step, but this point is worth remembering for future tests.

Finally, we attempt to generate the ideal ququat state $|\gamma_4\rangle = |00\rangle + |11\rangle + |22\rangle + |33\rangle$. Based on the our qutrit measurement results, we set the FWM pump power to provide us with $\simeq 2000$ coincidence counts per measurement. Upon performing a tomography, we obtain the reconstructed density matrix shown in Fig. 7.17. This measured state has a fidelity of $F(\hat{\rho}_{m4}, \hat{\rho}_{\gamma_4}) = 64.9 \pm 0.5\%$ with the ideal state. The corresponding linear entropy of this state is $S_L(\hat{\rho}_{m4}) = 0.506 \pm 0.008$. If we compare this state to the Fig. 3.1, we see that this

state does not quite violate Bell's inequality. Fortunately, we are close to creating a state that does violate it, and we have plausible culprits for the cause in degradation.

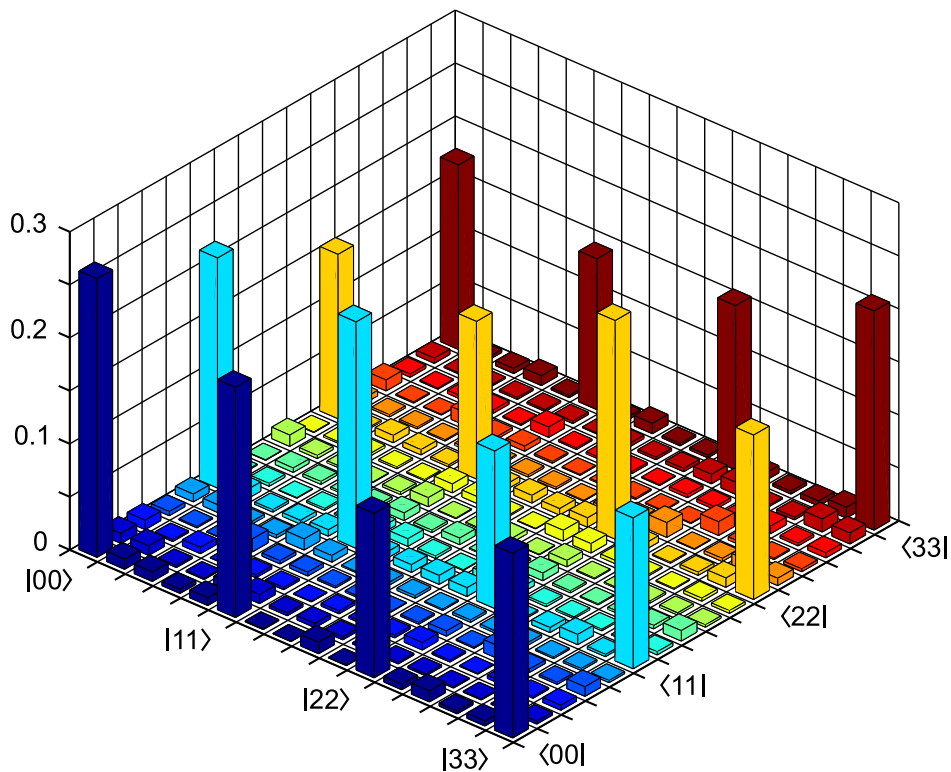


Figure 7.17. We show the density matrix of a ququat state. The fidelity of this state to $|00\rangle + |11\rangle + |22\rangle + |33\rangle = 64.9 \pm 0.5\%$. The linear entropy of this state is $S_L(\hat{\rho}_{m4}) = 0.506 \pm 0.008$. This data corresponds to $\simeq 2000$ coincidence counts per measurement.

As noted earlier, collecting the required data for a ququat state takes over seven hours. If a couple hour qutrit tomography provides instabilities, then a ququat tomography is bound to experience the effects more negatively. Improving the subsystem stabilities for day-long operation should affect these results quite positively. In order to improve results, there are multitude of steps we can take. We plan to investigate operating at higher pair-production rates, reduce data collection times, remove potentially unnecessary steps such as dark-count

collection, automate delay line adjustments for superposing and selecting time-bins, and build in additional feedback mechanisms to monitor subsystem stabilities.

With these improvements, we hope to improve our ququat fidelities, but since we have not yet performed any tomographic simulations with randomized coincidence counts for ququat states, we cannot provide any insight on the expected fidelities. Of course, we anticipate that these results can be improved significantly based on the ideal ququat line (red dotted line) shown in Fig. 7.12.

Hence, in this chapter, we have shown that we are able to create, manipulate, and measure entangled two-qubit states, entangled two-qutrit states, and entangled two-ququat states. Not shown here, but verified experimentally, is the ability to generate separable two-photon states. We trust the reader understands that generating such a state is trivial. We generate time-bin entanglement by using the FWM process in standard optical fiber. Although many other sources can replicate this result, using standard fiber is convenient since our entire system is fiber-based. We designed and built an UMZI that manipulates the time-bins and enables us to perform a projective measurement on these superpositions, akin to a waveplate in a polarization state tomography. Finally, our cross-bar switch is essential for selecting narrow time-bins (≤ 100 ps) for the measurement process. These demonstrations open up avenues to further explore higher-dimensional Hilbert spaces.

CHAPTER 8

Conclusion and Future Work

We have developed, characterized, and demonstrated an all-optical switch with practical applications in QIP. Our switch was built upon a prior one-input, two-output design^[1-3]. The novelty of the switching demonstrated in this thesis includes the addition of a second circulator to enable two-input, two-output operation. This new geometry enables the switch to behave as unitary quantum gate. Additionally, we modified the switch design and pulse-generation electronics to enable high-rate switching.

In order to test such high rates, we designed and built an electrical synchronization setup that enables us to pulse-pick 100-ps-wide signals at rates up to 1.25 GHz. The rate can be tuned to any integer divider of 1.25 GHz between 2 and 32. Using this tunability, we have demonstrated pulse-picking, switching, and single-photon detection at 50-MHz and 250-MHz rates. Also, the pulse-picking electronics has been designed to select up to four consecutive pulses from a 10-GHz laser. In this fashion, we can test switching rates up to 10 GHz using detectors that operate at the slower rates (≤ 1.25 GHz).

Regarding the switch's performance, it exhibits an insertion loss of 2.3 dB. At the cost of potential experimental inconvenience, the loss can be further reduced by splicing most, if not all, connections between the individual components. By selecting the length of in-Sagnac optical fiber, we can determine the switching window, i. e., the duration during which switching is possible. This parameter limits the arrival rate of any signal we want to route. Given the current selection of O-band signal and C-band XPM pump, the switching

window width is defined by multiplying the in-Sagnac fiber length by 2.0 ps/m. We have shown a switching window as short as $\simeq 45$ ps, thereby implying that our switch can route signals that arrive at a rate > 20 GHz.

We also tested our switch's ability to transmit a polarization-entangled quantum state. The measured switching fidelity, which quantifies the comparison between the switched state and unswitched state, for our switch is $> 98\%$. This result verifies that any transmitted state does not experience much degradation due to active switching.

The ability to retain polarization-encoded information, and the high speed switching performance enables us to perform other tests. In one such test, we successfully recovered one channel from a two-temporal-channel quantum data stream, where the two channels were separated by 155 ps. Each channel contains a state with a measured fidelity to an arbitrary maximally entangled state $\simeq 97.5\%$. The measured fidelity between the states in these two channels was $1.8 \pm 1.0\%$, thereby indicating that they are nearly mutually orthogonal. When both channels were simultaneously present in the data stream, we measured a fidelity of $68.6 \pm 1.0\%$ to an arbitrary maximally entangled state. When we switch one channel out from the data stream, and measure the resulting state, it should be very similar to the unswitched state measured by itself. This recovered state has a fidelity of $96.2 \pm 1.2\%$ with the corresponding state. This spatio-temporal demonstration points to the utility of our switch as a high-speed routing device for polarization-encoded information, perhaps in a network setting with shared data transfer fibers.

In another application, we use the switch's high-speed spatio-temporal mapping functionality to perform projective measurements on time-bin-entangled states that exist in higher-dimensional Hilbert spaces. Each time-bin in these states is 100 ps wide. We have demonstrated the ability to measure states up to a dimensionality of four. Our best measured qubit

state has a fidelity to $|00\rangle + |11\rangle$ of $96.3 \pm 0.7\%$. For a qutrit state, we measured a fidelity to $|00\rangle + |11\rangle + |22\rangle$ of $85.7 \pm 0.8\%$. Given the aforementioned qubit fidelity, this measured qutrit fidelity is close to the expected qutrit fidelity of $\simeq 88\%$ obtained from simulations. Finally, we tried to generate and measure a ququat state. The resulting state has a fidelity of $64.9 \pm 0.5\%$ to the maximally entangled state $|00\rangle + |11\rangle + |22\rangle + |33\rangle$. The measured qubit, qutrit, and ququat linear entropies are $S_L(\hat{\rho}_2) = 0.076 \pm 0.019$, $S_L(\hat{\rho}_3) = 0.281 \pm 0.014$, and $S_L(\hat{\rho}_4) = 0.506 \pm 0.008$, respectively.

We hope that over the course of this dissertation, and punctuated by the summary of results above, we have convinced the reader of the merits of our cross-bar switch. Albeit, we recognize that there is always room for improvement. For instance, the required XPM pulse energy to obtain a π -phase shift for complete switching is $\simeq 2.6$ nJ, which is a lot of power. As such, in the next section, we look at potential tasks and directions to improve and build upon the work presented.

8.1. Future work

In this section, we will look at the future direction of the work demonstrated in this thesis. We divide the section into tasks for the near-term, medium-term, and long-term. In doing so, we hope to address various ideas we have to improve the current system, as well as ideas to improve the entire platform for switching and measurement to enable further exploration of QIP. We divide this section up based upon the timeline that we believe can affect change to improve our results.

8.1.1. Near term

Most of the changes for the near term are aimed at reducing the time required to obtain all the necessary measurements. Given the reasonably good results for qubit and qutrit states, we believe that long-term fluctuations in temperature (on the order of several hours) cause the fibers to move thereby changing the measured state. Also, such drifts can change the phase between superposed time-bins due to fiber shifts in the UMZI.

One way to diagnose if this type of drift is causing problems is to compare our measured ququat states with tomographic simulations. Unfortunately, we have not yet performed the corresponding tomographic simulations for such states. So an immediate task would be to complete these simulations.

Equipped with these simulation results, we can determine how good our measured ququat results actually are. Based on this, we can better determine the next steps. If we are near the predicted limit (as we are for qutrits), then we will attempt to improve each qubit measurement. If instead, there is a significant gap between the expected results and our measured results, we will need to improve the stability of all the subsystems for the longer durations required to collect all the data.

In addition to improving subsystem stability, we can improve the losses through the many components and connections. Reducing losses will improve our single-photon collection statistics. By improving the collection efficiency, we should be able to collect data faster thereby reducing the duration required to perform a complete measurement. In particular, we can reduce the losses through the UMZI and switch by splicing the individual components to one another.

Another near-term demonstration that we can perform is to reconfigure the electronics to pulse-pick at 250 MHz. We can then use the available Nucrypt CPDS-2000 detectors, clocked at 1.25 GHz, to repeat the aforementioned results at higher rates. Again, this enables us to reduce the data-collection time with the hope of avoiding the long-term drifts that corrupt our measured state.

Moving to the faster detectors will also warrant rewriting the data collection code. Given the need to write code, at this time, it may also make sense to investigate and potentially employ compressive sensing algorithms for quantum state reconstruction^[117]. Compressive sensing techniques offer a significant improvement on the required number of measurement settings for reconstructing pure states; such states are akin to the ones we generate. Yet again, this change can reduce the data collection time.

8.1.2. Intermediate term

In this section, we consider tasks that can improve the characteristics or performance of the higher-dimensional setup. Unlike most of the near term tasks, the suggestions that we posit here may require reconfiguring aspects of the experiment since they cannot immediately be realized. Additionally, they potentially add functionality or features that should be of interest as we explore higher-dimensional states further.

The first improvement would be to introduce a phase modulator upstream from the time-bin-entanglement source. Currently, if three FWM pump pulses generate the state $|00\rangle + |11\rangle + |22\rangle$, the addition of a phase modulator can produce slightly more exotic states of the form $|00\rangle + e^{i\phi_1} |11\rangle + e^{i\phi_2} |22\rangle$. In this fashion, we can create a variety of states and measure them. Such a state generator has potential applications for testing violations of Bell's inequalities or creating codewords for information transfer.

Assuming we have developed a system that is stable over the duration of days, and in the spirit of pushing the current system to its limits, another intermediate term project is to increase the dimensionality of the generated and measured states. Currently, we are limited by the number of splitters and combiners we use in the pulse-picking electronics. Inserting an additional layer of splitters and combiners to that setup can provide up to eight time-bins. Of course, increasing the system to that dimension requires the insertion of another motorized delay line in each UMZI and at each input of the cross-bar switch. This is because each delay line provides up to 560-ps adjustment, and we require more than 800 ps. Alternatively, we can consider other methods to obtain the required delays in a stable and reproducible manner. A final consideration to realize yet higher-dimensional states is the coherence time of the pulsed laser. Our current U2T laser exhibits $\simeq 50\%$ visibility between pulses that are separated by 1700 ps^[39]. As such, an eight-dimensional qudit may begin to push the limits of the desired coherence between pulses. As an aside, and motivated by this coherence concern, we also will want to model the effect of decoherence on the entanglement quality of our generated states.

Another potential improvement would entail replacing the input BS of the UMZI with a changeover switch, described in §6.1. The current setup requires us to discard half of our signal and idler photons after the WDMs. Using a low-loss, high-speed changeover switch obviates that issue because we simply route different time-bins to opposite arms and delay appropriately to obtain the desired superposition. As before, this increases our data collection statistics and therefore reduces the data collection time. Unfortunately, this is an intermediate term goal because it requires developing or purchasing additional components, such as EDFAs, amplitude modulators, and electronics. These components will be used to

drive the changeover switches as well as control the timing to ensure appropriate routing of the time-bins. This is a potentially expensive and time-consuming process.

Given that we have shown the ability to generate and measure higher-dimensional quantum states, one potential direction is to realize an experimental demonstration of one of the various motivating applications for such states. These applications include dense coding^[4] or increased robustness to noise and loss^[7] for information transfer. Such a demonstration will require building out the infrastructure to manipulate the quantum state for testing. Since we have the ability to generate and measure various degrees of dimensionality, we can provide a comparison study to verify the theoretical improvements by moving to higher dimensions.

8.1.3. Long term

The suggestions for the work described in this section are long-term in nature because each of them require significant time investment, and could potentially serve as a significant piece of someone's thesis work. They also present potential ways to improve the switching technology to combat the shortcomings of this design. Although inspired by the work presented in this thesis, the proposed projects will likely require a lot of redesigning and development to realize ideal goals of rapid switching and measurement of time-bin entangled states.

As mentioned earlier, the cross-bar switch has two main drawbacks: (1) it requires high XPM pulse energies to achieve complete switching, and (2) although it is compact, it is not very scalable. To tackle the first challenge, we propose further research into using more exotic fibers or materials in the Sagnac loop. These fibers will ideally have a higher $\chi^{(3)}$ and reduced cross-sectional area to increase the phase imparted due to the XPM process. Additional fiber engineering can provide control over the group velocity difference between the pump and signal to enable even shorter switching windows and therefore higher operating

speeds. Also, controlling the guided frequencies of the fiber can enable local applications of the switch at wavelengths with higher single-photon detection efficiencies. In short, there is a wealth of potential for exploring this switching geometry and mechanism by engineering the Sagnac fiber. This potential flexibility can enable catered uses of the switch for specific applications.

In order to address the second challenge, we propose moving this architecture to an integrated photonics platform. For instance, using integrated silicon waveguides can achieve the higher $\chi^{(3)}$ and smaller mode volumes. Also, building on the years of knowledge from the semiconductor industry, we can efficiently develop many such switches in a small confined space. Also, since these devices will likely be small, the propagating signal will accumulate less loss as it travels from device to device. One challenge for such a system is that, to the best of our knowledge, circulators do not yet exist for integrated photonics devices. Fortunately, we can employ a Mach-Zehnder interferometer geometry rather than the Sagnac geometry^[111]. Such a design is viable because in the integrated platform, we anticipate significantly less phase fluctuations, thus obviating the requirement of active stabilization.

Finally, motivated by my experience designing and building a real-time entangled photon polarimeter (see Appendix C), I believe that judicious application of our high-speed switches can enable us to perform fast time-bin quantum state tomographies. This is in lieu of the current polarization state tomographies. Of course, realizing this requires reconsidering the UMZI since we no longer need the PBS at the output. This implies that we need to determine another method to create the temporal superpositions with variable phase. The phase tunability will likely require many additional phase modulators, and the appropriate driving electronics. Since we also anticipate many switches to route the appropriate superposed

signals to the desired detectors, we feel that such an experiment would benefit greatly from an integrated photonics setup with computer controlled devices.

Hopefully, we have sufficiently excited the reader regarding the potential improvements for our all-optical, low-loss, high-speed, cross-bar switch with an eye to the long-term developments that can enable significant advances in the field of QIP.

References

- [1] Hall, M. A., Altepeter, J. B., & Kumar, P. *Ultrafast switching of photonic entanglement*. Physical Review Letters, **106**(5):053901, 2011.
- [2] Hall, M. A., Altepeter, J. B., & Kumar, P. *All-optical switching of photonic entanglement*. New Journal of Physics, **13**(10):105,004, 2011.
- [3] Hall, Matthew A. *Network Technologies for O-Band Quantum Telecommunications*. Ph.D. thesis, Northwestern University, Evanston, IL, 2010.
- [4] Barreiro, Julio T, Wei, Tzu-Chieh, & Kwiat, Paul G. *Beating the channel capacity limit for linear photonic superdense coding*. Nature physics, **4**(4):282–286, 2008.
- [5] Vértesi, Tamás, Pironio, Stefano, & Brunner, Nicolas. *Closing the detection loophole in bell experiments using qudits*. Physical review letters, **104**(6):060,401, 2010.
- [6] Lanyon, Benjamin P, Barbieri, Marco, Almeida, Marcelo P, Jennewein, Thomas, Ralph, Timothy C, Resch, Kevin J, Pryde, Geoff J, O'Brien, Jeremy L, Gilchrist, Alexei, & White, Andrew G. *Simplifying quantum logic using higher-dimensional hilbert spaces*. Nature Physics, **5**(2):134–140, 2008.
- [7] Gröblacher, Simon, Jennewein, Thomas, Vaziri, Alipasha, Weihs, Gregor, & Zeilinger, Anton. *Experimental quantum cryptography with qutrits*. New Journal of Physics, **8**(5):75, 2006.
- [8] Shor, P. W. *Polynomial-time algorithms for prime factorization and discrete logarithms on a quantum computer*. SIAM Review, **41**:303–332, 1999.

- [9] Grover, Lov K. *Quantum mechanics helps in searching for a needle in a haystack.* Phys. Rev. Lett., **79**:325–328, 1997.
- [10] Bennett, C. H. & Brassard, G. *Quantum cryptography: Public key distribution and coin tossing.* In *IEEE International Conference on Computers, Systems, and Signal Processing*, p. 175. IEEE, 1984. Bangalore.
- [11] Ekert, Artur K. *Quantum cryptography based on bell's theorem.* Phys. Rev. Lett., **67**:661–663, 1991.
- [12] Vandersypen, L. M. K., Steffen, M., Breyta, G., Yannoni, C. S., Sherwood, M. H., & Chuang, I. L. *Experimental realization of shor's quantum factoring algorithm using nuclear magnetic resonance.* Nature, **414**:883–887, 2001.
- [13] Jones, Jonathan A. *Quantum computing with nmr.* Progress in nuclear magnetic resonance spectroscopy, **59**(2):91–120, 2011.
- [14] Pu, H. & Meystre, P. *Creating macroscopic atomic Einstein-Podolsky-Rosen States from Bose-Einstein Condensates.* Phys. Rev. Lett., **85**(19):3987–3990, 2000.
- [15] Byrnes, Tim, Wen, Kai, & Yamamoto, Yoshihisa. *Macroscopic quantum computation using bose-einstein condensates.* Phys. Rev. A, **85**:040,306, 2012.
- [16] You, L. & Chapman, M. S. *Quantum entanglement using trapped atomic spins.* Phys. Rev. A, **62**(5):052,302–052,307, 2000.
- [17] Tiecke, TG, Thompson, JD, de Leon, NP, Liu, LR, Vuletić, V, & Lukin, MD. *Nanophotonic quantum phase switch with a single atom.* Nature, **508**(7495):241–244, 2014.
- [18] Goban, A, Hung, C-L, Yu, S-P, Hood, JD, Muniz, JA, Lee, JH, Martin, MJ, McClung, AC, Choi, KS, Chang, DE et al. *Atom-light interactions in photonic crystals.* Nature communications, **5**, 2014.

- [19] Miniatura, C, Kwek, L-C, Ducloy, M, Gremaud, B, Englert, B-G, Cugliandolo, L, Ekert, A, & Phua, KK. *Ultracold Gases and Quantum Information: Lecture Notes of the Les Houches Summer School in Singapore: Volume 91, July 2009*. Oxford University Press, 2011.
- [20] Loss, Daniel & DiVincenzo, David. *Quantum computation with quantum dots*. Phys. Rev. A, **57**:120–126, 1998.
- [21] Eriksson, Mark A, Friesen, Mark, Coppersmith, Susan N, Joynt, Robert, Klein, Lev-ente J, Slinker, Keith, Tahan, Charles, Mooney, PM, Chu, JO, & Koester, SJ. *Spin-based quantum dot quantum computing in silicon*. In *Experimental Aspects of Quantum Computing*, pp. 133–146. Springer, 2005.
- [22] Barends, R, Kelly, J, Megrant, A, Veitia, A, Sank, D, Jeffrey, E, White, TC, Mutus, J, Fowler, AG, Campbell, B, Chen, Y, Chen, Z, Chiaro, B, Dunsworth, A, Neill, C, O’Malley, P, Roushan, P, Vainsencher, A, Wenner, J, Korotkov, AN, Cleland, AN, & Martinis, JM. *Superconducting quantum circuits at the surface code threshold for fault tolerance*. Nature, **508**(7497):500–503, 2014.
- [23] Devoret, MH & Schoelkopf, RJ. *Superconducting circuits for quantum information: an outlook*. Science, **339**(6124):1169–1174, 2013.
- [24] Nemoto, Kae, Trupke, Michael, Devitt, Simon J., Stephens, Ashley M., Scharfenberger, Burkhard, Buczak, Kathrin, Nöbauer, Tobias, Everitt, Mark S., Schmiedmayer, Jörg, & Munro, William J. *Photonic architecture for scalable quantum information processing in diamond*. Phys. Rev. X, **4**:031,022, 2014.
- [25] Ohlsson, Nicklas, Krishna Mohan, R, & Kröll, Stefan. *Quantum computer hardware based on rare-earth-ion-doped inorganic crystals*. Optics communications, **201**(1):71–77, 2002.

- [26] O’Brien, J. L. *Optical quantum computing*. Science, **318**:1567, 2007.
- [27] Knill, E., Laflamme, R., & Milburn, G. J. *A scheme for efficient quantum computation with linear optics*. Nature, **409**:46–52, 2001.
- [28] Sangouard, Nicolas, Simon, Christoph, de Riedmatten, Hugues, & Gisin, Nicolas. *Quantum repeaters based on atomic ensembles and linear optics*. Rev. Mod. Phys., **83**:33–80, 2011.
- [29] Lanting, T, Przybysz, AJ, Smirnov, A Yu, Spedalieri, FM, Amin, MH, Berkley, AJ, Harris, R, Altomare, F, Boixo, S, Bunyk, P et al. *Entanglement in a quantum annealing processor*. Physical Review X, **4**(2):021,041, 2014.
- [30] Rnnow, Troels F., Wang, Zhihui, Job, Joshua, Boixo, Sergio, Isakov, Sergei V., Wecker, David, Martinis, John M., Lidar, Daniel A., & Troyer, Matthias. *Defining and detecting quantum speedup*. Science, **345**(6195):420–424, 2014.
- [31] Cho, Adrian. *Quantum or not, controversial computer yields no speedup*. Science, **344**(6190):1330–1331, 2014.
- [32] Einstein, A., Podolsky, B., & Rosen, N. *Can quantum-mechanical description of physical reality be considered complete?* Phys. Rev., **47**(10):777–780, 1935.
- [33] Bell, John S. *On the einstein-podolsky-rosen paradox*. Physics, **1**(3):195–200, 1964.
- [34] Lanyon, B., Weinhold, T., Langford, N., Barbieri, M., James, D., Gilchrist, A., & White, A. *Experimental demonstration of a compiled version of shor’s algorithm with quantum entanglement*. Phys. Rev. Lett., **99**:250,505, 2007.
- [35] Bouwmeester, Dik, Pan, Jian-Wei, Mattle, Klaus, Eibl, Manfred, Weinfurter, Harald, & Zeilinger, Anton. *Experimental quantum teleportation*. Nature, **390**(6660):575–579, 1997.

- [36] Krauter, H, Salart, D, Muschik, CA, Petersen, Jonas Meyer, Shen, Heng, Fernholz, Thomas, & Polzik, Eugene Simon. *Deterministic quantum teleportation between distant atomic objects*. Nature Physics, **9**(7):400–404, 2013.
- [37] Hall, Matthew A., Altepeter, Joseph B., & Kumar, Prem. *Drop-in compatible entanglement for optical-fiber networks*. Opt. Express, **17**(17):14,558–14,566, 2009.
- [38] Medic, M., Altepeter, J. B., Hall, M. A., Patel, M., & Kumar, P. *Fiber-based telecommunications-band source of degenerate entangled photons*. Optics Letters, **35**(6):802–804, 2010.
- [39] Patel, Monika. *Indistinguishable Photon Sources Sources for Practical Quantum Communication*. Ph.D. thesis, Northwestern University, Evanston, IL, 2011.
- [40] Patel, Monika, Altepeter, Joseph B, Huang, Yu-Ping, Oza, Neal N, & Kumar, Prem. *Independent telecom-fiber sources of quantum indistinguishable single photons*. New Journal of Physics, **16**(4):043,019, 2014.
- [41] Patel, Monika, Altepeter, Joseph B, Huang, Yu-Ping, Oza, Neal N, & Kumar, Prem. *Erasing quantum distinguishability via single-mode filtering*. Physical Review A, **86**(3):033,809, 2012.
- [42] Takesue, Hiroki & Inoue, Kyo. *Generation of polarization-entangled photon pairs and violation of Bell’s inequality using spontaneous four-wave mixing in a fiber loop*. Phys. Rev. A, **70**(3):031,802, 2004.
- [43] Takesue, Hiroki & Inoue, Kyo. *Generation of 1.5 – μm band time-bin entanglement using spontaneous fiber four-wave mixing and planar light-wave circuit interferometers*. Phys. Rev. A, **72**(4):041,804, 2005.
- [44] Takesue, Hiroki. *Long-distance distribution of time-bin entanglement generated in a cooled fiber*. Opt. Express, **14**(8):3453–3460, 2006.

- [45] Agrawal, Govind P. *Nonlinear Fiber Optics*. Elsevier, fourth edition, 2007.
- [46] Lin, Q., Yaman, F., & Agrawal, Govind P. *Photon-pair generation in optical fibers through four-wave mixing: Role of Raman scattering and pump polarization*. Physical Review A (Atomic, Molecular, and Optical Physics), **75**(2):023803, 2007.
- [47] Werner, Reinhard F. *Quantum states with einstein-podolsky-rosen correlations admitting a hidden-variable model*. Physical Review A, **40**(8):4277, 1989.
- [48] Thew, RT, Nemoto, Kae, White, Andrew G, & Munro, William J. *Qudit quantum-state tomography*. Physical Review A, **66**(1):012,303, 2002.
- [49] Altepeter, Joseph B. *Testing the Limits of Nonlocality*. Ph.D. thesis, University of Illinois at Urbana-Champaign, Urbana, IL, 2006.
- [50] Collins, Daniel, Gisin, Nicolas, Linden, Noah, Massar, Serge, & Popescu, Sandu. *Bell inequalities for arbitrarily high-dimensional systems*. Physical review letters, **88**(4):040,404, 2002.
- [51] Jozsa, R. *Fidelity for mixed quantum states*. Journal of Modern Optics, **41**:2315–2323, 1994.
- [52] White, A. G., James, D. F. V., Eberhard, P. H., & Kwiat, P. G. *Nonmaximally entangled states: Production, characterization, and utilization*. Physical Review Letters, **83**:3103–3107, 1999.
- [53] Coffman, V., Kundu, J., & Wootters, W. K. *Distributed entanglement*. Phys. Rev. A, **61**(5):052306, 2000.
- [54] Silva, Marcus, Rötteler, Martin, & Zalka, Christof. *Thresholds for linear optics quantum computing with photon loss at the detectors*. Phys. Rev. A, **72**:032,307, 2005.
- [55] Ralph, T. C., Hayes, A. J. F., & Gilchrist, Alexei. *Loss-tolerant optical qubits*. Phys. Rev. Lett., **95**:100,501, 2005.

- [56] Ironside, CN, Aitchison, JS, & Arnold, JM. *An all-optical switch employing the cascaded second-order nonlinear effect*. Quantum Electronics, IEEE Journal of, **29**(10):2650–2654, 1993.
- [57] Langrock, Carsten, Kumar, Saurabh, McGeehan, John E, Willner, AE, & Fejer, MM. *All-optical signal processing using $\chi^{(2)}$ nonlinearities in guided-wave devices*. Light-wave Technology, Journal of, **24**(7):2579–2592, 2006.
- [58] Wooten, Ed L, Kissa, Karl M, Yi-Yan, Alfredo, Murphy, Edmond J, Lafaw, Donald A, Hallemeier, Peter F, Maack, David, Attanasio, Daniel V, Fritz, Daniel J, McBrien, Gregory J et al. *A review of lithium niobate modulators for fiber-optic communications systems*. Selected Topics in Quantum Electronics, IEEE Journal of, **6**(1):69–82, 2000.
- [59] McCusker, Kevin T, Huang, Yu-Ping, Kowligy, Abijith S, & Kumar, Prem. *Experimental demonstration of interaction-free all-optical switching via the quantum zeno effect*. Physical Review Letters, **110**(24):240,403, 2013.
- [60] Bajcsy, M, Hofferberth, Sebastian, Balic, V, Peyronel, T, Hafezi, Mohammad, Zibrov, Alexander S, Vuletic, V, & Lukin, Mikhail D. *Efficient all-optical switching using slow light within a hollow fiber*. Physical review letters, **102**(20):203,902, 2009.
- [61] Lenihan, A.S., Salem, R., Murphy, T.E., & Carter, G.M. *All-optical 80-Gb/s time-division demultiplexing using polarization-insensitive cross-phase modulation in photonic crystal fiber*. Photonics Technology Letters, IEEE, **18**(12):1329–1331, 2006.
- [62] Betlej, A, Suntsov, S, Makris, KG, Jankovic, L, Christodoulides, DN, Stegeman, GI, Fini, J, Bise, RT, & DiGiovanni, DJ. *All-optical switching and multifrequency generation in a dual-core photonic crystal fiber*. Optics letters, **31**(10):1480–1482, 2006.

- [63] Belotti, Michele, Galli, Matteo, Gerace, Dario, Andreani, Lucio C, Guizzetti, Giorgio, Md Zain, Ahmad R, Johnson, Nigel P, Sorel, Marc, & De La Rue, Richard M. *All-optical switching in silicon-on-insulator photonic wire nano-cavities*. Optics express, **18**(2):1450–1461, 2010.
- [64] Almeida, Vilson R, Barrios, Carlos A, Panepucci, Roberto R, & Lipson, Michal. *All-optical control of light on a silicon chip*. Nature, **431**(7012):1081–1084, 2004.
- [65] Boyraz, Özdal, Koonath, Prakash, Raghunathan, Varun, & Jalali, Bahram. *All optical switching and continuum generation in silicon waveguides*. Optics Express, **12**(17):4094–4102, 2004.
- [66] Haché, Alain & Bourgeois, Martin. *Ultrafast all-optical switching in a silicon-based photonic crystal*. Applied Physics Letters, **77**(25):4089–4091, 2000.
- [67] Tanabe, Takasumi, Notomi, Masaya, Mitsugi, Satoshi, Shinya, Akihiko, & Kuramochi, Eiichi. *All-optical switches on a silicon chip realized using photonic crystal nanocavities*. Applied Physics Letters, **87**(15):151,112, 2005.
- [68] Dawes, Andrew MC, Illing, Lucas, Clark, Susan M, & Gauthier, Daniel J. *All-optical switching in rubidium vapor*. Science, **308**(5722):672–674, 2005.
- [69] Chen, Wenlan, Beck, Kristin M, Bücker, Robert, Gullans, Michael, Lukin, Mikhail D, Tanji-Suzuki, Haruka, & Vuletić, Vladan. *All-optical switch and transistor gated by one stored photon*. Science, **341**(6147):768–770, 2013.
- [70] Hogari, K. & Matsumoto, T. *Electrostatically driven fiber-optic micromechanical on/off switch and its application to subscriber transmission systems*. Lightwave Technology, Journal of, **8**(5):722–727, 1990.
- [71] De Dobbelaere, P., Falta, K., Gloeckner, S., & Patra, S. *Digital MEMS for optical switching*. Communications Magazine, IEEE, **40**(3):88–95, 2002.

- [72] Ji, Chang-Hyeon, Yee, Youngjoo, Choi, Junghoon, Kim, Seong-Hyok, & Bu, Jong-Uk. *Electromagnetic 22 MEMS optical switch*. Selected Topics in Quantum Electronics, IEEE Journal of, **10**(3):545–550, 2004.
- [73] Bernstein, J.J., Taylor, W.P., Brazzle, J.D., Corcoran, C.J., Kirkos, G., Odhner, J.E., Pareek, A., Waelti, M., & Zai, M. *Electromagnetically actuated mirror arrays for use in 3-D optical switching applications*. Microelectromechanical Systems, Journal of, **13**(3):526–535, 2004.
- [74] dAlessandro, Antonio. *Acousto-optic switching*. In *Optical Switching*, pp. 83–109. Springer, 2006.
- [75] Verhagen, Ewold, Deleglise, Samuel, Weis, Stefan, Schliesser, Albert, & Kippenberg, Tobias J. *Cavity quantum optomechanics: Coupling light and micromechanical oscillators*. In *Micro Electro Mechanical Systems (MEMS), 2014 IEEE 27th International Conference on*, pp. 140–142. IEEE, 2014.
- [76] Huo, Juan, Liu, Kun, & Chen, Xianfeng. *1×2 precise electro-optic switch in periodically poled lithium niobate*. Optics express, **18**(15):15,603–15,608, 2010.
- [77] Wang, Qing & Yao, Jianping. *A high speed 2×2 electro-optic switch using a polarization modulator*. Optics express, **15**(25):16,500–16,505, 2007.
- [78] Ye, Qing, Qiao, Lei, Gan, Jiulin, Cai, Haiwen, & Qu, Ronghui. *Fiber sagnac π -shifted interferometer for a polarization-independent pmnt high-speed electro-optic switch*. Optics letters, **35**(24):4187–4189, 2010.
- [79] Metcalf, Benjamin J, Spring, Justin B, Humphreys, Peter C, Thomas-Peter, Nicholas, Barbieri, Marco, Kolthammer, W Steven, Jin, Xian-Min, Langford, Nathan K, Kundys, Dmytro, Gates, James C et al. *Quantum teleportation on a photonic chip*. Nature Photonics, **8**(10):770–774, 2014.

- [80] Kimble, H.J. *The quantum internet*. Nature, **453**(7198):1023–1030, 2008.
- [81] Salem, R., Lenihan, A.S., Carter, G.M., & Murphy, T.E. *160-Gb/s polarization-independent optical demultiplexing in 2-m nonlinear fiber*. Photonics Technology Letters, IEEE, **18**(21):2245–2247, 2006.
- [82] Volz, Thomas, Reinhard, Andreas, Winger, Martin, Badolato, Antonio, Hennessy, Kevin J, Hu, Evelyn L, & Imamoglu, Ataç. *Ultrafast all-optical switching by single photons*. Nature Photonics, **6**(9):605–609, 2012.
- [83] Yoshiki, Wataru & Tanabe, Takasumi. *All-optical switching using kerr effect in a silica toroid microcavity*. Optics express, **22**(20):24,332–24,341, 2014.
- [84] Pelc, Jason S, Rivoire, Kelley, Vo, Sonny, Santori, Charles, Fattal, David A, & Beausoleil, Raymond G. *Picosecond all-optical switching in hydrogenated amorphous silicon microring resonators*. Optics express, **22**(4):3797–3810, 2014.
- [85] Doran, N. J. & Wood, David. *Nonlinear-optical loop mirror*. Opt. Lett., **13**(1):56–58, 1988.
- [86] Blow, K. J., Doran, N. J., Nayar, B. K., & Nelson, B. P. *Two-wavelength operation of the nonlinear fiber loop mirror*. Opt. Lett., **15**(4):248–250, 1990.
- [87] Sakamoto, T., Lim, Han Chuen, & Kikuchi, K. *All-optical polarization-insensitive time-division demultiplexer using a nonlinear optical loop mirror with a pair of short polarization-maintaining fibers*. Photonics Technology Letters, IEEE, **14**(12):1737–1739, 2002.
- [88] Lim, Han Chuen, Sakamoto, T., & Kikuchi, K. *Polarization-independent optical demultiplexing by conventional nonlinear optical loop mirror in a polarization-diversity loop configuration*. Photonics Technology Letters, IEEE, **12**(12):1704–1706, 2000.

- [89] Bülow, H. & Veith, G. *Polarisation-independent switching in a nonlinear optical loop mirror by a dual-wavelength switching pulse*. Electronics Letters, **29**(7):588–589, 1993.
- [90] Krenn, Mario, Huber, Marcus, Fickler, Robert, Lapkiewicz, Radek, Ramelow, Sven, & Zeilinger, Anton. *Generation and confirmation of a (100×100) -dimensional entangled quantum system*. Proceedings of the National Academy of Sciences, **111**(17):6243–6247, 2014.
- [91] Pors, Bart-Jan, Miatto, Filippo, Eliel, ER, Woerdman, JP et al. *High-dimensional entanglement with orbital-angular-momentum states of light*. Journal of Optics, **13**(6):064,008, 2011.
- [92] Molina-Terriza, Gabriel, Torres, Juan P, & Torner, Lluís. *Twisted photons*. Nature Physics, **3**(5):305–310, 2007.
- [93] Richart, D, Fischer, Y, & Weinfurter, H. *Experimental implementation of higher dimensional time–energy entanglement*. Applied Physics B, **106**(3):543–550, 2012.
- [94] Mower, Jacob, Zhang, Zheshen, Desjardins, Pierre, Lee, Catherine, Shapiro, Jeffrey, & Englund, Dirk. *High-dimensional quantum key distribution using dispersive optics*. Phys. Rev. A, **87**:062,322, 2013.
- [95] Lee, Catherine, Zhang, Zheshen, Mower, Jacob C, Steinbrecher, Greg, Zhou, Hongchao, Wang, Ligong, Horansky, Robert, Verma, Varun B, Allman, Michael, Lita, Adriana et al. *High-dimensional time-energy entanglement-based quantum key distribution using dispersive optics*. In *CLEO: QELS_Fundamental Science*, pp. FM4A–3. Optical Society of America, 2014.
- [96] Broadbent, Curtis J. *Applications of High-Dimensional Photonic Entanglement*. Ph.D. thesis, University of Rochester, Rochester, NY, 2010.

- [97] Nisbet-Jones, Peter BR, Dilley, Jerome, Holleczek, Annemarie, Barter, Oliver, & Kuhn, Axel. *Photonic qubits, qutrits and ququads accurately prepared and delivered on demand*. New Journal of Physics, **15**(5):053,007, 2013.
- [98] Donohue, John, Agnew, Megan, Lavoie, Jonathan, & Resch, Kevin. *Coherent ultrafast measurement of time-bin encoded photons*. Phys. Rev. Lett., **111**:153,602, 2013.
- [99] Wang, S., Chan, C., Moraw, P., Reilly, D., Altepeter, J., & Kanter, G. *High-speed tomography of time-bin-entangled photons using a single-measurement setting*. Phys. Rev. A, **86**:042,122, 2012.
- [100] Barreiro, Julio, Langford, Nathan, Peters, Nicholas, & Kwiat, Paul. *Generation of hyperentangled photon pairs*. Phys. Rev. Lett., **95**:260,501, 2005.
- [101] Graham, T., Barreiro, J., Mohseni, M., & Kwiat, P. *Hyperentanglement-enabled direct characterization of quantum dynamics*. Phys. Rev. Lett., **110**:060,404, 2013.
- [102] Gauthier, Daniel, Guilbert, Hannah, Zhu, Yunhui, Shi, Meizhen, McCusker, Kevin, Christensen, Bradley, Kwiat, Paul, Brougham, Thomas, Barnett, Stephen M, & Chandar, Venkat. *Quantum key distribution using hyperentanglement*. In *Quantum Information and Measurement*, pp. QT4A–2. Optical Society of America, 2012.
- [103] Yan, Hui, Zhang, Shanchao, Chen, J., Loy, M., Wong, G., & Du, Shengwang. *Generation of narrow-band hyperentangled nondegenerate paired photons*. Phys. Rev. Lett., **106**:033,601, 2011.
- [104] Liu, Kui, Guo, Jun, Cai, Chunxiao, Guo, Shuaifeng, & Gao, Jiangrui. *Experimental generation of continuous-variable hyperentanglement in an optical parametric oscillator*. Phys. Rev. Lett., **113**:170,501, 2014.
- [105] Gisin, Nicolas, Ribordy, Grégoire, Tittel, Wolfgang, & Zbinden, Hugo. *Quantum cryptography*. Rev. Mod. Phys., **74**(1):145–195, 2002.

- [106] Scarani, Valerio, Bechmann-Pasquinucci, Helle, Cerf, Nicolas J, Dušek, Miloslav, Lütkenhaus, Norbert, & Peev, Momtchil. *The security of practical quantum key distribution*. Reviews of modern physics, **81**(3):1301, 2009.
- [107] Pan, Jian-Wei, Chen, Zeng-Bing, Lu, Chao-Yang, Weinfurter, Harald, Zeilinger, Anton, & Żukowski, Marek. *Multiphoton entanglement and interferometry*. Reviews of Modern Physics, **84**(2):777, 2012.
- [108] Migdall, A. L., Branning, D., & Castelletto, S. *Tailoring single-photon and multiphoton probabilities of a single-photon on-demand source*. Phys. Rev. A, **66**(5):053,805, 2002.
- [109] Castelletto, SA, Degiovanni, IP, Schettini, V, & Migdall, AL. *Reduced deadtime and higher rate photon-counting detection using a multiplexed detector array*. Journal of Modern Optics, **54**(2-3):337–352, 2007.
- [110] Mortimore, D.B. *Fiber loop reflectors*. Lightwave Technology, Journal of, **6**(7):1217–1224, 1988.
- [111] Rambo, Timothy M, McCusker, Kevin, Huang, Yu-Ping, & Kumar, Prem. *Low-loss all-optical quantum switching*. In *Photonics Society Summer Topical Meeting Series, 2013 IEEE*, pp. 179–180. IEEE, 2013.
- [112] Huang, Yu-Ping & Kumar, Prem. *Quantum theory of all-optical switching in nonlinear sagnac interferometers*. New Journal of Physics, **14**(5):053,038, 2012.
- [113] Durt, Thomas, Cerf, Nicolas, Gisin, Nicolas, & Żukowski, Marek. *Security of quantum key distribution with entangled qutrits*. Phys. Rev. A, **67**:012,311, 2003.
- [114] James, Daniel FV, Kwiat, Paul G, Munro, William J, & White, Andrew G. *Measurement of qubits*. Physical Review A, **64**(5):052,312, 2001.
- [115] Altepeter, Joseph B, Jeffrey, Evan R, & Kwiat, Paul G. *Photonic state tomography*. Advances in Atomic, Molecular, and Optical Physics, **52**:105–159, 2005.

- [116] Kaznady, Max S & James, Daniel FV. *Numerical strategies for quantum tomography: Alternatives to full optimization*. Physical Review A, **79**(2):022,109, 2009.
- [117] Gross, David, Liu, Yi-Kai, Flammia, Steven T, Becker, Stephen, & Eisert, Jens. *Quantum state tomography via compressed sensing*. Physical review letters, **105**(15):150,401, 2010.
- [118] Nielsen, Michael A. & Chuang, Isaac L. *Quantum Computation and Quantum Information*. Cambridge University Press, 2000.
- [119] Kwiat, Paul G., Mattle, Klaus, Weinfurter, Harald, Zeilinger, Anton, Sergienko, Alexander V., & Shih, Yanhua. *New high-intensity source of polarization-entangled photon pairs*. Phys. Rev. Lett., **75**(24):4337–4341, 1995.
- [120] Altepeter, J.B., Jeffrey, E.R., & Kwiat, P.G. *Phase-compensated ultra-bright source of entangled photons*. Opt. Express, **13**(22):8951–8959, 2005.
- [121] Peng, Cheng-Zhi, Yang, Tao, Bao, Xiao-Hui, Zhang, Jun, Jin, Xian-Min, Feng, Fa-Yong, Yang, Bin, Yang, Jian, Yin, Juan, Zhang, Qiang et al. *Experimental free-space distribution of entangled photon pairs over 13 km: towards satellite-based global quantum communication*. Physical review letters, **94**(15):150,501, 2005.
- [122] Aspelmeyer, Markus, Böhm, Hannes R, Gyatso, Tsewang, Jennewein, Thomas, Kaltenbaek, Rainer, Lindenthal, Michael, Molina-Terriza, Gabriel, Poppe, Andreas, Resch, Kevin, Taraba, Michael et al. *Long-distance free-space distribution of quantum entanglement*. science, **301**(5633):621–623, 2003.
- [123] Li, Xiaoying, Voss, Paul L., Sharping, Jay E., & Kumar, Prem. *Optical-fiber source of polarization-entangled photons in the 1550 nm telecom band*. Phys. Rev. Lett., **94**(5):053,601, 2005.

- [124] Fan, J., Eisaman, M. D., & Migdall, A. *Bright phase-stable broadband fiber-based source of polarization-entangled photon pairs*. Physical Review A (Atomic, Molecular, and Optical Physics), **76**(4):043836, 2007.
- [125] Takesue, Hiroki, Fukuda, Hiroshi, Tsuchizawa, Tai, Watanabe, Toshifumi, Yamada, Koji, Tokura, Yasuhiro, & Itabashi, Sei-ichi. *Generation of polarization entangled photon pairs using silicon wire waveguide*. Optics express, **16**(8):5721–5727, 2008.
- [126] Altepeter, Joseph B., Jeffrey, Evan R., Medic, Milja, & Kumar, Prem. *Multiple-qubit quantum state visualization*. In *Conference on Lasers and Electro-Optics/International Quantum Electronics Conference*, p. IWC1. Optical Society of America, 2009.
- [127] Altepeter, Joseph B, Oza, Neal N, Medić, Milja, Jeffrey, Evan R, & Kumar, Prem. *Entangled photon polarimetry*. Optics express, **19**(27):26,011–26,016, 2011.
- [128] van Haasteren, Arjan JP, van der Tol, Jos JGM, van Deventer, M Oskar, & Frankena, Hans J. *Modeling and characterization of an electrooptic polarization controller on linbo 3*. Lightwave Technology, Journal of, **11**(7):1151–1157, 1993.
- [129] Feynman, Richard P, Leighton, Robert B, & Sands, Matthew. *Lectures on Physics, vol. III*. Addison-Wesley Reading, Mass., 1971.
- [130] Kaye, Phillip, Laflamme, Raymond, & Mosca, Michele. *An introduction to quantum computing*. Oxford University Press Inc., NY, 2007.
- [131] Wikipedia. *Bracket notation—wikipedia, the free encyclopedia*, 2014. [Online; accessed 22-November-2014].
- [132] Wikipedia. *Linear algebra—wikipedia, the free encyclopedia*, 2014. [Online; accessed 22-November-2014].
- [133] Wikipedia. *Hilbert space—wikipedia, the free encyclopedia*, 2014. [Online; accessed 22-November-2014].

APPENDIX A

Dark-Count Subtraction Calculations

In this appendix, we will show how to perform dark-count subtraction for our coincidence (§A.1) and accidental (§A.2) measurements. We base this calculation from an internal document, written by Kim Fook Lee, explaining how he calculated these values for previous experiments done in our lab. Here, we make modifications to account for detection events, i. e., detector trigger gates, instead of measurement integration time.

For this appendix, we assume we have two detectors labelled x and y . Since most of the variable definitions are symmetric for these two detectors, we will occasionally use the subscript z where $z \in \{x, y\}$. We start by defining the single counts measured on these two detectors as S_x and S_y , respectively. We can rewrite each of these as

$$\begin{aligned} S_x &= L_x + D_x \\ S_y &= L_y + D_y, \end{aligned} \tag{A.1}$$

where L_z are “light” counts from FWM or Raman photons, and D_z are dark counts from the detectors. Experimentally, the single counts are measured results, i. e., an input to these calculations. Similarly, we measure our coincidence counts ($C_{x,y}$) between the two detectors. In other words, for every pair of detectors, we must measure five quantities: S_x, S_y, D_x, D_y , and $C_{x,y}$. Additionally, for reasons we discuss later, we must also know the number of gates (detection events) possible, which we label g .

A.1. Dark-count-subtracted coincidences

Since a coincidence is any event where both detectors fire simultaneously, it should be straightforward to see that

$$C_{x,y} = C(S_x, S_y) = C(L_x, L_y) + C(L_x, D_y) + C(D_x, L_y) + C(D_x, D_y), \quad (\text{A.2})$$

where $C(a, b)$ is a function that returns the coincidences due to a and b . The first term of the right hand side corresponds to each detector firing due to their respective light photons. The second and third terms correspond to one detector firing due a light photon, while the other detectors fires due to a dark count. The last term is then due to each detector simultaneously registering a dark count.

Assuming we cool the fiber to minimize Raman photons, if we want our true coincidences from FWM photons, then we need to solve for $C(L_x, L_y)$. We remark here that we cannot measure the light counts L_z directly. Instead, we recognize the following relations, and substitute them in instead:

$$\begin{aligned} C(L_x, D_y) &= C(S_x, D_y) - C(D_x, D_y) \\ C(D_x, L_y) &= C(D_x, S_y) - C(D_x, D_y). \end{aligned} \quad (\text{A.3})$$

Using these relations, and doing trivial algebraic gymnastics, we obtain

$$\tilde{C}_{x,y} = C(L_x, L_y) = C_{x,y} - C(S_x, D_y) - C(D_x, S_y) + C(D_x, D_y) \quad (\text{A.4})$$

Here, the tilde above the left-side term denotes that it is a dark-count-subtracted quantity.

We will use this notation through the remainder of this chapter.

Now that we have this equation, we must determine how to calculate the actual counts for $C(a, b)$. In order to do this, we recognize that the probability of a coincidence is merely the product of the independent probabilities that detectors x and y fire. Mathematically, we express this probability as

$$P(a \cap b) = P(a) \times P(b). \quad (\text{A.5})$$

Since these values are the probability per detection event, we can determine the expected number of coincidence counts by multiplying $P(a \cap b)$ and the number of detection events. For our experiments, we typically use the number of detection gates, g , to represent the latter value. So, we can write the following equation to solve for the number of coincidences due to events a and b :

$$C(a, b) = g \cdot P(a \cap b). \quad (\text{A.6})$$

As a reminder, a and b represent a specific event happening, such as registering a dark count on detector x . Thus, using the measured counts for event a , we can determine the probability $P(a)$ by dividing the measured counts by the total duration of the measurement. For example, if we want to know the probability of a dark count on detector x over g detection events, then we simply solve $P(D_x) = D_x/g$. Based on this relation, and by combining Eq. (A.5) and Eq. (A.6), we obtain the equation

$$C(a, b) = \frac{a \cdot b}{g}. \quad (\text{A.7})$$

Substituting this into Eq. (A.4) yields

$$\tilde{C}_{x,y} = C_{x,y} - \frac{1}{g}(S_x D_y - D_x S_y + D_x D_y), \quad (\text{A.8})$$

where, to summarize, the first term on the left-hand side represents the measured coincidence counts, and the second term—all in the parentheses—represents statistically calculated accidental counts from measured events.

A.2. Calculated and dark-count-subtracted accidentals

When calculating accidentals, the process is very similar. Using the probabilistic derivations above, we can calculate accidentals in one of two ways. First, is the non-dark-count-subtracted method. The calculation for this is

$$A_{x,y} = \frac{S_x S_y}{g}. \quad (\text{A.9})$$

If we wish to calculate dark-count-subtracted accidentals, then we can use

$$\begin{aligned} \tilde{A}_{x,y} &= \frac{L_x L_y}{g} = \frac{(S_x - D_x)(S_y - D_y)}{g} \\ &= \frac{1}{g}(S_x S_y - S_x D_y - D_x S_y + D_x D_y). \end{aligned} \quad (\text{A.10})$$

We remark here that for mathematical brevity, the aforementioned dark-count-subtracted coincidences in Eq. (A.8) can be rewritten in terms of measured coincidences and both types of calculated accidentals as follows:

$$\tilde{C}_{x,y} = C_{x,y} - A_{x,y} + \tilde{A}_{x,y}. \quad (\text{A.11})$$

Once we have all of these relations for coincidences and accidentals derived, we can trivially solve for the CAR as shown below:

$$R_{x,y} = \frac{C_{x,y}}{A_{x,y}} \quad (\text{A.12})$$

and

$$\tilde{R}_{x,y} = \frac{\tilde{C}_{x,y}}{\tilde{A}_{x,y}}. \quad (\text{A.13})$$

Again, the tilde merely represents that the data uses dark-count subtraction.

We use the relations presented in this appendix to prepare the counts that are inputs to our tomography code. For all tomographies taken prior to the higher-dimensional Hilbert space experiment, we used the non-dark-count-subtracted coincidences $C_{x,y}$ and accidentals $A_{x,y}$. All CAR measurements and tomographies taken for the higher-dimensional Hilbert space experiment required using dark-count-subtracted coincidences $\tilde{C}_{x,y}$ and accidentals $\tilde{A}_{x,y}$ because the system was lossy. Since this yields a poor signal-to-noise ratio, we opted to improve our measurements by removing the “noise”.

APPENDIX B

Tomographic Simulations

In this appendix, we will take a look at how the tomographic simulations in this dissertation were performed. We use these simulations to produce some of the theoretical results shown in Chp. 7 and Appendix C. We will not discuss the actual tomography algorithms used. Instead, we point the reader to other references for those details^[114–116]. We suffice it to say here that we use codes programmed in MATLAB, primarily by Joseph Altepeter and Evan Jeffery, to calculate the tomographies.

The basic process to simulate a tomography is to first create the coincidence counts that resemble experimental data. The next step is to process them using the tomography code, either maximum-likelihood^[114], or linear-least-squared-fit algorithms^[116]. Finally, compared the retrieved state with some other states. Then repeat this process numerous times with randomly varying input coincidence counts, i. e., run the Monte Carlo method.

In order to generate the coincidence counts, we provide an input ideal density matrix, $\hat{\rho}_{ideal}$. Using this density matrix, we can calculate a probability matrix, P_{ij} that represents the probability of measuring a coincidence count between detectors i and j , for various measurements. We obtain this by calculating $P_{ij} = \langle \psi_j | \hat{\rho}_{ideal} | \psi_i \rangle$. $|\psi\rangle$ represents the states of the projective measurements we want to perform. So for a full 36-measurement polarization tomography, we will have 36×4 such probabilities corresponding to the $|\psi\rangle \in \{|H\rangle, |V\rangle, |D\rangle, |A\rangle, |R\rangle, |L\rangle\}$ bases and coincidence counts between the four

detectors. We refer to these projectors as M_{proj} . By providing the average number of coincidence counts (C_{avg}), and optional parameters such as coincidence-to-accidental ratio (CAR) and transmission loss (η), we can calculate the expected number of coincidence counts (C_{exp}) for each pair of detectors using

$$C_{exp} = \eta \left(C_{avg} + \frac{C_{avg}}{CAR} \right). \quad (\text{B.1})$$

Note that the first term corresponds to true coincidences, whereas the second term represents accidental coincidences. We then randomize the coincidence counts according to a Poissonian distribution and supply the resulting counts to the tomography code. The code yields us with its best guess for our state, described as a density matrix $\hat{\rho}_{meas}$. We can use that density matrix and calculate comparative metrics such as fidelity or linear entropy. By repeating this process many times, we can obtain statistical values to characterize the quality of the state we are trying measure. Figure B.1 shows a flowchart for the process described above.

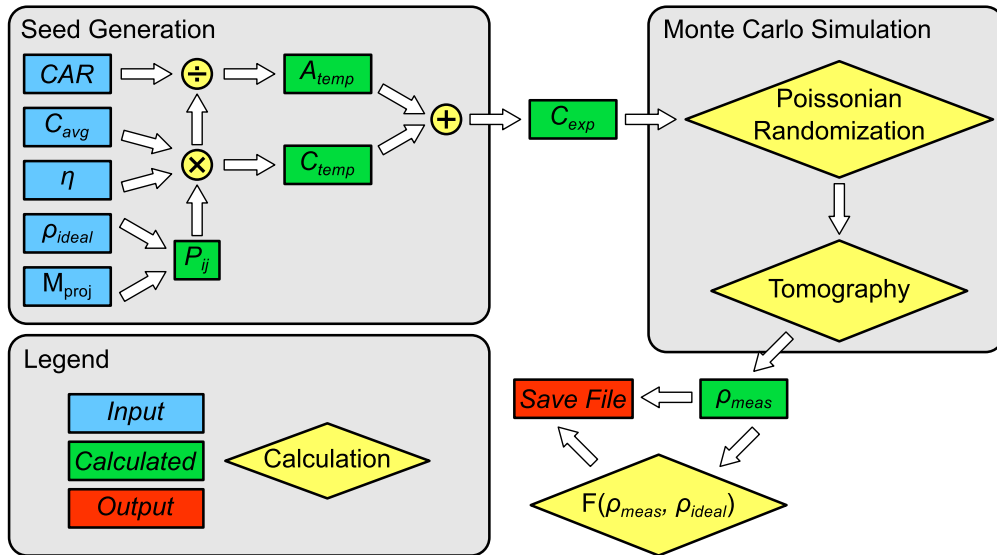


Figure B.1. Flowchart for tomographic simulations

B.1. Example tomography simulation code

In this section, we show an example code similar to the code used to simulate tomographies for the entangled-photon polarimetry work shown in Appendix C. Note that this code sets and creates the appropriate variables and matrices, and then writes them into a script files that MATLAB can read. MATLAB then performs the tomographic reconstruction, and saves the resulting data to a file which can be independently analyzed.

```

1  #!/usr/bin/python
2  """
3      countsVsPrecision.py
4      File to create a plot of simulated precision
5      based on idealized lab conditions for a source
6  """
7
8  from pylab import *
9  from numpy import *
10 import os
11 import numpy2matlab
12
13 ## Establish input parameters
14 totalTime = 9
15 timeBetwProj = 0 # List the Time between projectors for tests
16 #timeBetwProj = 1/54. # List the Time between projectors for eom
17 #timeBetwProj = 3 # List the Time between projectors for WPs
18
19 ## Variable for number of "Monte Carlo" simulations to run
20 simul = 2000
21
22 ## Using input parameters, determine dependent parameters
23 timePerMeas = totalTime/9. - timeBetwProj
24 if timePerMeas < 0:
25     print('Time Travel not allowed!! timePerMeas was calculated' + \
26           ' to be negative. Set to 0.')
27     timePerMeas = 0
28
29 ## Determine useful variables
30 root2 = 1/sqrt(2)
31 H = array([1,0])
32 V = array([0,1])
33 D = root2*(H+V)
34 A = root2*(H-V)
35 R = root2*(H+V*1j)
36 L = root2*(H-V*1j)

```

```

37 ## Two-qubit states are Kroenecker Products of 1-qubit states
38 HH = kron(H,H)
39 HV = kron(H,V)
40 VH = kron(V,H)
41 VV = kron(V,V)
42
43 ## Maximally entangled state
44 maxEnt = 0.5*array([[1,0,0,1], [0,0,0,0], [0,0,0,0], [1,0,0,1]])
45 ## Totally mixed, separable state
46 mixed = 0.25*array([[1,0,0,0], [0,1,0,0], [0,0,1,0], [0,0,0,1]])
47 ## rho = theoretical state (99% fidelity to maximally entangled state?)
48 #rho = .03*mixed + .97*maxEnt
49 #rho = mixed
50 rho = maxEnt
51 rho = rho / trace(rho)
52
53 psi = array([H,D,R])
54 psi_perp = array([V,A,L])
55 ## Below: dim(psi) = 4 x 9 x 4
56 ## psi = [TT, TR, RT, RR] where T = transmitted, & R = reflected
57 psi = array([kron(psi, psi), kron(psi, psi_perp),
58             kron(psi_perp, psi), kron(psi_perp, psi_perp)])
59 #print(psi)
60
61 ## Define pr as the probability matrix for each measurement
62 ## pr = < psi | rho | psi >
63 ## dim(pr) = 4 x 9
64 pr = array([dot(conj(psi[m,n,:]), dot(rho, psi[m,n,:])) \
65            for m in range(size(psi,0)) \
66            for n in range(size(psi, 1))]).reshape(4,9)
67 #print(pr)
68
69 ## Define measurement matrices for the measurements we make
70 meas_q1 = array([[ 0, 180, 0, 90], \
71                 [ 0, 180, 0, 90], \
72                 [ 0, 180, 0, 90], \
73                 [22.5, 180, 45, 90], \
74                 [22.5, 180, 45, 90], \
75                 [22.5, 180, 45, 90], \
76                 [ 0, 180, 45, 90], \
77                 [ 0, 180, 45, 90], \
78                 [ 0, 180, 45, 90]])
79
80 meas_q2 = array([[ 0, 180, 0, 90], \
81                 [22.5, 180, 45, 90], \
82                 [ 0, 180, 45, 90], \
83                 [ 0, 180, 0, 90], \
84                 [22.5, 180, 45, 90], \
85                 [ 0, 180, 45, 90], \

```

```

86         [ 0, 180, 0, 90], \
87         [ 22.5, 180, 45, 90], \
88         [ 0, 180, 45, 90]])
89
90 ## Define countRate as total number of counts from which we calculate trues
91 ## Counts per measurement (ideal, i.e. w/o Poissonian randomization)
92 countRate = (1, 2, 5, 10, 20, 50, 100, 200, 500, 1000, 2000, 5000, 10000, \
93             20000, 50000, 100000, 200000, 500000, 1000000, 2000000, 5000000, \
94             10000000, 20000000, 50000000, 100000000, 200000000, 500000000)
95
96 ratio = (3)
97
98 for cR in countRate:
99     accRate = cR/ratio
100     ## Create coinc array w/ data about all the "ideal" tomographic
    measurement
101     ## dim(coinc) = 4 x 9
102     ## coinc[0] = TT
103     ## coinc[1] = TR
104     ## coinc[2] = RT
105     ## coinc[3] = RR
106     trues = array([(cR*pr[n])*timePerMeas \
107                   for n in range(size(pr, 0))])
108     acc = array([0.25*accRate*timePerMeas \
109                for n in range(size(pr))]).reshape(9,4)
110
111     coinc = trues.T + acc
112
113     ## Write an automatically generated MATLAB script to take the
    tomographies
114     ## using the seeds generated above and find the fidelities
115     scriptname = "tomo_simul.m"
116     rhoFidOutname = "rho_fidelity.txt"
117     coincStr = numpy2matlab.array2matlab('coinc', real(coinc), ';\n')
118     rhoStr = numpy2matlab.array2matlab('rho_0', rho, ';\n')
119     accStr = numpy2matlab.array2matlab('acc', acc, ';\n')
120     meas_q1Str = numpy2matlab.array2matlab('measQ1', meas_q1, ';\n')
121     meas_q2Str = numpy2matlab.array2matlab('measQ2', meas_q2, ';\n')
122
123     saveName = 'simVars_' + str(int(cR)) + \
124               '_' + str(int(accRate)) + '_' + str(totalTime) + \
125               '_' + str(timeBetwProj) + '.mat'
126     coincName = 'coinc_' + str(int(cR)) + \
127                '_' + str(int(accRate)) + '.mat'
128     script = open(scriptname, 'w')
129     if os.path.exists(saveName):
130         print('Using old file: ' + saveName)
131         script.write('load ' + saveName + ';\n')
132         script.write('oldSize = size(f,2);\n')

```



```

133     else:
134         print('Saving to New file: ' + saveName)
135         script.write('clear;\n')
136         script.write('oldSize = 0;\n')
137     script.write('format compact;\n')
138     script.write(coincStr)
139     script.write(rhoStr)
140     script.write(accStr)
141     script.write('acc = acc.*ones(9,4);\n')
142     script.write(meas_q1Str)
143     script.write(meas_q2Str)
144     script.write('meas(:, :, 1) = measQ1;\n')
145     script.write('meas(:, :, 2) = measQ2;\n')
146     script.write('ctalkQ1 = [1,0;0,1];\n')
147     script.write('ctalkQ2 = [1,0;0,1];\n')
148     script.write('for n = 1:' + str(simul) + '\n')
149     script.write('    index = oldSize + n\n')
150     script.write('    coinc_rand(:, :, index) = poissrnd(coinc);\n')
151     #script.write('    rho_1 = simple_linear_2q_4d_tomography( ... \n')
152     #script.write('    meas, coinc_rand(:, :, index), acc, ctalkQ1,
ctalkQ2);\n')
153     script.write('    rho(:, :, index) = simple_linear_2q_4d_tomography(
... \n')
154     script.write('    meas, coinc_rand(:, :, index), acc, ctalkQ1,
... \n')
155     script.write('    ctalkQ2);\n')
156     script.write('    rho(:, :, index) = make_legal(rho(:, :, index));\n')
157     script.write('    f(index) = fidelity(rho(:, :, index), rho_0);\n')
158     script.write('    save('\'' + coincName + '\'', '\coinc_rand\');\n')
159     script.write('    save('\'' + saveName + '\'', '\rho\'', '\f\');\n')
160     script.write('end\n')
161     script.close()
162     os.system('matlab -nosplash -nodesktop -r \'tomo_simul; quit;\'' )

```

Tomographic Simulation Example

B.2. Code used to obtain error bars for tomography measurements

The process by which we obtain error bars on our measurements is very similar to the simulation process. For this reason, we show example code here for how to do so. The difference between this code and the tomographically simulated code is that here, we do not artificially generate our coincidence counts. Instead, we use the measured coincidence counts and Poissonianly randomize those.

```

1 % This function will accept parameters for taking a tomography and return
2 % the mean fidelity, tangle, and linear entropy along with their standard
3 % deviations for a given "numSim" number of Monte Carlo Simulations
4
5 % It is assumed that the input variables can be Poissonianly randomized.
6
7 function [fMean, fErr, tMean, tErr, slMean, slErr] = getTomoErrorBars(meas
   , coinc, acc, ctalk_q1, ctalk_q2, numSim)
8
9 for ii=1:numSim
10     [rho, intens, fval] = simple_2q_4d_tomography(meas, poissrnd(coinc),
   ...
11     poissrnd(acc), ctalk_q1, ctalk_q2);
12
13     f(ii) = general_bell_fidelity(rho);
14     t(ii) = tangle(rho);
15     sl(ii) = linear_entropy(rho);
16 end
17
18 fMean = mean(f);
19 fErr = std(f);
20 tMean = mean(t);
21 tErr = std(t);
22 slMean = mean(sl);
23 slErr = std(sl);

```

Error Bar Calculation Code

APPENDIX C

Real-time Entangled Photon Polarimetry**C.1. Introduction**

Photonic entanglement is a fundamental resource for quantum information processing and quantum communications^[118]. Engineering suitable entanglement sources for a particular application, or integrating those sources into a larger system, however, can be a challenging experimental task. Generating high-quality entanglement requires protecting against or compensating for decoherence, single-qubit rotations, and partial projections. For both free-space^[119–122] and fiber/waveguide-based entanglement sources^[37,38,123–125], this means compensating for any polarization rotations or decohering effects which may occur in transit to a destined application. In addition to the aforementioned static effects, it is necessary to test the source’s stability in the face of real-time system perturbations such as atmospheric turbulence or fiber breathing owing to environmental fluctuations. At present, the best available technique for measuring two-qubit entangled states is quantum state tomography^[114,115], a procedure which can provide a precise reconstruction of the quantum state, but which generally requires 5–30 minutes to complete. This long measurement time can make debugging systematic experimental problems—particularly those with short timescales—challenging, if not impossible.

The field of classical optical communications has faced similar problems when transmitting polarized light over long distances. A *polarimeter* is a common tool that is used to debug unwanted polarization rotations or depolarization effects (i.e., polarization decoherence). A

polarimeter actively monitors the polarization state of a classical optical field, providing an experimenter with a real-time picture of the optical field’s Stokes vector (i.e., its polarization state). Similarly, an *entangled photon polarimeter*—a measurement device capable of performing quantum tomographies and displaying the reconstructed two-qubit states in real time—would be a valuable tool for optimizing and deploying entangled photon sources.

In this appendix, we present our experimental implementation of an entangled photon polarimeter, which is capable of displaying nine reconstructed density matrices per second via complete quantum state tomographies. This represents a speed improvement of 2–3 orders of magnitude over the best quantum state tomography systems currently in use in laboratories around the world. Using this new tool, we record the first live video—at 9 frames-per-second (fps)—of a two-photon quantum state’s transition from separability to entanglement. We also use this space to describe the design, assembly, and characterization of the polarimeter, which uses a pair of computer-controlled, electro-optically-modulated polarization controllers (polcons). We also discuss some setbacks encountered during the development and the solutions employed to either remedy or circumnavigate them. But first, we start with a look at a little theoretical background for two-qubit polarimetry.

C.2. Two-qubit polarimetry

Two-qubit polarimetry is a specific example of two-qubit *quantum state tomography*, a procedure for reconstructing an unknown quantum state from a series of measurements (generally either 9 or 36 coincidence measurements performed using two single-photon detectors per qubit^[115]), each performed on an ensemble of identical copies of the unknown state. Three key parameters can be used to characterize any experimental apparatus for quantum state tomography: the time required to complete the state reconstruction procedure and the

accuracy and precision with which the reconstructed density matrix represents the unknown quantum state.

The time required to complete a quantum state tomography, T , is dependent on the number of two-qubit measurement settings taken per reconstruction, M ; the time per measurement setting, τ_m ; the time to switch between measurement settings, τ_s ; and the time necessary to numerically reconstruct the unknown density matrix from an analysis of the measurement results, τ_a :

$$T \equiv M \times (\tau_m + \tau_s) + \tau_a. \quad (\text{C.1})$$

The accuracy and precision of a tomography are closely related, both indicating how closely the reconstructed density matrix, $\hat{\rho}$, matches the “true” unknown density matrix, $\hat{\rho}_{\text{ideal}}$. The “accuracy” of a tomographic reconstruction measures error due to systematic effects, such as improperly performed projective measurements, uncharacterized drifts in the detectors’ efficiency, or a non-identical ensemble of unknown quantum states. The “precision” of a tomographic reconstruction measures the statistical error in $\hat{\rho}$, and is strongly dependent on the total number of measurable states N in the identical ensemble (which is in turn dependent on the entanglement source’s pair production rate, R , and the total single-qubit measurement efficiency, η). In general, the tomographic precision decreases as T (and therefore N) decreases^[116]. For sufficiently small T , we can neglect systematic effects and quantify tomographic *precision* (as a function of N and of $\hat{\rho}_{\text{ideal}}$) to be the average fidelity between $\hat{\rho}$ and $\hat{\rho}_{\text{ideal}}$:

$$F_p(N, \hat{\rho}_{\text{ideal}}) \equiv \overline{F(\hat{\rho}, \hat{\rho}_{\text{ideal}})} = \overline{\left(\text{Tr} \left\{ \sqrt{\sqrt{\hat{\rho}} \hat{\rho}_{\text{ideal}} \sqrt{\hat{\rho}}} \right\} \right)^2}. \quad (\text{C.2})$$

Note that the equation above uses the usual definition for fidelity between two mixed states^[51], which for a pure $\hat{\rho}_{\text{ideal}} \equiv |\psi\rangle\langle\psi|$, simplifies to the more familiar $F(\hat{\rho}, \hat{\rho}_{\text{ideal}}) \equiv$

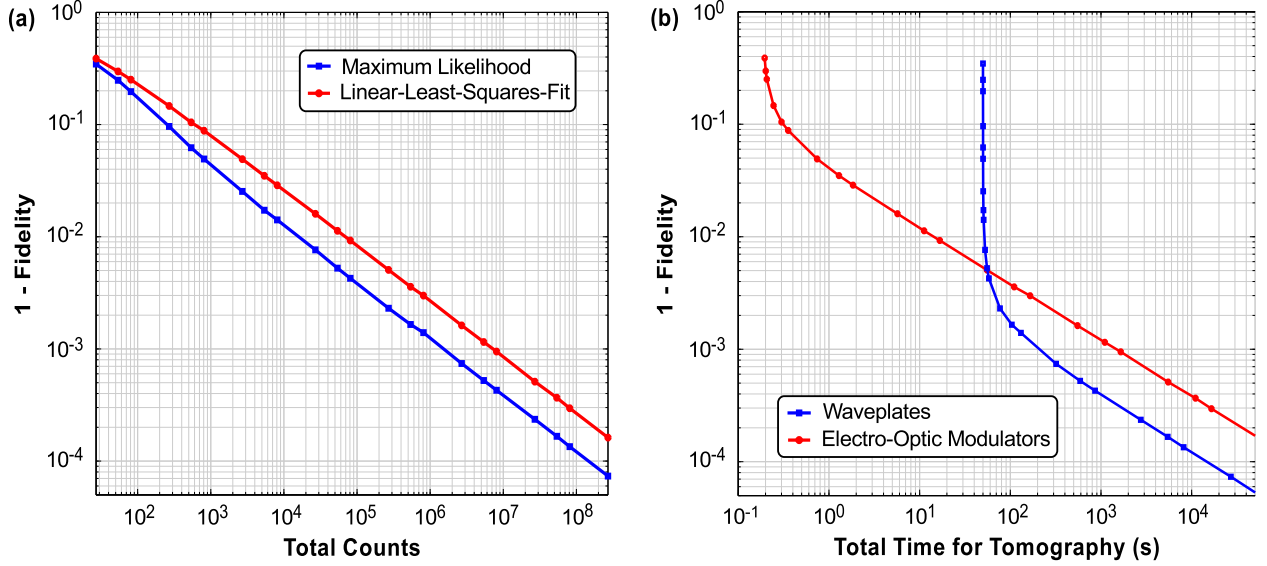


Figure C.1. (a) Tomographic precision $F_p(N, \hat{\rho}_{\text{ideal}})$ for $\hat{\rho}_{\text{ideal}} = |\phi^+\rangle\langle\phi^+|$ with $|\phi^+\rangle = \frac{1}{\sqrt{2}}(|HH\rangle + |VV\rangle)$. Each data point represents a 2000-tomography numerical Monte Carlo simulation of the average fidelity between the reconstructed density matrix and $\hat{\rho}_{\text{ideal}}$, under realistic assumptions about the system noise (a coincidence-to-accidental ratio of 3). Each simulated tomography utilizes four detectors and nine coincidence measurements, such that each unknown quantum state in the N -state ensemble is projected onto one of nine four-element orthonormal bases (e.g., HH, HV, VH, VV). Results for both the maximum likelihood technique and the truncated-eigenvalue, linear-least-squares-fit technique are shown. For a given N , the maximum likelihood technique is slightly more precise^[116]. (b) Using the same simulated data, F_p is shown as a function of total tomography time T for two different experimental systems: a traditional free-space tomography system with $\eta = 0.1$, $\tau_s = 5$ s, $\tau_a = 5$ s and an entangled photon polarimeter with $\eta = 0.07$, $\tau_s = 0.02$ s, $\tau_a = 0.001$ s. In both systems $R = 10^6$ pairs/second and $M = 9$.

$\text{Tr}\{\hat{\rho}\hat{\rho}_{\text{ideal}}\} = \langle\psi|\hat{\rho}|\psi\rangle$. Figure C.1(a) shows $F_p(N)$ for $\hat{\rho}_{\text{ideal}} = |\phi^+\rangle\langle\phi^+|$ with $|\phi^+\rangle = \frac{1}{\sqrt{2}}(|HH\rangle + |VV\rangle)$, where each data point represents a Monte Carlo simulation of the average fidelity between a reconstructed density matrix and the ideal unknown state.

Two-qubit polarimetry is an application of two-qubit polarization tomography which maximizes precision for very short T (≤ 1 s), allowing an experimenter to manipulate an entangled photon source using real-time tomographic feedback (by updating after every measurement,

the time between updates can be reduced to $T/9$). (In this appendix, *entangled photon polarimetry* refers to the application of two-qubit polarimetry to entangled photon states.) Because maximizing precision requires maximizing N , the ideal entangled photon polarimeter will minimize both the time between measurements (τ_s) and the time for numerical analysis (τ_a):

$$N = R\eta^2 M\tau_m = R\eta^2 (T - M\tau_s - \tau_a). \quad (\text{C.3})$$

Although Eq. (C.3) can be used to derive the total time necessary to perform a single tomography with a given precision, an entangled photon polarimeter will likely perform many tomographies in series. In this configuration, the tomographic measurements and the numerical analysis of those measurements can be parallelized in one of two ways. For $\tau_a < M(\tau_m + \tau_s)$, a complete set of M measurements can be analyzed at the same time the next set of M measurements are being performed, leading to one tomographic result being displayed to the experimenter every $M(\tau_m + \tau_s)$ seconds. For $\tau_a < \tau_m + \tau_s$, a tomographic result can be analyzed and displayed after every *measurement*, rather than after every complete set of M measurements. In other words, after every measurement, the *previous* M measurements are used to reconstruct an updated density matrix, leading to a faster refresh rate based on a tomographic “rolling average”. Similarly, this configuration can be altered in real time to utilize even more measurements (e.g., $4M$) for increased precision (analogous to averaging multiple traces on an oscilloscope).

C.3. Building the polarimeter

Now that understand some of key parameters involved with obtaining accurate and precise results, we look at how we build our polarimeter. This subsystems of this device are divided into several main components: optical elements, digital-to-analog converters (DACs),

amplifiers, photon detection, and computer control (see Fig. C.2). After a brief discussion of the overall design goal, and the preliminary constraints, we will elaborate on the process involved for bringing each of these main components online. Finally, we will discuss some of the larger problems that came up during this entire process.

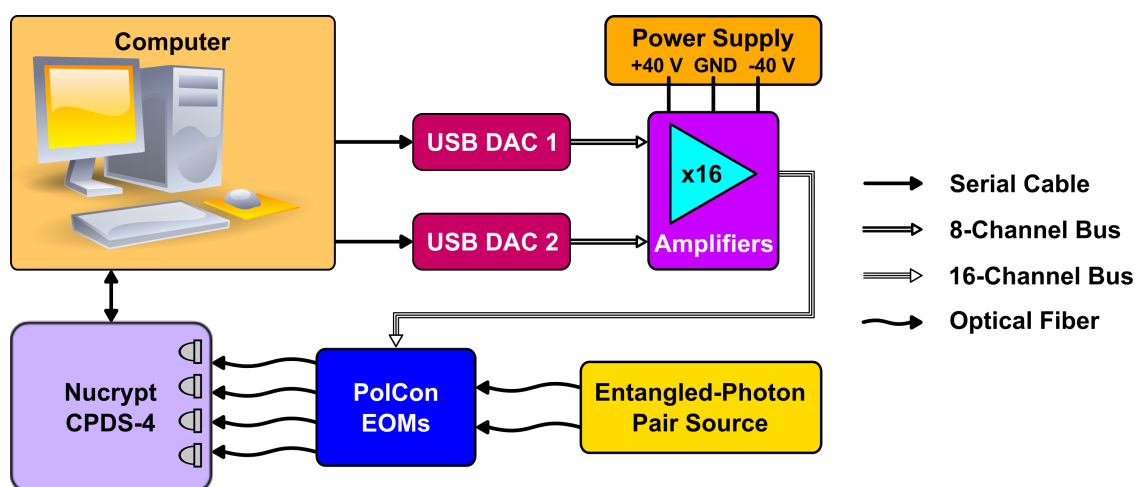


Figure C.2. High-level block diagram of the polarization controller apparatus.

C.3.1. Design goal

This project's goal is to develop and build a system that can rapidly control the polarization of light via a computerized interface. In order to demonstrate this ability, we opted to demonstrate a real-time entangled photon polarimeter. Such a device has applications for high-speed measurement of polarization-based entangled states that are useful for photonic QIP.

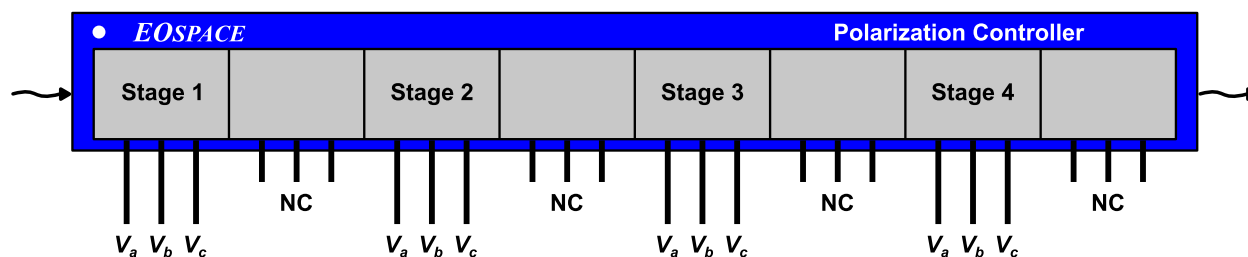


Figure C.3. Connections to the Eospace polcon. The white dot corresponds to pin 1 just as seen on the actual polcon device. (NC = Not Connected)

C.3.2. Design criteria

In order to achieve the goal, we need to consider the many different aspects of our design, including the constraining factors. Based on these, we decide what components need to be made, purchased, and/or used.

The functional workhorse for this project are the polcons, purchased from Eospace (Model PC-B4-00-SFU-SFU-UL). The remainder of the system was designed around these devices. We have two four-stage polcons, each with 24 connection pins. Each stage has three voltage-control leads, and the remaining 12 pins are not connected. By grounding the central pin of each stage, we require eight independently controlled voltages for each polcon.

Table C.1. Polcon pin lookup table

Pin	1	2	3	4	5	6	7	8	9	10	11	12	13	14	15	16	17	18	19	20	21	22	23	24
Stage	1			NC			2			NC			3			NC			4			NC		
Voltage	V_a	V_b	V_c				V_a	V_b	V_c				V_a	V_b	V_c				V_a	V_b	V_c			

In order to drive these 16 voltages, we use two 12-bit, eight channel DACs purchased from ACCES I/O (Model USB-DA12-8A). These DACs were primarily selected for the number of available channels, and the rate at which we can update the values. These DACs are quoted to perform in streaming mode at rates up to 125 kHz. Since amplifiers are used to provide

the appropriate voltages to the polcons, output voltage was not a major concern.

$$\begin{aligned}
 V_a &= V_0 \cdot \lambda \frac{\tau}{\pi} \cdot \sin(\alpha) - V_\pi \cdot \lambda \frac{\tau}{2\pi} \cdot \cos(\alpha) + V_{a,bias} \\
 V_b &= 0 \text{ (Ground)} \\
 V_c &= V_0 \cdot \lambda \frac{\tau}{\pi} \cdot \sin(\alpha) + V_\pi \cdot \lambda \frac{\tau}{2\pi} \cdot \cos(\alpha) + V_{c,bias}
 \end{aligned}
 \tag{C.4}$$

In accordance with the documentation provided by EOSPACE, we used Eq. (C.4), to simulate the range of voltages required for the polcons. These equations relate the rotation angle (α) and retardance (τ) of a waveplate to the necessary voltages based on a given geometry of the lithium niobate (LiNbO_3) waveguides and the electrodes. This allows us to treat each stage as an independent waveplate with an adjustable rotation angle and retardance. Note that all angles in Eq. (C.4) are specified in radians. A derivation of Eq. (C.4) is provided in §C.10.

Based on simple calculations, we determined that a voltage range of ± 40 V should be sufficient. Since the DACs provide a ± 5 V signal source, an eightfold amplifier circuit is necessary for each channel. Also, a high-power DC supply with a rail-to-rail voltage potential of 80 V is necessary in order to provide DC voltages between ± 40 V without clipping.

Optically speaking, we need a source of light with the operating wavelength at 1550 nm. For characterization, we use a CW laser (Santec TSL-210), but for performing entangled photon polarimetry, we need an entangled photon source; we use a fiber-based two-qubit degenerate entangled photon source developed in our lab^[38].

Optically downstream from each polcon, we also put a fiber-connectorized polarizing beamsplitter (FPBS) to project the polarization state onto the orthogonal outputs before

performing coincidence count detection using a Nucrypt single-photon detector array. These FPBSs were purchased from General Photonics (Model PBC-001-P-03-SM-FC/PC)

Finally, uniting everything, we need a method to send commands to the DACs and read data from the detectors. Any computer with two USB ports for the DACs, and one serial port for the detectors should suffice. We opted to use Photonix in the lab because of its speedy processor, and Linux programming environment.

C.3.3. Background for waveplates

Since we treat each stage as a waveplate, a brief discussion of waveplates is given here. A waveplate is an optical device that adds a phase between orthogonal polarizations of light. The amount of phase, called the retardance, is traditionally based on geometric factors. A waveplate is further characterized by its ordinary and extraordinary axes. These axes specify orthogonal linear polarizations which we call horizontal (H) and vertical (V). Occasionally, we also refer to these axes as the slow and fast axes. These axes are special in that if H- (or V-) polarized light is incident and aligned with the either axis, it is unaffected. Alternatively, if diagonal light (conventionally defined as $D = H + V$) is incident upon the waveplate, then the H-polarized component and the V-polarized component will have a phase between them equal to the retardance of the waveplate.

Standard waveplates are available as half-waveplates (HWP) and quarter-waveplates (QWP). The half and quarter distinction tell us that the retardance is equal to a half or quarter of the given operating wavelength. For example, at 1550 nm, a HWP applies a 775-nm phase shift between the H and V components of incident light.

The aforementioned discussion is primarily relevant for light which is aligned to the optic axes of the waveplate. Of course, either the light or the waveplate can be rotated to provide

variations on the output. Hence an additional relevant factor is the orientation angle of the waveplate. Combined with knowledge of the orientation angle, and the retardance, we can quickly determine the output polarization of light given the input polarization through a known, characterized waveplate.

Unlike typical waveplates, the polcons are not constrained by physical geometry. Instead, since they operate as electro-optic modulators (EOMs), they adjust the properties of the internal waveguide, thereby changing the properties of the transmitted electromagnetic wave. This characteristic works to our advantage because each stage of each polcon behaves like a waveplate with variable retardance and orientation angle. This affords tremendous flexibility when manipulating states.

The next optical component of the design is a fiber-connectorized polarizing beamsplitter (FPBS). The FPBS is simply a device that uses optical properties of the propagating medium to direct light of orthogonal polarizations to two different outputs. We use the FPBS to measure our state since we can measure the output ports separately using the Nucrypt detectors.

C.4. Hardware

C.4.1. Digital-to-analog converters

As mentioned before, the polcons are driven by a low-voltage supply from the DAC which is subsequently amplified. Based on simple simulations, we determined that we can operate the polcons with ± 40 V supply. This supply enables us to treat each stage of the polcon as a waveplate with a variable retardance of up to half a wavelength. Based on an online search of DACs, we deemed it sufficient to use a supply that provides ± 5 V since this is easier and cheaper to obtain than a ± 40 -V supply.

Another factor used to select an appropriate DAC was the rate at which the signal could be updated. Noting that the operating baudrate of the serial port used to read data from the detectors is 115,200 bits per second, we selected a device that can update at 125 kHz. This should be plenty sufficient for the current needs. Future designs can optimize the readout rates by using faster protocols like USB for all communication interfaces. Based on these criteria, we purchased the ACCES I/O USB-DA12-8A DACs for our digital-to-analog converters.

C.4.2. Amplifiers

We now look to the design of the amplifier circuits with an eightfold gain for each channel. In order to determine which op-amps are suitable for the design, we need to consider three main factors: the current draw, supply voltages, and switching rate.

Using the supply voltages as a preliminary screening, we searched for high-power op-amps, and settled on the OPA453 op-amps. It is useful to note here that the OPA453 was chosen instead of its sister product, the OPA452, because the OPA453 is designed to operate at gains higher than five; our amplification is a factor of eight. These op-amps are rated to operate at 80 V, which is perfect for the ± 40 -V supply we wish to drive.

Also, the recovery time for the OPA453 is 1 μ s, i.e. 1-MHz switching rate. This is sufficiently larger than the 125-kHz rate determined by the DACs, and therefore we deduce that switching rate will not be an issue with these op-amps.

Finally, modeling each stage according to Fig. C.4, and using the following equation, $i_x = c_x(\Delta v_x/\Delta t)$, $x \in a, c$, it is trivial to show that the maximum current draw is 150 μ A. Since each amplifier can support up to 50 mA of current draw, and each stage gets its

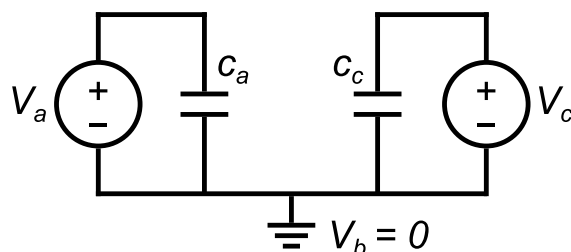


Figure C.4. The circuit model for each stage of the polcon. Note that V_b is grounded.

own op-amp, this OPA453 is the perfect selection for this application. Note that measured average capacitance between any two connected pins of the polcon was on the order of 15 pF.

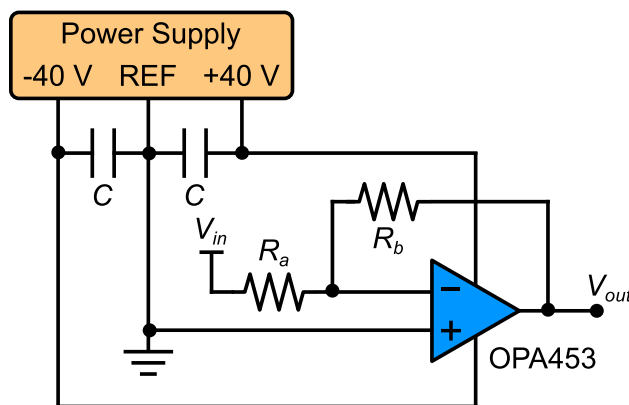


Figure C.5. Electrical schematic of the amplifier circuitry. $C = 10 \mu\text{F}$, $R_a = 5 \text{ k}\Omega$, $R_b = 40 \text{ k}\Omega$. Therefore, the gain is $R_b/R_a = 8$.

Looking at Fig. C.5, you will see that the op-amps are wired with resistors in an inverting amplifier configuration. The resistors were chosen to provide the desired gain factor of eight. It is critical to note the inverting nature in order to properly send the software code for driving the DACs.

C.4.3. Heat considerations for op-amps

As can be expected with high-power applications, heat dissipation is an important factor that must be considered. At the small currents which are being driven, it may seem unimportant,

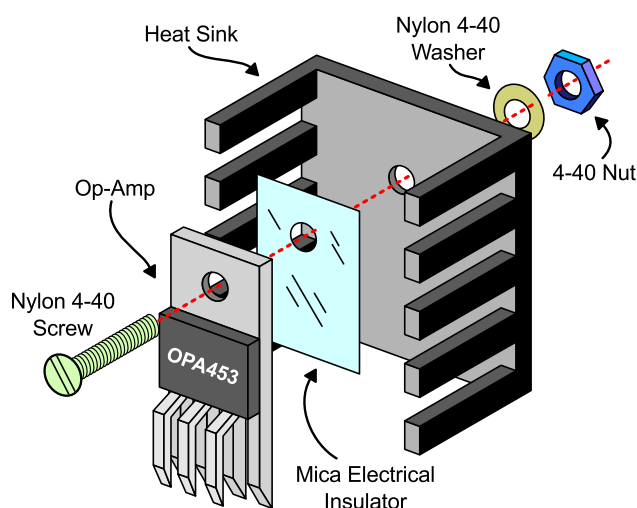


Figure C.6. Drawing of the Heat Sink assembly. Note that we use a mica insulator, nylon screws, and nylon washers to prevent the grounded backplate of the op-amp (OPA453) from accidentally conducting electricity through the much larger heat sink.

but with 16 of these op-amps in a small enclosure, heat can become a factor. For this reason, each op-amp is connected to a heat sink, and the enclosure lid is currently left open to allow for dissipation. Since the back plates of the op-amps are connected to GND, the heat sinks are attached to them using nylon screws and with a mica plate in between to electrically isolate the heat sinks while retaining thermal conductivity. A drawing for this assembly is shown in Fig. C.6. Future plans exist to create vents in the lid so that the box can be closed while enabling the heat to dissipate easily. In the event that this is not sufficient, a fan may be attached.

C.4.4. Power supply

Rather than spend extra money on a pre-built ± 40 V power supply, we scavenged around the lab and used a mish-mash of various parts to build my own “custom” supply. We did not design and build one using transformers, rectifier and switching circuitry. Instead, we used

three pre-built power supplies of different voltages (two ± 15 V, and one ± 12 V) along with a follow-up circuit in order get the ± 40 V supply with a central pick-off we call REF. The circuitry for the power-supply is shown in Fig. C.7. Essentially, we treat the three supplies as +30 V and +24 V supplies by ignoring their reference outputs and using only the poles of the supply. By wiring these three in series, we can obtain an 84 V supply which we can subsequently modify to get the desired ± 40 V.

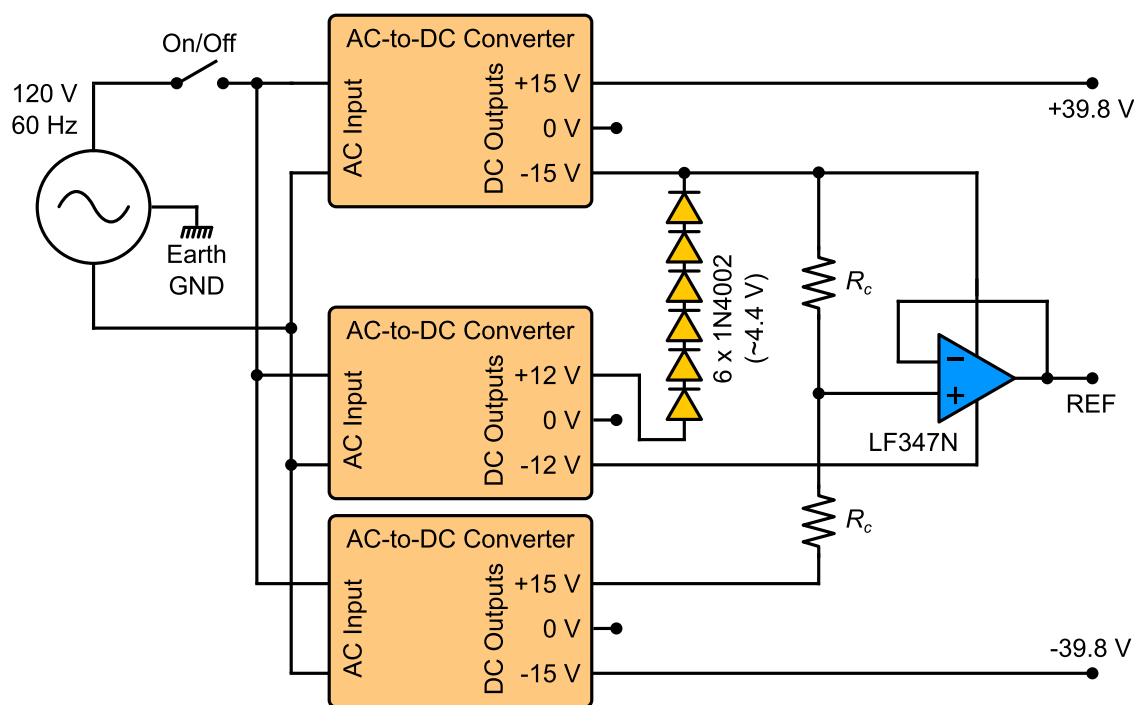


Figure C.7. Electrical schematic of the power supply. We use three AC-to-DC converters (transformers) to generate an $\simeq 84$ V power supply. We then use six diodes (1N4002) to create a $\simeq 4$ -V drop in voltage. Finally, we use a generic op-amp (LF347N) in a unity-gain configuration. The output of the op-amp establishes the reference (REF) for the +40-V and -40-V supplies. $R_c = 100$ k Ω

The first modification is the use of the six 1N4002 diodes. These diodes are used to simply step down the voltage by approximately 4 V (assuming that each Si diode has a forward bias voltage of ~ 0.6 – 0.7 V). The next modification is to add a voltage divider followed by

an op-amp on the middle connection. The voltage divider is used to make the ± 20 V into a +10 V and -10 V with a central reference voltage (REF). The op-amp is wired in the unity gain configuration and is used to simply prevent any variation on the reference voltage caused by fluctuations of load current.

In order to determine the appropriate op-amp for this selection, we looked for two main criteria: current draw, and supply voltage. The largest conceivable current draw on this op-amp happens if all 16 DACs are switched simultaneously and instantly from their maximum values to their minimum values. Using the aforementioned $150 \mu\text{A}$ calculation, this would require an op-amp that can tolerate a 2.4 mA. The other criteria was that the supply voltage for the op-amp be ± 20 V. The selected op-amp for this application was the LF347N. This op-amp can tolerate a load current up to 11 mA and can work with supply voltages up to ± 30 V making it suitable for this application.

C.4.5. Polarization control box

For the polcons, the electrical considerations of how the wiring was done is discussed in the next section. Optically speaking, when placing the polcons in their housing, a lot of care was taken to maximize the bending radius of the fibers. This enable it to fit properly in the case, but not bend too much so as to introduce unnecessary loss. Similar considerations were made for the other optical elements in the housing, the FPBSs. Also, while placing the optics in the polcon Box, we taped down the fiber to mitigate polarization drifts due to fiber breathing and environmental fluctuations. Ideally, the fibers will not move much since the lid has now been placed on the box preventing significant movement of the fiber.

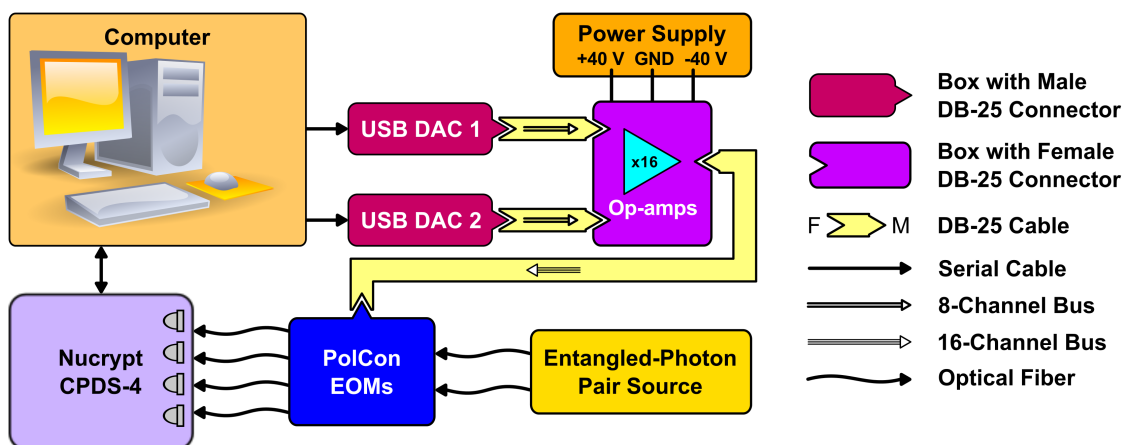


Figure C.8. High-level diagram showing the interfaces and connections between different parts of the entire setup. Note that the arrows for the cables/adapters do not indicate direction of data transfer. The direction of data transfer is indicated by the arrows inside the DB-25 cables which indicate the number of data lines used on that bus.

C.4.6. Hardware interconnects

When assembling all these different parts, with 16 independent voltages being controlled, it becomes very important to follow the interfaces between devices. Also care must be taken not to accidentally cross some wires for the “homemade” amplifiers. In general, a D-Sub 25-pin (DB-25) connector is utilized throughout the design. This was chosen for the ability to transfer 16 (or more) voltages in a small form factor. Also, it was the output choice made by the ACCES I/O DACs making it convenient for to retain the connector throughout the rest of the design. Shown in Fig. C.8 is a high-level drawing of the setup indicating whether a male or female DB-25 connector is used for each of the different parts.

Note that the connection from the amplifiers to the polcon box is a single DB-25 cable. In an effort to avoid confusion, the pin connections shown in Table C.2 were made. For the reader’s convenience, we show the pinout numbering of the male and female connectors in Fig. C.9. The reader will note that the lower numbered pins connect to the polcon and

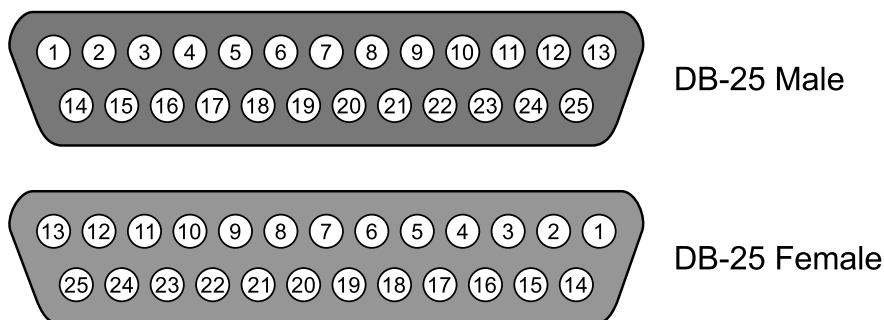


Figure C.9. Pinout numbering for male and female DB-25 Connectors. The male connector is used on the polcon box, while the female connector is used as the output from the amplifier box.

FPBS with lower serial numbers. Also, both devices use the same REF for their common ground. This REF is connected to each stage's V_b . Corresponding V_a and V_c are also kept on contiguous pins. This makes it easier to address them from software. For reference, a reverse look-up table is also provided.

C.4.7. Single-photon detection

Single-photon detection is performed using a four-detector array of InGaAs avalanche photodiodes (APDs) operated in the gated Geiger mode. By increasing the speed of these detectors from 8.3 MHz to 50 MHz, the entangled photon polarimeter achieves a 6-fold speed increase relative to previous implementations of quantum state tomography which utilized the same telecom-band detection systems. Moreover, by synchronizing the detector-array's control software with the EOM-based analyzers, we have reduced the switching time to $\tau_s = 20$ ms. By upgrading the detector control software to eliminate extraneous electronic delays, we anticipate that this will approach the 125 kHz limit ($\tau_s = 10 \mu\text{s}$) imposed by the EOM voltage controllers. The quantum efficiency of each detector at 1550-nm is approximately 20%, with a measured dark-count rate of $1\text{--}4 \times 10^{-4}$ per pulse.

Table C.2. Pin connections for the polcons and the DB-25 connector on the polcon box. Channel A of the polcon box uses EOSPACE polcon with serial #140526 and General Photonics FPBS with serial #90030926. Channel B uses EOSPACE polcon with serial #140527 and General Photonics FPBS with serial #90030932

Pin Lookup				
DB-25 Pin #	Polcon Pin #	Polcon Channel	Polcon Stage #	Value
1	1	A	1	V_a
2	3	A	1	V_c
3	7	A	2	V_a
4	9	A	2	V_c
5	13	A	3	V_a
6	15	A	3	V_c
7	19	A	4	V_a
8	21	A	4	V_c
9	Not Connected			
10	Not Connected			
11	Not Connected			
12	2, 8, 14, 20	A & B	ALL (1-4)	REF
13	2, 8, 14, 20	A & B	ALL (1-4)	REF
14	1	B	1	V_a
15	3	B	1	V_c
16	7	B	2	V_a
17	9	B	2	V_c
18	13	B	3	V_a
19	15	B	3	V_c
20	19	B	4	V_a
21	21	B	4	V_c
22	Not Connected			
23	Not Connected			
24	Not Connected			
25	Not Connected			

C.5. Software

Almost all the code for this project was written using Python. A small portion of code was written in C++. The software written for this project falls into three categories: driver software, interface software, and application software. The driver software is low-level code written to talk to the physical apparatus. This type of code was specifically written for

Table C.3. Pin connections for the polcons and the DB-25 connector on the polcon box. Channel A of the polcon box uses EOSPACE polcon with serial #140526 and General Photonics FPBS with serial #90030926. Channel B uses EOSPACE polcon with serial #140527 and General Photonics FPBS with serial #90030932

Reverse Pin Lookup			
Polcon Channel A Pin #	Polcon Box	DB-25 Pin #	Polcon Channel B Pin #
1	1	14	1
2	12	13	2
3	2	15	3
4	NC	NC	4
5	NC	NC	5
6	NC	NC	6
7	3	16	7
8	12	13	8
9	4	17	9
10	NC	NC	10
11	NC	NC	11
12	NC	NC	12
13	5	18	13
14	12	13	14
15	6	19	15
16	NC	NC	16
17	NC	NC	17
18	NC	NC	18
19	7	20	19
20	12	13	20
21	8	21	21
22	NC	NC	22
23	NC	NC	23
24	NC	NC	24

communication with the DACs. Interface software is written in order to talk to a preexisting code or interface. Code of this form was written for communication with the detectors, and the DACs. Finally, application software is written for end-user goals. This type of code unifies the other codes as a sort of wrapper and produces some sort of useful result. The application software is very useful for automating entire processes as we have done for the entangled photon polarimeter.

C.5.1. Interface to DACs

Low-level code was written to control the DACs. This was necessary because ACCES I/O claimed to have Linux support for their devices, but unfortunately, the USB-DA12-8A was the only device in their product line without support. In order to control the DACs, we used some of their supplied C++ code for their similar devices and modified it so that we could produce the desired voltages on our devices. After getting this to work, we spent some time trying to implement the same effect using Python in order to unify all the automation code. Unfortunately, a direct port of the code was unsuccessful. Finally, we resorted to writing a wrapper method in Python which would execute the compiled version of the C++ code using a command-line interface and supply the required parameters such as the byte mask, and output DAC values (in hex) as arguments.

After some use, a problem was discovered with using these DACs. The DACs would demonstrate some discontinuities during a linear scan of the voltages. At the time of this publication, the source of this problem is uncertain, and efforts to find the problem remain underway. We believe the problem lies with the aforementioned C++ code. Indicators currently seem to point to the fact the problem can be resolved using properly written C++ code which utilizes streaming the data in accordance with the DACs stream mode.

The discontinuities make it difficult to properly get the desired output voltages. Fortunately, by ignoring the lowest few bits, the desired tests/experiments can be run with minimal disruption to the goals.

C.5.2. Brief description of libraries for polcons

In order to control the polcons using the DACs, a few modules were written. The DACmodule contains most of the methods used to interface directly with the DACs. These methods include ways to convert between a desired voltage to the corresponding decimal value of the DAC.

A separate module, called eomModule, was written to control the polcons (aka EOMs) specifically. This module contains different classes used to organize the data into useful packages. These packages allow the user to interface with each individual stage, or with a polcon as a whole. Within each of the different classes, there are the methods which are relevant for that class. For instance, since updates to all the stages on a polcon are done together, the “Update polcon” method is found in the class for the polcons. Methods for each polcon stage enable one to set the proper V_a and V_c for that stage based upon a given desired retardance and orientation angle.

It should be noted here that there are a few other parameters that also need to be known (and properly characterized) for each polcon stage. These parameters are the various voltage constants seen in Eq. (C.4): V_0 , V_π , $V_{a,bias}$, and $V_{c,bias}$. In the eomModules, we refer to these parameters as $V_{settings}$ or voltage settings. Each stage’s voltage settings are also contained as variables in the class describing that polcon stage. In general, we used the pre-calibrated values for the voltage settings provided by EOSPACE, but as discussed later, we do adjust them a little to assist in determining the canonical points.

C.5.3. Interface to detectors

Since the Nucrypt detectors already have a built-in menu system and interface, some code needed to be written to use that framework. The code is distributed into different sections. The first section is used to initialize parameters for detection. These parameters include the repetition rate, and thresholding values for each of the detection channels. Another section involves code written to read out the data.

Each readout consists of a set of 23 numbers on one line from the Nucrypt detectors. Each line represents a predetermined number of detection windows (or triggers), typically 1 million. The first number is merely a number which tells us which line we are reading. The next four numbers represent the number of detections (or singles) on each detector A–D. The next two numbers are the coincidence counts and the detectors' reported accidental counts between detectors A and B. The following five pairs are the coincidence and accidental counts between detectors C/D, A/C, B/D, A/D, and B/C respectively. The following two numbers are the four-fold coincidence and accidental counts between all the detectors. Finally, the last four numbers report the after-pulses on each detector. In short, the pattern is as follows:

S_{A-D} C_{AB} A_{AB} C_{CD} A_{CD} C_{AC} A_{AC} C_{BD} A_{BD} C_{AD} A_{AD} C_{BC} A_{BC} C_{ABCD} A_{ABCD} AP_{A-D}

Before this project, during any detector read, we would need to specify the number of these readout lines we would like to measure in rapid succession. We refer to this number as the cycles we would like to read. When the cycles are completed, the detectors automatically sum the results of the readout lines. This final line is then collected by the computer and used to produce statistically valuable data which can be processed.

Unfortunately, each time the detectors start a read of n cycles, there is an inherent 0.1-s delay. This conflicted with our final speed goals for the entangled photon polarimeter; so a method of communicating and reading the detectors more rapidly needed to be devised and implemented.

After much contemplation, and discussion with Joe Altepeter, we implemented a makeshift solution which we refer to as the free-running mode. Essentially, in order to avoid the delay for each read of the cycles, we would set our number of cycles to a very large number. We could then collect the data line by line, and use the computer to post-process, i. e. sum, the data, rather than burden the detectors with this task. This gives us the benefit of having only one 0.1-s delay when the readout is started initially.

C.5.4. Data processing

After the detection is done, we are left with a large file which has collected the readout lines from the detectors. All of this data needs to be processed into more useful results. Once again, in order to make the data more statistically valuable, the first post-processing done is to sum a predetermined number of lines. Using these summed lines, we then calculate the statistical accidental counts based on the following equation, where x and y are the detector labels, and g is the number of detection gates, i. e. lines that summed \times one million.

$$A_{xy} = (S_x S_y) / g$$

Collecting the coincidences with the calculated accidental counts, we save the data into large files.

For the entangled polarimetry project, we use programs written by Joe Altepeter and Evan Jeffrey to analyze these large data files and process the tomographies using a linear-least-squares-fit algorithm^[116], as opposed to a maximum likelihood algorithm^[114]. Subsequently, the processed data is used to display two-qubit ellipsoid representations of the entanglement^[126]. The double-ellipsoid visualization technique plots the surface of remotely preparable states for two-qubits in Poincaré space. The positions of the points on this surface indicate states which can be remotely prepared, while their color indicates the measurement which must be performed on the other qubit to remotely prepare them. Totally uncorrelated states are plotted as individual points on the two spheres, maximally entangled states are plotted as spheres of radius one, and partially mixed states as ellipsoids inside the surface of the sphere. Every two-qubit state has a unique graphical representation. For an example of this visualization, see Fig. C.11.

C.6. Characterization and calibration

C.6.1. Procedure for determining the canonical bases

A polarimeter (ThorLabs DPC/TXP 5004) has often been used during the development of these devices to try to calibrate the voltage values needed to obtain the six canonical bases (H, V, D, A, R, and L). The polarimeter displays the polarization of the input light on the Poincaré sphere, and lists the Stokes parameters for that polarization. Using the latter, we can calculate orthogonality between different pairs of bases.

In order to find the six orthogonal points and thus control the polcons reliably, we need to satisfy two criteria. The first is to have a known optical input to the device, and the second is to be able to adjust the stage under test (SUT) to a desired starting point. Since we already have a FPBS after our polcons, we simply shined light through the “output”

of the polcon box. This assures us that the light will have a fixed input polarization, thus satisfying our first criteria.

Using the numbering convention described earlier for the polcon stages, we now set a pre-stage (in our case stage 4) to its default voltage settings (the values provided by EOSPACE). Equipped with the polarimeter, iterating between adjustments of the retardance and orientation angle for the pre-stage, and adjusting the voltage settings for the SUT, we search for a location on the Poincaré sphere where the polarization does not change significantly. Once this location is determined, we label that H, and then search for the remaining five canonical points by simply adjusting the retardance and orientation angle of the SUT.

After approximately finding the canonical points' Stokes parameters, a simple calculation in Matlab can yield the orthogonality between any of these. This is used to verify that we have useful canonical points. Finally, to ensure that the tomography code works properly and the detector channels correspond to the proper transmission/reflection ports from the FPBS, we check that right-handedness of the measured Stokes parameters. If they are found to be left-handed, then we simply flip the orientation angle measurement used to obtain the R and L canonical points, i. e., relabel R to L and vice versa.

C.6.2. Power supply and DAC calibration

A few simple tests have been done to better calibrate the power supply, and DACs. The power supplies have been tested and have a voltage range of approximately ± 39.8 V. The DACs have also been tested for stability, and repeatability. The DACs seem to be stable on the order of 10mV. These small fluctuations are not large enough to affect the eventual polarization significantly.

Other than the DACs discontinuities which were discussed earlier, the DACs also have one small flaw. Each channel of the DAC has a small shift from the ideal value. For example, if we aim to set all the DAC channels at 5 V by setting the hex code to 0x0FFF, one channel may be at 4.98 V while another may be near 5.1 V. The shifts from the ideal value vary on the order of 10-100 mV. Fortunately, it seems that all the channels shift is just a shift and not some nonlinearity. Hence, a small software correction should resolve this problem. At the time of publication, the software correction has not yet been implemented since the current experiments have not required the levels of precision afforded by such a change.

In terms of repeatability, the DACs have demonstrated reliable results. In other words, these DACs are very precise, but not particularly accurate; the accuracy can of course be improved by implementing the software based correction. Now that we know how to build the setup, and calibrate the components, let us look at the experimental details used to test the entangled-photon polarimeter.

C.7. Experimental details

The entangled photon polarimeter presented here is based on a previous apparatus for free-space telecom-band quantum state tomography^[38,115], which although accurate, is too slow to provide real-time feedback. Three key improvements have dramatically improved the tomographic speed while maintaining precision: bulk wave plates have been replaced with fast electro-optic modulators (EOMs), an array of four single-photon detectors triggered at 8 MHz have been replaced with an array that is triggered at 50 MHz, and the traditional maximum likelihood reconstruction technique has been replaced with a much-faster linear-least-squares-fit method.

Below, we briefly discuss the differences between these two techniques after reviewing the entangled photon source used to test the tomography apparatuses. Figure C.1(b) highlights the differences between the two techniques, showing the expected tomographic precision F_p as a function of total tomography time T .

C.7.1. Entangled photon source

To test the entangled photon polarimeter, we utilize a fiber-based, frequency-degenerate, 1550-nm, polarization entangled photon-pair source^[38]. The source utilizes spontaneous four-wave-mixing in dispersion-shifted fiber and is pumped by 50-MHz repetition rate dual-frequency pulses spectrally carved from the output of a femtosecond pulsed laser. Because the output photons are identical, reverse Hong-Ou-Mandel interference in a Sagnac loop is used to deterministically split the output photons into separate output single-mode fibers. See Fig. C.10(a).

The same source is used to test two separate tomography systems, the automated wave-plate-based apparatus first described in^[38] and the entangled photon polarimeter presented here.

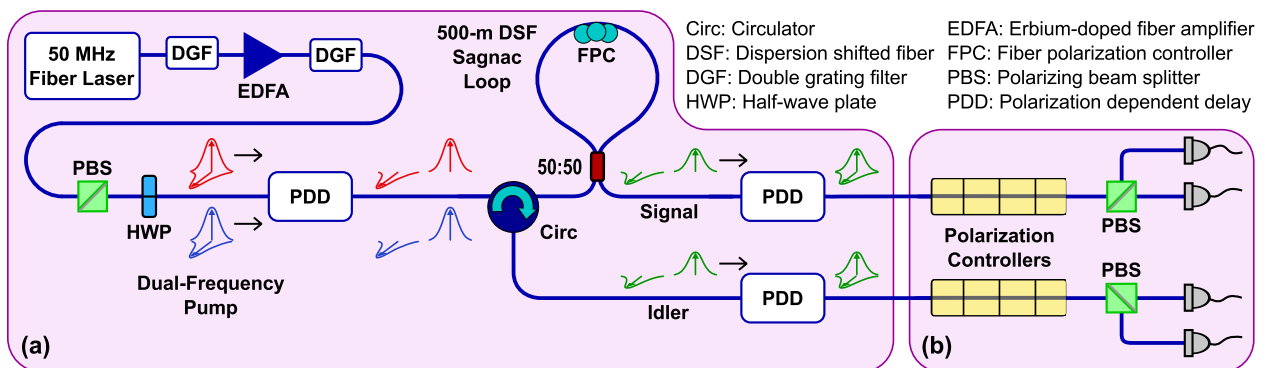


Figure C.10. (a) The entangled photon source used to test the entangled photon polarimeter^[38]. (b) The entangled photon polarimeter, composed of fast electro-optic modulators, in-fiber polarizers, and a four-detector array^[127].

C.7.2. Polarization measurements

Traditionally, two-qubit polarization tomography is performed using bulk, free-space, birefringent crystals (i.e., wave plates). A quarter- and a half-wave plate followed by a polarizer on each of the two qubits can implement an arbitrary projective measurement^[115]. By collecting photons from both the transmitted and the reflected ports of each qubit’s polarizer, one can project an unknown photon pair into one of four orthonormal basis states, defined by the wave plates. If well characterized, this can lead to a very accurate tomography, though the measurement-to-measurement transition time τ_s will in general be very large (≈ 5 s). For the fiber-based source above, this type of polarization analyzer will lead to a single-qubit loss of ≈ 1.5 dB (including the fiber to free-space to fiber coupling losses).

To decrease τ_s , we have constructed an all-fiber/waveguide polarization analyzer based on electro-optic modulators (EOMs). These LiNbO₃ EOMs (EOSpace, model PC-B4-00-SFU-SFU-UL) allow precise control of both the retardance and optic axis of a birefringent crystalline waveguide using the fringe fields from three electrodes. In general, this process has an extremely short response time leading to EOM switching rates of up to 10 MHz. In practice, we are able to implement arbitrary polarization measurements at 125 kHz, which is a limit set by the speed of our computer-controlled voltage sources.

Although high-speed, EOMs are more difficult to precisely characterize than bulk wave plates; using a standard polarimeter we have characterized the six transformations performed by each EOM-based analyzer (corresponding to projections onto the H, V, D \equiv (H + V)/ $\sqrt{2}$, A \equiv (H – V)/ $\sqrt{2}$, R \equiv (H + i V)/ $\sqrt{2}$, and L \equiv (H – i V)/ $\sqrt{2}$ basis states). EOM projections deviated from an ideal measurement by an average of 2.1 degrees on the Poincaré sphere. The single-qubit losses of the EOM-based analyzers varied between 3.0–3.4 dB.

C.7.3. Tomographic reconstruction

Traditionally, the maximum likelihood technique has been used to reconstruct a two-photon state's density matrix from a series of coincidence measurements, which numerically solves for the density matrix $\hat{\rho}$ most likely to reproduce the measured counts^[114,115]. This method always produces a legal state, but is relatively slow ($\tau_a \approx 5$ s).

By using a simpler analysis technique based on a linear least-squares fit, we are able to increase the state reconstruction speed by more than three orders of magnitude^[116]. We use the 2-qubit Stokes vector as a linear model, and solve the following least-squares problem:

$$wM \cdot S = wC. \quad (\text{C.5})$$

Here, M is the set of measurements, which can be arbitrary POVMs; C is the measured counts, and S is the Stokes vector we solve for; w is a weight vector representing the distribution width for each measurement. We assume the counting process to be Poissonian, and use the large-N limit where the Poisson distribution is approximated as a Gaussian with width \sqrt{N} . To guarantee a legal density matrix, we post-process the least-squares fit by truncating the negative eigenvalues^[116]. We have found that this type of linear fit provides results identical to those obtained via the maximum likelihood method with a negligible drop in precision (see Fig. C.1(a)), only much faster (~ 1.3 ms per tomography using Matlab on a 2.4-GHz CPU).

This three-order-of-magnitude speed increase allows us to display a new frame (i.e., tomography result) after every measurement, reconstructed using the previous M measurements. For four-detector, complete-basis polarization analyzers (described above), only nine

measurements are needed to perform a complete tomography. Note that it is often experimentally optimal to perform a redundant set of 36 measurements in order to detect and/or correct for systematic errors such as source intensity drift, detector efficiency drift, or polarizer crosstalk^[115].

C.8. Entangled photon polarimeter performance

After setting up all of the electronics and optics, programming the appropriate software, and resolving the experimental hurdles, we are finally able to test the entangled photon polarimeter. In order to do this, we tell the software to cycle through the 36 projective measurement settings. We need to ignore some of the data we receive from the free-running detector readouts during the interim periods when the computer switches between the two polcons settings for their respective canonical points. Thus, in our test run, we would omit every sixth line of data. Keeping this in mind, we would essentially sum over five lines of data for each measurement used in the tomography. After that, we would simply run the code in very long loops, and use only the previous 36 summed measurements in the tomography code and visualization. Stated a little differently, only the 36 most recent measurements affect the frame that is visible on the screen at any time. This implies that the first 36 frames that are displayed on the screen are not valid frames to consider when using the polarimeter.

Using entangled states generated by the degenerate entangled photon source, and with the calibrated canonical points, we were able to test the polarimeter. Figure C.11 shows frames from a video demonstrating real-time adjustment of a state from separable to maximally entangled. This video updates the on-screen frames at a rate of 3 Hz, and uses the Altepeter spheres visualization of entanglement^[126]. For this measurement, the polarimeter was set to

time-average over the last 15 seconds of data, while performing one complete tomography every four seconds.

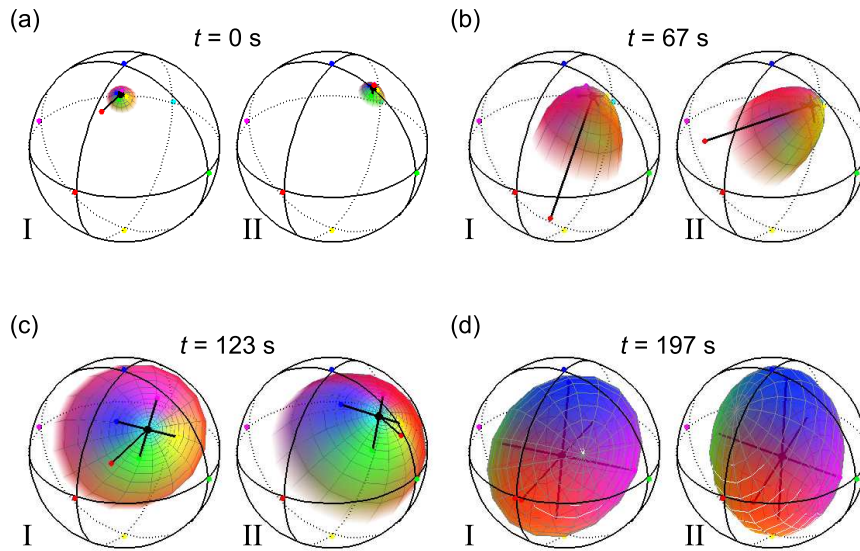


Figure C.11. Individual frames from a 3 frame-per-second (fps) real-time video recording of a two-photon state's transition from separability to maximal entanglement. (a) $t = 0$ s. (b) $t = 62$ s. (c) $t = 123$ s. (d) $t = 197$ s. State (a) is completely separable, while state (d) has 83% fidelity with a maximally entangled state.

We then improved the device operation by reducing some overhead from the detectors. We took another set of data and made another video. Frames from this video are shown in Fig. C.12 using the more traditional density matrix representation. This video operated at 9 fps, and one complete tomography was taken each second.

To verify the polarimeter's stability, we recorded three 9-fps live videos of a two-photon polarization state using the 36-measurement configuration. First we recorded two videos where the measured state is not changed during the course of the measurement run, for a totally separable pure state, $|DV\rangle$, and a maximally entangled state, $|\phi^+\rangle$. By analyzing

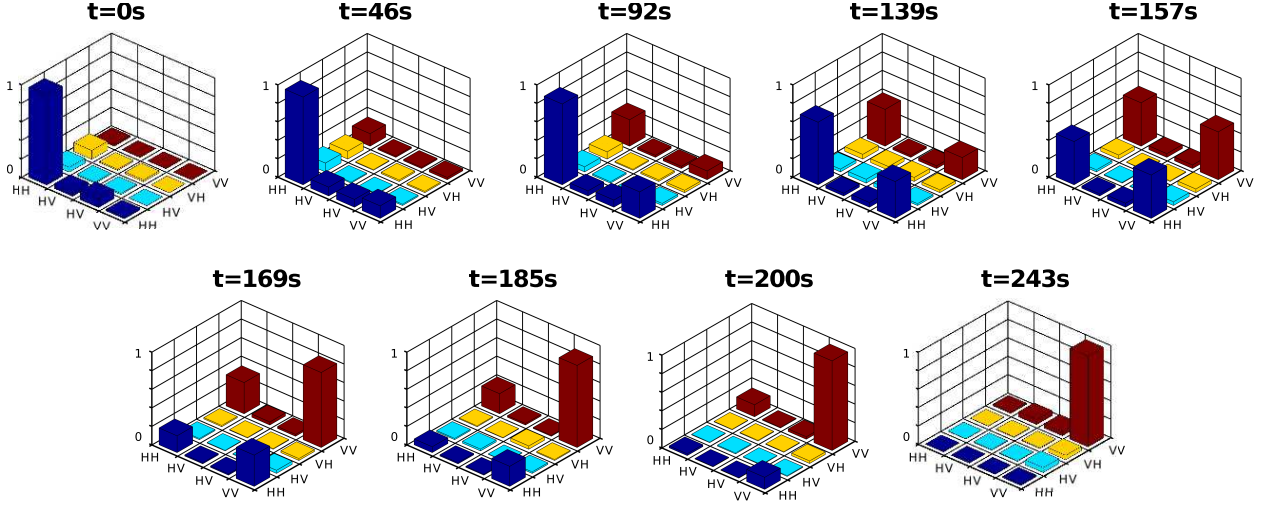


Figure C.12. Selected frames from a nine fps video of a two-qubit photon state's transition from separability ($|HH\rangle$ at $t=0$ s) to entanglement ($|HH\rangle + |VV\rangle$ at $t=157$ s) to separability ($|VV\rangle$ at $t=243$ s). Each frame shows a density matrix reconstructed using the previous 36 measurements (≈ 4 s of data).

each frame and comparing it to the target state, we directly measured the system precision to be $98\% \pm 1\%$ (for $|DV\rangle$) and $95\% \pm 2\%$ (for $|\phi^+\rangle$).

By utilizing fast EOM-based analyzers, a four-detector array triggered at 50 MHz, and a linear least-squares algorithm for tomographic reconstruction, the entangled photon polarimeter is capable of performing nine tomographies per second. Operated at this speed, $\tau_m = 80$ ms, $\tau_s = 20$ ms, and $\tau_a = 1$ ms. Total single-qubit insertion loss is measured to be $\eta = 3\text{--}3.4$ dB (not including detector inefficiency). The tomographic precision is estimated using a Monte Carlo simulation of this polarimeter's application to the entanglement source pictured in Fig. C.10 (resulting in ≈ 1000 coincidences per second). For nine-measurement tomographies ($T \approx 1$ s), $F_p(\hat{\rho}, \hat{\rho}_{\text{ideal}}) \approx 92\%$. For 36-measurement tomographies ($T \approx 4$ s), $F_p(\hat{\rho}, \hat{\rho}_{\text{ideal}}) \approx 96\%$. So in conclusion, we have built and demonstrated a device that uses

EOM-based polarization controllers to act as a real-time entangled-photon polarimeter for potential applications in QIP.

C.9. Troubleshooting

In our quest to develop the entangled photon polarimeter, we ran into a few main hurdles. The first hurdle was overcoming the inherent delay of the detectors during the initialization of each readout cycle. This was overcome using the makeshift free-running mode of operation for the detectors which is described above.

The next hurdle we ran into was that we obtained poor detection statistics. Poor statistics significantly limit the usefulness of the polarimeter since it requires us to integrate longer in order to obtain useful statistical values. The insufficient statistics was due to two factors. First, some components in the optical setup were dirty. After cleaning the optical paths of the culprits, our results improve, but only minimally. The larger problem of obtaining poor results lie with a dying detector (detector B on the Nucrypt box). This detector has been increasingly performing poorer and poorer as noted through discussions with Milja Medic and Matt Hall from their experiments. In order to overcome the poor statistical data, we simply integrated our results for longer durations. This unfortunately meant that we were unable to reach the more rapid goals originally set for the project.

As discussed earlier, DAC discontinuities also contributed to a hurdle for the development of the polarimeter. These discontinuities were for the most part ignored in the latter stages since they did not factor into the usage. Unfortunately, this will not likely be case for all future experiments and projects. As addressed earlier, this problem is being looked into with more detail at the time of publication.

Finally, as a result of the DAC discontinuities, we get imperfect canonical bases. The solution for this will be very trivial once the source of the discontinuities is discovered, and resolved. After we are rid of the discontinuities, simply calibrating the polcon stages with their proper voltage settings, we should be able to obtain the canonical basis more easily.

C.10. Derivation of polcon driving equations

Here we will derive the equations shown in Eq. (C.4). These equations describe the manner in which one can obtain the voltages required to drive the polcons. The derivation is based upon the steps taken by van Haasteren, et al^[128].

In order to derive these equations, we start by taking a look at the index ellipsoid for LiNbO₃ with an external electric field, E , with components in the x -direction and y -direction, E_x and E_y respectively.

$$\frac{1}{n_1^2}x^2 + \frac{1}{n_2^2}y^2 + \frac{1}{n_3^2}z^2 + \frac{2}{n_4^2}yz + \frac{2}{n_5^2}xz + \frac{2}{n_6^2}yz = 1 \quad (\text{C.6})$$

Using the electro-optic tensor for LiNbO₃, we can show that the index change due to the presence of the field is given by

$$\begin{pmatrix} \Delta\left(\frac{1}{n_1^2}\right) \\ \Delta\left(\frac{1}{n_2^2}\right) \\ \Delta\left(\frac{1}{n_1^2}\right) \\ \Delta\left(\frac{1}{n_1^2}\right) \\ \Delta\left(\frac{1}{n_1^2}\right) \\ \Delta\left(\frac{1}{n_1^2}\right) \end{pmatrix} = \begin{pmatrix} 0 & -r_{22} & r_{13} \\ 0 & r_{22} & r_{13} \\ 0 & 0 & r_{33} \\ 0 & r_{42} & 0 \\ r_{42} & 0 & 0 \\ -r_{22} & 0 & 0 \end{pmatrix} \begin{pmatrix} E_x \\ E_y \\ E_z \end{pmatrix} \quad (\text{C.7})$$

Based on this and accounting for the fact that our LiNbO₃ polcon is a uniaxial, x -cut, z -propagating waveguide, we can obtain the following relations.

$$\begin{aligned}
\frac{1}{n_1^2} &= \frac{1}{n_0^2} - r_{22}E_y + r_{13}E_z & \frac{1}{n_2^2} &= \frac{1}{n_0^2} + r_{22}E_y + r_{13}E_z \\
\frac{1}{n_3^2} &= \frac{1}{n_e^2} + r_{33}E_z & \frac{1}{n_4^2} &= r_{42}E_y \\
\frac{1}{n_5^2} &= r_{42}E_x & \frac{1}{n_6^2} &= -r_{22}E_x
\end{aligned} \tag{C.8}$$

Note here that n_o and n_e are the ordinary and extraordinary indices of LiNbO₃

By plugging these relations into Eq. (C.6), ignoring the E_z component of the electric field, and looking only at the intersection of the resulting index ellipsoid with the xy -plane, we obtain Eq. (C.9) for an ellipse.

$$\left(\frac{1}{n_o^2} - r_{22}E_y\right)x^2 + \left(\frac{1}{n_o^2} + r_{22}E_y\right)y^2 - 2r_{22}E_xxy - 1 = 0 \tag{C.9}$$

$$ax^2 + 2bxy + cy^2 + 2dx + 2fy + g = 0 \tag{C.10}$$

$$\varphi = \frac{1}{2} \arctan\left(\frac{2b}{a-c}\right) \tag{C.11}$$

Equation (C.10) is the general equation for a quadratic, and Eq. (C.11) defines the angle between the x -axis and the major axis of an ellipse. Thus, by equating the coefficients in Eq. (C.9) with those in Eq. (C.10) for a general ellipse, and using Eq. (C.11), we can obtain

$$\varphi = \frac{1}{2} \arctan\left(\frac{r_{22}E_x}{r_{22}E_y}\right) \tag{C.12}$$

Here, we assume that our crystal's axes are aligned with the x -axis, y -axis, and z -axis of the electric field. Equipped this knowledge, we define the physical orientation angle as φ , the angle between the x -axis and the major axis of the ellipse described by Eq. (C.9) as shown in Fig. C.13.

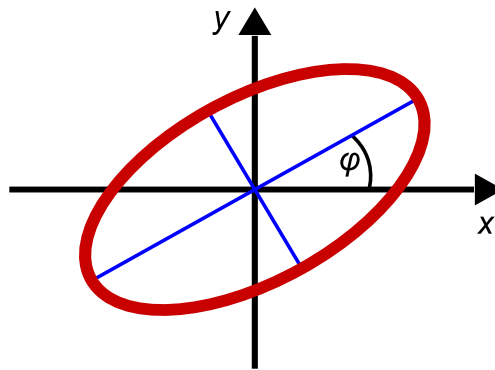


Figure C.13. Cross-section of the index ellipsoid for LiNbO_3 and the xy -plane.

Based on the physical interpretation of the index ellipse, we realize that $n_o^3 r_{22} E_x$ and $n_o^3 r_{22} E_y$ represent the indices of refraction along the x and y axes. Using this knowledge, we can define two phase retardances show in Eq. (C.13). These retardances are derived by simply multiplying the aforementioned indices by the length of electrode in order to obtain the optical path, and then converting the lengths into phase.

$$\tau_1 = \frac{\omega}{c} L r_{22} n_o^3 E_x \quad (\text{C.13a})$$

$$\tau_2 = \frac{\omega}{c} L r_{22} n_o^3 E_y \quad (\text{C.13b})$$

Using these phase retardances and Eq. (C.12), it is trivial to define a phase retardance τ at the output of the waveguide as:

$$\tau = \tau_2 \cos(2\varphi) - \tau_1 \sin(2\varphi) \quad (\text{C.14})$$

For future use, and convenience, we rewrite Eq. (C.12) as follows.

$$\varphi = \frac{1}{2} \arctan\left(\frac{\tau_1}{\tau_2}\right) \quad (\text{C.15})$$

So now to make this useful, we want to come up with a means to convert the voltages on terminals V_a and V_c into the parameters τ and φ . In LiNbO_3 , the relationship between the applied voltage differences and the external electric field is linear. Thus, we can write the following matrix relationship.

$$\begin{bmatrix} \tau_1 \\ \tau_2 \end{bmatrix} = \begin{bmatrix} t_{11} & t_{12} \\ t_{21} & t_{22} \end{bmatrix} \begin{bmatrix} U_s \\ U_{as} \end{bmatrix} \quad (\text{C.16})$$

As per van Haasteren's paper^[128], we define the symmetric and antisymmetric potentials, U_s and U_{as} , in terms of V_a and V_c (when V_b is ground) as

$$\begin{bmatrix} U_s \\ U_{as} \end{bmatrix} = \begin{bmatrix} \frac{1}{2} & \frac{1}{2} \\ -1 & 1 \end{bmatrix} \begin{bmatrix} V_a \\ V_c \end{bmatrix} \quad (\text{C.17})$$

We now introduce two terms, V_π and V_0 . The first parameter corresponds to the voltage required to induce a π -phase shift between the TE and TM modes, and the latter parameter is the voltage required to rotate all the power from the TE mode to the TM mode, or vice versa. Setting these voltages such that $t_{11} = \pi/\lambda V_0$, and $t_{22} = \pi/\lambda V_\pi$, and by setting

$t_{12} = t_{21} = 0$, we can easily show that

$$V_a = 2V_0 \cdot \frac{\lambda}{2\pi} \cdot \tau_1 - V_\pi \cdot \frac{\lambda}{2\pi} \cdot \tau_2 \quad (\text{C.18a})$$

$$V_c = 2V_0 \cdot \frac{\lambda}{2\pi} \cdot \tau_1 + V_\pi \cdot \frac{\lambda}{2\pi} \cdot \tau_2 \quad (\text{C.18b})$$

During this derivation, we have neglected the effect of the intrinsic birefringence of the LiNbO₃ crystal. In order to correct for this effect, we add bias voltages to Eqs. (C.18). This can also be corrected for during the derivation in a couple different locations. For example, we can introduce a term τ_i which describes a phase retardance due to the influence of birefringence into Eq. (C.14) and Eq. (C.15) by replacing τ_2 with $\tau_2 + \tau_i$. This method is used in van Haasteren's derivation.

Once we have corrected for the intrinsic birefringence effect, and supplying in the trigonometric relations for τ , we get our result shown in Eqs. (C.19). As a sanity check, we verify that these match the equations in Eqs. (C.4).

$$V_a = 2V_0 \cdot \frac{\lambda}{2\pi} \tau \cdot \sin(\alpha) - V_\pi \cdot \frac{\lambda}{2\pi} \tau \cdot \cos(\alpha) + V_{a,bias} \quad (\text{C.19a})$$

$$V_b = 0 \text{ (Ground)} \quad (\text{C.19b})$$

$$V_c = 2V_0 \cdot \frac{\lambda}{2\pi} \tau \cdot \sin(\alpha) + V_\pi \cdot \frac{\lambda}{2\pi} \tau \cdot \cos(\alpha) + V_{c,bias} \quad (\text{C.19c})$$

APPENDIX D

Interfacing with various lab equipment

Since I, along with Joe Altepeter, encouraged the adoption of Linux as our group’s primary operating system, I include here instructions for installation, use, and troubleshooting of programs that may be useful for future users in our lab. Where appropriate, I also show and explain useful code (scripts) for interfacing with, and/or collecting data from various instruments used in our lab. I also include in this appendix scripts for plotting and saving the collected data.

For most of the code shown in the appendix, I use python. If instead, I am referring to a terminal prompt, or a bash script, it will either be explicitly noted or the traditional “`>> cmd`” for the command line prompt will be shown.

D.1. Determining the serial port for a connected device

In this section, we will learn how to determine which port a device is connected to after we plug it into the computer. For the sake of this appendix, I use the terms “USB” and “serial” interchangeably. In general, when Linux adds a USB port for communication, it assigns the port to `/dev/ttyUSBn`, where n is usually (although not always) the lowest available integer. While this is convenient, it can often become confusing when many serial devices (CPDS detectors, AWP, measurement equipment, etc) are connected to the same computer. Although it would be useful to have a script automatically diagnose which device maps to which port, it has sufficed thus far to run the following command twice—once with

the desired device on, and once with it off—and look for which device was removed and added.

```
>> dmesg | grep ttyUSB
```

Sometimes, simply turning the device off and on again is insufficient. In these scenarios, unplug the USB cable, wait briefly (≈ 10 s), and then re-plug the cable into the socket. If the computer still does not recognize your device, consider rebooting the computer with the device plugged in or not plugged in. Ideally, one of these situations should enable you to recognize the device's port. Note that by rebooting the computer, you may re-map the ports. Thus, you will need to verify all other device mappings again.

Oftentimes, without requiring a power cycle, the output of the `dmesg` command provides some insight to the port-device mapping. For instance, there are typically four AWP's that are referenced by `FTDI USB Serial Device converter now attached to ttyUSBn`. Once you know the four numbers for n , you can individually probe those ports using the AWP's `identify` command.

Similarly, devices which are shown as `p12303 converter` are serial-to-USB adapters. In our setup, these correspond to the detector and the MDLs. By looking at the associated device ID number—typically `usb 2-1.p(.q)`—one can decipher whether the device is the detector or the MDLs that are connected to a USB hub. As a hint, the device that is listed as `usb 2-1.p` is usually the detector, whereas the devices that include the additional suffix `.q` are the MDLs connected to the USB hub.

D.1.1. User privileges for `ttyUSBn` access

As is true with much of Linux, user permissions are very important for accessing files and devices. (For more information on Linux user permissions, google "Linux File Permissions").

By default, the owner of all serial connections is `root`, and the group with whom it is shared is `dialout`. As such, it is VERY important to add all potential users to the `dialout` group. You can check whether you are in the `dialout` group by typing in the terminal the command:

```
>> groups
```

This lists all the groups of which you are a member, and one of them should be `dialout`. If you are not, you (or an administrator) can add you to the `dialout` group using the command:

```
>> sudo usermod -a -G dialout nealoza
```

where you can replace "nealoza" with the appropriate username. Once this is done, you should be able to communicate with all serial ports on the computer. Now that we have the ability to talk to the serial ports, we will next look at an interface for Linux that we can use to leverage this ability.

D.2. Setting up minicom

In this section, I describe how to setup and use a program called `minicom` to communicate to many RS-232C, USB, GPIB, and other serial connections. In our lab, we often use `minicom` to run commands for communicating with the Nucrypt CPDS detectors. Since this appendix is written for Unix-based computers, including OS X, if you wish to you use Windows as your OS, please use `hyperterminal` for your serial communication needs.

D.2.1. Installing and basic usage of minicom

If `minicom` has not already been installed, use the following command in a terminal to install it:

```
>> sudo apt-get install minicom
```

This will require administrator privileges, so if you do not have that for the computer, either obtain access or have an administrator install the program. Once the program is installed, you can run the program using

```
>> minicom
```

If you wish to enable the colorful interface which often helps when trying to find counts using the CPDS4 detectors, you can use the command

```
>> minicom -c on
```

Using these commands, you now have access to `minicom`. If, at any time, you are uncertain about which commands you can use to adjust your `minicom` behavior or interface, type `CTRL-A Z` to bring up the Help Menu. If things are setup correctly, you will likely use this sparingly.

When you are done using `minicom`, you can type `CTRL-A X` to exit the interface and return to the computer terminal.

D.2.2. Settings for `minicom`

Once the user can start `minicom`, they need to ensure that the program is setup correctly. In order to view or adjust settings for `minicom`, the user must access the `minicom` settings page. From the terminal, the user can type:

```
>> minicom -s
```

If `minicom` is already open, the user can just type `CTRL-A O`. The main parameters of interest are as follows: serial port, baudrate, data lengths, parity, hardware flow control, and software flow control.

The serial port is typically set to `/dev/ttyUSBn`. Again, n is an integer. Adjust the baudrate appropriately for the device with which you are communicating.

Communication with the CPDS detectors uses a baudrate of 115200. Waveplates and measurement instruments can also work at this baudrate, although other instruments, such as the CSA, use the traditional baudrate of 9600. Consult their manuals to determine the appropriate baudrate.

The data length should be set to eight bits. The parity should be turned off, i.e., set to 'N' for 'None'. There should be one stop bit. These three settings are often expressed more simply as 8N1.

The hardware and software flow control should be set to "Yes" and "No", respectively.

D.2.3. Troubleshooting `minicom`

1) I receive a `"/dev/ttyUSBn locked"` error when I try to initialize `minicom`.

First, ensure that you are part of the `dialout` group. If not, see the instructions above in section (SECTION) to add your username. If you are a `dialout` member, check to see if someone else has an open instance of `minicom` for that port. If no one else is using it and you do not have another window with it open, have an administrator delete the lock file from `/var/lock/`. The file will typically have a name like `/var/lock/LCK..ttyUSB0`.

2) After `minicom` is initialized, the screen stays blank.

Check to make sure the device you are controlling is on. If it is on, then the likeliest problem is that the serial port setting is incorrect. Follow the instructions in section (SECTION) to determine and adjust the settings appropriately.

3) I seem to be able to do something, but all I see is nonsense symbols and characters.

Check the baudrate at which you should be operating the device in question. Oftentimes, a wrong baudrate yields improper data communication which translates to gobbledygook on the screen.

D.3. Interfacing with and Plotting from Lab Instruments

In this section, I present the code that we use to interface with, and in some cases, plot data from various lab instruments. The instruments that I will show the code for here are: (1) Tektronix CSA-803 Communication Signal Analyzer with SD-24 and SD-40 sampling head modules, hereinafter called CSA; (2) Agilent 86140b Optical Spectrum Analyzer, hereinafter called OSA; (3) Lecroy LT354 Oscilloscope, hereinafter called Lecroy Oscilloscope; (4) Agilent E4430A Electrical Spectrum Analyzer, hereinafter called ESA; (5) Agilent 86100A (86105A) Digital Communication Analyzer, hereinafter called DCA; (6) Arduino Uno.

D.3.1. Plotting for the CSA

```
1 import os.path
2 import sys
3 import array
4 import time
5 import serial
6 import string
7 import numpy
8 import pylab
9 import pickle
10
11 if __name__ == '__main__':
12     # Prologix GPIB-USB Controller serial port
13     comport = "/dev/ttyUSB5"
14     # HP33120A GPIB address (can be checked on the CSA front Panel)
15     addr = 17
16
17     # Open serial port to communicate with CSA
18     ser = serial.Serial( comport, 9600, timeout=0.5 )
19
20     # Set mode as CONTROLLER
21     ser.write("++mode 1\n")
22
23     # Set CSA address
24     ser.write("++addr " + str(addr) + "\n")
25
26     # Turn off read-after-write to avoid "Query Unterminated" errors
27     ser.write("++auto 0\n")
```

```

28
29 # Do not append CR or LF to GPIB data
30 ser.write("++eos 3\n")
31
32 # Assert EOI with last byte to indicate end of data
33 ser.write("++eoi 1\n")
34 #end GPIB configuration
35 # =====
36
37 # Ask CSA for data points from the specified trace
38 #output will be in ascii format
39 #####
40 # Change the TRACE# in following command to select #
41 # TRACE0 = Channel 3 and 4 (SD-30 Sampling Head) #
42 # TRACE1 = Channel 3 and 4 (SD-30 Sampling Head) #
43 # TRACE2 = Channel 1 (SD-24 Sampling Head) #
44 # TRACE3 = Channel 2 (SD-24 Sampling Head) #
45 #####
46 cmd = "OUTPUT TRACE3;ENDCG WAV:BIN;BYT.OR LSB;CURVE? "
47 #send command to CSA
48 ser.write(cmd + "\n") # \n must be included to signal that the command
49 #has ended (this is for the GPIB USB adapter)
50 #instruct computer to listen for response
51 ser.write("++read eoi" + "\n") # \n must be included to signal that the
52 #command has ended
53 #read response
54 text = ser.read(100000)
55 #print(text)
56
57 #now convert the text data to a list of integers
58 points = list()
59 buff = ""
60 i = 0
61 #loop through the preamble without recording any of it
62 while(text[i]!='\n'):
63     i+=1
64 #skip the last character of pre-amble
65 i+=1
66
67 while(i < len(text)):
68     #read the numbers fore each data point digit-by-digit and store each
69     #digit in a buffer.
70     if(text[i]!='\n'):
71         buff=string.join([buff,text[i]], sep='')
72     #Once a comma is reached, convert the buffered string
73     #to an integer and concatenate to the list of datpoints
74     else:
75         points.append(int(buff))
76         buff=""

```

```

75     i+=1
76     #concatenate the last buffered value onto the list of data points
77     points.append(int(buff))
78     #print(points)
79
80     #command to ask CSA what the x increments are for the data-points
81     cmd = "WFMPRE? Xincr "
82     #send command
83     ser.write(cmd + "\n")
84     #instruct computer to listen for response
85     ser.write("++read eoi" + "\n")
86     #read response from CSA
87     xincSTR=ser.read(1000)
88     #now convert the string into a floating point number
89     buff = ""
90     i = 0
91     #loop through the preamble without recording any of it
92     while(xincSTR[i]!=':'):
93         i+=1
94     #skip the last character of pre-amble
95     i+=1
96
97     while(i<len(xincSTR)):
98         #convert to a number by iteratively appending each digit of the
99         #string to a buffer
100        if(xincSTR[i]!='E'):
101            buff=string.join([buff,xincSTR[i]], sep='')
102            i+=1
103        #when the next character in the string ie "E" the buffer is full,
104        #and we have read all the digits of the mantissa of the float
105        else:
106            #convert the buffer to a float
107            mantissa=float(buff)
108            i+=1 #skip the 'E'
109            break
110        #clear the buffer
111        buff=""
112        #convert the remainder of the string to a number by iteratively
113        #appending each digit of the string to a buffer
114        while(i<len(xincSTR)):
115            buff=string.join([buff,xincSTR[i]], sep='')
116            i+=1
117        #when the end of the string has been reached, convert the buffer to an
118        #int
119        exponent=int(buff)
120        #multiply the mantissa by the appropriate power of ten to get the x
121        #increment
122        xinc = mantissa*pow(10, exponent)

```



```

119 #command to ask CSA what the x offset (xzero) is for the data-points
120 cmd = "WFMPRE? XZErO "
121 ser.write(cmd + "\n")
122 ser.write("++read eoi" + "\n")
123 xzeroSTR=ser.read(1000)
124 buff = ""
125 i = 0
126 while(xzeroSTR[i]!=':'):
127     i+=1
128 i+=1
129 while(i<len(xzeroSTR)):
130     if(xzeroSTR[i]!='E'):
131         buff=string.join([buff,xzeroSTR[i]], sep='')
132         i+=1
133     else:
134         mantissa=float(buff)
135         i+=1
136         break
137 buff=""
138 while(i<len(xzeroSTR)):
139     buff=string.join([buff,xzeroSTR[i]], sep='')
140     i+=1
141 exponent=int(buff)
142 xzero = mantissa*pow(10, exponent)
143
144
145
146 #command to ask CSA what the scale factor is for the data-points
147 cmd = "WFMPRE? YMUlt "
148 ser.write(cmd + "\n")
149 ser.write("++read eoi" + "\n")
150 ymultSTR=ser.read(1000)
151 buff = ""
152 i = 0
153 while(ymultSTR[i]!=':'):
154     i+=1
155 i+=1
156 while(i<len(ymultSTR)):
157     if(ymultSTR[i]!='E'):
158         buff=string.join([buff,ymultSTR[i]], sep='')
159         i+=1
160     else:
161         mantissa=float(buff)
162         i+=1
163         break
164 buff=""
165 while(i<len(ymultSTR)):
166     buff=string.join([buff,ymultSTR[i]], sep='')
167     i+=1

```

```

168 exponent=int(buff)
169 ymult = mantissa*pow(10, exponent)
170
171
172
173 #command to ask CSA what the x offset is for the data-points
174 cmd = "WFMPRE? YZEro "
175 ser.write(cmd + "\n")
176 ser.write("++read eoi" + "\n")
177 yzeroSTR=ser.read(1000)
178 buff = ""
179 i = 0
180 while(yzeroSTR[i]!=':'):
181     i+=1
182 i+=1
183 while(i<len(yzeroSTR)):
184     if(yzeroSTR[i]!='E'):
185         buff=string.join([buff,yzeroSTR[i]], sep='')
186         i+=1
187     else:
188         mantissa=float(buff)
189         i+=1
190         break
191
192 buff=""
193 while(i<len(yzeroSTR)):
194     buff=string.join([buff,yzeroSTR[i]], sep='')
195     i+=1
196 exponent=int(buff)
197 yzero = mantissa*pow(10, exponent)
198
199
200 #create an array, xvals, of the same length as points, populate xvals
with the appropriate time values, and store in the numpy array x
201 xvals = range(len(points))
202 for i in xvals:
203     xvals[i] = xzero+xinc*xvals[i]
204 x = numpy.array(xvals)
205
206 #create an array, yvals, of the same length as points, convert the
points values to voltage values and store in the numpy array y
207 yvals = range(len(points))
208 for i in yvals:
209     yvals[i] = yzero + ymult*points[i]
210 y = numpy.array(yvals)
211
212 #plotting the scope trace
213 print("len(x)", x.size, "len(y)", y.size)
214 pylab.plot(x,y)

```

```
215 pylab.xlabel("Time (s)")
216 pylab.ylabel("Amplitude (V)")
217 pylab.show()
218 # Name the files for the x and y values here
219 numpy.savetxt('XBarSwCW_0015_100m_x.txt', x);
220 numpy.savetxt('XBarSwCW_0015_100m_y.txt', y);
221
222 # fx= open('savxFile.txt', 'w');
223 # fy= open('savyFile.txt', 'w');
224 # fx.write('x = ' + str(x) + ';\n');
225 # fy.write('y = ' + str(y) + ';\n');
226 # fx.close();
```

CSA Code: Tektronix CSA803 w/ SD-24 and SD-40

D.3.2. Plotting for the OSA

```

1 import numpy, pylab, glob
2
3 fileList = glob.glob('./Filter Characterization/*.CSV');
4 #fname = "./osaSpectra/OSAdgf.csv";
5
6 for fname in fileList:
7     picName = fname.strip('./').strip('CSV');
8     f = open(fname);
9     allData = f.read().split();
10    szData = len(allData);
11    plotInfo = [allData[i].split(',') for i in range(0,47)]
12    xStart = float(plotInfo[11][1]);
13    xStop = float(plotInfo[12][1]);
14    xDiff = xStop-xStart;
15    xInc = xDiff/1000;
16    allData = [allData[i].split(',') for i in range(47, szData-3)]
17    raData = numpy.array(allData);
18    raData = numpy.reshape(raData, -1);
19    flData = numpy.array([float(raData[i]) for i in range(len(raData))])
20    flData = numpy.reshape(flData, (-1, 2));
21    xData = (flData[:,0] - flData[0,0])*xInc+xStart;
22    yData = flData[:,1];
23    pylab.plot(xData, yData);
24    pylab.xlabel('Wavelength (nm)');
25    pylab.ylabel('Amplitude (dBm)');
26    pylab.xlim(xData[0], xData[-1])
27    pylab.xticks(numpy.arange(11)*xDiff/10+xStart);
28    pylab.ylim(-65, 5)
29    pylab.title(fname)
30    pylab.savefig(picName);
31    #pylab.show();
32    pylab.clf();

```

OSA Code: Agilent 86140b

D.3.3. Plotting for the Lecroy Oscilloscope

```

1 import numpy, pylab, glob, time
2
3 psUnit = 1; # Variable to choose between ms or ps (0 = ms, 1 = ps)
4
5 fileList = glob.glob('./*.txt');
6 #fileList = ['./IMRAautoCorr120716.txt'];
7 #fname = './1550autoCorrG.txt';
8 #fname = './IMRAautoCorr10.txt';
9 for fname in fileList:
10     picName = fname.strip('./').strip('txt');
11     f = open(fname);
12     allData = f.read().split();
13     szData = len(allData);
14     plotInfo = [allData[i].split(',') for i in range(0,7)]
15     allData = [allData[i].split(',') for i in range(7, szData)]
16     raData = numpy.array(allData);
17     raData = numpy.reshape(raData, -1);
18     flData = numpy.array([float(raData[i]) for i in range(len(raData))])
19     flData = numpy.reshape(flData, (-1, 2));
20     xData = (flData[:,0] - flData[0,0])*1000*(29*psUnit+1);
21     yData = flData[:,1];
22     pylab.plot(xData, yData);
23     if psUnit == 1:
24         pylab.xlabel('Time (ps)');
25     else:
26         pylab.xlabel('Time (ms)');
27     pylab.ylabel('Amplitude (V)');
28     pylab.xlim((xData[0], xData[-1]));
29     pylab.xticks(xData[-2]*numpy.arange(11)/10);
30     pylab.title(fname);
31     pylab.minorticks_on();
32     pylab.grid(which='minor');
33     pylab.savefig(picName);
34     #pylab.show();
35     pylab.clf();

```

Oscilloscope Code: Lecroy LT354

D.3.4. Plotting for the ESA

```

1 #####
2 # This code returns plots of the ESA (Agilent E4403b)
3 #####
4 import numpy, pylab, glob, time
5
6 # Create variable to determine how to output plot
7 # Set to 0 to only show on screen
8 # Set to 1 to save to a file
9 # Set to 2 to do both
10 saveFile = 0
11
12 prefix = '../PLDRODebug/'
13 suffix = '.CSV'
14 # Uses glob to grab every file in a directory
15 #fileList = glob.glob(prefix+'*'+suffix)
16 # For single file use, comment the line above and uncomment the line below
17 fileList = [prefix+ 'TRACE006' +suffix]
18
19 ctrFreq = -1
20 span = -1
21 rbw = -1
22 vbw = -1
23 refLevel = -1
24
25 # Iterate through all files selected using glob
26 for fname in fileList:
27     plotData = []
28     # Create the name for the file we will save the plot to
29     plotName = fname.strip(prefix).strip(suffix)
30
31     # Open File
32     print('Opening ' + fname)
33     f = open(fname)
34     # Read in all the data and divide by lines
35     allData = f.read().splitlines()
36     # Return the size of the file (as a # of lines)
37     szData = len(allData)
38
39     # Parse the "header" information from the file, otherwise
40     # parse the actual (plottable) data from the file
41     for line in allData:
42         ll = line.split(',')
43         ll[0] = ll[0].strip()
44         if ll[0] == 'Center Frequency:':
45             ctrFreq = float(ll[1])
46             print('Center Frequency = ' + str(ctrFreq*1e-9) + ' GHz')

```

```

47     elif ll[0] == 'Span:':
48         span = float(ll[1])
49         print('Span = ' + str(span) + ' Hz')
50     elif ll[0] == 'Resolution Bandwidth:':
51         rbw = float(ll[1])
52         print('RBW = ' + str(rbw) + ' Hz')
53     elif ll[0] == 'Video Bandwidth:':
54         vbw = float(ll[1])
55         print('VBW = ' + str(vbw) + ' Hz')
56     elif ll[0] == 'Reference Level:':
57         refLevel = float(ll[1])
58         print('Reference Level = ' + str(refLevel) + ' dBm')
59     elif ll[0].isdigit():
60         xval = float(ll[0])*1e-6
61         yval = float(ll[1])
62         plotData.append([xval, yval])
63
64     xmin = (ctrFreq - span/2)*1e-6
65     xmax = (ctrFreq + span/2)*1e-6
66     print('Range:' + str(xmin) + ' MHz to ' + str(xmax) + ' MHz')
67     # Convert the data into a numpy array (for plotting)
68     numpyData = numpy.array(plotData)
69     numpyData = numpy.reshape(numpyData, (-1, 2))
70     # Select out the x and y data
71     xData = numpyData[:,0]
72     yData = numpyData[:,1]
73
74     # Plot the data!
75     pylab.plot(xData, yData, linewidth=2.0, marker='o')
76     # Add the required "extra" stuff to the plot
77     pylab.xlabel('Frequency (MHz)')
78     pylab.ylabel('Power (dBm)')
79     pylab.xlim((xmin, xmax))
80     numTicks = 5
81     pylab.xticks((xmax-xmin)*numpy.arange(numTicks)/(numTicks-1)+xmin)
82     #pylab.title(fname)
83     #pylab.minorticks_on()
84     #pylab.grid(which='minor')
85
86 # Save the data to a file
87 if saveFile == 0:
88     pylab.show()
89 elif saveFile == 1:
90     pylab.savefig(plotName)
91 else:
92     pylab.show()
93     pylab.savefig(plotName)
94 # Clear the figure from the screen or buffer
95 pylab.clf()

```

96

97 # Aaaaaaand we're done!

ESA Code: Agilent E4430A

D.3.5. Plotting for the DCA

```

1 # Plot the spectrogram of files obtained from Southern Photonics FROG
2
3 import numpy, pylab, glob
4 from matplotlib import ticker
5
6 fileList = glob.glob('./SwTraces/130818/run3/*.txt')
7 print(fileList.sort())
8 #fname = "./waveform1.txt"
9
10 for fname in fileList:
11     picName = fname.strip('./SwTraces/130818/run3/').strip('.txt')
12     print(picName)
13     pwr = int(picName[-9:-7])
14
15     f = open(fname)
16     readData = f.read() # Read all raw data as strings
17     readLines = readData.split('\r\n')
18     #szLines = len(readLines)
19     #parseLines = [readLines[ii].split(',') for ii in range(0,szLines)]
20     #header = parseLines[0:18]
21     #data = parseLines[18:]
22     #print(data)
23     #data = numpy.array([float(data[ii]) for ii in range(0,szData)])
24     data = readData.split()
25     szData = len(data)
26     data = [data[ii].strip(',') for ii in range(0,szData)]
27     header = data[0:43]
28     data = data[43:]
29     szData = len(data)
30
31     points = int(header[3])
32     xOff = float(header[22])*(10**12) # Scaled for ps
33
34     data = numpy.array([float(data[ii]) for ii in range(0,szData)])
35     data = data.reshape(points,2).transpose()
36     data[0] = data[0]*(10**12) # Scale for ps
37     data[1] = data[1]*(10**6) # Scale for ps
38
39     (val, mod) = divmod(pwr/2, 3)
40     if mod == 0: clr = (0, 0, val/4.+0.25)
41     elif mod == 1: clr = (0, val/4.+0.25, 0)
42     else: clr = (val/4.+0.25, 0, 0)
43
44     print(val, mod, clr)
45     pylab.plot(data[0]-xOff, data[1], label=(str(pwr*100)+' mW'), \
46               color=clr, linewidth=2)

```

```
47
48     # Plot the data
49     pylab.xlabel('Time (ps)')
50     pylab.ylabel('Power (uW)')
51     pylab.grid('on')
52     pylab.legend()
53     #pylab.title(picName)
54 #pylab.show()
55     pylab.savefig('./' + picName)
56 #pylab.clf()
57 f.close()
```

DCA Code: Agilent 86100A w/ 86105A

D.3.6. PID feedback control using Arduino Uno

The code in this subsection uses the Arduino coding language which is based on the Processing and Wiring programming languages.

```

1  /*
2   PIDfeedback.ino
3   Code to use Arduino as a PID feedback controller for two UMZIs
4   (UMZI = Unbalanced Mach-Zehnder Interferometers)
5  */
6
7  #include <PID_v1.h>
8
9  // Define variables/constants for changing PWM frequency
10 // from prescale = 64 (default) to prescale = 1
11 // corresponding to freq = 488.28125 Hz to freq = 31.25 kHz (respectively)
12 // Changes the clock for PWM on pins 3 and 11
13 // Google "arduino TCCR2B" for more information
14 const byte mask = B11111000; // Mask bits that are not prescale values
15 const int prescale = 1;
16
17 // Variables used for debugging
18 // 0 = Off or False
19 // 1 = On or True
20 #define turnOn 1
21 #define dispON 0
22 #define dlyOn 0
23
24 /* *****
25  Many variables are arrays of two elements.
26  The first is to control one UMZI, and the
27  second is to control the other UMZI.
28  ***** */
29
30 // Define variables we'll connect to
31 double inPID;
32 double outPID[2];
33 double setPID[2];
34
35 // Define the PID gain parameters
36 const double Kk = 0.005;
37 const double Ki[2] = {Kk, 0.0003};
38
39 const double setV = 1.0; // in V (between 0 and 5 V) <<<-----SET
    VOLTAGE-----<<<<<<
40 const double setPt[2] = {0.25, 0.25}; // Fraction between [0,1] for where
    to set the setPoint

```

```

41
42 // Declare pin labels here for universal usage
43 const int inPin[2] = {A3, A1}; // Set analog pin A3 for PID1 in
44 const int outPin[2] = {3, 11}; // Set digital pin 3 for PID1 out
45
46 double err = 0.0;
47
48 /*
49  1 <= upLim <= 255
50  0 <= loLim <= 254
51 */
52 const int upLim = 255;
53 const int loLim = 0;
54 const int diff = 250; // margin between limit and reset point
55
56 void setup() {
57   Serial.begin(9600); // Connect to serial monitor (baudrate = 9600)
58
59   // Set the PWM to output in Fast PWM mode to increase frequency to ~62.5
   kHz
60 // TCCR2A = _BV(COM2A1) | _BV(COM2B1) | _BV(WGM21) | _BV(WGM20);
61 // TCCR2B = _BV(CS22);
62 // Set the PWM frequency to 31.25 kHz
63 TCCR2B = (TCCR2B & mask) | prescale;
64 pinMode(outPin[0], OUTPUT);
65 pinMode(outPin[1], OUTPUT);
66
67 //pinMode(aInPin, INPUT);
68 outPID = {128, 128};
69 //setPID = setV*1024/5.0;
70 setPID[0] = 1024*setPt[0];
71 setPID[1] = 1024*setPt[1];
72 }
73
74 void loop() {
75   // Run loop to perform a task (repeatedly)
76   #if turnOn
77     processPID(inPin[0], outPin[0], setPID[0], &outPID[0], Ki[0]);
78     processPID(inPin[1], outPin[1], setPID[1], &outPID[1], Ki[1]);
79   #endif
80 }
81
82 void processPID(int inPort, int outPort, double sPID, double* oPID, double
   Kit) {
83   inPID = analogRead(inPort);
84   err = sPID - inPID;
85   *oPID += Kit*err;
86
87   if(*oPID >= upLim) {

```

```
88     *oPID = upLim-diff;
89     #if dispON
90         Serial.print("\n^^^^^^^^^^^^^^^^\n");
91     #endif
92 }
93 else if(*oPID <= loLim){
94     *oPID = loLim+diff;
95     #if dispON
96         Serial.print("\n#####\n");
97     #endif
98 }
99
100 analogWrite(outPort, *oPID);
101
102 #if dispON
103     Serial.print("Err: ");
104     Serial.print(err);
105     Serial.print("\t outPID: ");
106     Serial.print(*oPID);
107     Serial.print("\t Set: ");
108     Serial.print(sPID);
109     Serial.print("\t inPID: ");
110     Serial.print(inPID);
111     Serial.print("\t inVolt: ");
112     Serial.print(inPID*5.0/1023.0);
113     Serial.print('\n');
114 #endif
115
116 #if dlyOn
117     delay(1000);
118 #endif
119 }
```

Arduino PID Feedback Control

APPENDIX E

Dirac Bracket Notation, Linear Algebra, and Hilbert Spaces

Although this information is located in books^[118,129,130] and on the internet^[131–133], we will briefly look at the definitions of states and operators using Dirac bracket notation and linear algebra. This is done for fun, (over-)completeness, and as a promise to my brother that he should be able to understand this dissertation based on our undergraduate coursework—or at least our shared life experiences.

Without further ado, any pure state can be represented as a vector. In Dirac notation, we reference a state with $|\psi\rangle$, or orally spoken “ket psi”. Here, ψ is just a label for the state. For all intents and purposes, that label could be 🐦, 🦇, ⚽, 🏏, ☯, 🏏, or 😊. The respective states for such labels would be $|\text{🐦}\rangle$, $|\text{🦇}\rangle$, $|\text{⚽}\rangle$, $|\text{🏏}\rangle$, $|\text{☯}\rangle$, $|\text{🏏}\rangle$, and $|\text{😊}\rangle$. We can thus write the state as a decomposition of its characteristic features, i.e., its bases. If we use $|\text{⚽}\rangle$ as an example, its bases include size, color, number of panels, location, and velocity. Characteristics which remain the same for the entire duration of the experiment or calculation can safely be ignored. For our example, assuming only one ball is used in a game (our proverbial “calculation”) and we consider discrete moments in time, then we can describe the ball’s location on the field as a function of two parameters, x and y . Visually, this is easily imagined as shown in Fig. E.1. Mathematically, we can write that state as

$$|\text{⚽}\rangle = x |\text{⚽}_X\rangle + y |\text{⚽}_Y\rangle. \quad (\text{E.1})$$

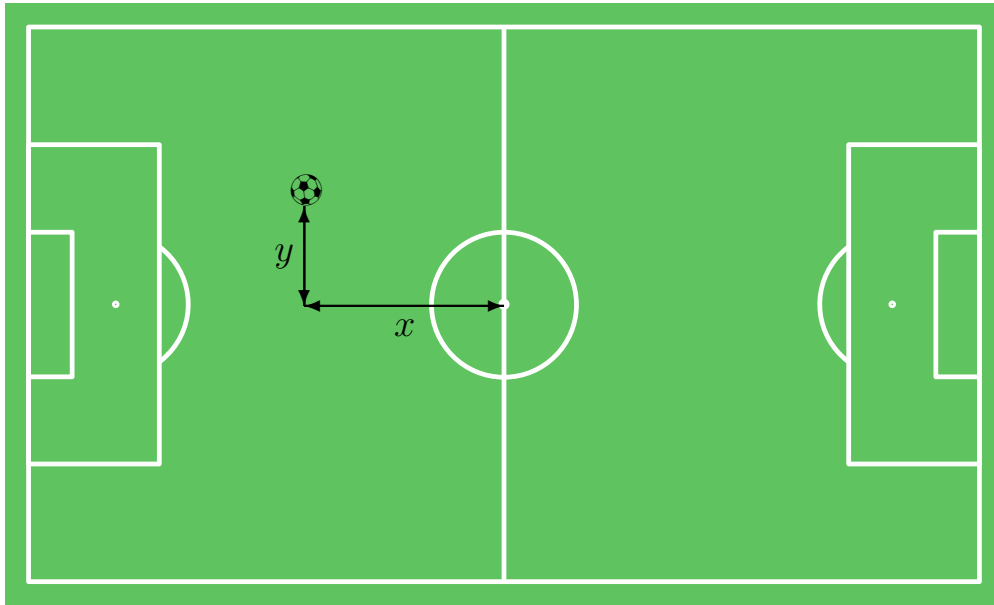


Figure E.1. Here we have a field with the ball at (x,y) .

The $|\odot_X\rangle$ and $|\odot_Y\rangle$ terms represent a *unit vector* in the X and Y directions. These are appropriately and separately scaled using the x and y coefficients to precisely locate the soccer ball. This notation can similarly be written using linear algebraic notation instead of Dirac notation.

$$|\odot\rangle = \begin{bmatrix} x \\ y \end{bmatrix} = x \begin{bmatrix} 1 \\ 0 \end{bmatrix} + y \begin{bmatrix} 0 \\ 1 \end{bmatrix}. \quad (\text{E.2})$$

Here, we explicitly denote the unit vectors, but we should recognize that those are not necessarily the only bases we can use; any orthogonal bases can be used. For instance, we can use $\begin{bmatrix} 1 \\ 1 \end{bmatrix}$ and $\begin{bmatrix} 1 \\ -1 \end{bmatrix}$ instead.

Once again, we remark that, in this example, the only degree of freedom we consider is the ball's location. Since this has *two* free parameters (x and y), we say that all states of this type exist in a *two*-dimensional Hilbert space. Additionally, sometimes these parameters

have boundaries. For soccer, the limits for x are -60 m and 60 m. Alternatively, y can range between -35 m and 35 m. Note that we assume the center of the field is the origin.

Instead, if we consider the color of the ball, we may use the following notation (both Dirac and linear algebraic):

$$|\text{⚽}\rangle = r |\text{⚽}_R\rangle + g |\text{⚽}_G\rangle + b |\text{⚽}_B\rangle = \begin{bmatrix} r \\ g \\ b \end{bmatrix} = r \begin{bmatrix} 1 \\ 0 \\ 0 \end{bmatrix} + g \begin{bmatrix} 0 \\ 1 \\ 0 \end{bmatrix} + b \begin{bmatrix} 0 \\ 0 \\ 1 \end{bmatrix}. \quad (\text{E.3})$$

For this example, there are three free parameters, implying that these states exist in a three-dimensional Hilbert space. Akin to an 8-bit *RGB* description for computer monitor pixel colors, we can limit the each of the free parameters to integers between 0 and 255.

When we simultaneously consider both location (L) and color (C), our state vector spans a six-dimensional Hilbert space. We denote this state as follows:

$$|\text{⚽}\rangle = |\text{⚽}\rangle_L \otimes |\text{⚽}\rangle_C = (x |\text{⚽}_X\rangle + y |\text{⚽}_Y\rangle) \otimes (r |\text{⚽}_R\rangle + g |\text{⚽}_G\rangle + b |\text{⚽}_B\rangle) \quad (\text{E.4})$$

These soccer ball's state vectors imply that the ball can, through some magic or fancy technology, change color depending on its location on the field. To make this mathematically

clearer, we expand Eq. (E.4) and write it explicitly as follows:

$$\begin{aligned}
 |\textcircled{\otimes}\rangle &= xr |\textcircled{\otimes}_X\rangle |\textcircled{\otimes}_R\rangle + xg |\textcircled{\otimes}_X\rangle |\textcircled{\otimes}_G\rangle + xb |\textcircled{\otimes}_X\rangle |\textcircled{\otimes}_B\rangle + yr |\textcircled{\otimes}_Y\rangle |\textcircled{\otimes}_R\rangle + yg |\textcircled{\otimes}_Y\rangle |\textcircled{\otimes}_G\rangle + yb |\textcircled{\otimes}_Y\rangle |\textcircled{\otimes}_B\rangle \\
 &= xr \begin{bmatrix} 1 \\ 0 \\ 0 \\ 0 \\ 0 \\ 0 \end{bmatrix} + xg \begin{bmatrix} 0 \\ 1 \\ 0 \\ 0 \\ 0 \\ 0 \end{bmatrix} + xb \begin{bmatrix} 0 \\ 0 \\ 1 \\ 0 \\ 0 \\ 0 \end{bmatrix} + yr \begin{bmatrix} 0 \\ 0 \\ 0 \\ 1 \\ 0 \\ 0 \end{bmatrix} + yg \begin{bmatrix} 0 \\ 0 \\ 0 \\ 0 \\ 1 \\ 0 \end{bmatrix} + yb \begin{bmatrix} 0 \\ 0 \\ 0 \\ 0 \\ 0 \\ 1 \end{bmatrix} = \begin{bmatrix} xr \\ xg \\ xb \\ yr \\ yg \\ yb \end{bmatrix}
 \end{aligned} \tag{E.5}$$

From this, it should be apparent that for each x, y location, there can exist a unique associated RGB color. This is the most general possible state for this “magical” type of soccer ball that can change colors based on its location on the field. This special connection or “magic” between the color and location is a type of *entanglement*. That is to say, knowing the location of the ball immediately tells information about the color of the ball. We remark that this entanglement is within a single ball’s degrees of freedom.

If, instead, the color and location do not depend on each other, then we can separate the terms (as initially written in Eq. (E.4)) and act on each degree of freedom independently. The state of a soccer ball of this type is referred to as *separable*.

Now, let us discuss when we have multiple soccer balls. We start with two soccer balls, $|\textcircled{\otimes}\rangle_1$ and $|\textcircled{\otimes}\rangle_2$. The subscripts outside the kets are used to identify the two soccer balls. Let us assume that these are the boring black soccer balls we started, and the only degree of

freedom of interest is their location. As such, we can write the two soccer ball's location as

$$\begin{aligned}
|\otimes\otimes\rangle &= |\otimes\rangle_1 \otimes |\otimes\rangle_2 = (x_1 |\otimes_X\rangle_1 + y_1 |\otimes_Y\rangle_1) \otimes (x_2 |\otimes_X\rangle_2 + y_2 |\otimes_Y\rangle_2) \\
&= x_1x_2 |\otimes_X\rangle_1 |\otimes_X\rangle_2 + x_1y_2 |\otimes_X\rangle_1 |\otimes_Y\rangle_2 + y_1x_2 |\otimes_Y\rangle_1 |\otimes_X\rangle_2 + y_1y_2 |\otimes_Y\rangle_1 |\otimes_Y\rangle_2 \quad (\text{E.6}) \\
&= x_1x_2 |\otimes_X\otimes_X\rangle + x_1y_2 |\otimes_X\otimes_Y\rangle + y_1x_2 |\otimes_Y\otimes_X\rangle + y_1y_2 |\otimes_Y\otimes_Y\rangle.
\end{aligned}$$

Here, in keeping with convention, we simplify the notation by removing the subscripts and combining both states' relevant parameter into the same ket, i. e., $|\otimes_X\rangle_1 |\otimes_X\rangle_2 = |\otimes_X\otimes_X\rangle$. When using the simplified notation, since we no longer have the identifying subscripts, the position of the terms in the ket is important. The first term represents the first soccer ball's position, whereas the second term represents the second ball's position. To impress upon the reader this importance, we highlight the distinction $|\otimes_X\otimes_Y\rangle \neq |\otimes_Y\otimes_X\rangle$, although $|\otimes_X\rangle_1 |\otimes_Y\rangle_2 = |\otimes_Y\rangle_2 |\otimes_X\rangle_1$.

Since you are an astute reader, you have already noticed that Eq. (E.4) and Eq. (E.6) are similar. Your hunch is correct; we treat independent degrees of freedom and independent discrete objects identically. This time, rather than possibly exhibiting intra-ball entanglement, we can have inter-ball entanglement. In other words, the location of the two balls can be linked "magically". In the extreme case, we can witness this entanglement if our state description implies that knowing the location of one ball deterministically tells you the location of the other ball. Alternatively, if the two ball's locations are truly independent, then we can describe that state as separable.

Up until this point, we have considered only kets and their tensor products to describe our state. There is an entirely different side of the Dirac bracket notation that we must consider, and that is the "bra". The bra of ψ is just the conjugate transpose (a.k.a. Hermitian

conjugate) of the ket of ψ . In other words, $\langle\psi|^\dagger = |\psi\rangle$ and $|\psi\rangle^\dagger = \langle\psi|$, where the \dagger indicates the Hermitian conjugate. In vector notation, since kets are column vectors, that implies that bras are row vectors, as shown for the soccer ball's location in Eq. (E.7).

$$\langle\textcircled{S}| = x^* \langle\textcircled{S}_X| + y^* \langle\textcircled{S}_Y| = x^* \begin{bmatrix} 1 & 0 \end{bmatrix} + y^* \begin{bmatrix} 0 & 1 \end{bmatrix} = \begin{bmatrix} x^* & y^* \end{bmatrix} \quad (\text{E.7})$$

Here, the little stars indicate the complex conjugate of those values. (Yes, we have now entered the imaginary plane).

Based on this, we can take the inner product of the bra and ket of a vector as shown below for two three-element vectors, A and B .

$$\langle A|B\rangle = (\langle A|)(|B\rangle) = \begin{bmatrix} A_1^* & A_2^* & A_3^* \end{bmatrix} \begin{bmatrix} B_1 \\ B_2 \\ B_3 \end{bmatrix} = A_1^*B_1 + A_2^*B_2 + A_3^*B_3 \quad (\text{E.8})$$

Note that the inner product of a state with itself is just the norm of the state. So for the soccer ball's location (assuming x and y can be complex), we obtain

$$\langle\textcircled{S}|\textcircled{S}\rangle = \begin{bmatrix} x^* & y^* \end{bmatrix} \begin{bmatrix} x \\ y \end{bmatrix} = x^*x + y^*y = |x|^2 + |y|^2 \quad (\text{E.9})$$

If instead, we choose to take an outer product of the ket and bra vectors, we obtain the following:

$$|A\rangle\langle B| = (|A\rangle)(\langle B|) = \begin{bmatrix} A_1 \\ A_2 \\ A_3 \end{bmatrix} \begin{bmatrix} B_1^* & B_2^* & B_3^* \end{bmatrix} = \begin{bmatrix} A_1B_1^* & A_1B_2^* & A_1B_3^* \\ A_2B_1^* & A_2B_2^* & A_2B_3^* \\ A_3B_1^* & A_3B_2^* & A_3B_3^* \end{bmatrix} \quad (\text{E.10})$$

This is useful when defining operators such as the density operator (density matrix) of pure states, as shown in §3.1.1.

There are many other useful realizations to be had with the Dirac bracket notation. Some such tasks include performing projective measurements or determining the probability of measuring a state given an input density matrix. Rather than explicitly showing their utility here, we encourage the reader to explore the field and discover these for themselves. We hope that this appendix does provide the reader with a sufficient basis to understand the notation used widely in this thesis, and the field at large.